The exploration of lanthanum based complexes oxides: preparation, characterization and gas sensing properties

By

Katekani Shingange

(M.Sc Physics)

Thesis presented in fulfillment of the requirements for the degree of

Doctor of Philosophy

at the

University of the Free State

Supervisor: Prof G.H Mhlongo

Co-supervisor: Prof H.C Swart

October 2019

DECLARATION

I, Katekani Shingange, hereby declare that the work contained in this thesis is my own original work and that I have not previously in its entirety or in part submitted it at any university for a degree.

Signature: ……

Date: ……

For my mother, Tinyiko S. Makhubele

ACKNOWLEDGEMENTS

- All things are started and sustained by God's Grace! Therefore I would like to thank the Almighty God for His steady love throughout!
- I would like to extend my utmost gratitude to my supervisors; **Professors Gugu.H Mhlongo and Hendrik. C. Swart,** thank you for the academic support and your patience throughout this journey.
- My heartfelt gratitude to **Prof Gugu Mhlongo,** who played a very encouraging role during this journey, Prof, thank you for your moral support and guidance, I am really grateful for having you as my career mentor!
- Sincere thank you to my mother; my number one fan; **Tinyiko Suzan Makhubele.** You made sure I receive education and you installed the love of science in me. Thank you for taking me to school and making sure I wrote all my homework. Thank you for your love, encouragement and prayers. Ndza nkhensa mhani! You are my inspiration!
- I would like to thank my family, especially my sisters **Vuyani** na **Masana Shingange and** my partner **Katekani Seyton Shihundla** for the support throughout this journey. I am also grateful to my two favourite girls **Wohlawuleka Shihundla and Kushonga Shingange** for helping me relax at times.
- Sincere appreciation to my colleague and friend **Rirhandzu Rikhotso,** baby all those lunch breaks together were really helpful, xo-xo!
- I would like to send my earnest gratitude to **Rapelang Motsoeneng**, **Nsindiso Sibanda (SwiC), Teboho Mokoena, Langutani Mathevula and Murendeni Nemufulwi**…y'all are wonderful... thank you!

- I would like to extend my gratitude to the department of Science and Innovation of South Africa and the Council for Scientific and Industrial Research (DSI/CSIR) Project numbers (CGER85X, HCARD03 and CGER77S) for the financial support.
- Great appreciation towards the Centre for Nanostructures and Advanced Materials (CeNAM) characterization facility, for TGA, XRD, SEM, TEM and BET characterization techniques.
- Thank you to the University of Free State for the XPS, ToF-SIMS and PL measurements, under the umbrella of the DST/NRF Sarchi chair in Advanced and Luminescent Materials (grant 84415)
- To everyone who assisted me academically from the CSIR and the UFS; thank you and May God bless you! I learnt a lot from different people throughout this journey, and I am really grateful to all lessons learnt.
- Lastly, I would like to thank myself for seeing this through and not stopping short!

Conferences, publications and honors

Conferences:

1 K. Shingange, H.C Swart, G.H Mhlongo. "Microwave-assisted synthesis of Au nanoparticles incorporated ZnO rose-like hierarchical structures and their gas sensing properties". 7th South African Conference on Photonic Materials, Brandfort, South Africa. 27-31 March 2017 (**Oral presentation**)

2 K. Shingange, H.C Swart, G.H Mhlongo. "Synthesis of La_2O_3 nanostructures via microwave-assisted hydrothermal method for potential use in gas sensing applications". NanoAfrica 2018, Kwa-Zulu Natal, South Africa. 22-25 April 2018 (**Poster presentation**)

3 (i) K. Shingange, H.C Swart, G.H Mhlongo. "La^{3+} doped ZnO nanofibers obtained through electrospinning: Influence of La^{3+} doping concentration on the structural, optical and gas sensing properties". 63rd Annual Conference of the South African Institute of Physics, Bloemfontein, South Africa. 25-29 June 2018 (**Oral presentation**)

(ii) K. Shingange, H.C Swart, G.H Mhlongo. "$LaAlO_3$ sheet-like nanostructures synthesized through microwave-assisted method and their gas sensing characteristics". 63rd Annual Conference of the South African Institute of Physics, Bloemfontein, South Africa. 25-29 June 2018. 25-29 June 2018 (**Poster presentation**)

4 K. Shingange, H.C Swart, G.H Mhlongo. "NH_3 sensing properties of Lanthanum doped ZnO nanofibers obtained through electrospinning method", Nanoscience's

young researchers Symposium (NYRS), Gauteng, South Africa. 16 November (**Oral presentation**) **1st Prize best presentation**.

5 K. Shingange, H.C Swart, G.H Mhlongo. "$LaBO_3$ (B= Fe, Co) nanofibers and their structural, optical and gas sensing characteristics". 8th South African Conference on Photonic Materials, Eastern Cape, South Africa.06-10 May 2019 (**Poster presentation**)

6 K. Shingange, H.C Swart, G.H Mhlongo. "Nano-sensors based on Semiconductor metal oxides". Max-Planck Post Lindau Seminar, Dusseldorf, Germany, 08 July 2019. **(Oral presentation)**

Publications:

1 K. Shingange, H.C Swart, G.H Mhlongo. "H_2S detection capabilities with fibrous-like La-doped ZnO nanostructures: A comparative study on the combined effects of La-doping and post-annealing" J Alloy. Compd.797 (2019) 284-301. *It is part of this work and has been discussed in chapter 4 of the thesis.*

2 Katekani Shingange, Hendrik Swart, Gugu.H Mhlongo. "Ultrafast Detection of Low Acetone Concentration Displayed by Au-Loaded $LaFeO_3$ Nanobelts owing to Synergetic Effects of Porous 1D Morphology and Catalytic Activity of Au Nanoparticles. *ACS Omega.*, 4 (2019) 19018-19029. *It is part of this work and has been discussed in chapter 7 of the thesis.*

3 K. Shingange, H.C Swart, G.H Mhlongo. "$LaBO_3$ (B= Fe, Co) nanofibers and their structural, luminescence and gas sensing characteristics". *Physica B.*, (2020) 578, 41883. *It is part of this work and has been discussed in chapter 5 of the thesis.*

4 K. Shingange, H.C Swart, G.H Mhlongo. "Design of porous p-type $LaCoO_3$ nanofibers with remarkable response and selectivity to ethanol at low operating

temperature" *Sens. Actuators B Chem.*, 308 (2020) 127670. *It is part of this work and has been discussed in chapter 6 of the thesis.*

5 K. Shingange, H.C Swart, G.H Mhlongo. "Design of $La_{1-x}Ce_xCoO_3$ ($0 \leq x \geq 0.2$) nanofibers and their improved ethanol sensing abilities at low operating temperatures" Under preparation for possible publication (2019). *It is part of this work and has been discussed in chapter 8 of the thesis*

Honors:

1 Lindau 2019 Young scientist

2 South African Women in Science Awards (SAWiSA) recipient-TATA Doctoral Scholarship Award

ABSTRACT

A series of 1D metal oxide nanostructures based on Lanthanum (La) were synthesized through electrospinning followed by calcination. Firstly, the effect of La doping on ZnO was studied by introducing different concentrations (0, 0.06, 0.3, 1 and 2 wt%) of La and subjecting the obtained products to different annealing temperatures of 500, 700 and 900 °C. All La-doped ZnO sensors displayed enhanced sensor responses toward H_2S as well as fast response/recovery times as compared to that of the pure ZnO based. Additionally, apart from the fact that these sensors displayed the highest responses, they also revealed relatively high selective responses to H_2S. The sensor based on 2 wt% doping annealed at 900 °C displayed the highest H_2S response as well as good repeatability, and stability. The H_2S sensing performance of the ZnO nanofibres (NFs) was attributed to synergetic effects of a higher surface area, large number of intrinsic defects and the catalytic activity of La.

Another study regarding $LaCoO_3$ and $LaFeO_3$ perovskites to investigate the influence of alternating the B-site cation on gas sensing revealed good acetone sensing at a low operating temperature of 120 °C with the $LaFeO_3$ NFs based sensor exhibiting high stable and selective response towards acetone with fast response and recovery time of 14 and 49 s. This high response was attributed to the high surface area and high density of oxygen related defects.

A further, investigation on the annealing effect on $LaCoO_3$ NFs based sensors obtained after annealing at different temperatures of 550, 650, and 700 °C was

conducted. Findings from field emission scanning electron microscope and high resolution transmission electron microscope demonstrated that the synthesized $LaCoO_3$ NFs consisted of a number of interconnected particles with average sizes of ~ 47, 58 and 77 nm, for 550, 650, and 700 °C annealing temperatures, respectively. Systematic gas sensing analysis revealed that the sensors based on $LaCoO_3$ NFs have substantial sensitivity to ethanol gas with the sensor obtained after annealing at 650 °C revealing an outstanding response of 32.4 toward 40 ppm at a lower optimum operating temperature of 120 °C. While it exhibited good selectivity to ethanol gas as well as fast response and recovery speeds of 26 and 66 s, respectively. The enhanced sensing capability of the $LaCoO_3$ NFs based sensor after annealing at 650 °C stems from combined effects of the interparticle NFs structure, which provided high surface area and porous channels. These allowed access to active sites as well as ease of gas diffusion and overlapping of the hole accumulation layers along the fiber direction producing continuous hole transfer channels.

For the study of the effect of loading different concentration of Au on $LaFeO_3$ nanobelts (NBs), the gas sensing findings revealed that Au/$LaFeO_3$ NBs based sensor with the Au concentration of 0.3 wt% displayed improved response of 125 to 40 ppm of acetone and rapid response and recovery times of 26 and 20s, respectively, at an optimal working temperature of 100 °C. Furthermore, all sensors demonstrated excellent response and remarkable selectivity towards acetone. The gas sensing mechanism of the Au/$LaFeO_3$ sensors was explained in consideration of the catalytic activity of the Au nanoparticles, which served as direct adsorption sites for oxygen and acetone

Lastly, a series of nanostructured $La_{1-x}Ce_xCoO_3$ perovskite oxides (x= 0-0.2), with NF morphology were prepared through the electrospinning method followed by annealing at 650 °C. The NF crystallite and particle size became smaller with an increasing Ce level, while the specific surface area increased linearly up to 25 m^2/g. X-ray diffraction revealed that Ce segregated as CeO_2 when the Ce addition level was x≥0.1. The NFs showed selectivity to ethanol with the pure $LaCoO_3$ showing its highest response of 32.4 at operating temperature of 120 °C, while $La_{1-x}Ce_xCoO_3$(x= 0.2) revealed a high response of 83.4 at 100 °C. The $La_{1-x}Ce_xCoO_3$ (x= 0.2) also displayed quick response and recovery times of 10 and 19s compared to the 240 and 286 s displayed by the pure $LaCoO_3$. The improved sensing performance can be attributed to the increased surface area brought upon by the reduced crystallite and particle size, which ensured exposure of more active sites. Also, X-ray photoelectron spectroscopy revealed an increased amount of the surface oxygen, which played a role in facilitating the adsorption and oxidation processes of the ethanol.

The sensing mechanisms involved between the nanostructures and the target gases are discussed in detail.

CONTENTS

Chapter 1 ____ *1*

Introduction ____ **1**

1.1 Synopsis ____ **1**

1.2 Problem statement ____ **4**

1.3 Study objectives ____ **5**

1.4 Thesis Chapters arrangement ____ **6**

1.5 References ____ **8**

Chapter 2 ____ *12*

Literature review ____ **12**

2.1 Introduction ____ **12**

2.2 n- and p-type conductivity in SMOs ____ **12**

2.3 Gas sensing mechanisms of n- and p-type SMOs ____ **13**

2.4 Make-up of a good SMO sensor ____ **15**

2.5 Influences on the sensing mechanism ____ **16**

2.5.1 Manipulation of the microstructure ____ 17

2.5.2 Doping to electronically sensitize the SMO ____ 18

2.5.3 Loading of noble metals to chemically sensitize the SMO ____ 19

2.6 Perovskite-based gas sensors ____ **20**

2.7 $LaCoO_3$ ____ **21**

2.8 $LaFeO_3$ ____ **22**

2.9 Manipulation of sensing performance of $LaCoO_3$ and $LaFeO_3$ ___ 23

2.9.1 Partial substitution of either A or B site cation ___ 23

2.9.2 Decoration with noble metals ___ 24

2.10 References ___ 1

Chapter 3 ___ 1

Material synthesis and characterization ___ 1

3.1 Introduction ___ 1

3.2 Electrospinning method ___ 1

3.3 Key experimental parameters ___ 2

3.3.1 Solution parameters ___ 3

3.3.2 Processing parameters ___ 4

3.4 Characterization techniques ___ 5

3.4.1 Structural and surface characterization techniques ___ 5

3.5 Thermal characteristics analysis ___ 16

3.5.1 Thermogravimetric Analysis (TGA) ___ 16

3.6 Optical characterization ___ 17

3.6.1 Photoluminescence (PL) ___ 17

3.7 Gas sensing experiment ___ 18

3.8 References ___ 20

Chapter 4 ___ 23

H_2S detection capabilities with fibrous-like La-doped ZnO nanostructures: A comparative study on the combined effects of La-doping and post-annealing ____ **23**

4.1 Introduction ____ **23**

4.2 Synthesis of the ZnO NFs ____ **26**

4.3 Characterization of the pure and La-doped ZnO NFs ____ **28**

4.4 Fabrication of pure and La-doped ZnO NFs-based sensors and their subsequent gas sensing tests ____ **29**

4.5 Results and discussion ____ **30**

4.5.1 Thermal Analysis ____ 30

4.5.2 Structural analysis ____ 32

4.5.3 Morphological analysis ____ 36

4.5.4 Surface analysis ____ 43

4.6 H_2S gas sensing properties ____ **51**

4.7 Gas sensing mechanism ____ **65**

4.8 Conclusion ____ **68**

4.9 References ____ **70**

Chapter 5 ____ ***75***

$LaBO_3$ (B= Fe, Co) nanofibers and their structural, luminescence and gas sensing characteristics ____ **75**

5.1 Introduction ____ **75**

5.2 Experimental procedure ____ **76**

5.3 Characterization ____ **77**

5.4 Gas sensors fabrication and measurements ____ **77**

5.5 Results ____ **79**

5.5.1 Structural and morphological characteristics ____ 79

5.5.2 Chemical composition analyses ____ 80

5.5.3 Surface area analysis ____ 83

5.5.4 Luminescence characteristics ____ 83

5.6 Gas sensing performance ____ **84**

5.7 Gas sensing mechanism ____ **87**

5.8 Conclusion ____ **90**

5.9 References ____ **92**

Chapter 6 ____ ***95***

Design of porous p-type $LaCoO_3$ nanofibers with remarkable response and selectivity to ethanol at low operating temperature ____ **95**

6.1 Introduction ____ **95**

6.2 Experimental section ____ **98**

6.2.1 Materials ____ 98

6.2.2 Synthesis of $LaCoO_3$ NFs ____ 98

6.3 Characterization ____ **98**

6.4 Fabrication of gas sensors ____ **99**

6.5 Results and discussions ____ **100**

6.5.1 Structural characteristics ____ 100

6.5.2 Morphological characteristics 103

6.5.3 Surface chemical composition analyses 106

6.5.4 Porous characteristics 108

6.6 Gas sensing characteristics 109

6.7 Sensing mechanism of $LaCoO_3$ NFs to ethanol gas 122

6.8 Conclusion 125

6.9 References 127

Chapter 7 134

Ultrafast detection of low acetone concentration displayed by Au loaded $LaFeO_3$ nanobelts owing to synergetic effects of porous 1d morphology and catalytic activity of Au nanoparticles 134

7.1 Introduction 134

7.2 Experimental section 137

7.2.1 Materials used 137

7.2.2 Preparation of the electrospinning precursor solutions 137

7.2.3 Fabrication of the pure and Au loaded $LaFeO_3$ NBs 138

7.3 Characterization of the pure and Au loaded $LaFeO_3$ NBs 138

7.4 Fabrication and measurement of gas sensors based on pure and Au loaded $LaFeO_3$ NBs 139

7.5 Results and discussion 140

7.5.1 Phase and Morphology analysis 140

7.5.2 Surface area and porosity analysis 145

7.5.3 Chemical composition analysis 146

7.6 Gas sensing performance of the pure and Au loaded $LaFeO_3$ NBs 149

7.7 Acetone sensing mechanism 155

7.8 Conclusion 159

7.9 References 160

Chapter 8 167

Design of $La_{1-x}Ce_xCoO_3$ ($0 \leq x \leq 0.2$) nanofibers and their improved ethanol sensing abilities at low operating temperatures 167

8.1 Introduction 167

8.2 Experimental details 170

8.2.1 Synthesis of $La_{1-x}Ce_xCoO_3$ NFs 170

8.3 Characterization of $La_{1-x}Ce_xCoO_3$ NFs 170

8.4 Preparation and gas sensing procedure of $La_{1-x}Ce_xCoO_3$ NFs 171

8.5 Results and discussion 172

8.5.1 Crystal phase composition, morphology, pore structure and surface chemistry of the $La_{1-x}Ce_xCoO_3$ composites 172

8.6 Gas sensing properties 180

8.7 Gas sensing mechanism of the $La_{1-x}Ce_xCoO_3$ NFs 187

8.8 Conclusion 189

8.9 References 190

Chapter 9 _____ *194*

Conclusion and future prospects _____ **194**

9.1 Conclusion _____ **194**

9.2 Future prospects _____ **195**

LIST OF FIGURES

Figure 2.1: Pie chart showing the SMOs studied as gas sensors [14]..... 13

Figure 2.2: Formation of electronic core-shell structures in SMOs..... 14

Figure 2.3: Schematic representation of the ABO_3 unit cell [78]..... 20

Figure 3.1: Schematic electrospinning setup utilized for preparation of nanostructured La-based metal oxide complexes..... 2

Figure 3.2: Schematic diagram of X-ray diffraction from the surface of a crystal [21]..... 6

Figure 3.3: Schematic representative of an X-ray diffractometer..... 7

Figure 3.4: Schematic diagram of the XPS process [17]. 8

Figure 3.5: Schematic set-up of XPS system [18]..... 9

Figure 3.6: Schematic set-up of ToF-SIMS system [23]..... 11

Figure 3.7: Schematic diagram of signals generated during incident beam and sample interaction [24]..... 12

Figure 3.8: Schematic set-up of the SEM [26]..... 13

Figure 3.9: Schematic diagram of the TEM [27]. 14

Figure 3.10: BET schematic representation [31]..... 15

Figure 3.11: Set up representative of the TGA [32]. 17

Figure 3.12: Schematic diagram of a photoluminescence spectrometer [21]. 18

Figure 3.13: Schematic diagram of the sensing station set-up..... 19

Figure 4.1: Schematic diagram of the electrospinning set-up. 28

Figure 4.2: The (a) top view, (b) bottom view and (c) sensor film connection during gas sensing measurements..... 30

Figure 4.3: TGA curves of the as-prepared PVP/La/ZnO composite fibers. 32

Figure 4.4: The XRD diffraction patterns for the pure and La-doped ZnO NFs annealed at (a) 500 °C, (b) 700 °C and (c) 900 °C. 35

Figure 4.5: SEM images of the (a) ZnO/PVP as-spun fibers, (b) pure and (c-f) La (0.06, 0.3, 1 and 2 wt%) doped ZnO NFs annealed at 500 °C. 40

Figure 4.6: SEM images of the (a) pure and (b-e) La (0.06, 0.3, 1 and 2 wt%) doped ZnO NFs annealed at 700 °C. 41

Figure 4.7: SEM images of the (a) Pure and (b-e) La (0.06, 0.3, 1 and 2 wt%) doped ZnO NFs annealed at 900 °C. 42

Figure 4.8: (a) TEM, (b) HR-TEM images (c) Selected Area Electron Diffraction (SAED) patterns, (d-g) EDS elemental maps and (h) EDS spectra of the 2 wt% La-doped ZnO NFs at 900 °C. 43

Figure 4.9: ToF-SIMS overlay images of the (a) Pure, (b) 0.3 wt% and (c) 2wt% La-doped ZnO NFs, showing the distribution of the Zn and La. 44

Figure 4.10: High resolution XPS spectra of the Zn2p core level regions for the pure and 2 wt% La-doped ZnO NFs at (a) 500, (b) 700 and (c) 900 °C. 46

Figure 4.11: High resolution XPS spectra of the La3d core level for the 2 wt% La-doped ZnO NFs annealed at (a) 500, (b) 700 and (c) 900 °C. 47

Figure. 4.12: The O1s spectra for the pure and the La = 2 wt% annealed at (a) and (d) 500, (b) and (e) 700 and (c) and (f) 900 °C. 48

Figure 4.13: Nitrogen adsorption/desorption isotherms of the pure and La-doped ZnO NFs with different La concentrations (0.06 to 2 wt%) at: (a) 500 °C, (b) 700 and (c) 900 °C. 51

Figure 4.14: The responses of pure ZnO and La-doped ZnO NFs based sensors annealed at (a) 500, (b) 700 and (c) 900 °C to 90 ppm of H_2S as the function of operation temperature. 54

Figure 4.15: Response-recovery curves of the pure and La (0.06, 0.3, 1 and 2 wt%) doped ZnO nanostructures annealed at (a) 500, (b) 700 and (c) 900 °C. ... 56

Figure 4.16: Sensor response of the pure and La (0.06, 0.3, 1 and 2 wt%) doped ZnO nanostructures annealed at (a) 500, (b) 700 and (c) 900 °C to different concentration of H_2S. ... 57

Figure 4.17: Response and recovery times for the pure and La-doped ZnO nanostructures for (a) 500, (b) 700 and (c) 900 °C annealing temperatures. ... 59

Figure 4.18: (a) Crystal size and (b) sensor response as a function of annealing temperature. ... 62

Figure 4.19: (a) Stability to 90 ppm H_2S over 30 days, (b) response to 90 ppm H_2S for five cycles of the La = 2 wt% at 900 °C based sensor and (c) Selectivity response of the pure and La-doped ZnO nanostructures towards 90 ppm of CH_4, NH_3, NO_2, H_2S and CO for samples annealed at 900 °C. ... 65

Figure 4.20: Proposed schematic diagram for the H_2S sensing mechanism by the ZnO NFs ... 68

Figure 5.1: Schematic of the set up for the sensing measurements. ... 79

Figure 5.2: Diffraction patterns and SEM micrographs of the (a) $LaFeO_3$ and (b) $LaCoO_3$ NFs. ... 80

Figure 5.3: XPS spectra of the (a-b) La 3d, (c) CO 2p, (d) Fe 2p, and (e-f) O 1s for the $LaCoO_3$ and $LaFeO_3$ NFs. ... 82

Figure 5.4: Nitrogen adsorption-desorption isotherms of the (a) $LaCoO_3$ and (b) $LaFeO_3$ NFs. ... 83

Figure 5.5: PL spectra of the $LaCoO_3$ and $LaFeO_3$ NFs after excitation at 325 nm using He-Cd laser as an excitation source. ... 84

Figure 5.6: (a) Current transients with the response versus gas concentration as inset, (b) responses to 40 ppm of different target gases and (c) repeatability measurements of $LaCoO_3$ and $LaFeO_3$ NFs based sensors. 89

Figure 6.1: Schematic diagram of the $LaCoO_3$ NFs synthesis and the fabrication of the sensors. 100

Figure 6.2: (a) XRD patterns and (b) enlarged perovskite peak range of the $LaCoO_3$ NFs annealed at different temperatures of 550, 650 and 700 °C. 102

Figure 6.3: SEM, TEM and HR-TEM images of the $LaCoO_3$ NFs obtained at (a, d and g) 550, (b, e and h) 650, (c, f and i) 700 °C, and the corresponding particle size distribution at (j) 550, (k) 650, (l) 700 °C. 105

Figure 6.4: XPS spectra of (a) La 3d, (b) Co 2p and (c-e) O 1s for the $LaCoO_3$ NFs annealed at 550, 650 and 700 °C. 107

Figure 6.5: Nitrogen adsorption-desorption isotherms for the $LaCoO_3$ NFs annealed at (a) 550, (b) 650 and (c) 700 °C. 109

Figure 6.6: Response curves of the $LaCoO_3$ NFs sensors at 550, 650 and 700 °C to ethanol gas at different operating temperatures of the $LaCoO_3$ NFs. 111

Figure 6.7: (a) Dynamic sensing transients to 2.5-40 ppm ethanol and (b) response of the sensors as a function of ethanol concentration. 112

Figure 6.8: The responses of the sensors based on the $LaCoO_3$ NFs to nine kinds of target gases at 40 ppm. 115

Figure 6.9: (a) The responses of all the $LaCoO_3$ NFs based sensors to 40 ppm ethanol under various RH, (b) the response-recovery curves of the NFs annealed at 650 °C to 40 ppm of ethanol under various RH and (c) responses of all the $LaCoO_3$ NFs based sensors to different humidity conditions without the ethanol. 117

Figure 6.12: Proposed ethanol sensing mechanism of the $LaCoO_3$ NFs.....124

Figure 7.1: Diffraction patterns of S1, S2, S3 and S4 respectively. 141

Figure 7.2: SEM images of the (a) as-spun, and (b) S1, (c) S2, (d) S3 and (e) S4 NBs, respectively after annealing at 500 °C.....143

Figure 7.3: TEM images of (a) S1, (c) S2, (e) S3 and (g) S4 with their corresponding EDS maps (b, d, f and h). Particle size distribution of the Au is represented as insets of each figure.....144

Figure 7.4: Nitrogen adsorption-desorption isotherms and the corresponding pore size distribution curves of S1, S2, S3 and S4. 146

Figure 7.5: (a) High magnification XPS spectra of (a-b) La 3d for S1 and S4, (c) Fe 2p for S1 and S4, (d) Au 4f for S4, (e-f) O 1s core levels of the for S1 and S4. 148

Figure 7.6: Responses of the S1, S2, S3 and S4 based sensors to 40 ppm of acetone at different operating temperatures. 150

Figure 7.7: Dynamic resistance curves of (a) S1, (b) S2, (c) S3, (d) S4 and (e) corresponding responses of S1-S4 to acetone concentrations ranging from 2.5 to 40 ppm.....153

Figure 7.8: (a) Gas responses to 40 ppm of different gases and (b) reproducibility of the S3 to 40 ppm acetone at 100 °C.....154

Figure 7.9: (a) Response histogram of S1-S4 based sensors and (b) S3 response and recovery curves to 40 ppm acetone in dry air and under different relative humidity of 30, 70 and 90% at 100 °C. 155

Figure 7.10: Proposed acetone sensing mechanism of the pure and Au loaded $LaFeO_3$ NBs. 157

Figure 8.1: XRD patterns of the $La_{1-x}Ce_xCoO_3$ (x = 0, 0.05, 0.1, 0.15 and 0.2) NFs. 173

Figure 8.2: SEM images of the $La_{1-x}Ce_xCoO_3$ NFs at different Ce content. 174

Figure 8.3: Nitrogen adsorption-desorption isotherms for the $La_{1-x}Ce_xCoO_3$ and their corresponding pore distribution as insets. 176

Figure 8.4: XPS spectra for (a) La 3d, (b) Co 2p, (c) Ce 3d and (d) O 1s for different Ce concentration. 179

Figure 8.5: Response curves of the $La_{1-x}Ce_xCoO_3$ NFs sensors to 40 ppm ethanol gas at different operating temperatures. 182

Figure 8.6: (a-e) Dynamic sensing transients to 2.5-40 ppm ethanol and (f) response of the sensors as a function of ethanol concentration. 184

Figure 8.7: (a) The responses of the sensors based on the $La_{1-x}Ce_xCoO_3$ NFs to different kinds of target gases at 40 ppm (b) Repeatable responses to 40 ppm ethanol for x = 0.2 and (c) Response stability of x = 0.2 to 40 ppm ethanol over two months.....186

Figure 8.8: Response to 40 ppm ethanol at different RH levels of 30, 50, 70 and 90%. 187

Chapter 1

Introduction

1.1 Synopsis

The ways of living are evolving every day, so does the technologies used on every day basis. One of the most recent and interesting technology that seems to be taking top spot in the research world is the nanotechnology. Nanotechnology is a technology that involves manipulation of materials at a nanoscale level (10^{-9} m). When materials are at this level, they start to exhibit unique and fascinating properties. Some of their unique properties include robustness, electrical conductivity and high surface area [1]. These properties of nanomaterials have created fascinating fields of study and applications in areas that can contribute towards improvement of everyday living.

One of the areas of applications benefiting from this nanotechnology is the gas sensing application. Gas sensing is an area that studies and applies materials into the use as gas sensor devices. Gas sensor is a device that is used to identify the changes in the make-up of the atmosphere's constituents using the air as reference. That is to say, a gas sensor identifies chemical gas molecules and converts the interaction into a physical signal [2]. These gas sensor devices are of paramount importance for many uses such as detection of gas leakages (for security and safety measures), in food processing (for food quality monitoring), as breathalysers (diagnosis of diabetes, liver diseases and for drunk and driving detection) [3-8], just to mention a few.

There are many materials that can be used as gas sensing materials such as carbon materials, optical fibers and semiconductor metal oxides (SMOs) [9-11]. Of all these materials, SMOs have been considered as great sensing materials and have been extensively studied for gas sensing application [12-17]. The interest in SMOs arise from the fact that SMOs have interesting properties that can be exploited for gas sensing, especially when they are in the nanostructured form [18-22]. These properties include high surface area, high electrical conductivity, physical and chemical stability, on top of this, SMOs are sensitive to both reducing and oxidizing gases [23-30].

Many SMOs have been used for the detection of many gases for different applications specifics. The mostly used SMOs are ZnO [10, 17], SnO_2 [31, 32], TiO_2 [33, 34], WO_3 [28, 35], In_2O_3 [36, 37], which are of n-type conductivity. In contrast, sensors based on SMOs of p-type conductivity such as CuO [38, 39], NiO [14, 40], CO_3O_4 [41, 42], $LaFeO_3$ [43, 44], Mn_3O_4 [45, 46], have been used, however, less than the n-type ones. This is because a response of a p-type sensor to a given gas is equal to the square root of the response obtained by an n-type sensor to the same gas and of the same morphology [15]. Nonetheless, the significance of p-type sensors should not be undermined considering the fact that these materials have been and still are used as catalysts to facilitate selective oxidation of different volatile organic compounds (VOCs) [47-49]. In this view, p-type SMOs are promising potentials for developing sensor materials with new functionalities. Of interest, p-type materials are also being used in composites with n-type materials to form p-n junctions and are used to modify gas sensing performance of the sensing materials by improving the electrical properties near the p-n interface [50]. Also, the typical adsorption of oxygen by p-type SMOs may

be exploited for the design of high performance gas sensing materials that are humidity independent with quick recovery kinetics [16]. Accordingly, p-type SMOs can provide a variety of new functionalities in SMOs sensors.

As part of the p-type oxides, perovskite oxides of ABO_3 structure have also been proven to be of unique class of SMOs. This family of oxides is known for its chemical and physical stability and mostly popular for its catalytic activities [12, 51-53]. Perovskite oxides including titanates ($SrTiO_3$, $CaTiO_3$, $BaTiO_3$, etc) and lanthanum-based perovskites ($LaCoO_3$, $LaFeO_3$, $LaNiO_3$, etc) have been demonstrated as good catalysts for the oxidation of methane and some VOCs [54-56]. Due to these qualities, perovskite oxides can be of new solutions for sensing applications.

Among the perovskites, lanthanum-based perovskites are considered of interest due to their unique electrical and electro catalytic properties. They have been found to possess exceptionally high thermal stability [57], indicating that they can provide microstructural and morphological stability to improve reliability and long-term sensor performance. A variety of them have also been used for gas sensing application towards CO, acetone, ammonia and ethanol [13,27,53,58, 59]. Their sensing performance has been found to be selective and stable. As much as this is desirable for sensing applications, there is still a need to work on their response which is normally lower than their n-type counterparts.

To achieve this, noble metals such as Ag, Pd and Au are dispersed into their surfaces to enhance not only their response but their selectivity and stability as well. On the other hand, partial substitution of either the A or the B site cation has been found to be an effective way to tune the sensing capabilities of these materials. Additionally, the microstructure of the perovskites can be manipulated

in order to tune the sensing properties, and one dimensional (1D) nanofibers have been found to be good morphology to couple with this class of materials due to the high surface-to-volume ratio and high porosity [60, 61].

1.2 Problem statement

Of late, there is an increase in the degree of air pollution caused by car emissions, refineries, industrials as well as power plants. Because of this, there is a need for gas sensors to monitor these air pollutants discharges as exposure to some of them can result in health problems or death. Not only are these gas sensors needed for environmental air monitoring, but even in the food industry for food quality monitoring by tracking concentrations of certain gases such as ethanol discharged by foodstuff such as fruit and milk. Further, gas sensors can be used as breathalysers to detect certain concentration of some volatile organic compounds (VOCs) such as acetone for diabetes diagnosis or ethanol for drunk and driving testing. Because of such needs, materials that can be used as sensors in the recognition of such gases are required for the prevention of gas leakages, environmental protection and also in areas for human health care.

The materials currently used for such devices are SMOs such as SnO_2, ZnO and WO_3. These materials have good responses to most reducing and oxidizing gases. However, most of them suffer from lack of selectivity especially towards VOCs due to their similarities, making it impossible for a sensor to properly identify the correct target gas. On the other hand, sensors based on these materials are operated at high temperatures above 400 °C thus consuming a lot of energy. Therefore, energy saving and reliable materials in terms of selective and stable response with fast response kinetics are in great need. Lanthanum-based

complexes such as $LaCoO_3$ and $LaFeO_3$ are promising materials for the application in gas sensing. This is due to their excellent catalytic properties which are proven by their many uses in catalysis, their affordability, high thermal and chemical stability. Though these complexes have remarkable features; most of them have p-type conductivity and their industrial application is limited from the fact that their response is equal to the square root of that of an n-type conducting semiconductor metal oxide with the same morphology configuration and conditions. Thus their response should be improved further. Decorating with noble metals and partial substitution has shown to further improve catalytic activity of La-based complexes which can improve gas sensing performance, thus these two modification methods can be used to improve the sensing performance of the La-based complexes.

1.3 Study objectives

This work is based on the study of structural, optical and gas sensing properties of La as a dopant, its perovskites namely $LaCoO_3$ and $LaFeO_3$. The effect of partial substitution and Au loading on the structural, morphological, optical and gas sensing properties is also studied.

The most important objective of this study is to do a thorough study on La as a dopant of ZnO, to study its perovskites ($LaFeO_3$ and $LaCoO_3$) in their pure form and when incorporated with noble metals (Au) or partially substituted (by Ce) on their La site and to master the electrospinning technique. To achieve that; the following objectives were set:

- To dope different concentrations of La into 1D ZnO nanostructures.

- To synthesize pristine 1D $LaCoO_3$ and $LaFeO_3$ using electrospinning followed by annealing method.
- To load Au unto 1D $LaFeO_3$ nanostructures.
- To partially substitute La by Ce on 1D $LaCoO_3$ nanostructures.
- Characterization of all synthesized nanostructures using Thermogravimetric Analysis (TGA), X-ray diffraction (XRD), Scanning electron microscope (SEM), Transmission electron microscope (TEM), Time-of-flight secondary ion mass spectroscopy (ToF-SIMS), Brunauer Emmett Teller (BET), Photoluminescence (PL) and X-ray photoelectron spectroscopy (XPS).
- Fabricate gas sensor devices based on the aforementioned nanostructures.
- Conduct sensing test measurements towards various gases, and operating temperatures.

1.4 Thesis Chapters arrangement

Chapter 1: A brief introduction to gas sensors and semiconductor metal oxides as sensing materials

Chapter 2: Literature survey on advancement of semiconductor metal oxide gas sensors

Chapter 3: Discusses electrospinning method and characterization techniques

Chapter 4: Studied the influence of La doping on ZnO nanostructures nanofibers

Chapter 5: Studied the variation of the B-site cation on the $LaBO_3$ (B= Co/Fe) nanofibers

Chapter 6: Studied the influence of annealing on $LaCoO_3$ nanofibers

Chapter 7: Studied the influence of Au loading on $LaFeO_3$ nanobelts

Chapter 8: Studied the influence of partially substituting the La site by Ce on $LaCoO_3$ nanofibers

Chapter 9: Summary and Future work

Chapter 10: List of publications and conferences

1.5 References

[1] H. Gleiter, Acta Mater., 48 (2000) 1-29.

[2] A. Hulanicki, S. Glab, F. Ingman, Pure. Appl. Chem., 63 (1991) 1247-1250.

[3] A. Dey, Mater. Sci. Eng. B., 229 (2018) 206-217.

[4] X. Gao, T. Zhang, Sens. Actuators B Chem., 277 (2018) 604-633.

[5] X.-J. Huang, Y.-K. Choi, Sens. Actuators B Chem., 122 (2007) 659-671.

[6] A. Loutfi, S. Coradeschi, G.K. Mani, P. Shankar, J.B.B. Rayappan, J. Food. Eng., 144 (2015) 103-111.

[7] B. Mandal, M. Das, M.T. Htay, S. Mukherjee, Mater. Res. Bull., 109 (2019) 281-290.

[8] D. Smith, C. Turner, P. Španěl, J. Breath. Res., 1 (2007) 014004.

[9] V. Schroeder, S. Savagatrup, M. He, S. Lin, T.M. Swager, Chem. Rev., 119 (2018) 599-663.

[10] V.S. Bhati, M. Hojamberdiev, M. Kumar, Energy Rep., DOI https://doi.org/10.1016/j.egyr.2019.08.070(2019).

[11] H.-N. Li, D.-S. Li, G.-B. Song, Eng. Struct., 26 (2004) 1647-1657.

[12] H. Aono, E. Traversa, M. Sakamoto, Y. Sadaoka, Sens. Actuators B Chem., 94 (2003) 132-139.

[13] J.-C. Ding, H.-Y. Li, X. Guo, Solid State Ion., 272 (2015) 155-159.

[14] I. Hotovy, V. Rehacek, P. Siciliano, S. Capone, L. Spiess, Thin Solid Films, 418 (2002) 9-15.

[15] M. Hübner, C. Simion, A. Tomescu-Stănoiu, S. Pokhrel, N. Bârsan, U. Weimar, Sens. Actuators B Chem., 153 (2011) 347-353.

[16] H.R. Kim, A. Haensch, I.D. Kim, N. Barsan, U. Weimar, J.H. Lee, Adv. Funct. Mater., 21 (2011) 4456-4463.

[17] J. Kim, K. Yong, J. Phys. Chem. C., 115 (2011) 7218-7224.

[18] W.-T. Koo, J.-S. Jang, S.-J. Choi, H.-J. Cho, I.-D. Kim, ACS Appl. Mater. Interfaces., 9 (2017) 18069-18077.

[19] S. Kumar, P. Sahare, J. Rare Earth., 30 (2012) 761-768.

[20] R. Leanza, I. Rossetti, L. Fabbrini, C. Oliva, L. Forni, Appl. Catal B Environ., 28 (2000) 55-64.

[21] W.-Y. Lee, H.J. Yun, J.-W. Yoon, J. Alloys. Compd., 583 (2014) 320-324.

[22] G. Li, X. Zhang, H. Lu, C. Yan, K. Chen, H. Lu, J. Gao, Z. Yang, G. Zhu, C. Wang, Sens. Actuators B Chem., 283 (2019) 602-612.

[23] G. Mhlongo, D. Motaung, I. Kortidis, N. Mathe, O. Ntwaeaborwa, H. Swart, B. Mwakikunga, S. Ray, G. Kiriakidis, Mater. Chem. Phys., 162 (2015) 628-639.

[24] C.W. Na, H.-S. Woo, I.-D. Kim, J.-H. Lee, Chem. Commun., 47 (2011) 5148-5150.

[25] K.-I. Choi, H.-R. Kim, J.-H. Lee, Sens. Actuators B Chem., 138 (2009) 497-503.

[26] J.-C. Ding, H.-Y. Li, T.-C. Cao, Z.-X. Cai, X.-X. Wang, X. Guo, Solid State Ion., 303 (2017) 97-102.

[27] I. Lee, B. Jung, J. Park, C. Lee, J. Hwang, C.-O. Park, Sens. Actuators B Chem., 176 (2013) 966-970.

[28] A.T. Mane, S.B. Kulkarni, S.T. Navale, A.A. Ghanwat, N.M. Shinde, J. Kim, V.B. Patil, Ceram. Int., 40 (2014) 16495-16502.

[29] J. Shi, R. Yan, Y. Zhu, X. Zhang, Talanta, 61 (2003) 157-164.

[30] K. Shingange, Z. Tshabalala, O. Ntwaeaborwa, D. Motaung, G. Mhlongo, J. Colloid Interface Sci., 479 (2016) 127-138.

[31] Y.-J. Choi, I.-S. Hwang, J.-G. Park, K.J. Choi, J.-H. Park, J.-H. Lee, Nanotechnology, 19 (2008) 095508.

[32] S. Das, V. Jayaraman, Prog. Mater. Sci., 66 (2014) 112-255.

[33] M. Arafat, A. Haseeb, S. Akbar, Sensors, 14 (2014) 13613-13627.

[34] B. Lyson-Sypien, M. Radecka, M. Rekas, K. Swierczek, K. Michalow-Mauke, T. Graule, K. Zakrzewska, Sens.Actuator. B., 211 (2015) 67-76.

[35] J. Lu, C. Xu, L. Cheng, N. Jia, J. Huang, C. Li, Mater. Sci. Semicond., 101 (2019) 214-222.

[36] X. Niu, H. Zhong, X. Wang, K. Jiang, Sens.Actuator. B., 115 (2006) 434-438.

[37] X. Sun, H. Ji, X. Li, S. Cai, C. Zheng, Mater. Lett., 120 (2014) 287-291.

[38] D.P. Volanti, A.A. Felix, M.O. Orlandi, G. Whitfield, D.J. Yang, E. Longo, H.L. Tuller, J.A. Varela, Adv. Funct. Mater., 23 (2013) 1759-1766.

[39] C. Yang, X. Su, F. Xiao, J. Jian, J. Wang, Sens. Actuators B Chem., 158 (2011) 299-303.

[40] I. Hotovy, J. Huran, P. Siciliano, S. Capone, L. Spiess, V. Rehacek, Sens. Actuators B Chem., 103 (2004) 300-311.

[41] H. Nguyen, S.A. El-Safty, J. Phys. Chem. C., 115 (2011) 8466-8474.

[42] C. Sun, X. Su, F. Xiao, C. Niu, J. Wang, Sens. Actuators B Chem., 157 (2011) 681-685.

[43] N.N. Toàn, S. Saukko, V. Lantto, Physica B., 327 (2003) 279-282.

[44] H. Fan, T. Zhang, X. Xu, N. Lv, Sens. Actuators B Chem., 153 (2011) 83-88.

[45] M. Amara, T. Larbi, A. Labidi, M. Karyaoui, B. Ouni, M. Amlouk, Mater. Res Bull., 75 (2016) 217-223.

[46] L. Zhang, Q. Zhou, Z. Liu, X. Hou, Y. Li, Y. Lv, Chem. Mater., 21 (2009) 5066-5071.

[47] S.C. Kim, W.G. Shim, Appl. Catal B Environ., 98 (2010) 180-185.

[48] Z.-Y. Tian, P.H.T. Ngamou, V. Vannier, K. Kohse-Höinghaus, N. Bahlawane, Appl. Catal B Environ., 117 (2012) 125-134.

[49] K. Pirkanniemi, M. Sillanpää, Chemosphere, 48 (2002) 1047-1060.

[50] Z. Zhang, C. Shao, X. Li, C. Wang, M. Zhang, Y. Liu, ACS Appl. Mater. Interfaces., 2 (2010) 2915-2923.

[51] B. Bashir, M.F. Warsi, M.A. Khan, M.N. Akhtar, Z.A. Gilani, I. Shakir, A. Wadood, Ceram. Int., 41 (2015) 9199-9202.

[52] E.L. Brosha, R. Mukundan, D.R. Brown, F.H. Garzon, J. Visser, M. Zanini, Z. Zhou, E. Logothetis, Sens. Actuators B Chem., 69 (2000) 171-182.

[53] Y. Chen, H. Qin, X. Wang, L. Li, J. Hu, Sens. Actuators B Chem., 235 (2016) 56-66.

[54] M. Goldwasser, M.E. Rivas, E. Pietri, M. Pérez-Zurita, M. Cubeiro, A. Grivobal-Constant, G. Leclercq, J. Mol. Catal A Chem., 228 (2005) 325-331.

[55] H. Arai, T. Yamada, K. Eguchi, T. Seiyama, Appl. Catal., 26 (1986) 265-276.

[56] B.P. Barbero, J.A. Gamboa, L.E. Cadús, Appl. Catal B Environ., 65 (2006) 21-30.

[57] H. Zhu, P. Zhang, S. Dai, ACS Catal., 5 (2015) 6370-6385.

[58] H. Liu, Y. Guo, R. Xie, T. Peng, G. Ma, Y. Tang, Sens. Actuators B Chem., 246 (2017) 164-168.

[59] X. Wang, H. Qin, L. Sun, J. Hu, Sens. Actuators B Chem., 188 (2013) 965-971.

[60] B. Ding, M. Wang, J. Yu, G. Sun, Sensors, 9 (2009) 1609-1624.

[61] J.-A. Park, J. Moon, S.-J. Lee, S.H. Kim, H.Y. Chu, T. Zyung, Sens. Actuators B Chem., 145 (2010) 592-595

Chapter 2

Literature review

2.1 Introduction

Since the discovery of SMOs as sensing materials, extensive amount of research has been focused into the development and improvement of these materials. The concept of using SMOs as gas sensing materials goes back to 1952 when Brattain and Bardeen reported for the first time gas sensitivity of Germanium [1]. Then Seiyama became the first to relate this phenomenon to the detection of CO_2, toluene and propane molecules using a ZnO based thin film in 1962 [2]. Still in 1962, Taguchi patented and afterward marketed a SnO_2 based gas sensor using a simple electrical circuit [3]. Right after the commercialization of the first SnO_2 based sensor device, an interest towards other SMOs was spiked among researchers. The interest in these SMOs is due to their affordability, ease in fabrication and use, and the ability to detect a variety of oxidizing and reducing gases. Nowadays SMOs are the most used group of inorganic materials as gas sensing materials [4-10]

2.2 n- and p-type conductivity in SMOs

Gas sensing mechanism is a surface based phenomenon, therefore the type of material, their chemical make-up and their surface area play an important role in the gas sensing characteristics. For SMOs, there are two classes based on their electrical conductivity, i.e. p- and n-type. P-type SMOs have holes as major charge carriers, whereas n-type have electrons as major charge carriers [11]. Both n and p-type SMOs have been used for the detection of toxic and harmful gases. Since

these two types of SMOs have different charge carriers, their gas sensing characteristics are bound to differ as well. However, the major charge carriers can be tuned by doping of acceptors or donors to achieve high response to gases or control other sensor performance characteristics. Between the two classes of SMOs, n-type are the ones mostly used; and this is due to the fact that their major charge carriers (electrons) are of great importance in a sensing process [12]. Also, it has been reported that the response of a p-type sensor to a specific gas is the square root of an n-type sensor with the same morphology configuration under the same gas conditions [13]. This discovery indicates that the responses of p-type based SMOs should be modified to be able to detect trace concentrations of different target gases. As can be seen from Figure 2.1, p-type sensors are the least studied SMO based sensors.

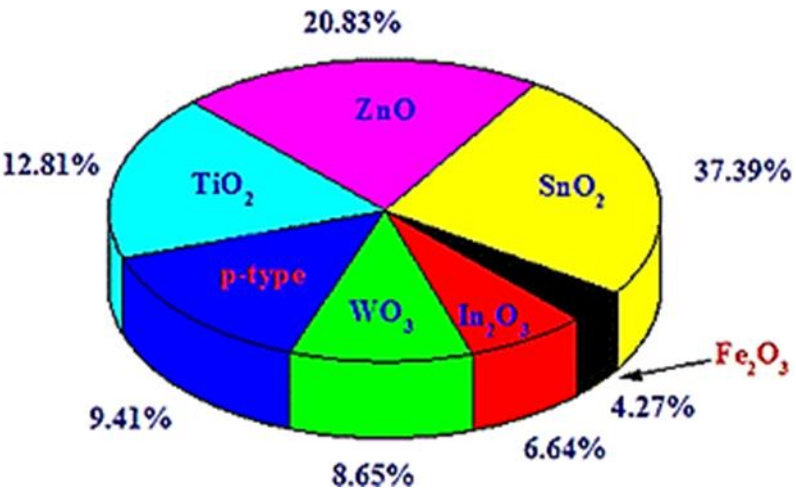

Figure 2.1: Pie chart showing the SMOs studied as gas sensors [14].

2.3 Gas sensing mechanisms of n- and p-type SMOs

When SMOs are exposed to ambient air at operating temperatures of 100-500 °C, oxygen molecules adsorb onto the surfaces of the SMOs form ionized oxygen

species by capturing electrons from the surfaces of the SMOs. The type of oxygen species depends on the operating temperature for instance O^-_2 is dominant at temperatures less than 150 °C, while O^- is abundant at temperatures between 150 and 400 °C and O^{2-} is dominant at temperatures more than 400 °C [15, 16]. Both p- and n-type SMOs develop electronic core-shell layers by adsorbing oxygen, however they display significantly different conduction behaviours [11]. For the n-type SMO, an electron depletion layer (EDL) will form near the surface followed by an increase in electrical resistance of the sensing material (Figure 2.2(a)). While in the case of a p-type sensor, a hole accumulation layer (HAL) will form near the surface of the material (Figure 2.2(b)), leading to a decrease in electrical resistance. When the n-type sensor is exposed to a reducing gas, the ionized oxygen species will oxidize the reducing gas releasing the trapped electrons back to the SMO. In contrast, for the p-type SMO, the resistance of the sensor will increase upon exposure to reducing gas while releasing electrons back into the SMO. The resistance of the p-type SMO is known to decrease upon exposure to oxidizing gases as the holes are increased in the HAL due to ion-sorption of oxidizing gas.

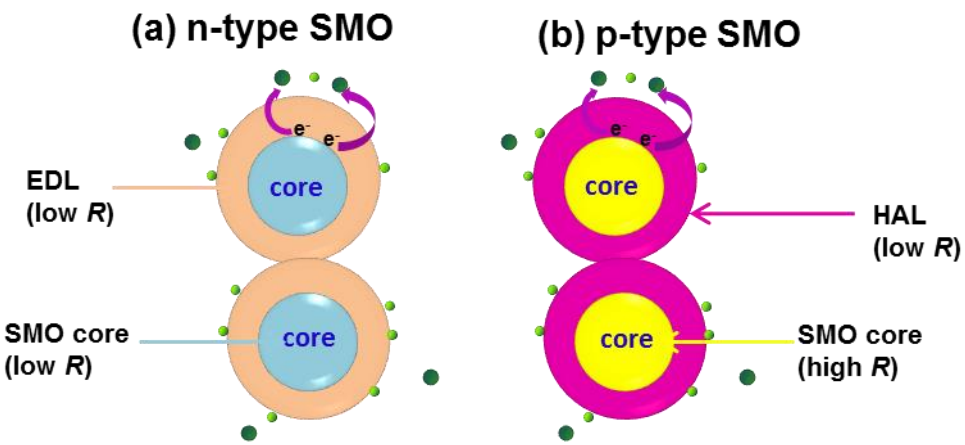

Figure 2.2: Formation of electronic core-shell structures in SMOs.

2.4 Make-up of a good SMO sensor

As mentioned previously, SMOs are sensitive to a variety of gas species, however for the SMO material to be deemed as a good sensor material it has to fulfil the following general characteristics of gas sensors:

i. **Response**: SMOs signal are based on changes of the resistance in the presence of the target gas *(Rg)* or in air *(Ra).* The ratio of the *Rg* and *Ra* gives the response of the SMO, depending on the conductivity. For n-type it is given by *Ra/Rg*, and for p-type it is given by *Rg/Ra* [17-19].

ii. **Operating temperature**: This is the temperature that the sensor material reaches its maximum response. Normally, the response of SMOs based sensors has been found to improve in proportion with the operating temperature. This is because at low working temperatures the reaction between target gas molecules and surface adsorbed oxygen species doesn't give high response as the target gas molecules do not have enough thermal energy to engage in a reaction with the surface oxygen species. Further increase of the operating temperature gives enough thermal energy to activate the target gas molecules, resulting in a rapid reaction with the oxygen species therefore leading to an increase in sensor response. However, at higher working temperatures the gas adsorption capacity and the usage of the sensing layer gets limited thus resulting in the decrease of the sensor response [20, 21].

iii. **Selectivity**: This is the ability of the sensor to be able to properly identify the correct gas in the midst of other gases more especially if they have similar properties. This characteristic of a sensor can be evaluated quantitatively by

taking the selectivity coefficient which is the ratio of the response of the highly selective gas to that of the interfering gases as:

$$K = R_1/R_2 \qquad (2.1)$$

where R_1 is the sensor response in the presence of the gas with the highest response and R_2 is the sensor response in the presence of the other target gases. The K values obtained are much greater than one which suggests that the sensor has greater ability to separate the specific target gas in the company of other gases [22, 23].

iv. **Limit of detection (signal-to-noise ratio>3):** This refers to the lowest amount of the target gas that can be detected by the sensor [23, 24].

v. **Response kinetics**: This refers to the amount of time taken by the sensor to reach 90% of its response signal value after introduction of the target gas (response time) and the amount of time the sensor takes to reach 90% of its initial baseline once the target gas had been removed (recovery time) [25, 26].

vi. **Stability:** The ability of the sensor to maintain its response over a long period of time without suffering from baseline drift or poisoning interactions [23, 27].

2.5 Influences on the sensing mechanism

The gas sensing of p-type SMOs is not as high as that one of n-type SMOs and hence it is important to enhance the gas response of p-type SMOs to use them in practical applications. In this case, gas response of p-type SMOs can be enhanced through various means including (1) manipulation of the microstructure of the nanostructures, (2) doping to electronically sensitize the SMO.and (3) loading of noble metals or metal oxides to chemically sensitize the SMO. However, to understand how these proposed options to tuning the gas sensing performance

of p-type SMOs, it is important to explore the important parameters in sensing i.e. the active adsorption sites.

2.5.1 Manipulation of the microstructure

Considering the fact that gas sensing mechanism is a surface reaction process, its response relies on the availability of active sites for gas adsorption. By increasing the specific surface area, the active adsorption sites required for interactions with the target gas also gets increased. Also, it is known that sometimes the structural defects in the SMO are also increased with the surface area thus influencing sensing performance. On the other hand, the morphology of the nanostructures has direct link to the specific surface area. For instance, previous findings have revealed that 0D-3D nanostructures possess different sensing performance [28-32]. Out of all these dimensions of the nanostructures, 1D nanostructure have been demonstrated as good candidates for gas sensing as they have high surface to volume ratio [25]. 1D nanostructures such as fibers present outstanding sensing performance owing to their morphological properties [33, 34]. In addition, nanofibers are made up of inter connected tiny particles making up the fibers morphology. Their style of connecting with each other creates pores which then result in ease of gas diffusion to all active sites. Moreover, due to the tiny size of the connected particles, the fibers offer high specific surface area, thus providing plenty of active sites for gas and oxide interactions [20]. To demonstrate the mechanism of the nanofibers is the work done by Khalil *et al* [35] whereby they optimized NiO nanofiber morphology through annealing and they realized that the nanofibers with the intermediate diameter, crystallinity and surface area were found to undergo the largest

resistance changes to which they attributed to their surface area, oxygen vacancies, crystallinity as well as morphology of their obtained nanofibers. From their study, it is important to point out that manipulation of the microstructure of the nanostructures can have an influence on their overall sensing performance of p-type SMO. Similar works on the manipulation of the microstructure of nanostructures to enhance sensing performance of p-type SMOs can be found elsewhere [36-44].

2.5.2 Doping to electronically sensitize the SMO

Since the resistance variations in SMOs is based on the charge carrier conduction in an oxide upon interaction with target gas, the amount of the charge carrier and the electrical configuration of the SMOs are key factors for manipulating the gas responses of SMOs [45]. Improvement of gas sensing response by altering the amount of charge carriers is called "electronic sensitization" [46]. Acceptor doping of n-type SMOs to reduce the amount of electrons in order to make n-type sensors more sensitive to reducing gases have been previously reported [47-50]. However electronically sensitizing p-type SMO is also an important way of producing practically applicable p-type based sensors considering the fact that it is highly challenging to obtain high response for p-type SMOs even when tiny sized nanostructures are used. Reports on electronically sensitizing p-type SMOs have been reported, such include the work by Kim *et al* [51] whereby they doped hollow NiO spheres with Fe. An increased response of the sensor to 100 ppm C_2H_5OH from 5.5 to 172.5 at operating temperature of 350 °C was observed and they attributed the response enhancement to electronic sensitization of NiO by Fe. Other similar works include the work by Yoon *et al* [52] on electronic

sensitization of C_2H_5OH response in p-type NiO nanofibers by Fe doping while Kim *et al* [53] reported on selective detection of NO_2 using Cr-doped CuO nanorods. These studies evidently confirmed that electronic sensitization is an influential means to develop highly sensitive p-type SMOs based sensors.

2.5.3 Loading of noble metals to chemically sensitize the SMO

Of all the available methods of manipulating the gas sensing performance of the SMOs, decorating of the SMO surface with noble metal nanoparticles such as Au, Ag, Pd and Pt have gained much interest due to the simplicity in the loading process and affordability [45]. Loading the SMO surface with noble metals have been shown to enhance the sensor response as well as response kinetics [54-60]. The improvement of gas sensing properties of SnO_2 by incorporation of metal particles was investigated by Yamazoe [61] in 1983. It was in this study they found that the quantity and size of the particles play a key role in the gas sensing performance, where nano-sized particles showed best response [61]. Ever since then, the effect of adding metal particles on the gas sensing performance have been extensively studied [62-67]. The nanoparticles must be in small amounts and homogeneously distributed on the host material to achieve best sensing performance [68, 69]. The mechanisms responsible for the enhanced response after the decoration with noble metal nanoparticles include electronic and chemical (spill-over) sensitization [67, 70]. During the sensing performance of these decorated SMOs, spill-over mechanism, Fermi level control and catalytic conversion on the decorated surfaces have to be taken into account [45] as this leads to better selectivity and higher response.

2.6 *Perovskite-based gas sensors*

Perovskite oxides is a family of oxides with a general formula ABO_3 whereby *A* and *B* are cations with different sizes. The *A* site cation is usually a rare earth, alkaline earth or alkali metal whereas the *B* site cation can be any of the transition metals namely Co, Fe, Cr and Mn [71-74]. Perovskites are interesting materials with exceptional properties such as thermal stability, redox behaviour, ionic conductivity, electronic structure and electron mobility [75-77]. A typical ideal cubic perovskite oxide unit cell is shown in Figure 2.3. The unit cell is from space group *Pm3m* whereby *A* coordinates with twelve oxygen anions and *B* coordinates with six oxygen anions.

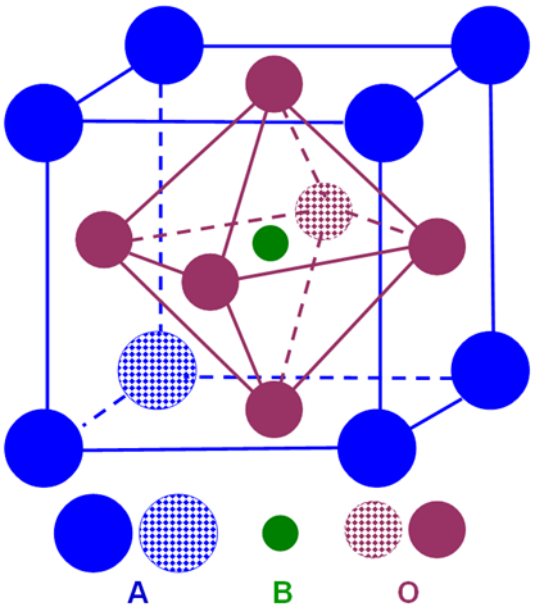

Figure 2.3: Schematic representation of the ABO_3 unit cell [78].

Perovskites are best known for their catalytic activity which is well demonstrated by their applications in catalysis and gas sensing [79-84]. The crystalline structure of the perovskites can be tuned by inserting a wide range of

either the A or B cation with different sizes and valences which can lead to the variation in the oxygen stoichiometry and vacancies [85]. Also, alternating the A or B cations offer flexibility with regard to designing their physi-chemical properties [85]. For instance, alternating Co, Mn or Fe on the B site provides redox active sites which assists in catalytic reactions [86, 87]. Further, partial substitution of A or B with other elements such as Ce or Sr introduces oxygen vacancies which assist in oxygen transfer thus increasing oxygen mobility [88, 89].

The huge family of perovskites and the allowance for a wide range of substitution give rise to the flexibility of their band structure and this influences the catalytic performance. For instance, B site cations play a role in modulating the electronic of perovskites, thus modifying the catalytic processes. This effect is controlled by the bond between the species on the B site and the oxygen species [85, 90].

Amongst the perovskites, lanthanum based perovskites ($LaCoO_3$, $LaFeO_3$, $LaMnO_3$, etc.) have been mostly studied and have revealed remarkable catalytic performance, making them ideal for gas sensing applications [72,73,91].

2.7 $LaCoO_3$

$LaCoO_3$ is a p-type semiconductor having a rhombohedral perovskite structure with unit cell parameters a= 5.4 Å and c= 13.1 Å and consisting of a narrow band gap (0.5–0.6 eV) at room temperature [92-94]. Its electronic structure depends on the spin state of the cations Co^{3+}. The temperature induced spin state excitation of Co^{3+} accounts for the transformations of $LaCoO_3$ from a nonmagnetic insulator to a paramagnetic semiconductor at 90–100 K. At a

temperature of 500 K, the material transforms into the paramagnetic metallic conductor possessing the high spin Co^{3+} states [95, 96]. Oxygen deficiency is an intrinsic property of the pure and doped $LaCoO_3$ compounds and the oxygen vacancies are the energetically favourable defects in lanthanum cobaltite. for this reason, the concentration of oxygen vacancies increases with the increase of temperature [97, 98]. In spite of this, the hole-type conduction can be rationalized by partial disproportionation of Co^{3+} into Co^{2+} and Co^{4+}. In this case the electrons are trapped at the Co^{2+} states, while Co^{4+} states bring about mobile holes [87, 99, 100]. In addition, $LaCoO_3$ is one of the competitive and promising materials for gas sensing due to its interesting physical properties such as catalytic oxidation of compounds and sensitivity to some gases. So far, many functional $LaCoO_3$ nanostructures with different architectures have been prepared and their sensing performance towards different gases has been investigated [72,79-81,100,101]. However, of the reported sensing performance of $LaCoO_3$ operates at high temperatures in the range of 200-600 °C to enhance their chemical reactivity which consumes a lot of energy [102]. Further, $LaCoO_3$ sensors suffer from poor sensor stability which is a disadvantage for practical applications.

2.8 $LaFeO_3$

$LaFeO_3$ crystallizes in a distorted perovskite structure with an orthorhombic unit cell [103]. $LaFeO_3$ perovskite shows oxygen-excess structure and p-type conductivity at atmospheric pressure and high temperature [104]. Further, Fe^{3+}ions in $LaFeO_3$ perovskite may get oxidized further to the Fe^{4+} ions in the presence of oxygen at high temperatures. On the other hand, Fe^{4+} ions are

unstable and may result in the formation of oxygen vacancies in the perovskite structure [104]. On the basis of this, $LaFeO_3$ has been identified as a promising gas sensor material due to its interesting properties such high electrical conductivity and catalytic activity for surface-driven redox reactions [91, 105]. However, its sensing performance such as sensitivity, selectivity and response kinetics can still be further improved.

2.9 Manipulation of sensing performance of $LaCoO_3$ and $LaFeO_3$

2.9.1 Partial substitution of either A or B site cation

As mentioned earlier, partial substitution of either A or B site cation in the perovskite can tune their properties and this can influence the gas sensor sensing performance. There are some cases whereby partial substitution of either A or B site cations resulted in positive influence on the sensing performance. For instance, Zhang *et al* [106] and Song *et al* [107] substituted Pb on the La site of $LaFeO_3$ and Co on the Fe site and they both observed an increased sensing performance. While substitution of Sr on the La site or of Mg on the Fe site by Lantto *et al* [108] did not result in any substantial advancement in gas sensing properties. In contrast, the response of $LaCoO_3$ to CO was improved by doping Sr on the La site and Cu or Ni on the Co site in the work done by Chai *et al* [109].

Cerium is usually reported as a good promoter which enhances catalytic oxygen activity [110]. For gas sensing, the availability of more oxygen on the surface may result in higher catalytic activity which may improve the gas performance. Partial substitution of La^{3+} by Ce^{4+} results in the reduction of Co^{3+} to Co^{2+} and/or a change in oxygen stoichiometry to ensure the charge compensation [80, 111].

An increase in the Ce level on the structure is expected to increase the number of surface oxygen, which is beneficial for gas reactions.

2.9.2 Decoration with noble metals

Incorporation of noble metals such as Ag, Au and Pd has been proven to be more effective since noble metal nanoparticles bring about chemical catalytic effect whereby the noble metal nanoparticles acts as direct active sites for the adsorption of analyte gas and assisting in the chemical reactions between the analyte gas and the sensing material [112]. Additionally, the noble metals can also fast track the transfer of electrons to the surfaces of the sensing material. The effect of decorating lanthanum based perovskites has been investigated. For example, Michel *et al* [113]decorated $LaCoO_3$ with Ag nanoparticles for gas sensing applications. They found that Ag-$LaCoO_3$ had better stability for the detection of CO, CO_2 and O_2 at in comparison to the pure $LaCoO_3$ 250 °C [113]. Cao *et al* [114] also observed enhanced ethanol response after modifying $LaFeO_3$ nanoparticles with Au and Cl. Other studies also reported the positive enhancements on gas sensing performance after decorating the perovskites surfaces with noble metal nanoparticles [105,115-117].

2.10 References

[1] W.H. Brattain, J. Bardeen, Bell Labs Tech. J., 32 (1953) 1-41.

[2] T. Seiyama, A. Kato, K. Fujiishi, M. Nagatani, Anal. Chem. 34 (1962) 1502-1503.

[3] N. Taguchi, Japanese Patent, S45-38200, (1962).

[4] S. Phanichphant, Procedia Eng, 87 (2014) 795-802.

[5] N. Yamazoe, K. Shimanoe, Procedia Chem., 1 (2009) 658-661.

[6] M. Chakraborty, M.S.J. Hashmi, Module in Materials Science and Materials Engineering, Elsevier (2019)

[7] M. Leidinger, M. Rieger, D. Weishaupt, T. Sauerwald, M. Nägele, J. Hürttlen, A. Schütze, Procedia Eng., 120 (2015) 1042-1045.

[8] E. Martinelli, D. Polese, A. Catini, A. D'Amico, C. Di Natale, Sens. Actuators B Chem., 161 (2012) 534-541.

[9] Y. Zhang, Y. Liu, L. Zhou, D. Liu, F. Liu, F. Liu, X. Liang, X. Yan, Y. Gao, G. Lu, Sens. Actuators B Chem., 273 (2018) 991-998.

[10] X. Zhang, W. Lan, J. Xu, Y. Luo, J. Pan, C. Liao, L. Yang, W. Tan, X. Huang, Sens. Actuators B Chem., 289 (2019) 144-152.

[11] H.-J. Kim, J.-H. Lee, Sens. Actuators B Chem., 192 (2014) 607-627.

[12] N. Yamazoe, G. Sakai, K. Shimanoe, Catal. Surv. Asia., 7 (2003) 63-75.

[13] M. Hübner, C. Simion, A. Tomescu-Stănoiu, S. Pokhrel, N. Bârsan, U. Weimar, Sens. Actuators B Chem., 153 (2011) 347-353.

[14] A. Mirzaei, B. Hashemi, K. Janghorban, J. Mater. Sci. Mater. Electron., 27 (2016) 3109-3144.

[15] N. Barsan, U. Weimar, J. ElectroCaram., 7 (2001) 143-167.

[16] F. Gu, D. You, Z. Wang, D. Han, G. Guo, Sens. Actuators B Chem., 204 (2014) 342-350.

[17] P.-S. Cho, K.-W. Kim, J.-H. Lee, J. Electroceram., 17 (2006) 975-978.

[18] M. Akiyama, J. Tamaki, N. Miura, N. Yamazoe, Chem. Lett., 20 (1991) 1611-1614.

[19] K. Fan, H. Qin, L. Wang, L. Ju, J. Hu, Sens. Actuators B Chem., 177 (2013) 265-269.

[20] K. Shingange, H.C. Swart, G.H. Mhlongo, J. Alloys. Compd., 797 (2019) 284-301.

[21] C. Wang, X. Cheng, X. Zhou, P. Sun, X. Hu, K. Shimanoe, G. Lu, N. Yamazoe, ACS Appl. Mater. Int., 6 (2014) 12031-12037.

[22] Y.-F. Sun, S.-B. Liu, F.-L. Meng, J.-Y. Liu, Z. Jin, L.-T. Kong, J.-H. Liu, Sensors, 12 (2012) 2610-2631.

[23] A. Wei, L. Pan, W. Huang, Mat. Sci. Eng B., 176 (2011) 1409-1421.

[24] P. Gründler, Chemical sensors: Springer Science & Business Media (2007)

[25] M. Arafat, B. Dinan, S.A. Akbar, A. Haseeb, Sensors., 12 (2012) 7207-7258.

[26] N. Tamaekong, C. Liewhiran, A. Wisitsoraat, S. Phanichphant, Sensors., 9 (2009) 6652-6669.

[27] G. Korotcenkov, Mater. Sci. Eng B., 139 (2007) 1-23.

[28] M. Amara, T. Larbi, A. Labidi, M. Karyaoui, B. Ouni, M. Amlouk, Mater. Res. Bull., 75 (2016) 217-223.

[29] S. Bai, T. Guo, Y. Zhao, J. Sun, D. Li, A. Chen, C.C. Liu, Sens. Actuators B Chem. 195 (2014) 657-666.

[30] V.S. Bhati, M. Hojamberdiev, M. Kumar, Energy. Rep., DOI https://doi.org/10.1016/j.egyr.2019.08.070 (2019).

[31] J. Cao, S. Wang, H. Zhang, T. Zhang, Mater. Sci. Semicond., 101 (2019) 10-15.

[32] K. Shingange, Z.P. Tshabalala, B.P. Dhonge, O.M. Ntwaeaborwa, D.E. Motaung, G.H. Mhlongo, Mater. Res. Bull., 85 (2017) 52-63.

[33] X.L. Xu, Y. Chen, S.Y. Ma, W.Q. Li, Y.Z. Mao, Sens. Actuators B Chem., 213 (2015) 222-233.

[34] Y. Zhang, X. He, J. Li, Z. Miao, F. Huang, Sens. Actuators B Chem., 132 (2008) 67-73.

[35] A. Khalil, J.J. Kim, H.L. Tuller, G.C. Rutledge, R. Hashaikeh, Sens. Actuators B Chem., 227 (2016) 54-64.

[36] J.E. Lee, D.Y. Kim, H.-K. Lee, H.J. Park, A. Ma, S.-Y. Choi, D.-S. Lee, Sens. Actuators B Chem., 292 (2019) 289-296.

[37] D. Li, Y. Tang, D. Ao, X. Xiang, S. Wang, X. Zu, Int. J. Hydrog. Energy, 44 (2019) 3985-3992.

[38] A.I. Ayesh, R.E. Ahmed, M.A. Al-Rashid, R.A. Alarrouqi, B. Saleh, T. Abdulrehman, Y. Haik, L.A. Al-Sulaiti, Sens. Actuators A Phys., 283 (2018) 107-112.

[39] C.-H. Wu, Z. Zhu, H.-M. Chang, Z.-X. Jiang, C.-Y. Hsieh, R.-J. Wu, J Alloys. Compd., 814 (2020) 151815.

[40] H. Gao, J. Guo, Y. Li, C. Xie, X. Li, L. Liu, Y. Chen, P. Sun, F. Liu, X. Yan, F. Liu, G. Lu, Sens. Actuators B Chem., 284 (2019) 305-315.

[41] T.P. Mokoena, H.C. Swart, D.E. Motaung, J. Alloys. Compd., 805 (2019) 267-294.

[42] Z. Deng, G. Meng, X. Fang, W. Dong, J. Shao, S. Wang, B. Tong, J. Alloys. Compd., 777 (2019) 52-58.

[43] H.J. Park, S.Y. Hong, D.H. Chun, S.W. Kang, J.C. Park, D.-S. Lee, Sens. Actuators B Chem., 287 (2019) 437-444.

[44] L. Hou, C. Zhang, L. Li, C. Du, X. Li, X.-F. Kang, W. Chen, Talanta, 188 (2018) 41-49.

[45] D. Zappa, V. Galstyan, N. Kaur, H.M.M. Arachchige, O. Sisman, E. Comini, Anal. Chim. Acta., 1039 (2018) 1-23.

[46] N. Yamazoe, Sens. Actuators B Chem., 5 (1991) 7-19.

[47] S. Pati, P. Banerji, S.B. Majumder, Int. J. Hydrog. Energy, 39 (2014) 15134-15141.

[48] K. Galatsis, L. Cukrov, W. Wlodarski, P. McCormick, K. Kalantar-zadeh, E. Comini, G. Sberveglieri, Sens. Actuators B Chem., 93 (2003) 562-565.

[49] X. Wang, T. Wang, G. Si, Y. Li, S. Zhang, X. Deng, X. Xu, Sens. Actuators B Chem., 302 (2020) 127165.

[50] L. Liu, Z. Zhong, Z. Wang, L. Wang, S. Li, Z. Liu, Y. Han, Y. Tian, P. Wu, X. Meng, Am. Ceram. Soc. Bull., 94 (2011) 3437-3441.

[51] H.-J. Kim, K.-I. Choi, K.-M. Kim, C.W. Na, J.-H. Lee, Sens. Actuators B Chem., 171 (2012) 1029-1037.

[52] J.-W. Yoon, H.-J. Kim, I.-D. Kim, J.-H. Lee, Nanotechnology, 24 (2013) 444005.

[53] K.-M. Kim, H.-M. Jeong, H.-R. Kim, K.-I. Choi, H.-J. Kim, J.-H. Lee, Sensors, 12 (2012) 8013-8025.

[54] T.-F. Dua, Y.-M. Zhang, J. Zhang, Z.-Q. Zhu, Q.-J. Liu, Materials Science Forum, 2016.

[55] J. Fu, C. Zhao, J. Zhang, Y. Peng, E. Xie, ACS Appl. Mater. Interfaces., 5 (2013) 7410-7416.

[56] R. Malik, V.K. Tomer, L. Kienle, V. Chaudhary, S. Nehra, S. Duhan, Adv. Mater. Interfaces., 5 (2018) 1701357.

[57] G.H. Mhlongo, D.E. Motaung, F.R. Cummings, H.C. Swart, S.S. Ray, Sci. Rep., 9 (2019) 9881.

[58] G.H. Mhlongo, D.E. Motaung, H.C. Swart, Mater. Lett., 160 (2015) 200-205.

[59] J. Moon, J.-A. Park, S.-J. Lee, T. Zyung, I.-D. Kim, Sens. Actuators B Chem., 149 (2010) 301-305.

[60] Q. Rong, Y. Zhang, J. Hu, K. Li, H. Wang, M. Chen, T. Lv, Z. Zhu, J. Zhang, Q. Liu, Sci. Rep., 8 (2018) 14220.

[61] N. Yamazoe, Y. Kurokawa, T. Seiyama, Sens. Actuators B Chem, 4 (1983) 283-289.

[62] R. Zhang, S.Y. Ma, Q.X. Zhang, K.M. Zhu, Y. Tie, S.T. Pei, B.J. Wang, J.L. Zhang, Mater. Lett., 254 (2019) 178-181.

[63] A. Natkaeo, D. Phokharatkul, J.H. Hodak, A. Wisitsoraat, S.K. Hodak, Sens. Actuators B Chem., 260 (2018) 571-580.

[64] J.-g. Kang, J.-S. Park, H.-J. Lee, Sens. Actuators B Chem., 248 (2017) 1011-1016.

[65] M.F. Fellah, Int. J. Hydrogen. Energy, 44 (2019) 27010-27021

[66] X. Hu, Z. Zhu, C. Chen, T. Wen, X. Zhao, L. Xie, Sens. Actuators B Chem., 253 (2017) 809-817.

[67] J.-K. Choi, I.-S. Hwang, S.-J. Kim, J.-S. Park, S.-S. Park, U. Jeong, Y.C. Kang, J.-H. Lee, Sens. Actuators B Chem., 150 (2010) 191-199.

[68] K. Shingange, H.C. Swart, G.H. Mhlongo, Physica B., 535 (2018) 216-220.

[69] K. Shingange, Z. Tshabalala, O. Ntwaeaborwa, D. Motaung, G. Mhlongo, J. Colloid. Interface. Sci., 479 (2016) 127-138.

[70] P. Rai, Y.-S. Kim, H.-M. Song, M.-K. Song, Y.-T. Yu, Sens. Actuators B Chem., 165 (2012) 133-142.

[71] B.P. Barbero, J.A. Gamboa, L.E. Cadús, Appl. Catal B Environ., 65 (2006) 21-30.

[72] E.L. Brosha, R. Mukundan, D.R. Brown, F.H. Garzon, J. Visser, M. Zanini, Z. Zhou, E. Logothetis, Sens. Actuators B Chem., 69 (2000) 171-182.

[73] H. Zhang, P. Song, D. Han, Q. Wang, Physica E., 63 (2014) 21-26.

[74] X. ZHANG, L. Huaju, L. Yong, S. Wenjie, Chinese J. Catal., 33 (2012) 1109-1114.

[75] M. Pena, J. Fierro, Chem. Rev., 101 (2001) 1981-2018.

[76] R.E. Schaak, T.E. Mallouk, Chem. Mater., 14 (2002) 1455-1471.

[77] S. Royer, D. Duprez, F. Can, X. Courtois, C. Batiot-Dupeyrat, S. Laassiri, H. Alamdari, Chem. Rev., 114 (2014) 10292-10368.

[78] http://www.globalsino.com/EM/page3533.html, (Accessed 03 October 2019).

[79] J.-C. Ding, H.-Y. Li, Z.-X. Cai, X.-X. Wang, X. Guo, Sens. Actuators B Chem., 222 (2016) 517-524.

[80] M. Ghasdi, H. Alamdari, S. Royer, A. Adnot, Sens. Actuators B Chem., 156 (2011) 147-155.

[81] L. Gildo-Ortiz, H. Guillén-Bonilla, V.M. Rodríguez-Betancourtt, O. Blanco-Alonso, A. Guillén-Bonilla, J. Santoyo-Salazar, I.C. Romero-Ibarra, J. Reyes-Gómez, Ceram. Int., 44 (2018) 15402-15410.

[82] C. Gong, G. Fan, Y. Hou, C. Song, Q. Huang, Z. Zhang, Front. Chem. Eng. China, 1 (2007) 6-10.

[83] W. Haron, A. Wisitsoraat, S. Wongnawa, Ceram. Int., 43 (2017) 5032-5040.

[84] K. Hayat, S.S. Shah, M. Yousaf, M.J. Iqbal, M. Ali, S. Ali, M. Ajmal, Y. Iqbal, Mat. Sci. Semicon. Proc., 41 (2016) 364-369.

[85] H. Zhu, P. Zhang, S. Dai, ACS Catal., 5 (2015) 6370-6385.

[86] M.M. Natile, E. Ugel, C. Maccato, A. Glisenti, Appl. Catal B Environ., 72 (2007) 351-362.

[87] P.H.T. Ngamou, N. Bahlawane, Chem. Mater., 22 (2010) 4158-4165.

[88] T. Nitadori, M. Misono, J. Catal., 93 (1985) 459-466.

[89] R.G. de la Cruz, H. Falcon, M. Pena, J. Fierro, Appl. Catal B Environ., 33 (2001) 45-55.

[90] D.N. Mueller, M.L. Machala, H. Bluhm, W.C. Chueh, Nature. commun., 6 (2015) 6097.

[91] X.-D. Zhang, W.-L. Zhang, Z.-X. Cai, Y.-K. Li, Y. Yamauchi, X. Guo, Ceram. Int., 45 (2019) 5240-5248.

[92] A. Chainani, M. Mathew, D. Sarma, Phys. Rev B., 46 (1992) 9976.

[93] H.R. Aliabad, V. Hesam, I. Ahmad, I. Khan, Physica B., 410 (2013) 112-119.

[94] T. Arima, Y. Tokura, J. Torrance, Phys. Rev B., 48 (1993) 17006.

[95] S. Mukhopadhyay, M. Finnis, N. Harrison, Phys. Rev B., 87 (2013) 125132.

[96] V. Aswin, A. Dogra, A. Gupta, J. Pulikkotil, RSC Adv., 6 (2016) 1403-1407.

[97] A. Mineshige, M. Kobune, S. Fujii, Z. Ogumi, M. Inaba, T. Yao, K. Kikuchi, J. Solid State Chem., 142 (1999) 374-381.

[98] M.S. Read, M.S. Islam, G.W. Watson, F. King, F.E. Hancock, J. Mater. Chem., 10 (2000) 2298-2305.

[99] V. Kharton, F. Figueiredo, A. Kovalevsky, A. Viskup, E. Naumovich, A. Yaremchenko, I. Bashmakov, F. Marques, J. Eur. Ceram. Soc., 21 (2001) 2301-2309.

[100] V. Chumakova, A. Marikutsa, M. Rumyantseva, D. Fasquelle, A. Gaskov, Sens. Actuators B Chem., 296 (2019) 126661.

[101] J.-C. Ding, H.-Y. Li, X. Guo, Solid State Ion., 272 (2015) 155-159.

[102] S. Yan, S. Ma, W. Li, X. Xu, L. Cheng, H. Song, X. Liang, Sens. Actuators B Chem., 221 (2015) 88-95.

[103] W.-Y. Lee, H.J. Yun, J.-W. Yoon, J. Alloys. Compd., 583 (2014) 320-324.

[104] I. Bhat, S. Husain, W. Khan, S.I. Patil, Mater. Res. Bull., 48 (2013) 4506-4512.

[105] Y. Zhang, J. Zhang, J. Chen, Z. Zhu, Q. Liu, Sens. Actuators B Chem., 195 (2014) 509-514.

[106] L. Zhang, J. Hu, P. Song, H. Qin, K. An, X. Wang, M. Jiang, Sens. Actuators B Chem., 119 (2006) 315-318.

[107] P. Song, H. Qin, X. Liu, S. Huang, R. Zhang, J. Hu, M. Jiang, Sens. Actuators B Chem., 119 (2006) 415-418.

[108] V. Lantto, S. Saukko, N.N. Toan, L.F. Reyes, C.G. Granqvist, J. Electroceram., 13 (2004) 721-726.

[109] Y.L. Chai, D.T. Ray, H.S. Liu, C.F. Dai, Y.H. Chang, Mater. Sci. Eng. A, 293 (2000) 39-45.

[110] N. Erdenee, U. Enkhnaran, S. Galsan, A. Pagvajav, J. Nanomater., 2017 (2017) 8.

[111] R. Leanza, I. Rossetti, L. Fabbrini, C. Oliva, L. Forni, Appl. Catal B Environ., 28 (2000) 55-64.

[112] Y. Luo, C. Zhang, B. Zheng, X. Geng, M. Debliquy, Int. J. Hydrog. Energy, 42 (2017) 20386-20397.

[113] C.R. Michel, A.H. Martínez-Preciado, E.R. López-Mena, A. Elías-Zuñiga, N. Cayetano-Castro, O. Ceballos-Sanchez, Sens. Actuators B Chem., 246 (2017) 181-189.

[114] E. Cao, A. Wu, H. Wang, Y. Zhang, W. Hao, L. Sun, ACS Appl. Nano. Mater., 2 (2019) 1541-1551.

[115] W. Wei, S. Guo, C. Chen, L. Sun, Y. Chen, W. Guo, S. Ruan, J. Alloys. Compd., 695 (2017) 1122-1127.

[116] M. Chen, D. Zhang, J. Hu, H. Wang, Y. Zhang, K. Li, Q. Rong, S. Zhou, J. Zhang, Z. Zhu, Q. Liu, Mater. Res. Bull., 111 (2019) 320-328.

[117] X. Wang, H. Qin, J. Pei, Y. Chen, L. Li, J. Xie, J. Hu, J. Rare Earth., 34 (2016) 704-71

Chapter 3

Material synthesis and characterization

3.1 Introduction

This chapter focuses on the description of the type of synthesis approach utilized to produce nanostructured La based oxide complexes as well as the characterization techniques used to establish their properties. Electrospinning followed by annealing method was used for the synthesis of the nanostructures. While their structural, surface, thermal, and optical characterizations were performed through the use of X-ray diffraction (XRD), X-ray photoelectron spectroscopy (XPS), Time-of-flight secondary ion mass spectroscopy (ToF-SIMS), Scanning electron microscopy (SEM), Transmission electron microscopy (TEM), Brunauer-Emmett Teller (BET), Thermogravimetric Analysis (TGA) and Photoluminescence (PL), respectively. Regarding their sensing performance studies, the sensing station was utilized to perform the sensing tests at various operating temperatures and gas concentrations.

3.2 Electrospinning method

Electrospinning has been actively exploited as a simple and versatile method for generating 1D nanostructures such as nanofibers and nanobelts made of various materials. Basically electrospinning is a fiber production method based on the application of electrical forces on a droplet of a polymer solution which is drawn and elongated until fibers with diameters at the micro- and nano-scale are produced [1, 2]. A typical electrospinning apparatus consists of a high voltage power supply, syringe pump, spinneret and conductive collector as illustrated in

Figure 3.1 for a horizontal configuration. For metal oxide/polymer based fibers, the annealing step (step 3 in Figure 3.1) is also included in order to obtain the pure metal oxide fibers by decomposing the polymer binder at an appropriate temperature.

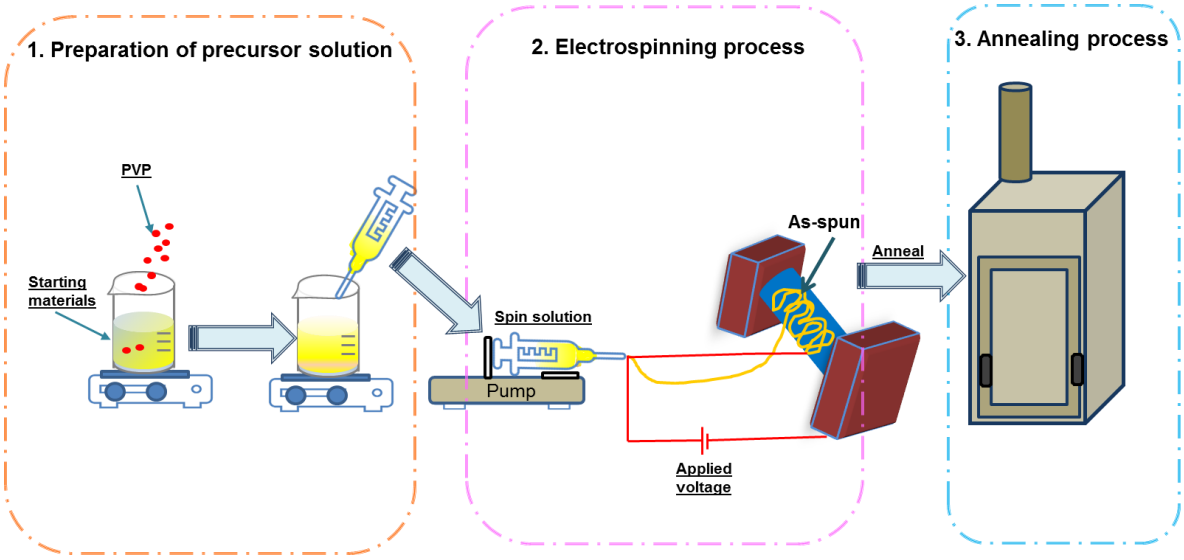

Figure 3.1: Schematic electrospinning setup utilized for preparation of nanostructured La-based metal oxide complexes.

3.3 Key experimental parameters

The morphology of the fibers is an aspect of paramount significance to direct the application of the electro-spun fibers in several technological fields. Therefore, in order to modify or obtain different fiber morphologies, various experimental parameters related to the polymer solution including molecular weight of polymer, concentration and viscosity as well as the processing parameters such as applied voltage, flow rate, collectors and working distance need to be optimized [3, 4].

3.3.1 Solution parameters

3.3.1.1 Polymer molecular weight, solution concentration and viscosity

The polymer molecular weight and solution concentration have a great influence on the viscosity of the final solution, which in turn can affect the morphology of the fibers. Polymers with high molecular weight have larger surface area that promotes the entanglement of polymer chains thus leading in increased solution viscosity which can results in the production of fibers with larger diameters [5]. Also, higher solution concentration leads to a larger number of chains. Low concentrated solutions results in beaded fibers, whereas extremely concentrated solutions can yield ribbon-like shaped fibers [4]. Therefore it is necessary to optimize the ideal concentration in order to obtain continuous fibers, and this depends on the polymer used [6].

3.3.1.2 Solution conductivity

The solution conductivity is another important parameter influencing the fiber morphology by facilitating the elongation of the droplet and its formation to a single or multiple jets. The solution conductivity is mainly determined by the type of polymer used, solvent and the salts. Additionally, the solution conductivity can be tuned by adding ionic salts which may result in good quality fibers with smaller diameters [7].

The salts concentration in this study were first optimized to get the desired viscosity and solution conductivity. It was established that the solution viscosity and conductivity relied heavily on the salt concentration, the polymer molecular weight and the solvent used.

3.3.2 Processing parameters

3.3.2.1 Applied voltage

In the course of the electrospinning process, the fibers are formed due to the polymer droplet elongation at the tip of the needle by means of electrostatic forces. For a particular applied voltage, the electrostatic forces acting on the droplet will be stronger than the superficial tension thus causing the droplet stretching [2]. Therefore, the precise applied voltage is a crucial parameter for effectively electrospinning fibers as it impacts the deformation of the droplet and the jet development. If a too low applied voltage is used, the polymer jet cannot be stabilized thus leading to non-fiber formation or fibers with non-uniform morphology and beads [4, 6]. Then again, if an extreme high voltage is used, thicker and non-uniform fibers can be formed which can negatively affect the nanofibers properties [8].

3.3.2.2 Flow rate

The flow rate of the polymer solution influences the size of the droplet, and in turn affects the fiber morphology. Generally, a lower flow rate is more recommended as the polymer solution will get enough time for polarization. If the flow rate is very high, fibers with thick diameters and beads will form, instead of smooth continuous fibers with small diameters [4].

3.3.2.3 Collectors

In the process of electrospinning, collectors usually act as the conductive substrate to collect the charged fibers. There are several types of collectors that can be used according to the desired final application including grids [9], parallel bars [10], rotating drums/cylinders [11], etc.

3.3.2.4 Working distance

The distance between the needle and the collector is important for proper fiber formation as during the travelling of the jet to the collector, the evaporation of the solvent take place allowing formation of uniform fibers. Generally, volatile solvents need smaller working distances as compared to less volatile ones[4] . If the working distance is too small films or tape-like fibers will form[6]. Shorter working distance (10 cm and less) in this work have resulted in formation of nanobelts whereas longer distance (15 cm and more) resulted in the formation of nanofibers.

3.4 Characterization techniques

3.4.1 Structural and surface characterization techniques

3.4.1.1 X-Ray Diffraction (XRD)

XRD is an analytical technique used for the analysis of various crystalline phases of samples[12]. XRD technique is based on the principle of Bragg's law[13]. Consider X-ray beam (I) with wavelength (λ) incident on a crystal as depicted in Figure 3.2. If the incident and the reflected beam (R) meet Bragg's condition, then Bragg's law is written as:

$$n\lambda = 2d\sin\theta \qquad (3.1)$$

Where $n=1$, d is the interplanar spacing and θ is the incident angle.

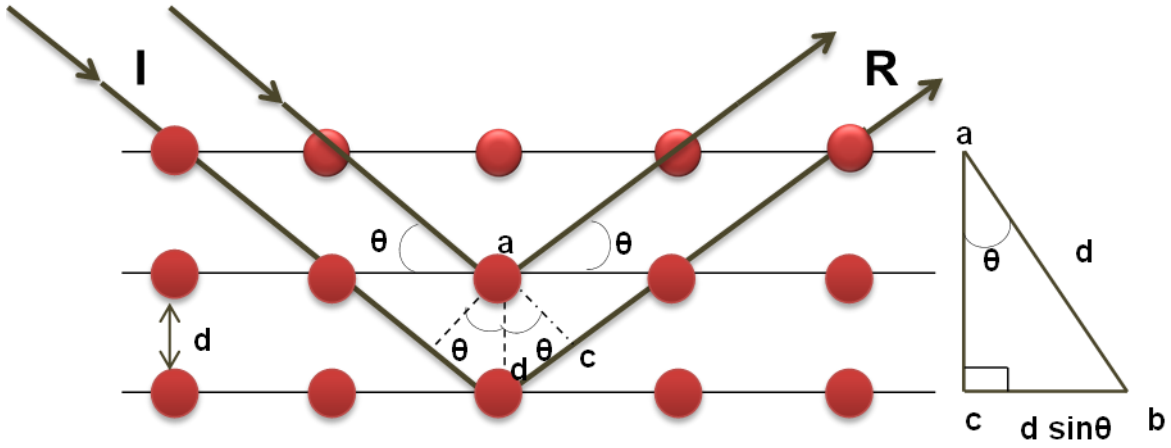

Figure 3.2: Schematic diagram of X-ray diffraction from the surface of a crystal [21].

The set-up for X-ray diffraction consists of three basic components including an X-ray tube; a sample holder and an X-ray detector (see Figure 3.3). The X-ray tube comprises of a copper block connected to an anode and cathode made of a metal and tungsten filament, respectively. Electrons are generated by heating up the cathode and accelerated to the anode by applying a very high potential difference between the anode and cathode. This process produces characteristic X-rays (mainly CuKβ (1.39 Å) and CuKα (1.54 Å), respectively. The CuKβ radiation is absorbed using a Nickel filament, which absorbs at wavelength below 1.54 Å. This wavelength is used to excite the sample.

The X-ray tube, sample and detector are arranged on the Bragg-Brentano θ−θ or θ−2θ geometry configuration. For the θ−θ configuration, the sample is fixed at the center of the goniometer, and both the X-ray source and detector rotates around a common axis positioned at the center of the goniometer. The sample lies on a horizontal plane that forms vertical planes at angle θ with both the X-ray source and the detector. The X-ray source and the detector rotate at the same

angular velocity while maintaining equal angles with the surface of the sample. The reflected beam is then captured when diffraction occurs at the Bragg angle. For the θ−2θ configuration, the X-ray source is at a fixed position forming an angle θ with the rotating sample. Therefore, the difference in the angle of the incident X-ray beam results from the sample's movement. The sample rotates in the same axis with the detector but the detector move at twice the speed of the sample, and hence the diffraction angle 2θ [14].

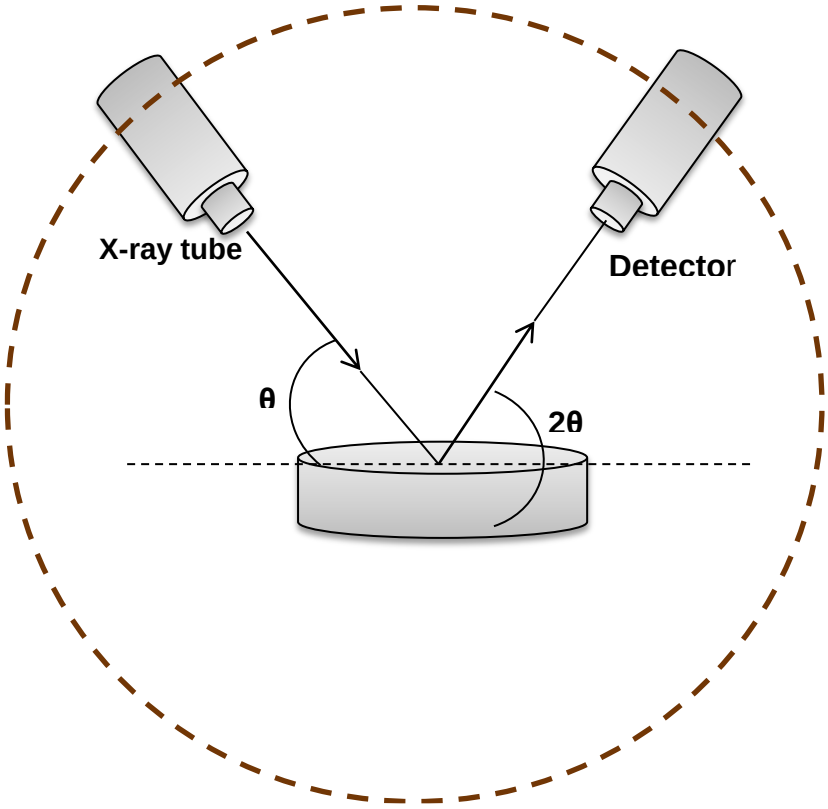

Figure 3.3: Schematic representative of an X-ray diffractometer.

For this work, X-ray diffraction (XRD) Panalytical X'pert PRO PW3040/60 X-ray diffractometer with Cu/Kα a Cu-Kα (λ=1.5405 Å) radiation was used to conduct structural analysis of the nanostructured La-based oxide complexes.

3.4.1.2 X-ray photoelectron spectroscopy (XPS)

XPS is a technique for qualitative and quantitative analysis of the elemental composition, chemical state and electronic states of elements on the surface of a material [15]. XPS is based on principle of photoelectric effect [16]. It uses highly focused monochromatised X-rays. Its mechanism involves the ejection of a photoelectron from the core level (K shell) of an atom by an incident X-ray beam as shown in Figure 3.4. A high sensitive spectrometer is used to determine the kinetic energy of the electron.

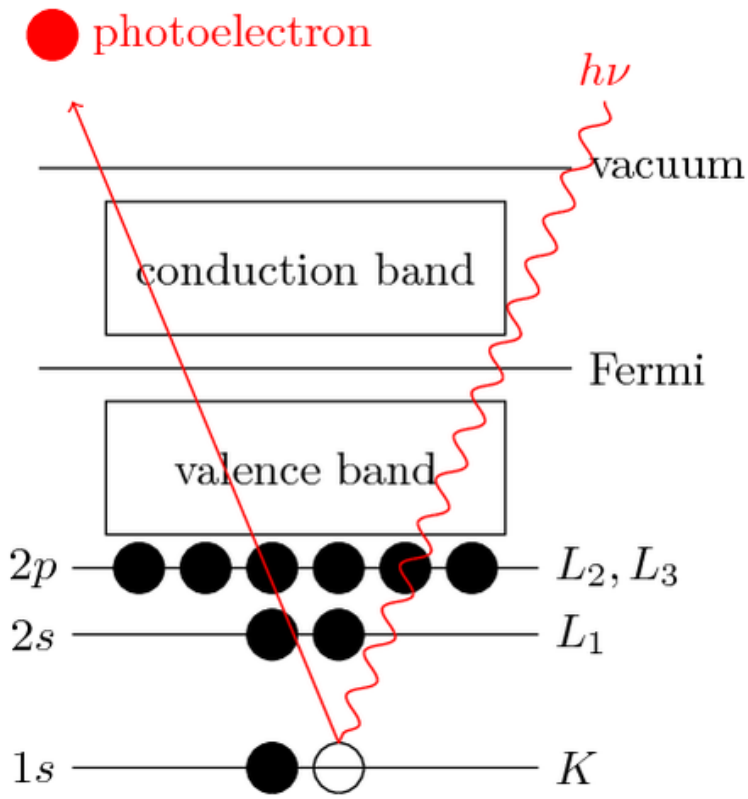

Figure 3.4: Schematic diagram of the XPS process [17].

The kinetic energy of the ejected photoelectron gives information about its binding energy which gives information on the chemical composition of the

sample since binding energies are characteristic for each element. The binding energy of the photoelectron (E_B) is related to the kinetic energy of the photoelectron measured by the spectrometer (Ek) through

$$E_B = h\nu - E_k - \varphi_A \quad (3.2)$$

Whereby $h\nu$ is the energy of primary X-ray beam, and φA is the work function of the spectrometer [15].

XPS measurements are conducted under ultra-high vacuum (UHV) chamber. A typical XPS set up is shown in Figure 3.5. For this work, a PHI 5000 Versaprobe X-ray photoelectron with monochromatic Al-Kα radiation ($h\nu$ = 1486.6 eV) was used for the XPS characterization.

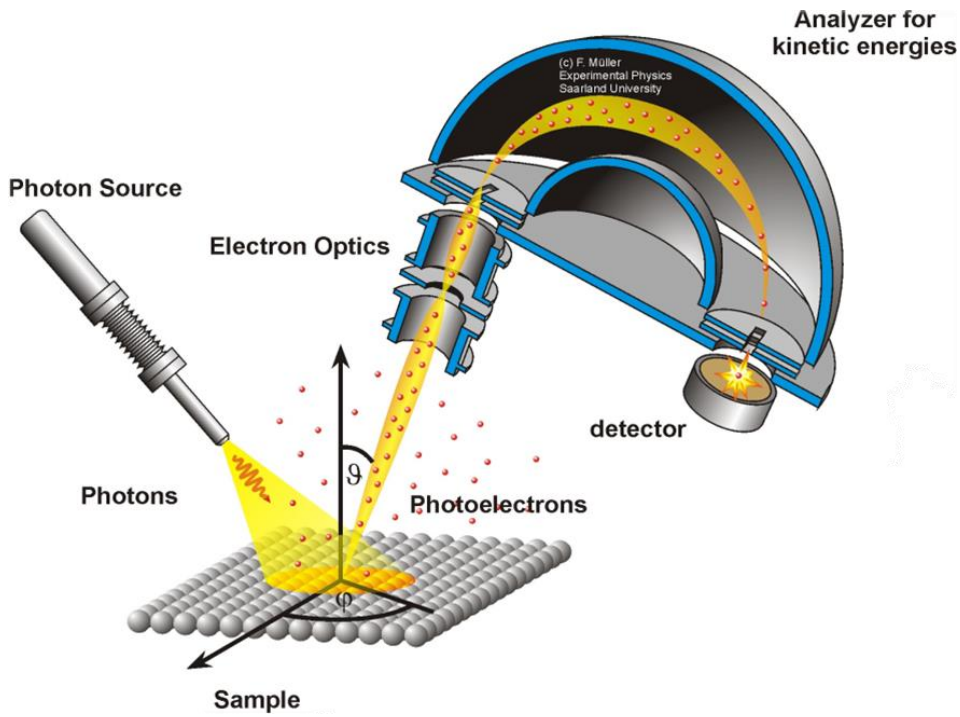

Figure 3.5: Schematic set-up of XPS system [18].

3.4.1.3 Time-of-flight secondary ion mass spectroscopy (ToF-SIMS)

ToF-SIMS is a technique based on the emission of secondary ions from the surface of a material after impact on the surface by an energy pulsed primary ion beam [19]. ToF-SIMS is a surface sensitive technique that has been used to characterize a variety of conducting and non-conducting surfaces [20].

The basic set-up for a ToF-SIMS experiment is shown in Figure 3.6. The impinging primary ion beam transfers energy to the atoms in the sample resulting in collision within the atoms in the sample. This energetic interaction produces a cloud of atoms and molecules among which some are ionized. The ionized particles of one polarity, atomic and molecular secondary ions are accelerated by an electric field through a 2 m field-free tube, where the secondary ions are separated based on their mass-to-charge ratio as [21]:

$$\frac{m}{z} = 2eEs(\frac{t}{d})^2 \qquad (3.3)$$

Where m is the mass, e is elementary charge, z is the number of elementary charges, s is the length of the tube over which an extraction potential is applied, t is time-of-flight, V is the applied voltage and d is the length of the secondary ions trajectory tube. The spectrum obtained with each primary ion pulse is collected and summed over many pulses. Finally, the spectrum is converted from a 'time-of-flight' scale into a mass scale via mass calibration using a number of known secondary ions [22]. For this work, the TOF-SIMS technique, equipped with a primary Bi^+ source and pulsed electron source of 30 eV for charge compensation was employed for the TOF-SIMS analysis.

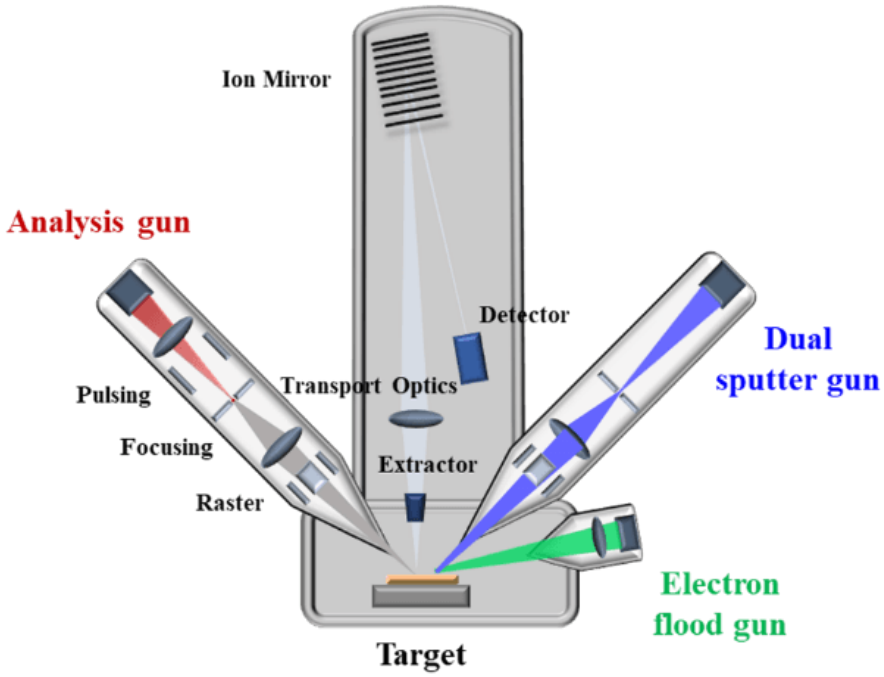

Figure 3.6: Schematic set-up of ToF-SIMS system [23].

3.4.1.4 Scanning electron microscopy (SEM)

SEM is an instrument that enables the observation and characterization of the surface of different organic and inorganic materials. In SEM, a sample surface is imaged by scanning it with a high-energy beam of electrons in a raster scan pattern. The electrons interact with atoms of the sample producing signals with information on the sample's topography, composition and other properties, such as electrical conductivity. The signals produced include: secondary electrons, backscattered electrons, characteristics X-rays, cathodoluminescence, Auger electrons, specimen current and transmitted electrons (see Figure 3.7). These signals give information about the sample's morphology, chemical composition, crystalline structure and the orientation of materials the sample [21].

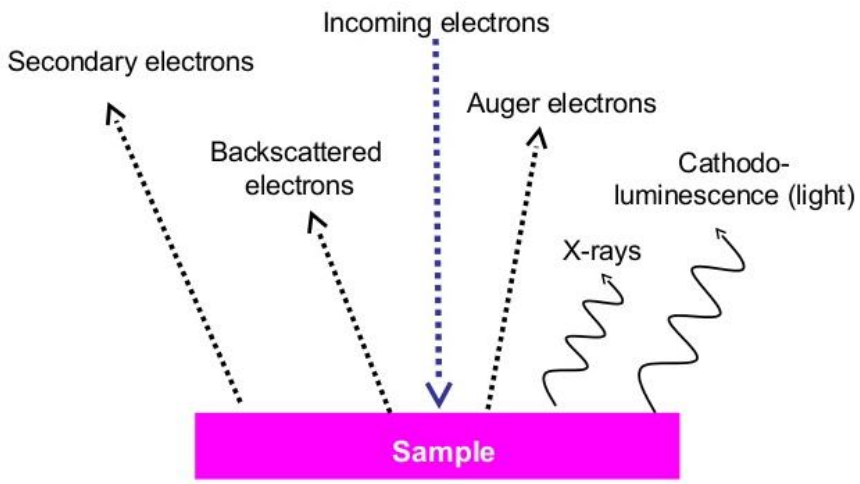

Figure 3.7: Schematic diagram of signals generated during incident beam and sample interaction [24].

Figure 3.8 depicts the schematic diagram of a typical SEM system which comprises of an electron gun, an anode, a set of lenses, sample stage and detectors. SEM operates in a very low vacuum pressure. The electron gun generates electrons with a beam diameter in the range of 10−100 nm. The anode accelerates the electrons with a voltage of 0.1-50 keV. The condenser lens narrows the electron beam to the diameter of 1−10 nm before reaching the sample's surface with electron-probe current in the range of 10^{-9}–10^{-12} A [25]. The objective lens then finely scans the electron beam across the sample's surface, by varying the potential difference between the plates of the lens. The different detectors are therefore used to detect the secondary electrons, backscattered electrons and the characteristic X-rays, respectively. For this work, a ZEIS-AURIGA field emission-scanning electron microscopy (FESEM) at an acceleration voltage of 3 kV was used.

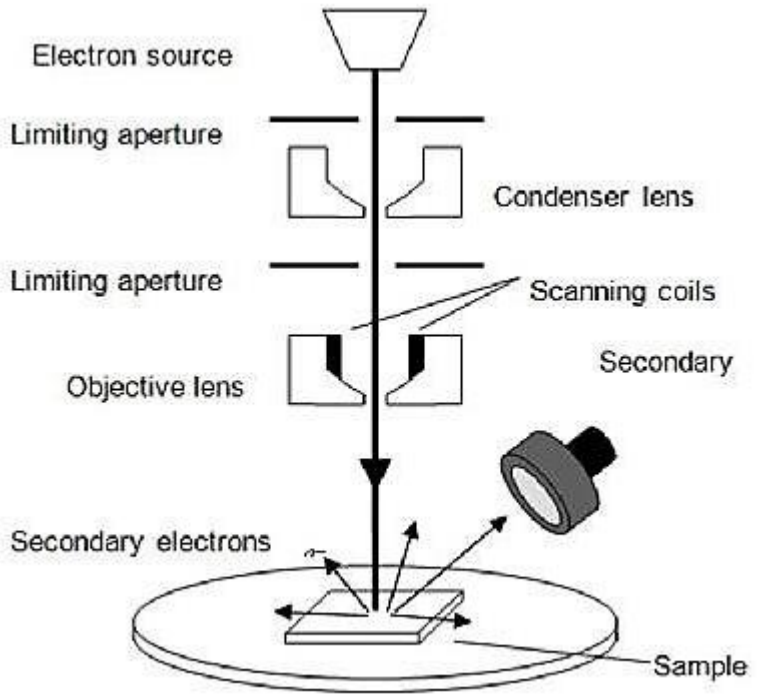

Figure 3.8: Schematic set-up of the SEM [26].

3.4.1.5 Transmission electron microscope (TEM)

TEM is a technique in which a thin specimen is irradiated with a beam of electrons of uniform current density. Electrons strongly interact with atoms of the sample by elastic and inelastic scatterings. An image with atomic resolution is generated from the interactions of the transmitted electrons through the sample. The image can be recorded digitally via a fluorescent screen coupled by a fiber-optic plate to a CCD camera, or by an image plate inside a vacuum or direct exposure of photographic emulsion. This technique is used to study the size, shape and the crystalline nature of a sample. A typical TEM schematic diagram is shown in Figure 3.9. For this study a JEOL TEM-2100 high resolution transmission electron microscopy (HR-TEM) with an accelerating voltage of 200 kV was used.

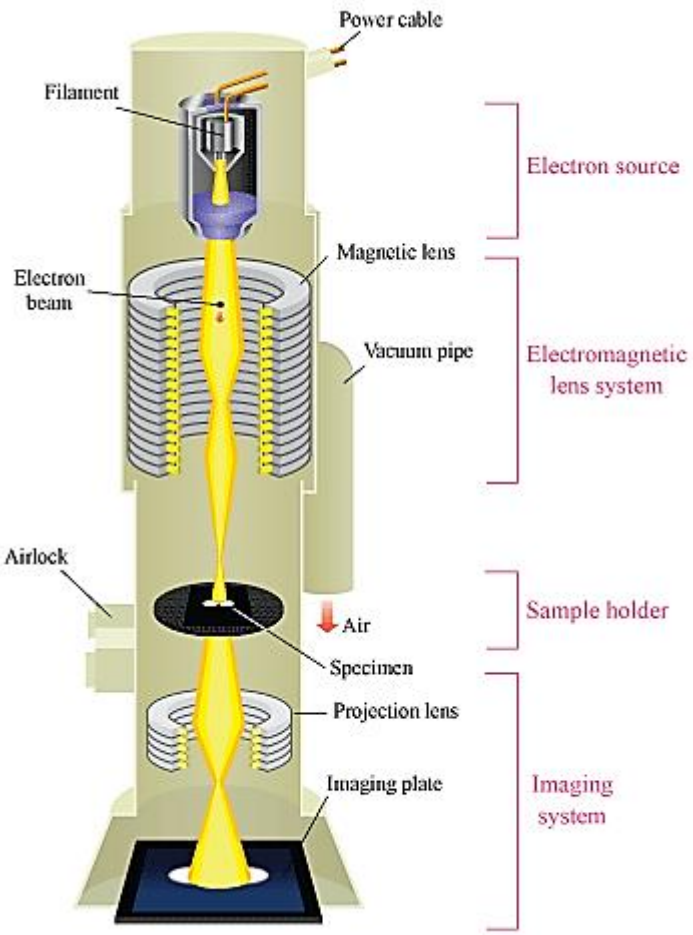

Figure 3.9: Schematic diagram of the TEM [27].

3.4.1.6 Brunauer-Emmett Teller (BET)

BET is a user-friendly technique used to characterize gas adsorption of a wide range of porous materials [28]. This technique uses nitrogen as an adsorptive gas at 77 K for investigation of materials surface area and porosity. The BET theory is based on a simplified model of physisorption [29] whereby the adsorbent surface is assumed as an array of equivalent sites in which gas molecules are adsorbed in a random manner. As the system pressure is increased, gas concentration also increases and multiple layers adsorb to the surface. The

material surface area is easily estimated if the number of N_2 molecules that form monolayer (densely packed single adsorbed layer) is known as [30]

$$Surface\ area = n_m \times \frac{N_a}{w} \times \sigma_A = \frac{V_m}{V_g} \times \frac{N_a}{w} \times \sigma_A \quad (3.4)$$

Whereby n_m is monolayer quantity (mol), V_m is the monolayer volume (cm^3), V_g is molar volume of gas at STP (22414 cm^3/mol), N_a is the Avogadro's number (6.023×10^{23} molecules/mol), w is the sample mass (g) and σ_A is the cross-sectional area of the adsorbate (m^2). Figure 3.10 shows a schematic representative of the nitrogen adsorption system. For this work, the nitrogen adsorption measurements were performed using a Micrometirics TRISTAR 3000 surface area analyser.

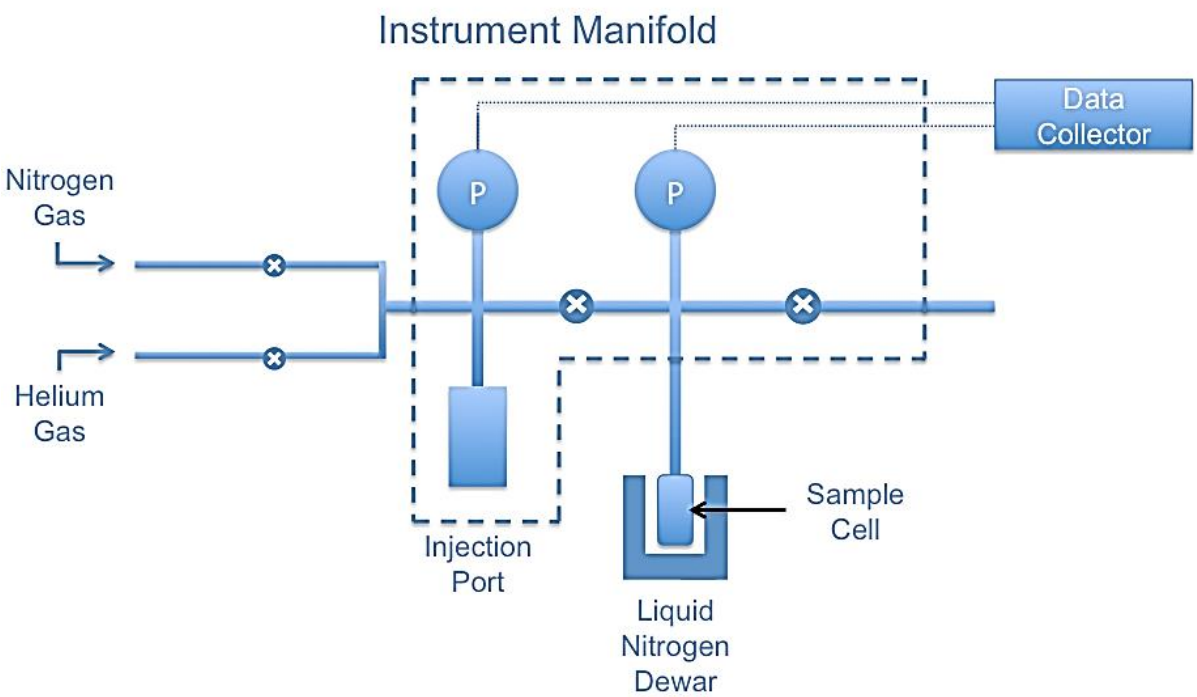

Figure 3.10: BET schematic representation [31].

3.5 Thermal characteristics analysis

3.5.1 Thermogravimetric Analysis (TGA)

TGA is a destructive technique that is used to measure the weight change and the rate of weight change as a function of temperature, time and atmosphere. The obtained measurements are used for determination of material composition, their thermal and oxidative stability, decomposition kinetics and the effect of reactive atmospheres on materials. A typical thermogravimetric analyzer consists of a precision balance with a sample pan located inside a furnace with a programmable control temperature. The temperature is generally increased at a constant rate (or for some applications the temperature is controlled for a constant mass loss) to incur a thermal reaction. The thermal reaction may occur under different atmospheres including ambient air, vacuum, inert gas, oxidizing or reducing gases, carburizing gases and corrosive gases, as well as different types of pressures including: a high vacuum, high pressure, constant pressure, or a controlled pressure. A TGA can be used for materials characterization through analysis of characteristic decomposition patterns. The basic principle of TGA is that as a sample is heated its mass changes. This change can be used to determine the composition of a material or its thermal stability up to 1000 °C. Usually, a sample loses weight as it is heated up due to decomposition, reduction, or evaporation. A sample could also gain weight due to oxidation or absorption. While in use, the TGA machine tracks the change in weight of the sample via a microgram balance. Temperature is monitored via a thermocouple. The TGA can also track change in weight as a function of time. Data can be graphed as weight percent versus time or temperature. Figure 3.11 shows the representative

schematic of TGA set up. For this work, a Perkin Elmer Thermogravimetric Analyzer Pyris 1 TGA was used.

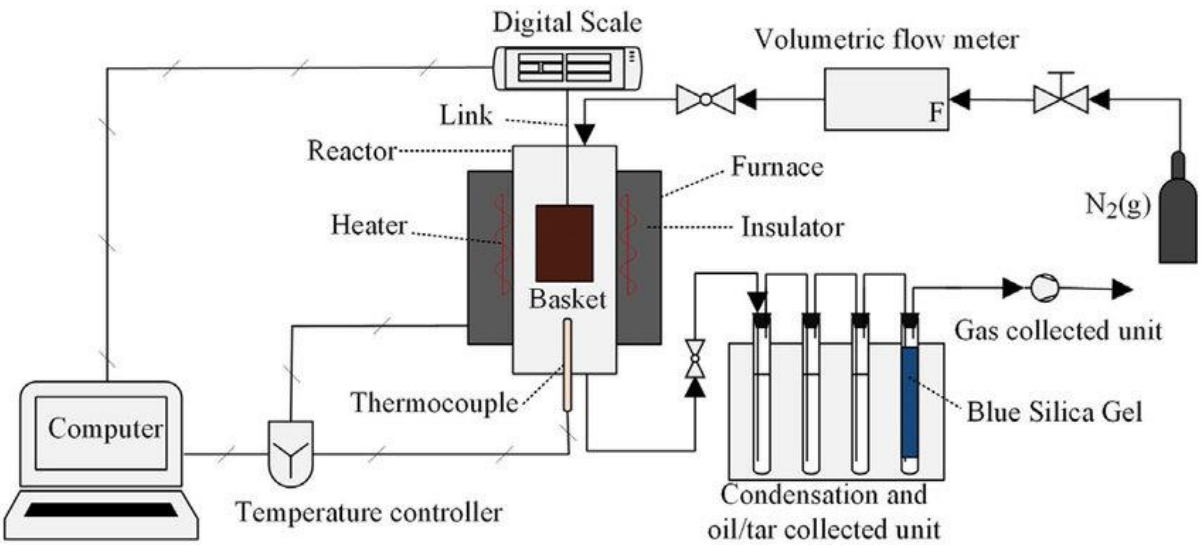

Figure 3.11: Set up representative of the TGA [32].

3.6 Optical characterization

3.6.1 Photoluminescence (PL)

Photoluminescence (PL) is a technique used to study electron transitions in materials. PL is a powerful tool to study point defects in wide-band gap semiconductors. The PL emission spectrum is obtained from a PL spectrometer by selecting a fixed excitation wavelength and scanning the emission as a function of wavelength. The PL excitation spectrum is produced when the emission spectrum is fixed at the emission maximum and the excitation source is scanned over the wavelength range of the absorption of the material [21]. The basic set-up of PL spectrometer (see Figure 3.12) contains two monochromators (wavelength selectors). One monochromator chooses the excitation wavelength from the light source, whereas the other monochromator chooses the emission

wavelength from the sample after excitation [21]. The general excitation sources are Xe lamp with continuous emission spectrum in the wavelength range of 160 - 2000 nm and lasers with a monochromatic wavelength [21].

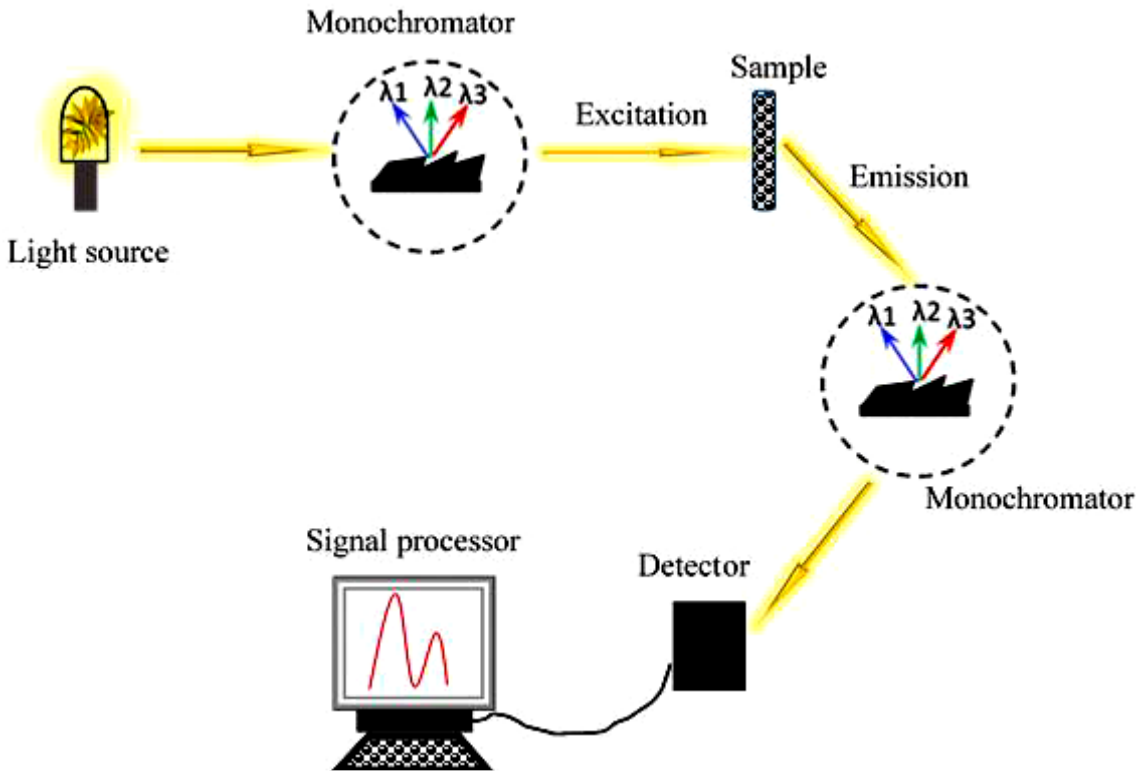

Figure 3.12: Schematic diagram of a photoluminescence spectrometer [21].

3.7 Gas sensing experiment

The gas sensing performance of the obtained samples was evaluated using the gas sensing instrument. For this work, a KENOSISTEC UHV and a Thin film Equipment gas station was used for the gas sensing tests. The system consists of a sensing chamber, eight gas inlets for different target gases, two thermostatic baths, twelve mass flow controllers (MFC) to control the gas capacity reaching the chamber, a sample stage, an air mixer and a dry air inlet which carries dry air

into the mixer. Thermostatic bath 1 supplies wet air into the air mixer to create humid environment. There are six heaters for the supply of voltage across the samples and six KEITHLEY picoammeter for the measurements of resistance changes in air *(Ra)* and in target gas *(Rg)*. The operating temperatures were calibrated by varying the voltage while monitoring the readings using a thermocouple. The response of the samples is then determined as the ratio of the electrical resistance in the gas to that in air (*Rg/Ra)* for the p-type sensors, and as Ra/Rg for the n-type sensors [15]. A typical set-up of the sensing station is shown in Figure 3.13.

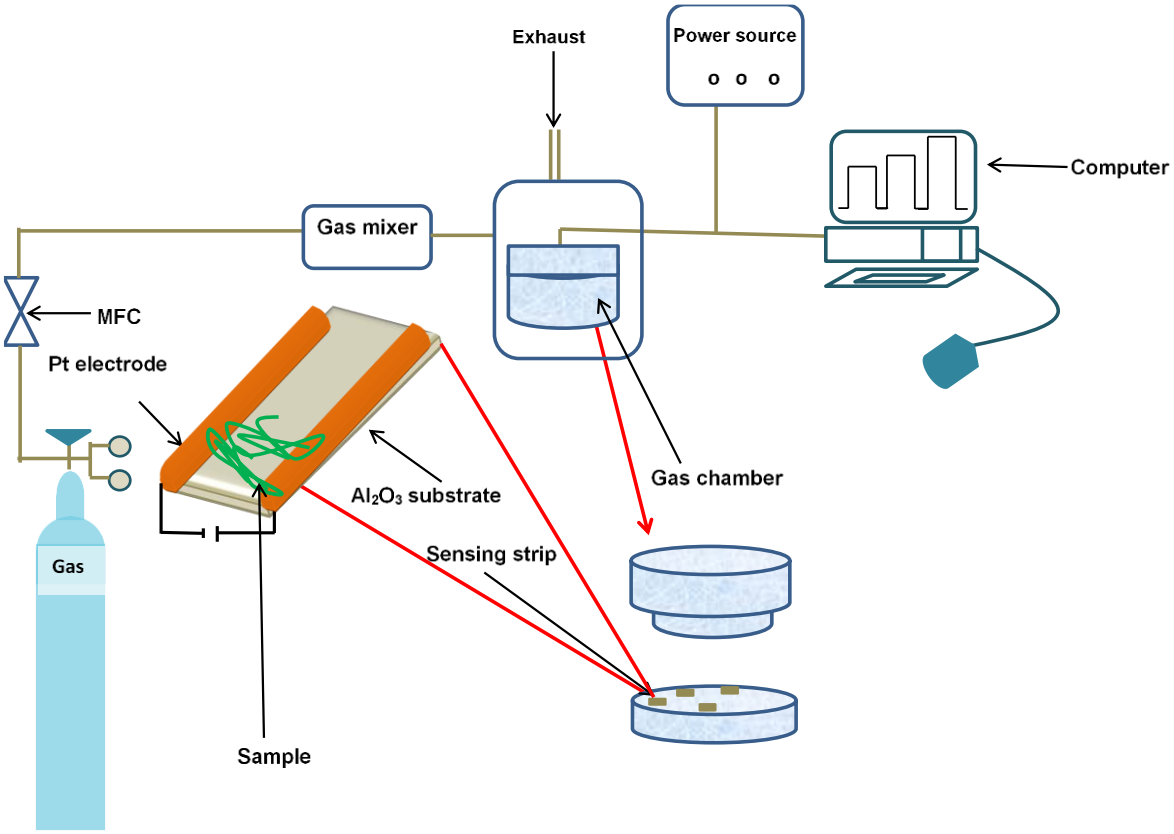

Figure 3.13: Schematic diagram of the sensing station set-up.

3.8 References

[1] A. Macagnano, E. Zampetti, E. Kny, Electrospinning for high performance sensors, Springer (2015)

[2] S. Agarwal, A. Greiner, J.H. Wendorff, Prog. Polym. Sci., 38 (2013) 963-991.

[3] Z.-M. Huang, Y.Z. Zhang, M. Kotaki, S. Ramakrishna, Compos. Sci. Technol., 63 (2003) 2223-2253.

[4] Z. Li, C. Wang, Springer Berlin, Heidelberg, (2013) 15-28.

[5] N. Bhardwaj, S.C. Kundu, Biotechnol. Adv., 28 (2010) 325-347.

[6] L.A. Mercante, V.P. Scagion, F.L. Migliorini, L.H.C. Mattoso, D.S. Correa, TrAC., 91 (2017) 91-103.

[7] X. Zong, K. Kim, D. Fang, S. Ran, B.S. Hsiao, B. Chu, Polymer, 43 (2002) 4403-4412.

[8] J.M. Deitzel, J. Kleinmeyer, D. Harris, N.C. Beck Tan, Polymer, 42 (2001) 261-272.

[9] B. Sundaray, V. Subramanian, T. Natarajan, R.-Z. Xiang, C.-C. Chang, W.-S. Fann, Appl. Phys. Lett., 84 (2004) 1222-1224.

[10] C. Xu, R. Inai, M. Kotaki, S. Ramakrishna, Biomaterials., 25 (2004) 877-886.

[11] C. He, W. Nie, W. Feng, J. Mater. Chem B., 2 (2014) 7828-7848.

[12] A. Benninghoven, Angewandte Chemie., 33 (1994) 1023-1043.

[13] B.D. Cullity, S.R. Stock, Elements of X-ray Diffraction, Prentice hall New Jersey (2001)

[14] A. Monshi, M.R. Foroughi, M.R. Monshi, WJNSE., 2 (2012) 154-160.

[15] K. Shingange, Magnetic, luminescence and gas sensing properties of various zinc oxide nanostructures: The influence of surface modification by gold on the gas sensing properties, University of the Free State, MSc Thesis (2016)

[16] K.K. Darrow, Rev. Sci. Instrum., 4 (1933) 467-472.

[17] http://www.texample.net/tikz/examples/principle-of-x-ray-photoelectron-spectroscopy-xps/, (Accessed 29 September 2019).

[18] https://epm.univie.ac.at/research/low-dimensional-quantum-solids/methods/, (Accessed 29 September 2019).

[19] Q.P. Vanbellingen, N. Elie, M.J. Eller, S. Della-Negra, D. Touboul, A. Brunelle, Rapid Commun. Mass Sp., 29 (2015) 1187-1195.

[20] L. Van Vaeck, A. Adriaens, R. Gijbels, Mass Spectrom. Rev., 18 (1999) 1-47.

[21] S.N. Ogugua, Preparation and characterization of powders and pulsed laser deposited thin films of rare-earths doped oxyorthosilicates, University of the Free State, PhD Thesis, (2017)

[22] F. Green, I. Gilmore, M. Seah, J. Am. Soc. Mass Spectrom., 17 (2006) 514-523.

[23] http://simslab.rice.edu/surface-analysis-lab/teaching-activities-resources/time-of-flight-secondary-ion-mass-spectrometry/, (Accessed 29 September 2019).

[24] https://www.slideshare.net/waqasjavaid547/scanning-electron-microscopy-28066279, (Accessed 29 September 2019).

[25] L. Reimer, Scanning electron microscopy: physics of image formation and microanalysis, Springer (2013)

[26] A. Mukhopadhyay, Guwahati: Satyendra Nath Bose National Centre for Basic Sciences, (2015).

[27] http://www.hk-phy.org/atomic_world/tem/tem02_e.html, (Accessed 29 September 2019).

[28] K. Sing, Colloid. Surf A., Physicochemical and Engineering Aspects, 187 (2001) 3-9.

[29] S. Brunauer, P.H. Emmett, E. Teller, Am. Ceram. Soc., 60 (1938) 309-319.

[30]
https://www.micromeritics.com/repository/files/Pharma_Excipents_Kenvin_Presentation.pdf, (Accessed 29 September 2019).
[31]
https://chem.libretexts.org/Bookshelves/Analytical_Chemistry/Book%3A_Physical_Methods_in_Chemistry_and_Nano_Science_(Barron)/02%3A_Physical_and_Thermal_Analysis/02.3%3A_BET_Surface_Area_Analysis_of_Nanoparticles, (29 September 2019).
[32] T. Onsree, N. Tippayawong, A. Zheng, H. Li, Case. Stud. Therm. Eng., 12 (2018) 546-55

Chapter 4

H_2S detection capabilities with fibrous-like La-doped ZnO nanostructures: A comparative study on the combined effects of La-doping and post-annealing

4.1 Introduction

Being one of the poisonous, flammable and colourless gases, Hydrogen sulphide (H_2S) often exists in nature and produced from many industrial processes such as coal gasifiers, waste management, petroleum refining, and natural gas production [1, 2]. As a hazardous substance, it has been found to cause headache, dizziness, nausea, chest distress, and even skin allergy at low concentration levels from 50 to 100 ppm [3] whereas at higher concentration levels more than 250 ppm, may affect the human's nervous system and may even be fatal [4, 5]. Thus, it is extremely significant to develop H_2S gas sensors showing high responsivity, long term stability and accurately differentiating it from mixed gas under various surroundings at moderate working temperatures. Tremendous efforts devoted in exploring various n- and p-type metal oxides such as SnO_2, ZnO, CuO as active sensing layers for development of gas sensors have been intensifying lately owing to their unique thermal and chemical stability [6, 7]. From a great deal of literature survey, grain size is one of the big key role parameters and by controlling it, pronounced sensing can be achieved [8, 9]. This is because, small grain size provides a high surface area with more active sites for adsorption and desorption of gas molecules. Additionally, it provides more grain boundaries, suggesting that a large amount of the gas molecules can diffuse along the boundaries, thus increasing sensitivity [10-12]. With that said, much research efforts have been dedicated into manipulation of these metal oxides, to

attain structures with nano-sized grains. One dimensional (1D) nanomaterials with nanofiber (NF)-like structures have been identified as the most promising structure amongst various structures as they are comprised of several nano-sized grains. Because of these many nano-sized grains, NFs have been demonstrated to possess high surface area and larger grain boundaries [13]. In particular, the electrospinning method is normally used for the synthesis of NFs as it provides low cost fabrication and minimal use of starting materials. Moreover, its processing parameters can be easily controlled [10, 14] leading to manipulation of the nanofiber morphology thus contributing to enhanced gas sensing performance.

With a wide band gap of 3.37 eV at room temperature, n-type ZnO has been explored to detect H_2S [15, 16]. However, its commercial/practical use is limited by poor response and stability, lack of selectivity as well as elevated operating temperature which results in high consumption of power and the likelihood of igniting explosive and flammable gases. Previous findings have revealed that high working temperatures may lead to further crystallization and crystallite size growth and this often result in sensitivity decline and sensor instability [17]. For this reason, it is of great importance to come up with novel solutions to lower the operating temperature of ZnO. Various approaches aimed at improving the sensing capabilities of ZnO-based sensing materials have been explored, including the incorporation of dopants [18, 19], the dispersion of noble metal nanoparticles as sensitizers or catalysts on the ZnO surface [20, 21], the preparation of mixed semiconductor metal oxides (SMOs) nanocomposites [22, 23], annealing [24, 25] and surface defect control [26, 27]. Doping of ZnO with an appropriate dopant has been demonstrated to offer possibilities of altering its

catalytic activity, grain size and surface area, thus improving its sensing performance [28, 29]. Rare earths, especially La, are regarded as suitable dopant candidates for ZnO due to their catalytic nature and fast oxygen ion mobility [30-32]. For instance, Xu *et al.* [32] observed excellent acetone sensing behaviour for La-doped ZnO NFs and assigned it to an increase in the surface adsorption and catalytic nature of La. On the other hand, Jeong *et al.* [33] attributed improved CO_2 sensing performance of La-loaded ZnO nanostructures to the large lattice distortion and joint effect between the Zn and La active materials for the CO_2 adsorption and reactivity on the surface. Although the introduction of metal additives has been validated as an effective approach in promoting the gas sensing capabilities of ZnO, the mechanism behind such enhanced sensing capabilities is not yet well understood. Similarly, La-doped ZnO nanostructures have not yet been explored in the context of H_2S detection. In addition, as annealing has been shown to influence the gas sensing properties of ZnO-based materials [25, 34], however, reports focusing on the combined effects of La-doping and annealing for gas sensing application are very limited, especially on La-doped ZnO. Furthermore, previous findings have revealed that the sensing mechanism of the H_2S gas of various SMO exhibits an enhanced response at lower operating temperatures. However, the recovery time has been often found to be poor and incomplete. As a result, additional approaches including UV irradiation and even heating in order to speed up the process of recovery have been tried-out. Therefore, finding a reliable approach to this recovery process issue upon H_2S detection is of fundamental importance. Lastly, variations of the ZnO nanostructures morphology during synthesis and post- synthesis have been also shown to have a great effect on the resulting gas sensing performance. In the case of annealing, it has been demonstrated that the physical and lattice

characteristics of the ZnO can be improved. Even though annealing is known to induce grain growth, studies have revealed that it can be used to optimize the grain size and crystallinity to obtain better sensing performance [8]. Katoch *et al.* [11] reported that simultaneous control of grain size and crystallinity through annealing play a significant role in improving the CO sensing performance of ZnO NFs. On the other hand, Zhang *et al.*[25], revealed that annealing ZnO nanorods significantly improved the crystal quality and this led to enhanced H_2 sensing performance.

In this context, we herein report on an electrospinning approach to develop La-doped ZnO NFs-based sensors with the ultimate aim of enhancing the sensor response performance to allow their wider utilization. A comparison of the H_2S gas sensing properties of the pure and La-doped ZnO NFs-based sensors with different La doping levels annealed at various temperatures were also conducted. To understand the influence of La-doping and annealing on the H_2S sensing performance of the ZnO NFs, further analysis were conducted using X-ray diffraction (XRD), scanning electron microscopy (SEM), transmission electron microscopy (TEM), X-ray photoelectron spectroscopy (XPS) and Brunauer-Emmett-Teller (BET) instrument. Finally, the possible sensing mechanism was examined to account for the differences between the various materials (i.e. pure and La-doped ZnO) and annealing conditions.

4.2 Synthesis of the ZnO NFs

Pure and La-doped ZnO NFs with different La concentrations were prepared using an electrospinning method and the experimental procedure was as follows: 0.6 g of zinc nitrate hexahydrate ($Zn(NO_3)_2.6H_2O$) and a specific amount of

lanthanum nitrate hydrate ($La(NO_3)_3.H_2O$ to prepare 0.06, 0.3,1 and 2 wt% of La, respectively were dissolved into a mixed solvent solution of distilled water and ethanol under vigorous stirring. Subsequently, 1 g of polyvinylpyrrolidone (PVP, Mw=1,300,000) was added into the dissolving solution with vigorous stirring for 4 hours to allow complete mixing of the precursors. The obtained homogeneous solution was loaded into a glass syringe for electrospinning at room temperature. The distance between the needle tip and the drum collector rotating at a speed of 100 rpm was set to 15 cm and the voltage to 20 kV. The as-spun fibers were collected on aluminium foil. After electrospinning, the fibers were peeled off from the aluminium foil and subjected to annealing at 500, 700 and 900 °C at a heating rate of 3°C min^{-1} for 2 hours in air. The experimental procedure employed for preparation of the ZnO NFs using electrospinning method is presented schematically in Figure 4.1.

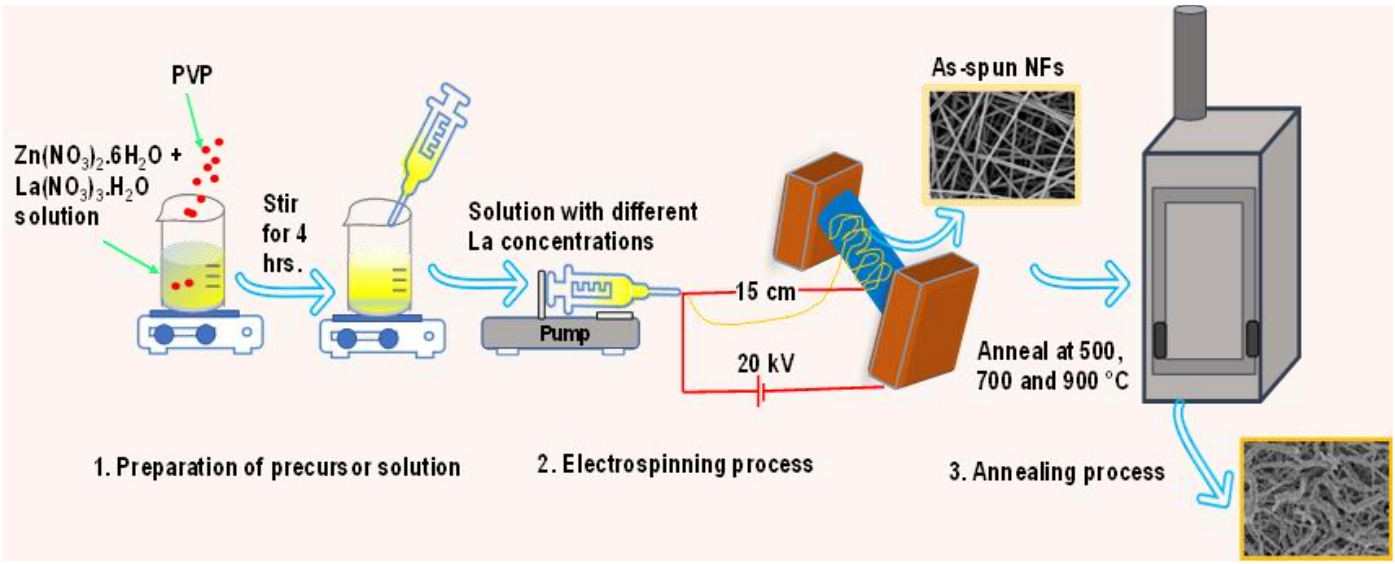

Figure 4.1: Schematic diagram of the electrospinning set-up.

4.3 Characterization of the pure and La-doped ZnO NFs

The thermal behaviour of the as-spun samples was investigated through the use of a Perkin Elmer Thermogravimetric Analyzer Pyris 1 TGA. The measurements were performed in air at temperatures ranging from room temperature to 950 °C at a heating rate of 10°C/min. To examine the crystal phase and purity of the pure and La-doped ZnO samples, a computer controlled Panalytical X'pert PRO PW3040/60 X-ray diffractometer with a Cu-Kα (λ=1.5405 Å) radiation was used. The chemical state analyses of both the pure and La-doped ZnO NFs were carried out by the use of a PHI 5000 Versaprobe X-ray photoelectron (XPS) with monochromatic Al-Kα radiation ($h\nu$ = 1486.6 eV). The chemical composition and dopant distribution in the host lattice was analysed through the use of a Time of Flight-Secondary Ion Mass Spectrometry (ToF-SIMS) technique, equipped with a primary Bi^+ source and pulsed electron source of 30 eV for charge compensation. The surface morphology of the samples was examined using a ZEIS-AURIGA scanning electron microscopy (SEM) at an acceleration voltage of 3 kV, and JEOL TEM-2100 transmission electron microscopy (TEM) with an accelerating voltage

of 200 kV equipped with electron dispersive X-ray Spectroscopy (EDS). The specific surface area studies of the NFs were measured using a Micrometirics TRISTAR 3000 surface area analyser. Preceding the analysis, the samples were degassed at 200 °C for 1 h under continuous flow of N_2 gas to remove adsorbed impurities.

4.4 Fabrication of pure and La-doped ZnO NFs-based sensors and their subsequent gas sensing tests

The procedure followed for fabrication of the ZnO NFs-based sensors was as follows; synthesized NFs (either pure or La-doped ZnO NFs) were dispersed in ethanol to form pastes which were drop-coated onto an alumina substrate bearing a pair of platinum (Pt) electrodes on the top surface to provide electrical contacts (Figure 4.2a), in addition to a micro-heater on the bottom surface (see Figure. 4.2b). Prior to carrying out the gas testing measurements, the deposited NF layers were dried at room temperature for 2 hours, and then heated to 500 °C for 2 h at a heating rate of 3 °C/min to achieve good adhesion. The gas sensing tests were conducted on different test gases namely, NH_3, H_2S, NO_2, CO and CH_4 by means of a KSGAS6S gas sensing station (KENOSISTEC, Italy). The desired concentrations of each gas in parts per million (ppm) were established by variation of the flow rate ratios of synthetic air and target gas source using mass flow controllers. The electrical responses of the ZnO based sensor devices were acquired by monitoring the electrical changes in resistance under a constant applied voltage during cyclic exposure to different target gas concentrations using a Keithley 6487 picoammeter/voltage source meter. The resistance of the sensors was recorded upon exposure to the test gas at different operating temperatures ranging from room temperature to 250 °C. The response of the sensors is defined as the ratio Ra/ Rg [34], where Ra is the sensor resistance in

air, and Rg is the sensor resistance in the presence of test gas. And the response and recovery times can be defined as the time taken by the sensor material to attain 90% of the response signal when exposed to the target gas, and the time taken by the sensor to return to 90% of its baseline once the target gas feed is switched off, respectively. Figure 4.2 shows the schematic of the fabricated sensors whereby V_S is the applied signal voltage and V_H is the heating voltage, respectively.

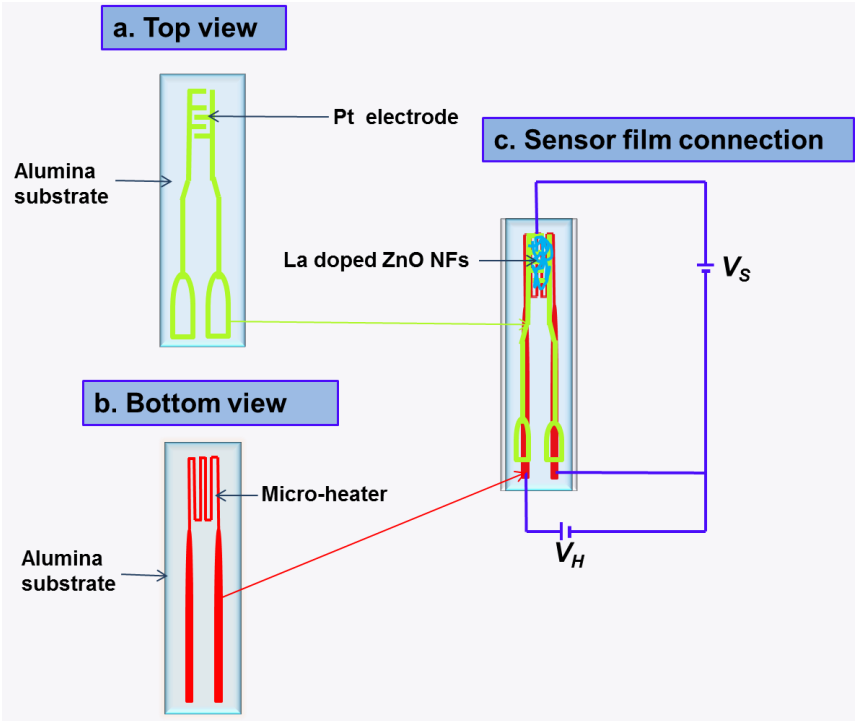

Figure 4.2: The (a) top view, (b) bottom view and (c) sensor film connection during gas sensing measurements.

4.5 Results and discussion

4.5.1 Thermal Analysis

To find the suitable annealing temperature, Thermogravimetric analyses were performed on the as-spun pure and La-doped PVP/ZnO with different La concentration in air at a temperature range between 30 °C and 1000 °C at a ramp rate of 10 °C/min. As shown in Figure 4.3 the pure PVP/ZnO sample showed three degradation steps in the range between 30 to 455 °C corresponding to the degradation of the nitrates, PVP, and volatiles with a total weight loss of 65%. The first degradation step between 30 to 150 °C corresponds to evaporation of the volatiles such as water and ethanol which contributed to 10% weight loss. The second degradation step of 13% weight loss which occurred between 310 to 362 °C resulted from decomposition of the zinc nitrate and PVP while the third dramatic weight loss of 42% which occurred between 370 and 453 °C can be associated with continued decomposition of the nitrates and PVP. Interestingly, the La = 1 and 2 wt% doped PVP/ZnO had an additional degradation step at temperature higher than 800 °C and this can be attributed to the change in crystal structure at higher temperatures [25, 35]. In addition, compared to the pure PVP/ZnO sample, the La-doped PVP/ZnO samples degraded at slightly higher temperatures and this could probably due to the interaction between the PVP, ZnO and La materials which resulted in high chain compactness [35, 36]. Based on this finding, three annealing temperatures of (500, 700 and 900 °C) were chosen to investigate the effect of annealing on structural, morphological and surface properties of ZnO NFs.

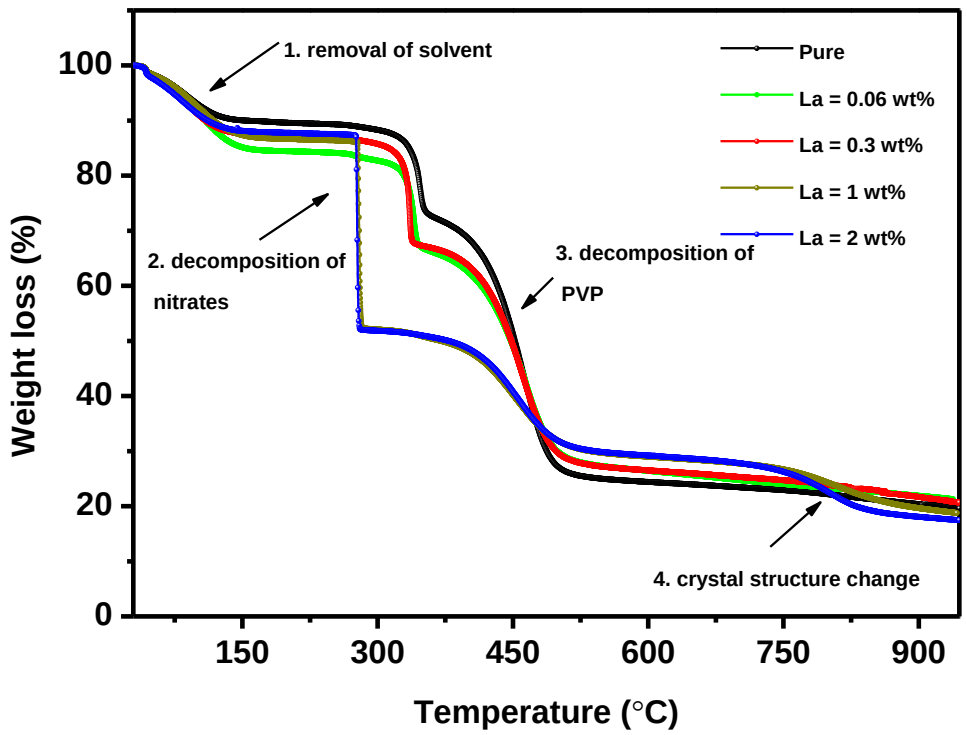

Figure 4.3: TGA curves of the as-prepared PVP/La/ZnO composite fibers**.**

4.5.2 Structural analysis

After successfully synthesizing the pure and La-doped ZnO NFs containing various doping levels (i.e. 0.06, 0.3 ,1 and 2 wt%) and annealed at various temperatures (i.e. 500 °C ,700 °C and 900 °C), their phase purities and crystal structures were examined by means of XRD. Figure 4.4 (a-c) shows the diffraction patterns acquired for the pure and La-doped ZnO samples. Following annealing at 500 °C, the diffraction patterns obtained from both the pure and La-doped ZnO were readily indexed to the wurtzite phase of ZnO, which corresponds to a hexagonal wurtzite structure of ZnO (JCPDS 036-1451) with a = 3.2488 Å and c = 5.2061 Å. No evidence of extra phases corresponding to La could be seen indicating that the La has been successfully doped into the ZnO lattice without any segregation as La_2O_3. However, with annealing at 700 °C

(Figure 4.4b), the hexagonal structure of ZnO was only maintained up to a La-doping level of 0.3 wt% while for the samples annealed at 900 °C (Figure 4.4c) the hexagonal structure of ZnO was maintained up to La-doping concentration of 0.06 wt%. New peaks belonging to La_2O_3 marked with asterisk (*) were observed at higher La-doping levels, suggesting that at an initial temperature of 500 °C La is incorporated as La^{3+} in the ZnO host whereas at higher temperatures of 700 and 900 °C part of it segregates as a second phase (La_2O_3) from the ZnO host.

It was further noticed that the intensities of the diffraction peaks deteriorated following La addition for all annealing temperatures (i.e. 500, 700 and 900 °C). This observation suggests deterioration of the ZnO lattice crystallinity upon the incorporation of La. The insets of Figure 4.3(a-c) illustrate a magnified diffraction peak corresponding to the (101) plane where an obvious shift to lower and higher diffraction angles was observed with varying La-doping levels for all annealing temperatures. The observed shift in diffraction peak positions towards higher and lower 2θ angles in this case indicates the shortening and elongation of the inter-planar distance, respectively, which in turn leads to compression and expansion of the ZnO lattice through the partial substitution of smaller ionic radii Zn^{2+} ions (0.074 nm) by larger ionic radii La^{3+} ions (0.122 nm), respectively. Furthermore, the observed shifts agree well with previous reports of doped ZnO nanostructures, thereby confirming that these shifts strongly depend on the dopant concentration [30, 37, 38]. This behaviour also suggests that the incorporation of La ions induces lattice strain in the ZnO lattice.

The average crystallite sizes(D) of the pure and La-doped ZnO NFs were also determined by measuring the full width at half maximum (FWHM) of the intense (101) diffraction peak using the Debye-Scherrer formula [39] and the values are

listed in Table 4.1. The crystallite size of the ZnO NFs was shown to decrease with La-doping (see Table 4.1) for all annealing temperatures. This can be associated with the distortion of the ZnO lattice by the larger La ions, which constrains the growth and nucleation rate of the ZnO NFs. Similar results were obtained by Devi *et al.* [40] for La-doped CuO and Lang *et al.* [41] for La-doped ZnO. However, with further increase of annealing temperature to 900 °C, the crystallite sizes values increased for all samples with the pure ZnO NFs displaying bigger crystallite sizes as compared to La-doped ones is expected as annealing at higher temperatures promotes crystal growth. Further, the presence of strain inside the ZnO lattice is considered as one of the important parameters contributing to the observed shift in diffraction peak positions as highlighted above, so the micro-strain (ε) has also been calculated using the peak position [42] of the (101) peak.

The micro-strain values for both the pure and La-doped ZnO NFs at different annealing temperatures were found to increase with increasing La concentration as shown in Table 4.1. This increasing behaviour in micro-strain values could be mainly due to distortion of the ZnO lattice created by the La dopant ions owing to the incompatibility or mismatch between the ionic radii of La^{3+} and Zn^{2+} [43, 44]. However, the micro-strain as a function of annealing temperature decreased for all samples, this is attributed to the fact that annealing at higher temperatures provides the atoms with higher energy to adjust their position in the lattice [8]. Based on the observed results, the effect of La-doping on the crystallite structure was also investigated by determining the lattice parameters (a and c) using the formula for the hexagonal phase based on Bragg's law [37]. The lattice parameters calculated for the pure and different La-doping levels at various

annealing temperatures are listed in Table 4.1, where it is obvious that the lattice parameters *a* and c varied upon increasing dopant concentration.

The addition of the La ions with large ionic radii than ZnO, coupled with the annealing temperatures caused peak position shift, broadening, degree of crystallinity change and also formation of a second phase. All these changes in the host lattice structure can be attributed to the lattice parameters variations.

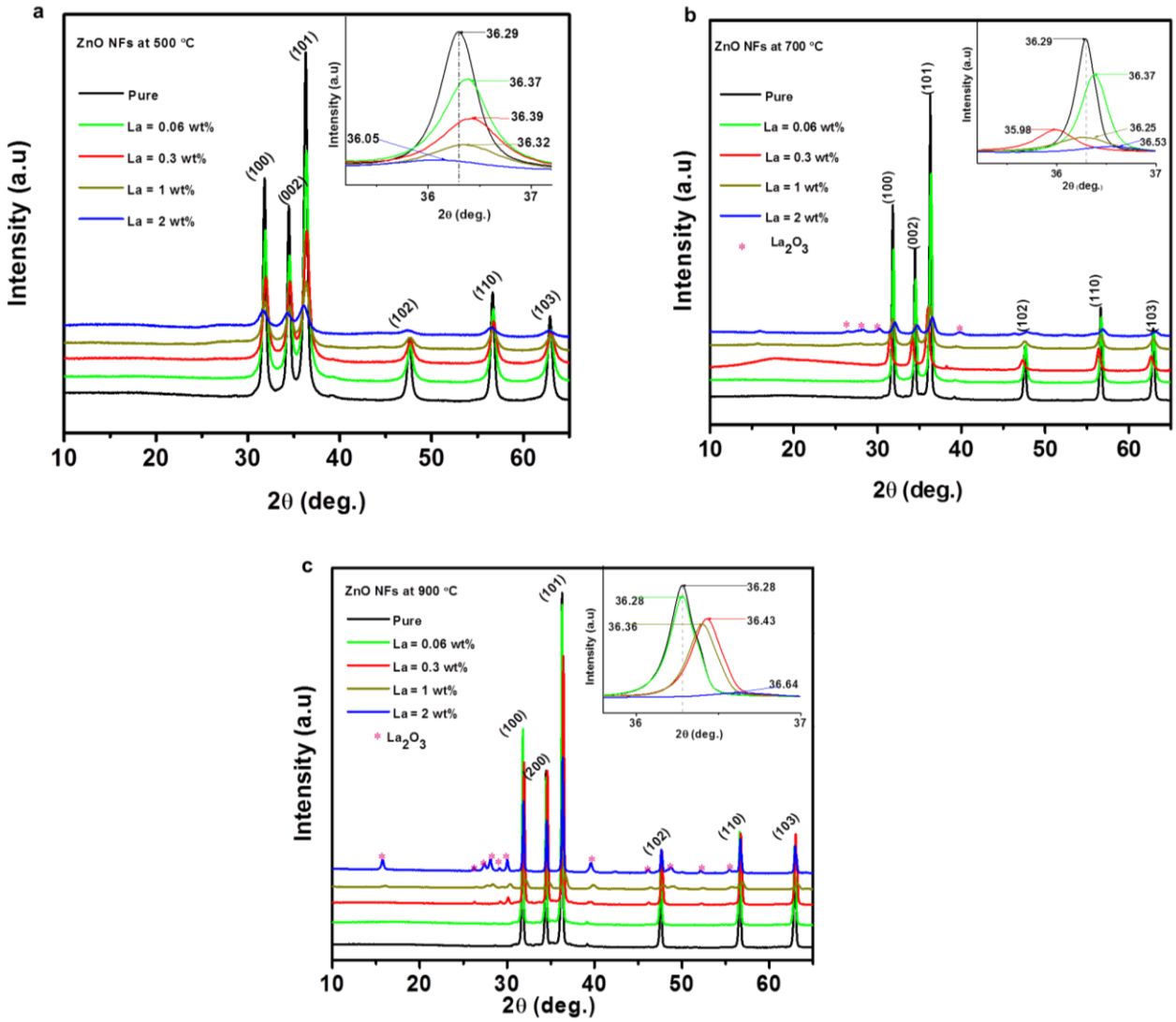

Figure 4.4: The XRD diffraction patterns for the pure and La-doped ZnO NFs annealed at (a) 500 °C, (b) 700 °C and (c) 900 °C.

Table 4.1: The variation of peak position, cell parameters *a* and *c,* inter-planar spacing *(d)*, average crystal size *(D)*, and Micro strain *(ε)* of the pure and La-doped ZnO nanostructures

Sample	2θ	Cell parameters		d(Å)	D(nm)	Micro-strain (ε) (10^{-3})
		a	c			
		Annealed at 500 °C				
Pure	36.29	3.2455	5.1245	2.47	25.0	1.39
0.06 wt% La	36.37	3.2375	5.1111	2.46	18.34	1.89
0.3 wt% La	36.39	3.2316	5.1037	2.46	11.64	2.97
1 wt% La	36.32	3.2385	5.1111	2.47	11.49	3.01
2 wt% La	36.05	3.2647	5.1364	2.48	3.59	9.63
		Annealed at 700 °C				
Pure	36.29	3.2464	5.1230	2.47	41.21	0.84
0.06 wt% La	36.37	3.2375	5.1096	2.46	29.53	1.17
0.3 wt% La	35.98	3.2759	5.1684	2.49	22.30	1.55
1 wt% La	36.25	3.2464	5.1230	2.47	14.21	2.43
2 wt% La	36.53	3.2200	5.0846	2.45	13.73	2.52
		Annealed at 900 °C				
Pure	36.28	3.2474	5.1245	2.47	51.72	0.67
0.06 wt% La	36.28	3.2474	5.1245	2.47	50.43	0.69
0.3 wt% La	36.43	3.2325	5.1023	2.46	43.29	0.80
1 wt% La	36.36	3.2407	5.1126	2. 46	49.42	0.70
2 wt% La	36. 64	3.2111	5.0686	2.45	19.86	1.74

4.5.3 Morphological analysis

To determine the morphology and microstructure of the pure and La-doped ZnO NFs, SEM and TEM were employed. Figure 4.5 to 4.7 present the SEM micrographs acquired both before and after La-doping with different La

concentrations and annealed at 500, 700 and 900 °C. It is important to note that prior annealing, the as-spun sample was firstly scanned to establish its morphology and it was realized that a mat of smooth randomly orientated fibers with diameters around 1.5 μm were formed as shown in Figure 4.5 (a). After subjecting the fibers to an annealing temperature of 500 °C, it was noticed from SEM micrographs obtained from both the pure and La-doped ZnO samples that the fibrous-like structure was still maintained. However, a closer inspection of the SEM micrographs revealed that these fibrous-like structures are composed of many small interconnected particles of 20-50 nm in diameter (see Figure 4. 5 b–e). In addition, the diameter of the NFs contracted from 1.5 μm of as-spun fibers to 60-100 nm in diameter following initial annealing probably due to decomposition of the PVP and the zinc nitrate precursors. Based on SEM observations, it is obvious that addition of La into ZnO lattice did not alter the mat of randomly orientated fibers although the size of the interconnected particles was found to be reduced upon increasing La-doping concentration. Reduction of the particle size means improvement of the surface-to-volume ratio of the NFs, and this may contribute during gas sensing by providing ample active sites for gas adsorption and desorption thus improving the sensing performance of the sensors. Upon annealing the samples at 700 °C (see Figure 4.6), the fiber-like structures consisting of small interconnected particles were still maintained, however; the interconnected particles were a bit loosened and inhomogeneous in terms of size. Moreover, the particle size exhibited growth in comparison to those annealed at 500 °C. With further annealing to 900 °C, the ZnO NFs transformed completely to an agglomerated nanoparticle morphology which showed even more growth in the particle size. Interestingly, the 2 wt% La-doped ZnO NFs still maintained their fibrous morphology, however, the interconnected

particles were found to be loosely connected and this is important in gas sensing as the loose particles provide more diffusion channels for gas molecules leading to enhanced gas sensing performance. The size of the nanoparticles in NFs can greatly influence the gas sensing properties of NFs as small particles will result in large number of grain boundaries between particles [8, 13]. Hence, the particle size growth at higher annealing temperatures is driven to reduce the number of boundaries between particles, thus affecting gas sensing properties. Particle size growth occurs through atomic migration or diffusion, and it is a thermal dependent process [45]. So the particle growth is a factor that affects the morphological change at higher annealing temperatures [46]. During the annealing process at higher temperatures (700 and 900 °C), the migration of the grain boundaries in the NFs is activated and the crystal atoms gain energy that assist them to overcome thermal energy barrier between crystal grains and they move freely in the lattice through diffusion. Therefore the NFs morphology will gradually evolve into a nanoparticle morphology [25]. The influence of the annealing temperature on the particle size (D) was estimated by measuring the diameters of several nanoparticles in individual NFs and the particle size distribution results are shown as insets of the SEM images. From the particle size distribution plots, it can be noticed that continuous rise of the annealing temperature results in the growth of the particles and also inhomogeneous distribution of the particle sizes.

For further examination of the structural features of the La-doped ZnO NFs, TEM and high resolution-TEM (HR-TEM) was utilized. The 2 wt% La-doped ZnO sample annealed at 900 °C was selected for this examination in this case. Figure 4.8a shows the TEM micrograph of the La-doped ZnO NFs (2 wt%) annealed at 700 °C; which affirms the fibrous-like structure morphology. The HR-TEM

micrograph shown in Figure 4.8b display clear lattice fringes with d-spacing of 0.28 and 0.32 nm, corresponding to the (100) and (110) planes of ZnO and La_2O_3 respectively. The selected area diffraction (SAED) patterns (Figure 4.8c) confirms that the NFs are polycrystalline in nature with Debye rings corresponding to diffractions from (100) and (101) planes of ZnO and also (110) plane of La_2O_3. These results are in good agreement with the XRD. To verify the existence of and distribution of La on the ZnO NFs surface, the EDS elemental maps and spectra were acquired (see in Figure 4.8d-h). Both the EDS elemental maps and spectra results revealed the uniform distribution and presence of Zn, O, and La elements, respectively.

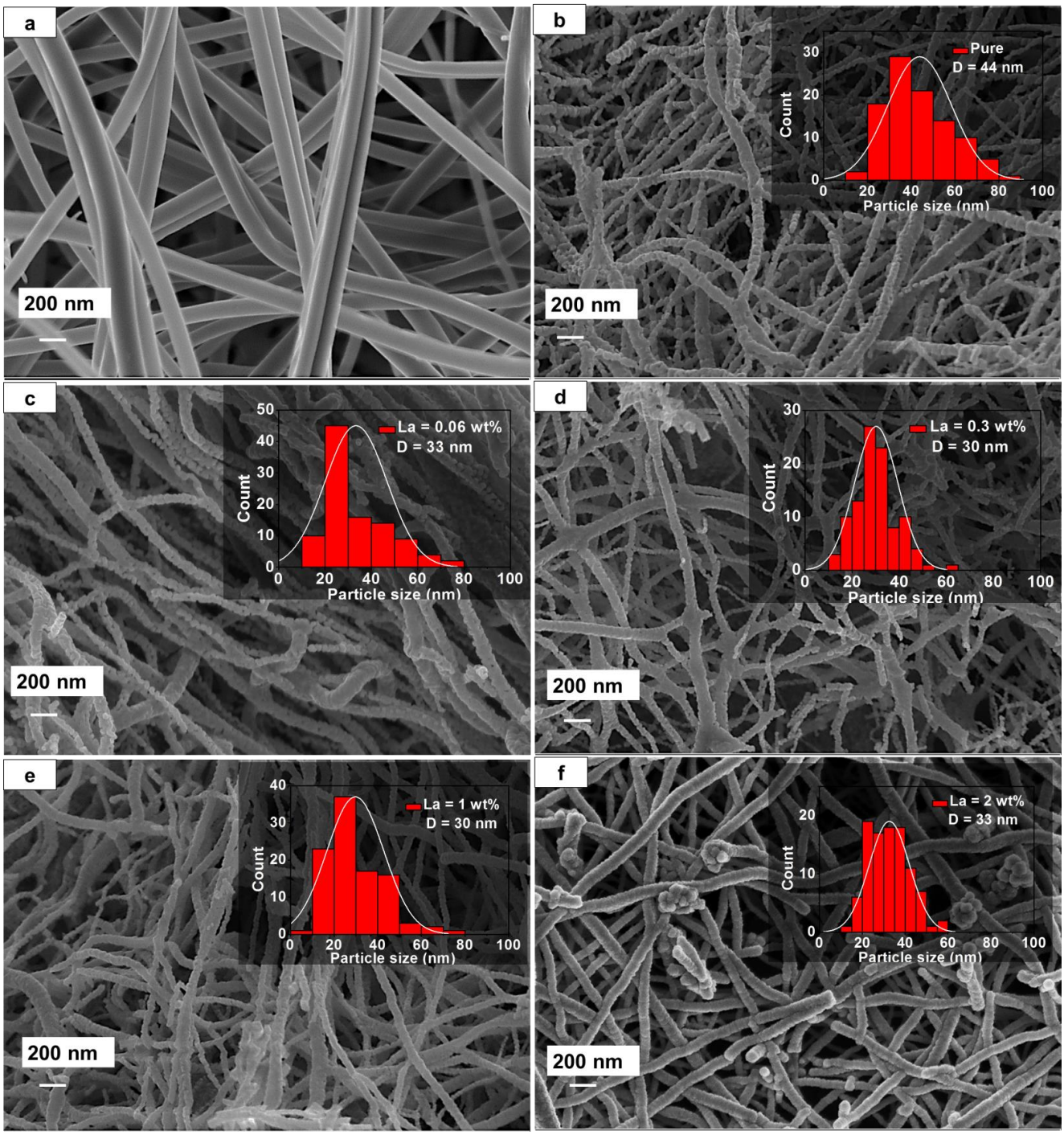

Figure 4.5: SEM images of the (a) ZnO/PVP as-spun fibers, (b) pure and (c-f) La (0.06, 0.3, 1 and 2 wt%) doped ZnO NFs annealed at 500 °C.

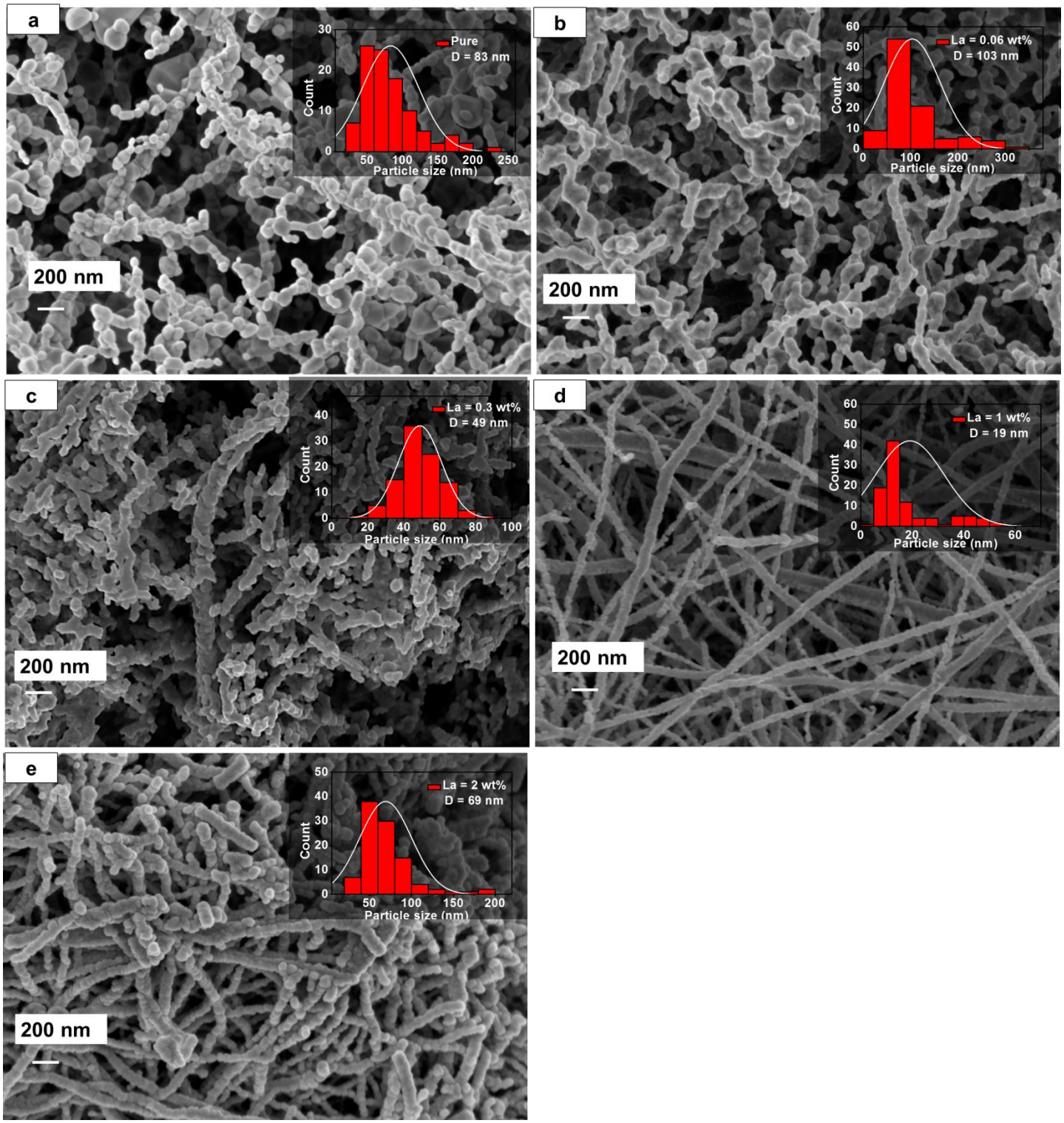

Figure 4.6: SEM images of the (a) pure and (b-e) La (0.06, 0.3, 1 and 2 wt%) doped ZnO NFs annealed at 700 °C.

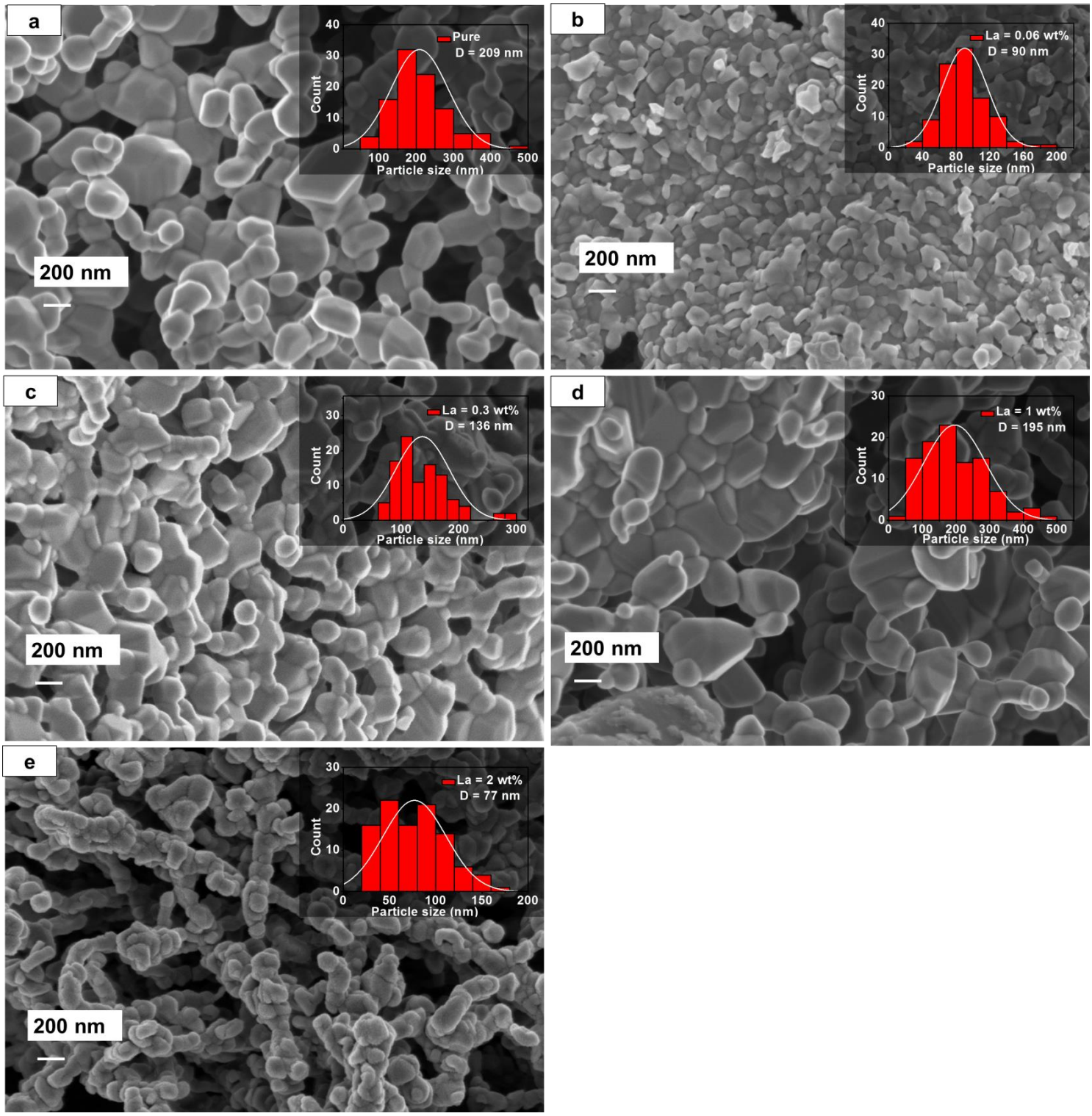

Figure 4.7: SEM images of the (a) Pure and (b-e) La (0.06, 0.3, 1 and 2 wt%) doped ZnO NFs annealed at 900 °C.

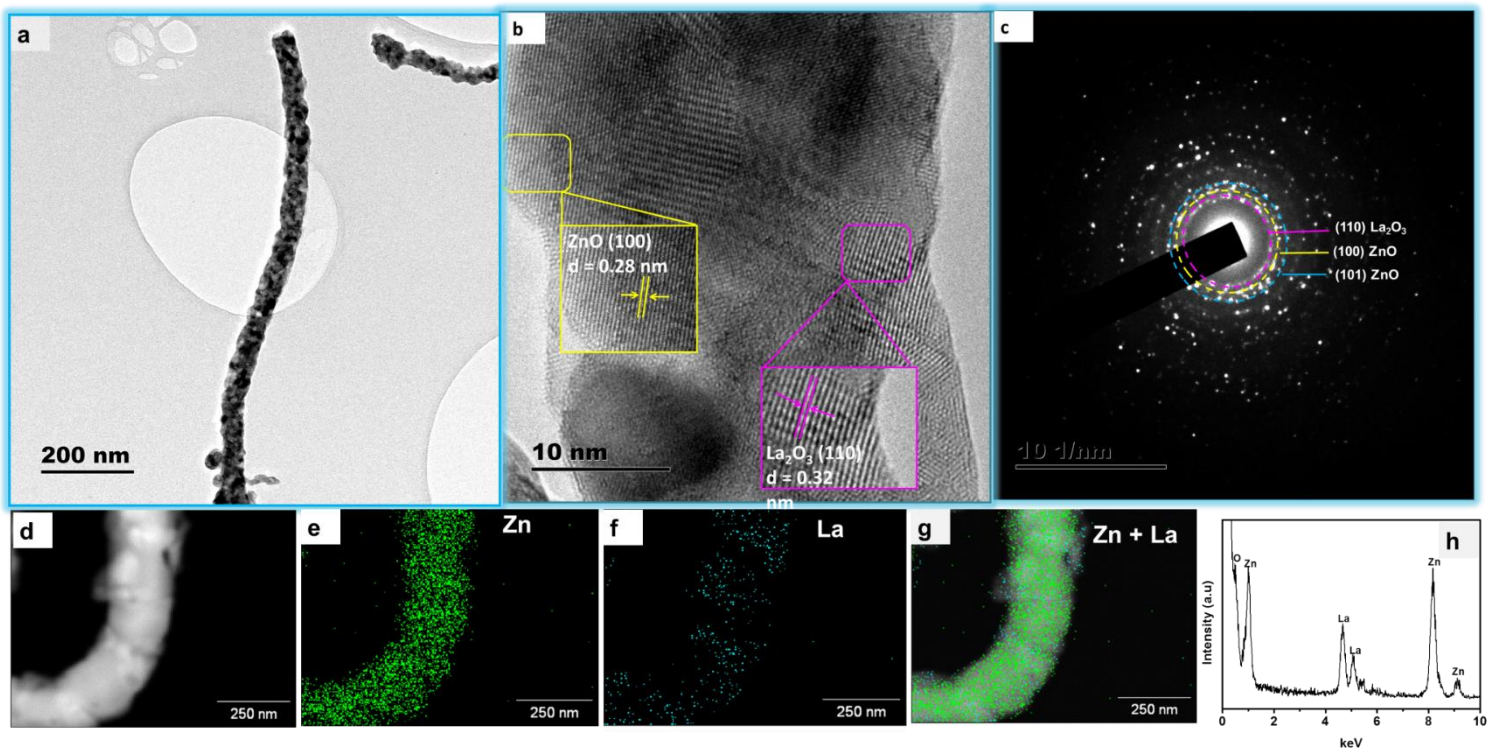

Figure 4.8: (a) TEM, (b) HR-TEM images (c) Selected Area Electron Diffraction (SAED) patterns, (d-g) EDS elemental maps and (h) EDS spectra of the 2 wt% La-doped ZnO NFs at 900 °C.

4.5.4 Surface analysis

4.5.4.1 ToF-SIMS analysis

To further verify the presence of the La^{3+} ions as well as to establish its homogeneity, ToF SIMS was employed. In this case, the pure, 0.3 and 2 wt% La-doped ZnO NFs annealed at 900 °C were chosen for this investigation. Figure 4.9 (a-c) show the ToF-SIMS maps for the pure ZnO, 0.3 and 2 wt% La-doped ZnO NFs, respectively where the elemental maps of Zn (red colour) and La (green colour) were observed. The elemental map acquired from the pure ZnO sample revealed a uniform distribution of Zn (see Figure 4.9 (a)). For the 0.3 wt% La sample (Figure 4.9 (b)) the La^{3+} ions were noticed to be homogeneously distributed on the

ZnO surface which is an indication that ZnO exist in a uniform phase. However, at a higher doping level of 2 wt% (Figure 4.9 (c)), the La^{3+} ions were found to agglomerate on the surface of the ZnO NFs thereby confirming that La_2O_3 segregated to the surface at higher doping concentrations.

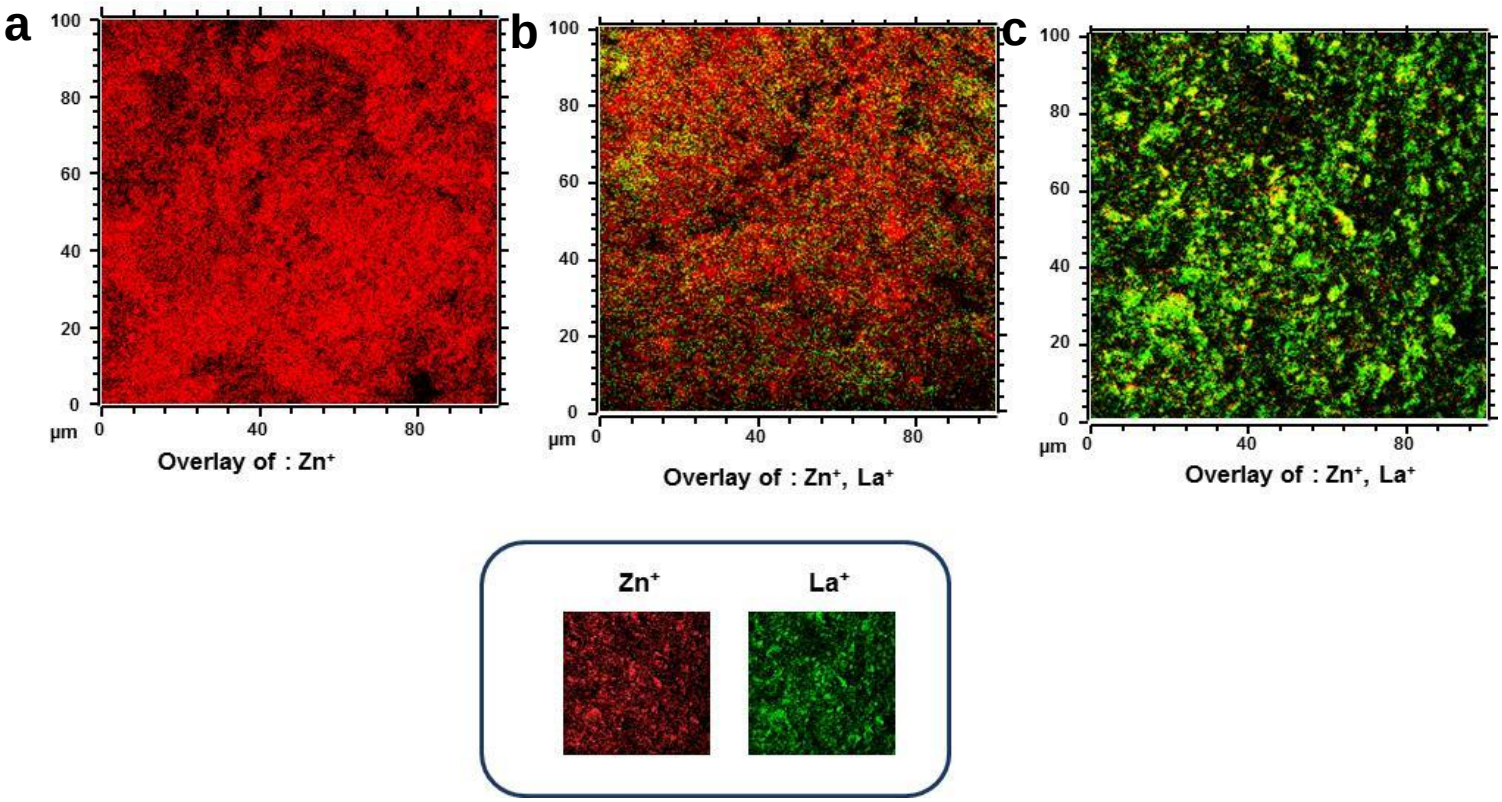

Figure 4.9: ToF-SIMS overlay images of the (a) Pure, (b) 0.3 wt% and (c) 2wt% La-doped ZnO NFs, showing the distribution of the Zn and La.

4.5.4.2 XPS analysis

Confirmation of the presence of La in the ZnO as well as the examination of the chemical states of the elements present in both pure and La-doped ZnO NFs was further conducted by XPS. The high-resolution XPS spectra corresponding to the core level of the Zn 2p obtained from the pure and 2 wt% La-doped ZnO NFs after annealing at 500, 700 and 900 °C presented in Figure 4.10 (a to c) show the

spin-orbit splitting of the Zn 2p3/2 and Zn 2p1/2 core level states positioned at 1021.1 and 1044.0 eV, indicating that the Zn atoms are in the +2 oxidation state, respectively [47]. The energy difference between the Zn 2p3/2 and Zn 2p1/2 is 23. 1 eV; and is in agreement with the standard value of 22.97 eV [48]. However, it was realized that at an annealing temperature of 900 °C the highly La-doped ZnO sample of 2 wt% revealed the splitting of each core level state into two additional peaks. This unusual Zn2p spectrum indicates that two chemical states of Zn occur in the La-doped ZnO sample at 900 °C [49]. It is also worth mentioning that La addition into ZnO led to shift in the binding energy positions of the Zn 2p3/2 and Zn 2p1/2 core level states signifying the change in their chemical environment. Therefore the shifts of the binding energies on the Zn2p are an indication of the interaction between ZnO and the ions from the dopant [31].

The high-resolution spectra for the La 3d core level are shown in Figure 4.11 (a-c), where detailed information regarding the chemical state of the doped La can be found. It can be seen that the La 3d core level spectra for the 2 wt% doped ZnO sample following annealing at 500, 700 and 900 °C splits into La 3d5/2 and La 3d3/2 components (see Figure 4.11 (a to c)), due to a spin-orbit interaction, so each line splits into a main and a 'shake-up' satellite line. The energy between the splitting of the main and the 'shake-up' satellite line is 4.1 eV [50, 51], indicating that the La ions exist mainly as La_2O_3 on the NFs surface while other are doped into ZnO lattice and this correlates well with XRD, HRTEM and ToF-SIMS results.

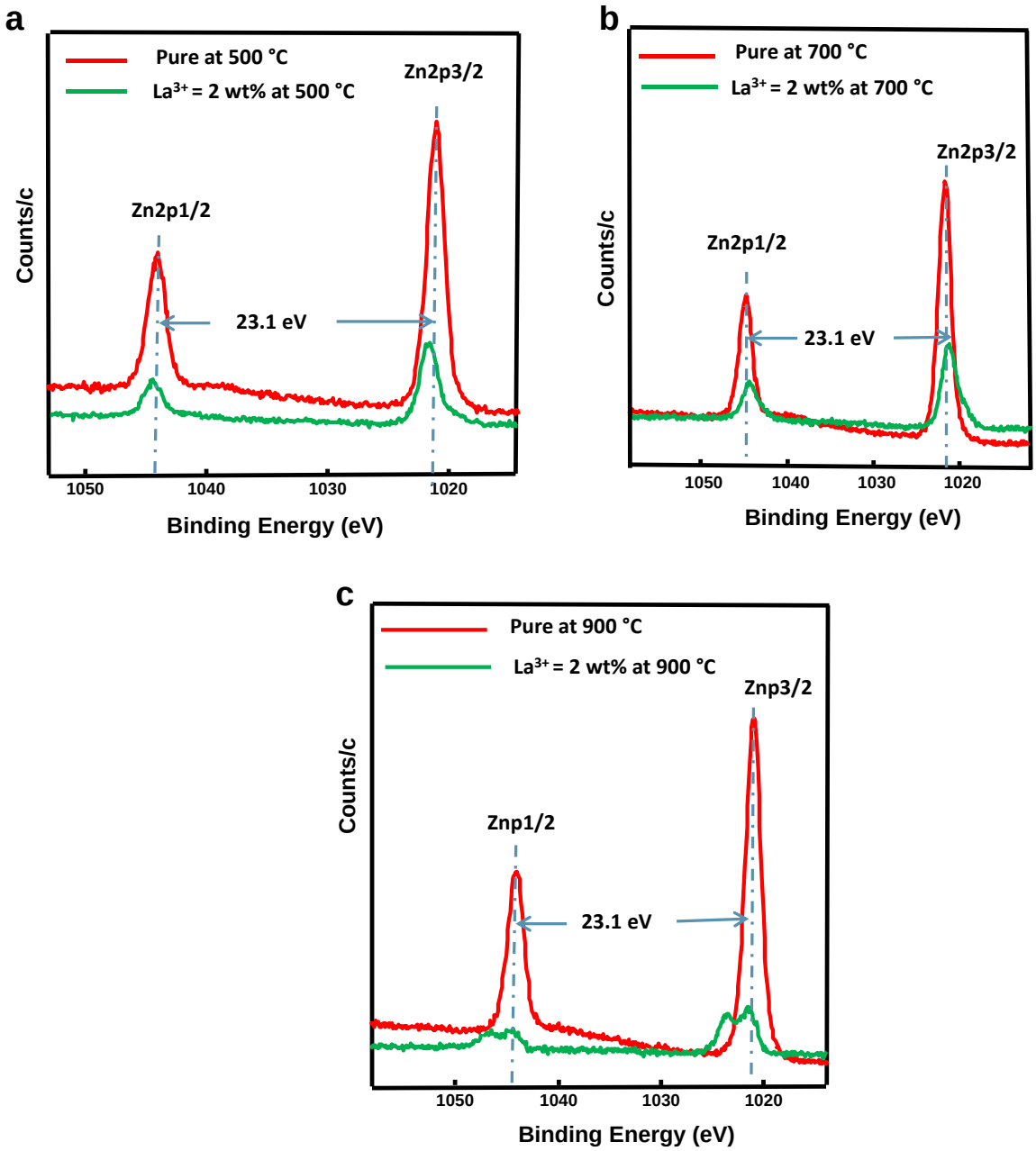

Figure 4.10: High resolution XPS spectra of the Zn2p core level regions for the pure and 2 wt% La-doped ZnO NFs at (a) 500, (b) 700 and (c) 900 °C.

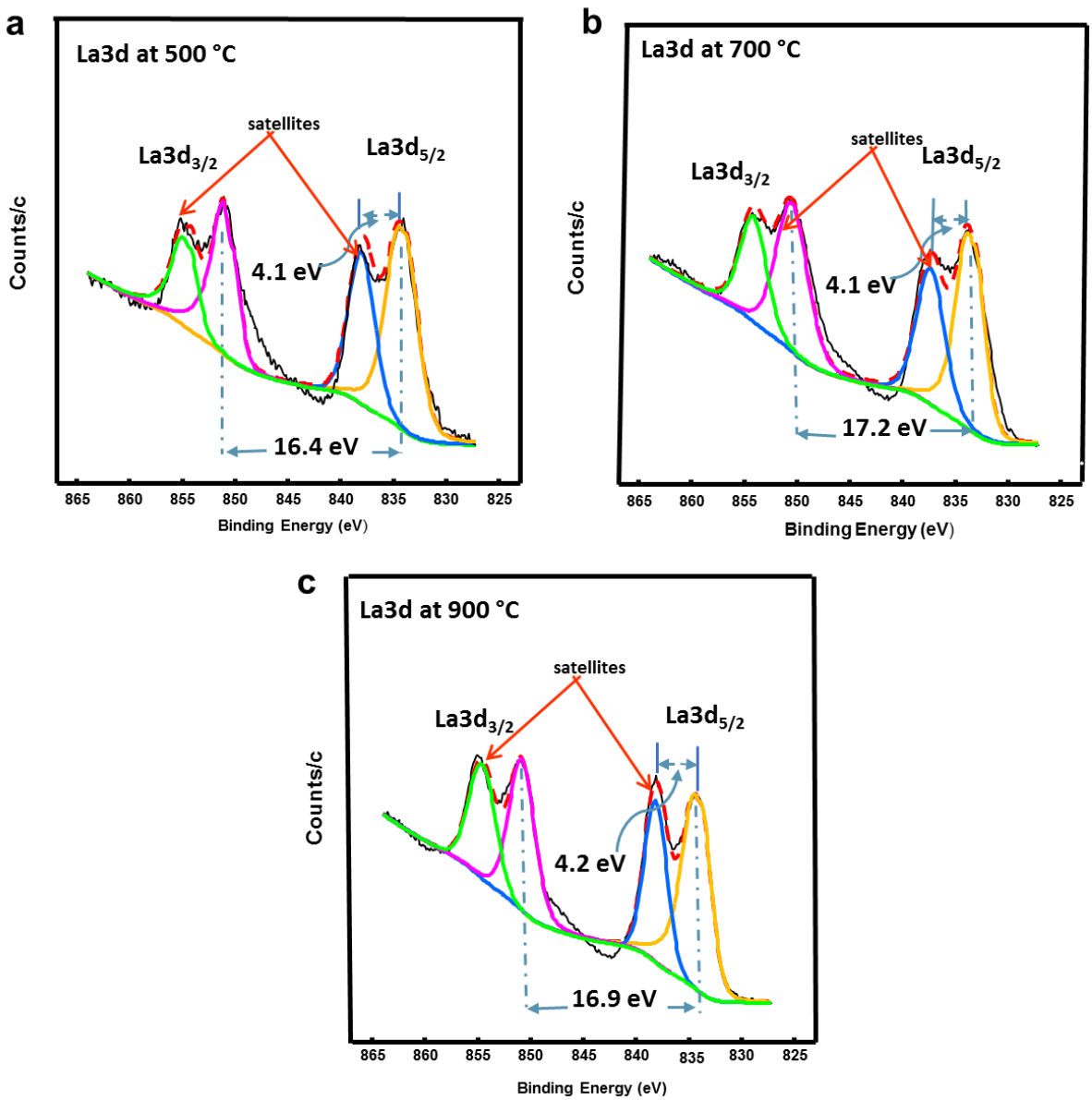

Figure 4.11: High resolution XPS spectra of the La3d core level for the 2 wt% La-doped ZnO NFs annealed at (a) 500, (b) 700 and (c) 900 °C.

Furthermore, the status of the oxygen species in the samples was verified by the asymmetric peaks as shown in Figure 4.12 (a-f), which were de-convoluted into three fitted peaks. The peaks were labelled as O_L, O_v, and O_c corresponding to the lattice oxygen species, oxygen deficiency and the surface chemisorbed oxygen species, respectively [20, 52]. Their binding energies and areas are listed in Table

4.2. The intensity and area of the O_L peak got reduced after La doping whereas the intensity and areas of O_v and O_c; were greatly increased by the La doping. The reduction of the O_L suggests the decrease in the amount of oxygen atoms in a fully oxidized stoichiometric surrounding. On the other hand; the increase of O_v component could provide more active sites on the sensor material for gas adsorption-desorption processes. Also, the increase of O_c component suggests that more surface chemisorbed oxygen species could accelerate the gas sensing reactions on the ZnO surface thus leading to a greater change in sensor response.

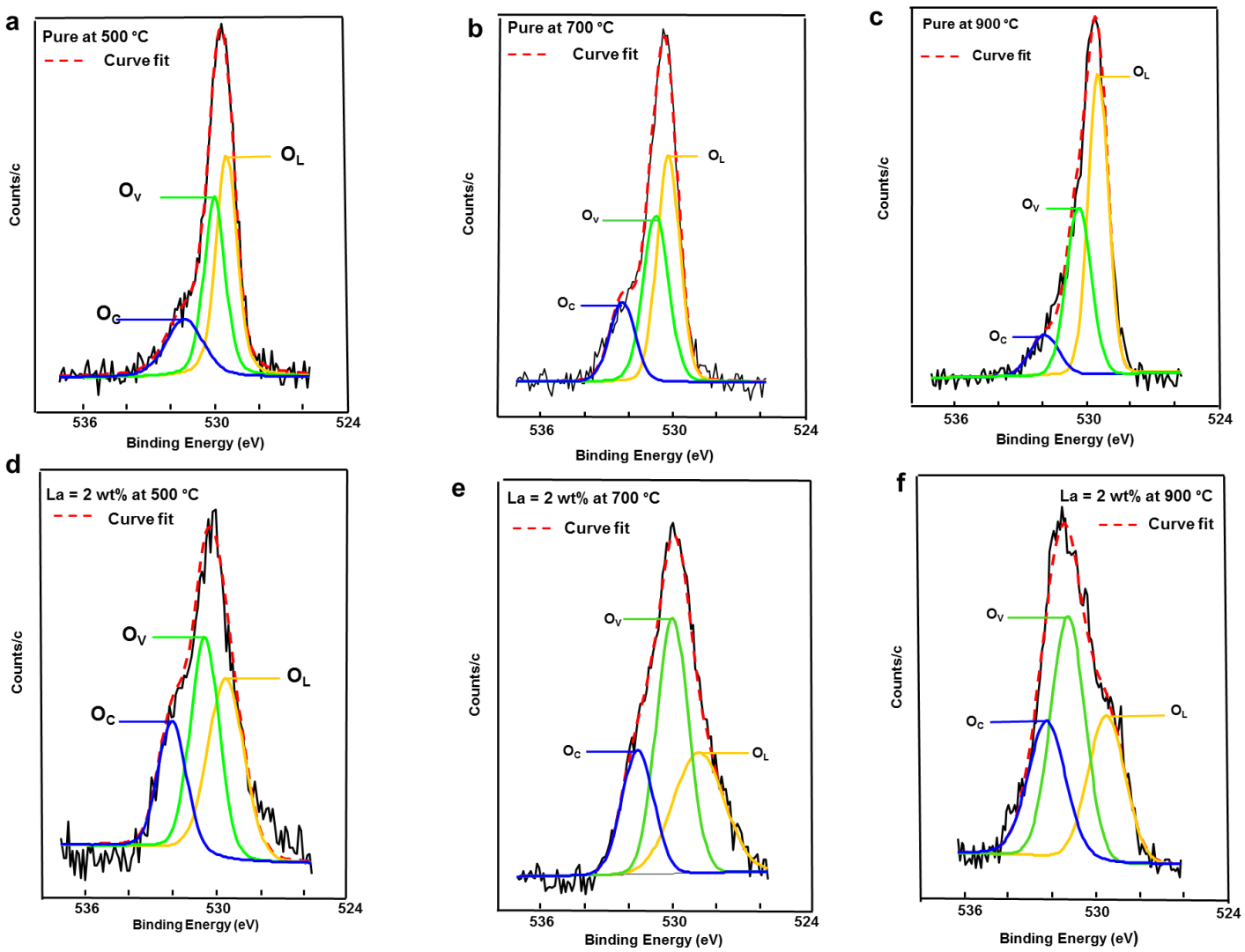

Figure. 4.12: The O1s spectra for the pure and the La = 2 wt% annealed at (a) and (d) 500, (b) and (e) 700 and (c) and (f) 900 °C.

Table 4.2: Data obtained from XPS analysis showing the values for the binding energies of O

Sample		Binding energies (eV)					
	O_L	Area	O_V	Area	O_C	Area	$0_V/0_L$
Annealed at 500 °C							
Pure	529.46	43.82	530.00	35.78	531.36	20.40	0.816
2 wt% La	529.56	39.76	530.52	38.32	532.01	21.92	0.963
Annealed at 700 °C							
Pure	530.17	45.06	530.74	37.07	532.28	17.87	0.822
2 wt% La	528.80	33.44	529.99	44.80	531.57	21.76	1.339
Annealed at 900 °C							
Pure	529.45	54.06	530.34	35.96	531.91	9.97	0.665
2 wt% La	529.43	28.61	531.40	43.16	532.47	28.23	1.508

4.5.4.3 *BET analysis*

Previous studies have demonstrated that annealing at higher temperatures lead to particle size growth [53] and this may deteriorate the surface area of the NFs, so to establish the relationship between the particle size and the surface characteristics of the pure and La-doped ZnO NFs, BET measurements were performed. Figure 4.13 depicts the nitrogen adsorption-desorption isotherms of the pure and La-doped ZnO NFs obtained following annealing at different temperatures of 500, 700 and 900 °C. All the isotherms at 500 °C can be classified as the IV type isotherm according to IUPAC. It can be noticed that all samples show a distinctive H3 type hysteresis loop at relatively high pressures for all isotherms, which is related to the filling and emptying of mesopores ranging from 2 to 50 nm in diameter by capillary condensation [54]. Additionally,

the observed hysteresis loop of all the samples approach P/P_0=1 thereby suggesting the occurrence of macropores (>50 nm) [55, 56]. The isotherms revealed a noticeable negative adsorption-desorption for the pure at 700 °C and for all the samples except 1 wt% at annealing 900 °C. Such isotherms suggest small surface area of the samples or that desorption takes place faster than adsorption.

At an initial annealing temperature of 500 °C, the pure ZnO NFs were found to have a specific surface area value of 10.84 m^2/g, (as shown in Figure. 4.13a). With addition of La into ZnO lattice at different La-doping levels of 0.06, 0.3, 1 and 2 wt%, the specific surface area values were shown to increase with an initial doping concentration of 0.06 wt% La showing the highest surface area of 147.46 m^2/g as shown in Figure 4.13 (a). The observed increase of surface area resulting from the addition of La on the ZnO NFs is an indication that more active sites develops through doping by La. The large surface area of the La-doped ZnO could provide more active sites hence improving gas sensitivity during gas sensing. However, the surface area drastically decreased at higher annealing temperatures of 700 and 900 °C (see values in Figure 4.13 (b) and (c)) which is attributed to the growth in the particles size induced by annealing at higher temperature [53]. Further, the adsorption-desorption isotherms displayed negative isotherms, which

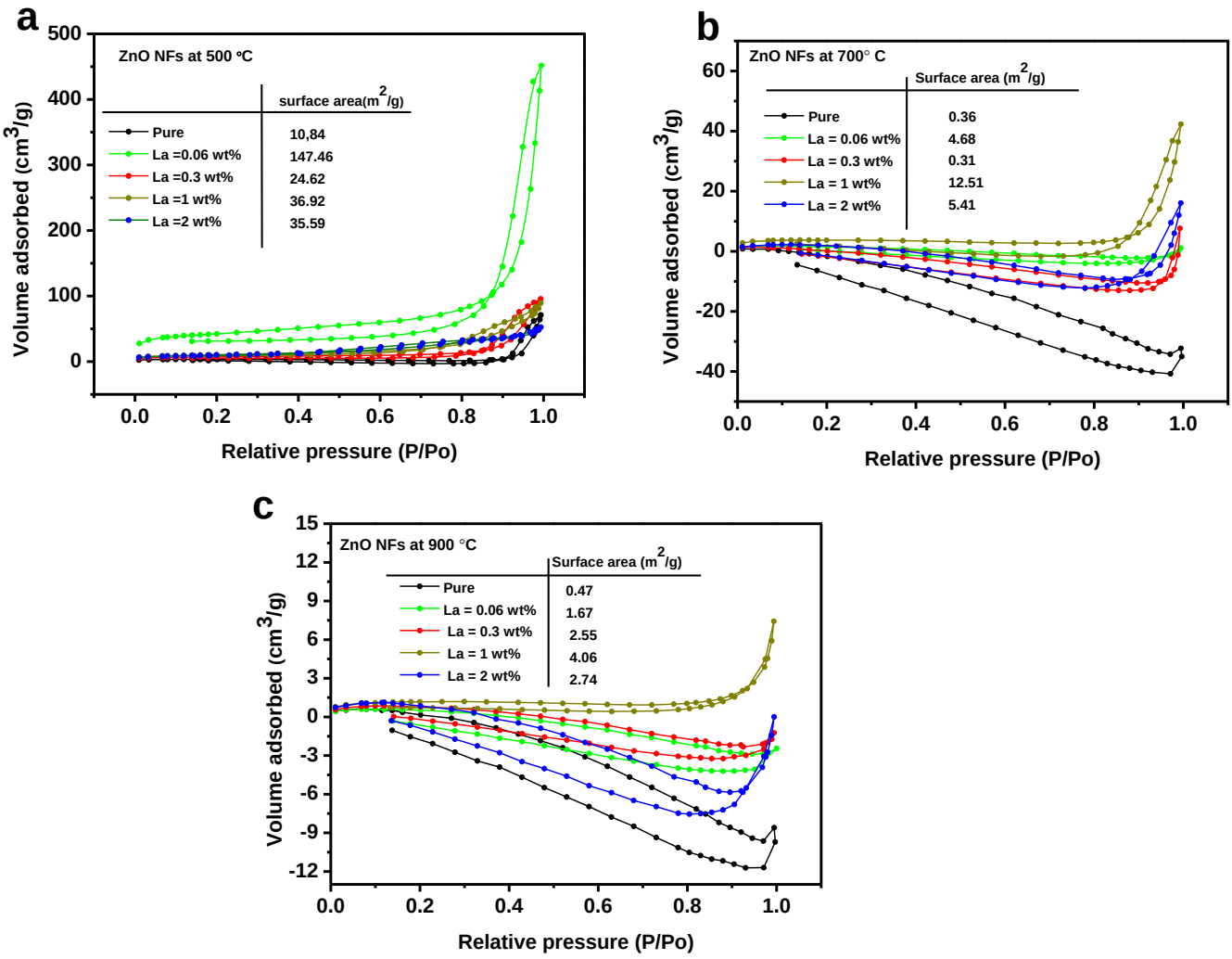

Figure 4.13: Nitrogen adsorption/desorption isotherms of the pure and La-doped ZnO NFs with different La concentrations (0.06 to 2 wt%) at: (a) 500 °C, (b) 700 and (c) 900 °C.

4.6 H_2S gas sensing properties

As mentioned earlier, H_2S is a very harmful or toxic, flammable and corrosive gas which has been reported to have a negative effect on human health and environment especially at very low concentrations (i.e. maximum limit is 250 ppm). Based on this, H_2S sensors that operate at low concentrations and working temperatures are desperately needed. Herein, the pure and La-doped ZnO NFs based sensors with different La-doping levels annealed at various temperatures

were fabricated and their gas sensing tests to H_2S were measured to investigate the effect of La-doping and annealing on the gas sensing behaviour of ZnO NFs. It is a known fact that the response of a ZnO gas sensor is highly dependent on its operating temperature. Reducing gases on the other hand are known to react more efficiently with chemisorbed oxygen on the surface of the SMO at a certain optimum operating temperature thus leading to an electrical resistance decrease upon exposure to that particular reducing gas. In this context, to determine the optimum operating temperature, the responses of the pure and La-doped ZnO NFs based sensors with different La-doping levels to 90 ppm of H_2S as a function of operating temperature were recorded.

Figure 4.14 (a-c) shows the temperature dependent sensing curves of the pure and La-doped ZnO NFs based sensors from 26 to 250 °C exposed to 90 ppm of H_2S. It can be observed that the responses of both the pure and La-doped ZnO NFs based sensors annealed at 500 and 900 °C increased with the working temperature and reached their maximum response value to H_2S at an operating temperature of 175 °C, and rapidly declined with a further increase of operating temperature to 250 °C whereas ZnO NFs based sensors annealed at 700 °C (Figure 4.14 (b)) displayed their maximum response value an optimal working temperature of 200 °C. Therefore, a working temperature of 175 °C sensors was chosen for sensors annealed at 500 and 900 °C while 200 °C was chosen for those annealed at 700 °C for comparison of the H_2S sensing characteristics for the pure and La-doped ZnO based sensors. It is also interesting to note that La-doping improved the sensor response to H_2S for all annealing temperatures with the 0.3 wt%, 1 wt% and 2 wt% La-doped ZnO NFs based sensors annealed at 500, 700 and 900 °C showing the best responses of 1022.1, 1633.4, and 6485,

respectively. The observed low sensors response at low temperatures could be probably due to less amount of adsorbed oxygen on the ZnO NFs surface. At optimum working temperature, it is an acknowledged fact that adsorption and desorption phenomenon reach an equilibrium state resulting in improved sensors response. However, at the operating temperature beyond the optimum one, the target gas desorption rate becomes faster than for adsorption thus promoting decline in sensors response. In actual facts, with higher working temperatures, the chemical reaction speed of a target gas with oxygen species chemisorbed on the ZnO NFs surface became faster as a result, the target gas molecules gained enough energy to withstand the activation energy barrier to react with adsorbed oxygen species on the surface. In this work, the optimum operating temperature of ZnO NFs based sensors was relatively low and this may be attributed to high gas adsorption ability of ZnO NFs which then led to a high usage rate of surface [57].

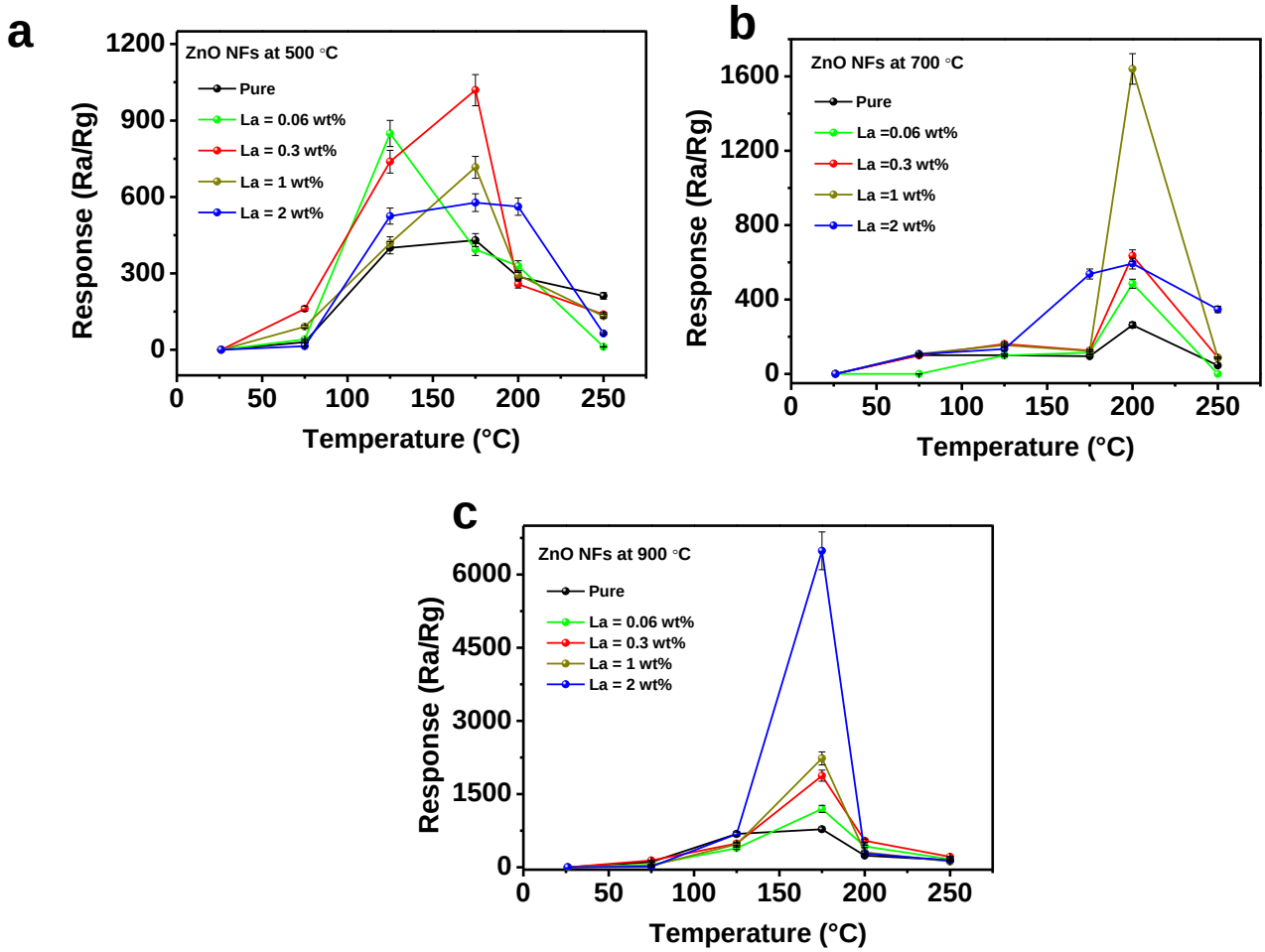

Figure 4.14: The responses of pure ZnO and La-doped ZnO NFs based sensors annealed at (a) 500, (b) 700 and (c) 900 °C to 90 ppm of H_2S as the function of operation temperature.

To further investigate the H_2S gas sensing capabilities of the pure and La-doped ZnO NFs based sensors, the sensing test measurements were conducted at various concentrations of H_2S ranging from 5-90 ppm at operation temperatures of 175 °C for annealing temperatures of 500 and 900 °C while 200 °C was used for those annealed at 700 °C and their response curves are presented in Figure 4.15 (a-c). As observed in Figure 4.15 (a-c), the responses of the pure and La-doped ZnO based sensors were found to rapidly increase with introduction of H_2S into the testing chamber and returned back to their baseline after the

withdrawal of H_2S indicating a good reversibility property of the sensors. In addition, the responses of the sensors increased with an increase of H_2S concentration up to 90 ppm without reaching saturation. Even though all sensors demonstrated good sensing behaviour towards H_2S over the concentration range of interest, La-doping tremendously improved the H_2S response, with 0.06, 1 and 2 wt% La-doped ZnO NFs-based sensors annealed at 500, 700, and 900 °C, respectively with 2 wt% exhibiting the highest response as compared to the rest of the La-doped ZnO sensors. This trend can be clearly seen from Figure 4.16 (a-c) where the responses of both the pure and La-doped ZnO NFs based sensors annealed at 500, 700, and 900 °C, respectively versus H_2S concentration from 5 to 90 ppm in steps on 10 ppm at the optimal working temperatures is plotted. It can be noticed from the curves that the responses of all the sensors showed a linear increase with an increase in the H_2S concentration, indicating the dependence of response to H_2S gas concentration. Furthermore, at low H_2S gas concentrations, all the sensors exhibited low responses, and this is probably due to a lower surface coverage of H_2S gas molecules, which in turn limits the surface reactions taking place between the H_2S gas molecules and the adsorbed oxygen species at the surface of the pure and La-doped ZnO NFs. At higher H_2S gas concentrations, the surface reaction is found to be improved owing to the increased surface coverage.

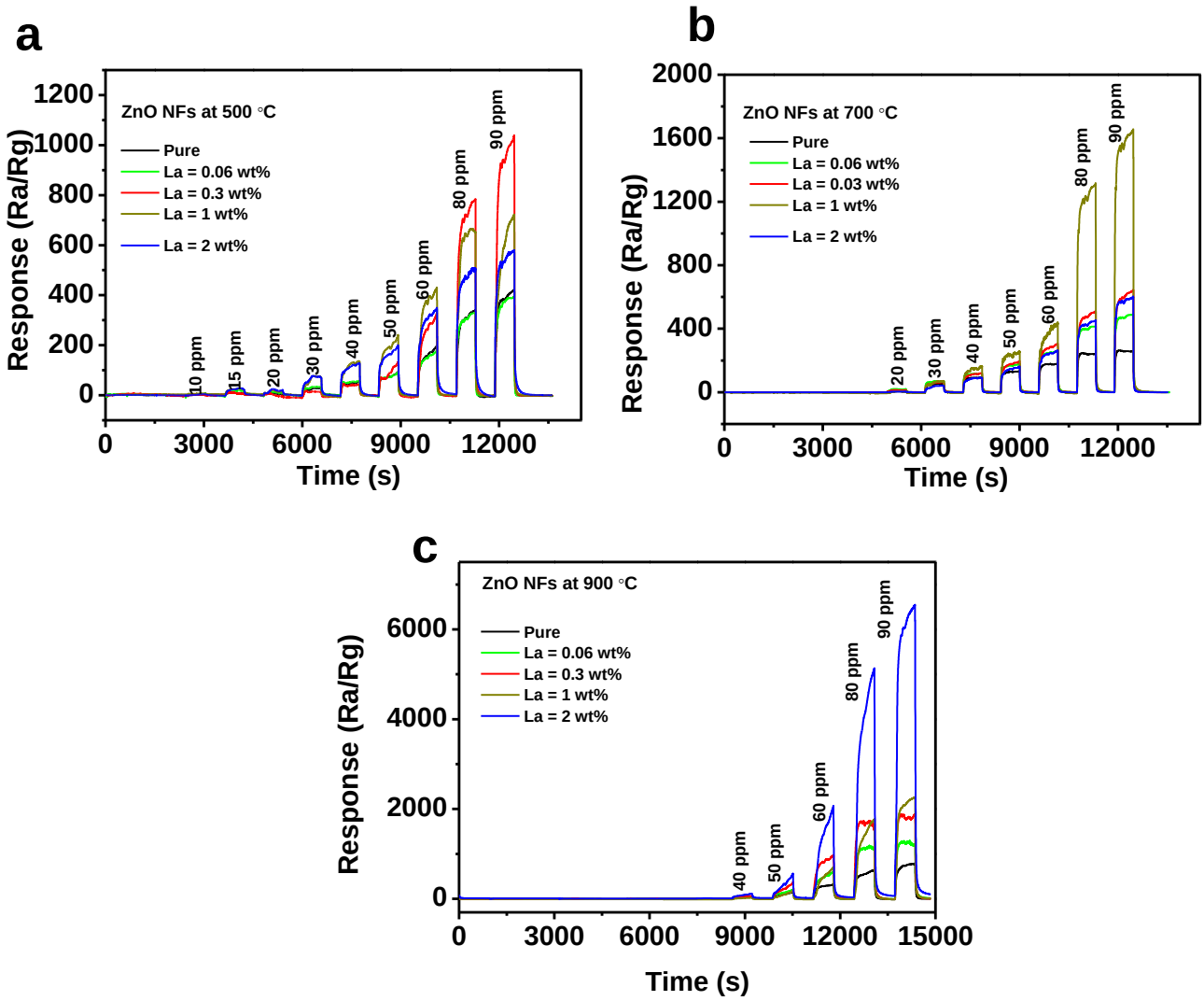

Figure 4.15: Response-recovery curves of the pure and La (0.06, 0.3, 1 and 2 wt%) doped ZnO nanostructures annealed at (a) 500, (b) 700 and (c) 900 °C.

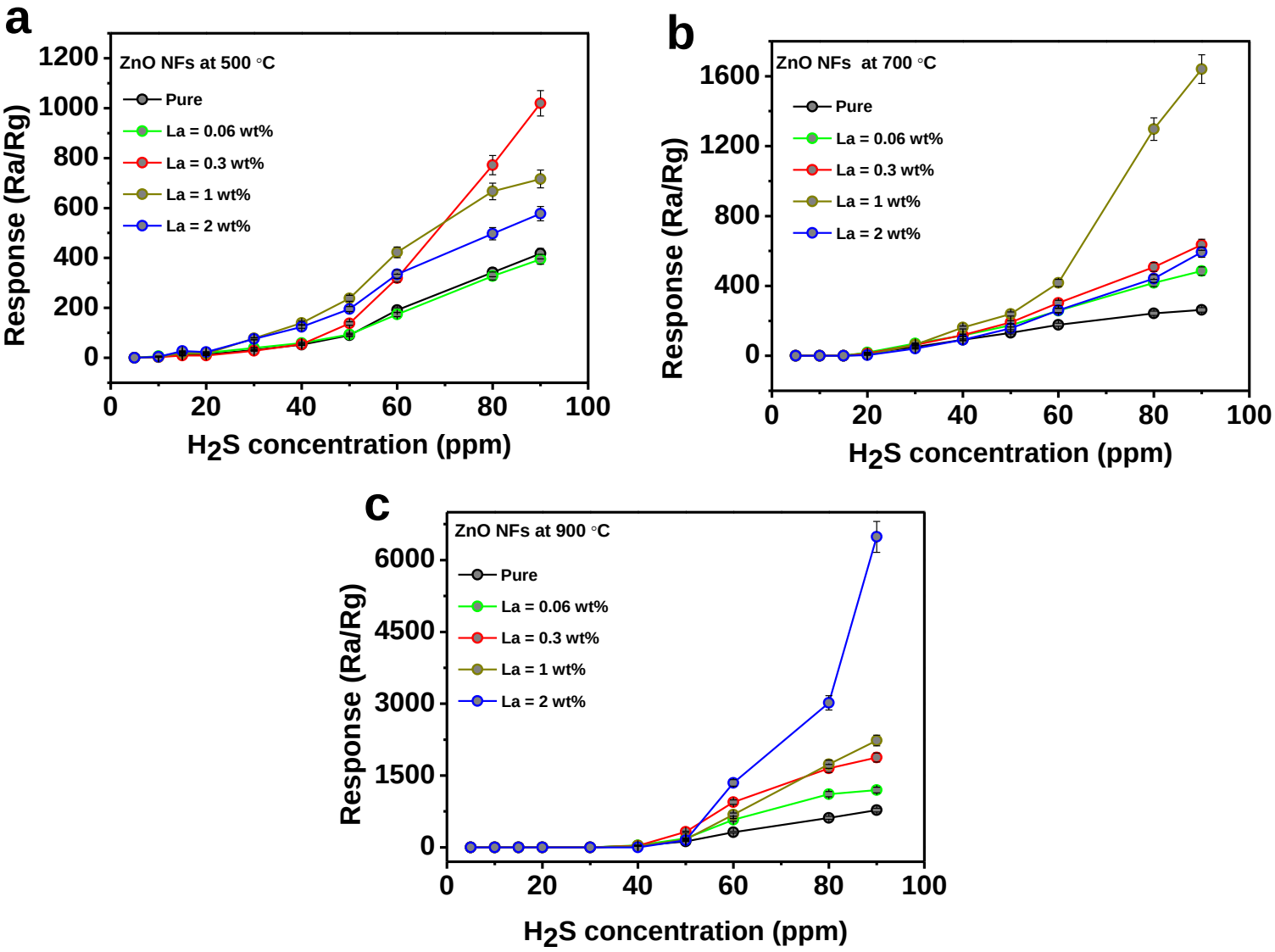

Figure 4.16: Sensor response of the pure and La (0.06, 0.3, 1 and 2 wt%) doped ZnO nanostructures annealed at (a) 500, (b) 700 and (c) 900 °C to different concentration of H_2S.

The catalytic effect of La on the ZnO NFs has been found to not only contribute to an enhanced response and lower detection limit, but also to enhance the response kinetics (i.e., the response/recovery times). Previous reports have revealed that La-doping onto SMOs can promote the adsorption and desorption of target gas molecules, thereby leading to rapid response/recovery times for the sensors [32, 58]. Figure. 4.17 (a-f) depicts the dynamic response characteristics

of various ZnO NFs sensors annealed at 500, 700, and 900 °C towards 90 ppm H_2S. Obviously, both the response and recovery times reduced significantly upon the introduction of La into ZnO. Such behaviour arises from a fact that La improves the catalytic properties on the surface of ZnO thus promoting faster adsorption and desorption of H_2S gas molecules on the sensor surface [32].

Prior studies have demonstrated the major influence of dopants on the sensor response since the dopant ions can improve the catalytic activity of the sensor material and alter the electrical transport properties by instigating more active sites for chemical reactions involving the target gas molecules and the sensor surface. Sensing tests findings herein clearly indicate that La-doped ZnO sensors possess superior sensing characteristics as compared to the pure ZnO ones. This enhanced response of the ZnO NFs based sensors following addition of trivalent lanthanum ions is probably due to the lattice distortion which resulted in smaller grain size as well as higher surface catalytic activity thus promoting a stronger interaction between H_2S gas molecules and the surface active sites [59, 60]. To provide explanation concerning the combined effect of La-doping and post-annealing on the enhancement of the sensing capabilities of the ZnO NFs based sensors, findings pertaining structural, morphological, chemical state and specific surface area were correlated with the sensing characteristics of the pure and La-doped ZnO NFs based sensors at various La-doping levels annealed at different temperatures.

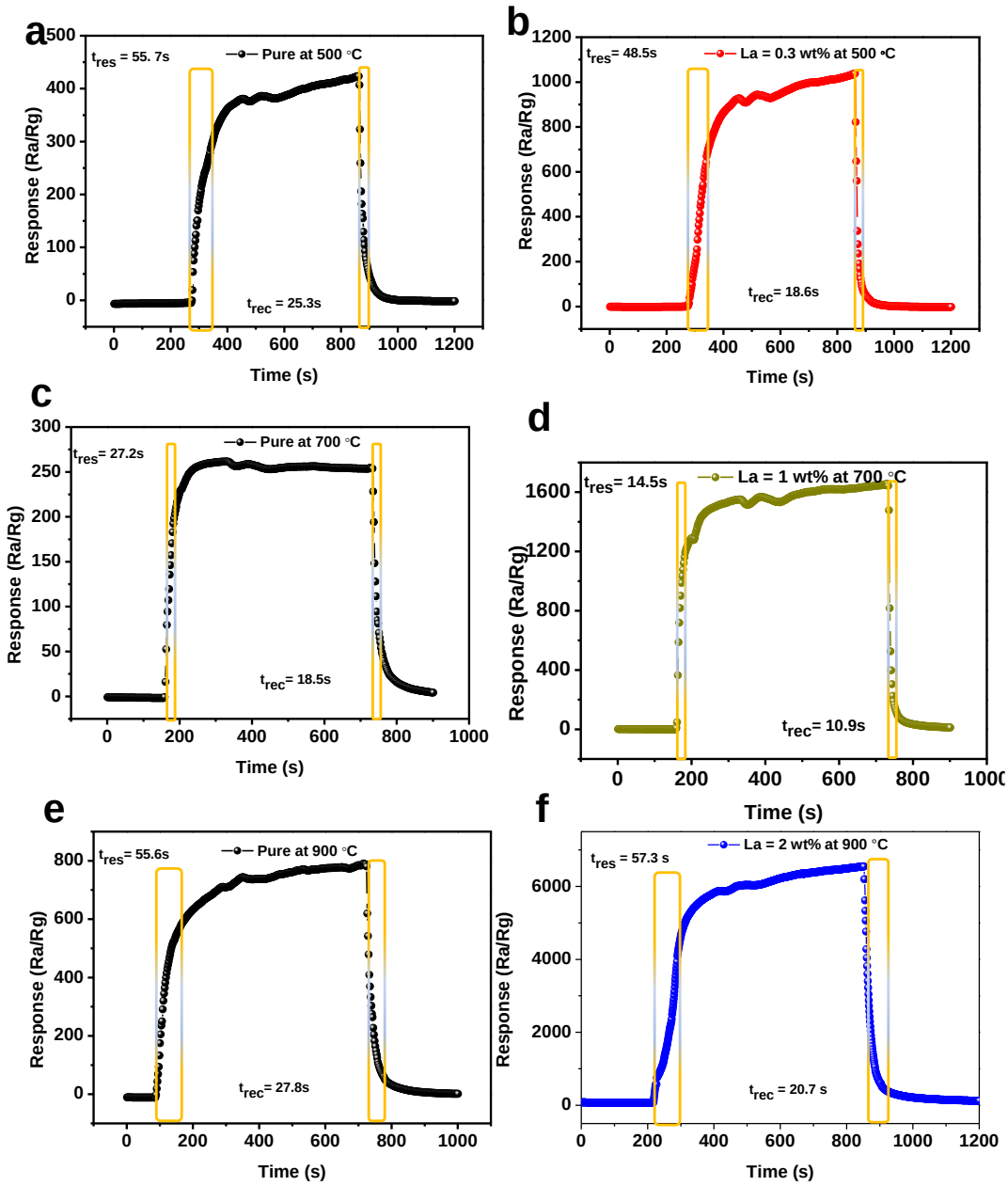

Figure 4.17: Response and recovery times for the pure and La-doped ZnO nanostructures for (a) 500, (b) 700 and (c) 900 °C annealing temperatures.

In as far as La-doping is concerned; it has been found that La-doping tremendously improved the H_2S response for all annealing temperatures. Firstly, it is generally accepted that higher surface area offers plenty active sites for gas adsorption of gas molecules and this often lead to sensor response increment [61]. BET analysis revealed larger surface area values for all La-doped ZnO NFs as compared to those of the pure ZnO NFs. This correlated with the decrease in

the grain sizes of the interconnected particles forming the fibrous structure with La-addition into ZnO for all annealing temperatures. Secondly, larger surface area which is associated with smaller grain size has been reported to result in the enhancement of the density of intrinsic defects which plays a major role in the sensing performance improvement of ZnO [62]. This arises from the fact that the existence of abundant defects, in particular the donor ones offer more channels for target gas molecules transportation leading to sensor response increment. In this study, analysis from XPS revealed the increase in the density of defects (i.e. oxygen vacancies (VO) denoted by the O_V peak) with La addition (see Table 4.2). So donor defects more especially VO cannot be ruled out as one of the possible reasons for the observed improved H_2S gas sensing response as they act as direct adsorption sites for H_2S on the surface of ZnO NFs during gas sensing consequently promoting adsorption of larger amounts of gas molecules thus playing a big role in improving the gas sensing response. In addition, XPS analyses further revealed an increase in the content of chemisorbed oxygen with La-doping which favours the gas molecules adsorption on the surface of the ZnO NFs thus contributing to intensified response towards H_2S. Lastly, according to BET results, the sensor based on the lowest La-doping concentration of 0.06 wt% annealed at 500 °C exhibited the highest surface area, and yet its sensing response was shown to be rather poor as compared to the rest of La-doped sensors. This is an indication that the dopant concentration plays a crucial role as it modifies the surface chemistry of the sensing material and thus it is important to optimize the dopant concentration to attain better sensing performance. Therefore, La dopant ions played a significant role in fast tracking the chemical reactions in the ZnO NFs based sensors owing to its catalytic activity.

Regarding the post-annealing effect on the enhancement of the sensing capabilities of the ZnO NFs based sensors, it was realized that the highly doped sensor (i.e. 2 wt% La) annealed at 900 °C displayed the highest response value of 6485 which is more than double the response values of the 0.3 wt% and 1 wt% La-doped sensors annealed at 500 and 700 °C, respectively. To better understand the enhanced sensing of the 2 wt% based sensor, it is important to understand the effect of the annealing temperature on the changes of crystal size and sensor response of all the ZnO NFs. To do so, the correlation of the crystallite size and sensor response as a function of annealing temperature was plotted and is shown in Figure 4.18 (a-b). It can be noticed that both the crystal size and H_2S response increased with increasing annealing temperature with the highest response attained at 900 °C for all sensors. Previous reports revealed sensor response deterioration with crystallite growth, however; current experimental findings showed high response to H_2S for all sensors displaying bigger crystallite size values with the 2 wt% demonstrating the highest response. The enhanced response obtained for the 2 wt% sensor suggests that other factors must be involved in the sensing mechanism besides the crystallite size. By paying attention to the annealing temperature which induced the crystal growth in this study; it can therefore be concluded that post-annealing at higher annealing temperatures process lead not only to the growth of crystallite size, but also to the improvement of crystallinity of the second phase of La_2O_3. Therefore, at 900 °C, the additional p-La_2O_3 phase was found to be improved and this played a significant role in gas sensing response improvement through modification of the gas adsorption kinetics and concentration of adsorption sites. Moreover, SEM observations revealed that the 2 wt% sensor maintained its NF morphology even after annealing at 900 °C, thus providing a diffusion pathway of the adsorbed gas

molecules on the surface of each NF into the grain boundaries thus creating electron depleted regions at the interfaces of neighbouring nanograins, ultimately forming a potential barrier for the electrons to flow across. The potential barriers thus modulate the resistance during the adsorption of gas molecules [13]. As much as the responses of the sensors were improved with the annealing temperature; it is worth noting that the annealing temperature also induced an increase in the lowest responding concentration as it was found to be 10 ppm, 20 ppm and 30 ppm for 500, 700 and 900 °C annealing respectively. This change in the lowest responding concentration may be due to the decreased surface area that is brought about with annealing temperature.

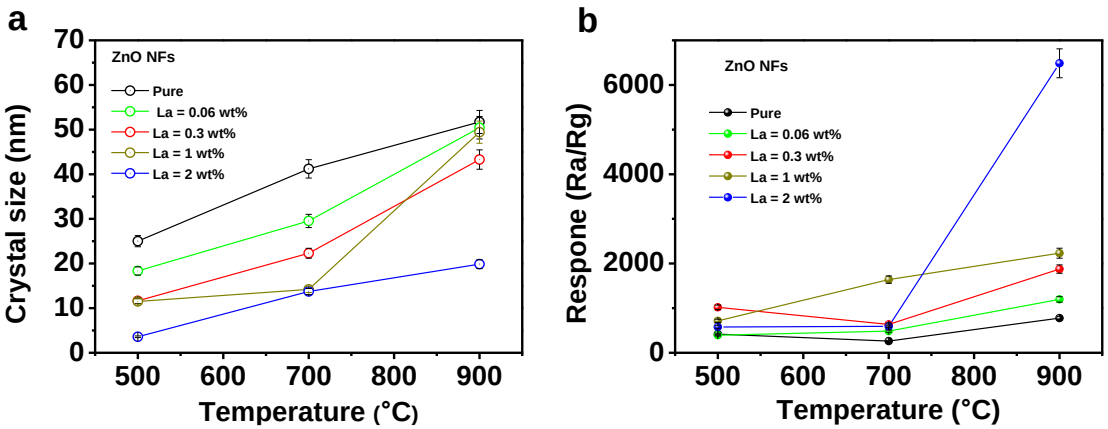

Figure 4.18: (a) Crystal size and (b) sensor response as a function of annealing temperature.

Further, the H_2S performance in this work was compared with some reported results based on doped metal oxides for H_2S detection and the literature survey findings are summarized in Table 4.3. From this table, it is clear that 2 wt% La-doped ZnO based sensor revealed a superior H_2S response value with the faster

recovery ability as compared to the listed sensors in Table 4.3. Thus, good H_2S sensing responses at a low detection concentration of 90 ppm make this sensor competitive when compared with other H_2S gas sensors.

Table 4.3: Comparison of the La-doped ZnO sensor responses and other materials doped ZnO to H_2S sensing responses.

Material and Morphology	**H_2S Concentration (ppm)**	**T (°C)**	**Gas sensing performance**			**Ref.**
			Response	**Response time(s)**	**Recovery time (s)**	
5.0 wt% La-doped In_2O_3	50	125	89.3	5	4 min	[60]
Cr-doped WO_3	100	80	7.14	336	300	[63]
Ni-doped ZnO nanorods	100	200	45.3	48	60	[19]
4Al-ZnO film	600	200	450	90	209	[64]
2 wt% La-doped ZnO, NFs	90	175	6485	53.7	20.7	This work

To gain more insight about the potential applicability for the detection of H_2S gas, both the stability and reproducibility studies were further conducted on the highly responsive La-loaded ZnO based sensor of 2 wt%. Figure 4.19 (a) displays the stability of the 2 wt% La-doped ZnO NFs annealed at 900 °C sensor to 90 ppm H_2S which was taken at an interval of 5 days for 30 days. The results demonstrate that the sensor response remained almost stable during long-time continuous measurements, therefore indicating good stability of the 2 wt% La-doped ZnO NFs annealed at 900 °C. The reproducibility of the 2 wt% La-loaded ZnO based sensor was investigated by repeatedly subjecting it to 90 ppm of H_2S gas at an optimal operating temperature of 175 °C. These tests were conducted five times under similar conditions to assess its repeatability characteristics. The

transient response-recovery curves showing five continuous reversible cycles are demonstrated in Figure 4.19 (b). It can be seen from this Figure 4.19 (b) that the response-recovery curves acquired for five cycles are almost constant suggesting a good reproducibility of the 2 wt% La-doped ZnO based sensor. On the other hand, since selectivity of a sensor towards a specific gas in the presence of other gases is a prerequisite for successful practical use, so both the pure and La-doped ZnO based sensors were subjected to 90 ppm of different gases, namely, NH_3, H_2S, CO, CH_4, and NO_2 at the same operating temperatures of 175 °C. As depicted in the histogram presented in Figure 4.19 (c), all the sensors displayed highest responses to H_2S for all annealing temperatures with the highly doped ZnO based sensor at 2 wt% annealed at 900 °C showing the highest response to H_2S as compared to the others. This indicates that the La-doped ZnO NFs sensors possess good selectivity towards H_2S and could be a promising gas active/sensing layer for detection of H_2S in real environments.

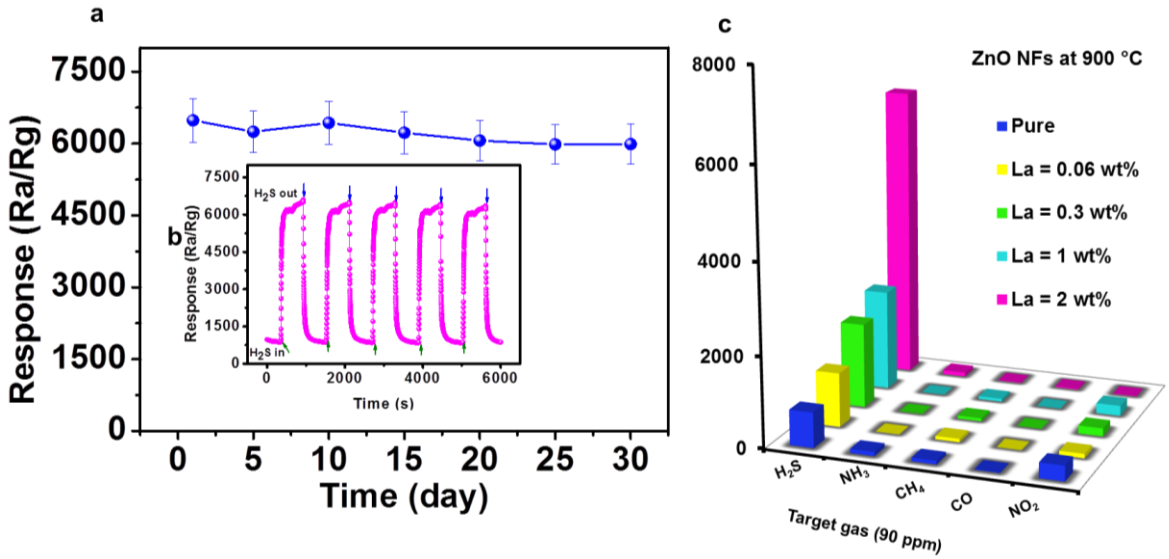

Figure 4.19: (a) Stability to 90 ppm H_2S over 30 days, (b) response to 90 ppm H_2S for five cycles of the La = 2 wt% at 900 °C based sensor and (c) Selectivity response of the pure and La-doped ZnO nanostructures towards 90 ppm of CH_4, NH_3, NO_2, H_2S and CO for samples annealed at 900 °C.

4.7 Gas sensing mechanism

In general, the sensing mechanism of SMOs is based in the change of electrical resistance on the surface of the SMO [65]. To explain the mechanism of the NFs, the schematic in Figure 4.20 has been used. When an n-type SMO such as ZnO is surrounded by air (Figure 4.20 (a)), oxygen molecules adsorb on its surface to form chemisorbed oxygen species by extracting electrons from the conduction band. The amount of the adsorbed oxygen relies on a few factors such as operating temperature, dopant concentration, particle size and surface area of the sensor material. In this work, both the pure and 2 wt% La doped ZnO NFs at 900 °C exhibited maximum response towards H_2S at 175 °C. So at this temperature, the sensor surface is dominated by the presence of adsorbed oxygen species namely O^- [66]. These oxygen species on the surface of ZnO then induce an electron depleted region resulting in the increase of surface potential

barrier and electrical resistance. When the sensor is exposed to H_2S as per equation:

$$H_2S_{(g)} + 2O^-_{(ads)} \rightarrow H_{2(g)} + SO_{2(g)} + 2e^- \quad (4.1)$$

The H_2S molecules react with the chemisorbed oxygen species (O^-) and the captured electrons are released back to the conduction band, thereby increasing the carrier concentration and reducing the ZnO electrical resistance. An additional chemical reaction can also take place simultaneously between the H_2S molecules and ZnO NFs as per below equation:

$$ZnO_{(s)} + H_2S_{(g)} \rightarrow ZnS_{(s)} + H_2O_{(g)} \quad (4.2)$$

Formation of the ZnS results in the collapse of the surface potential barrier which leads to the release of large amount of electrons, which drastically changes the resistance of the sensor material. Upon exposure to air, ZnS is then recovered back to ZnO as per equation:

$$ZnS_{(s)} + 3O_{2(g)} \rightarrow 2ZnO_{(s)} + 2SO_{2(g)} \quad (4.3)$$

ZnO is suggested to be a non-regenerable oxide adsorbent like CuO since it gets chemically converted to ZnS and CuS upon exposure to H_2S [67, 68]. Conversion of the sensor material during the reaction with H_2S is an important mechanism as it changes the conductivity and thus creating high sensitivity in sensing materials. For instance; Motaung *et al.* [69] and Kaur *et al.* [70] also reported the conversion of ZnO to ZnS upon exposure to H_2S. A few other reports on ZnO based H_2S sensors have demonstrated the conversion of ZnO to ZnS, whereby they observed improved sensor material sensitivity [3, 71]. They attributed the sensitivity to the exothermic and spontaneous reaction represented by equation (4.2), which is believed to be the reason for higher response of ZnO to H_2S [72]. However, some of these studies reported a slow recovery back to oxide form upon exposure to air, thus leading to longer recovery times in which they

attributed it to slow oxidation of the sensor material when in air and/or poisoning of the sensor material by the sulfur compounds [68, 73]. In this work, the ZnO NFs based sensors can be easily regenerated when H_2S is desorbed.

As for the 2 wt% La doped ZnO NFs based sensor in this work; a p-n interface was formed between the n-type ZnO and the p-type La_2O_3. The electrons in the ZnO transfers to the La_2O_3 and the holes in the La_2O_3 transfers to the ZnO until equilibrium is reached at the fermi level, resulting in wider depleted regions, thus leading to a remarkable increase in resistance when in air (see Figure 4.20 (c)). Exposing the 2 wt% La doped ZnO NFs based sensor to H_2S (Figure 4.20 (d)) will cause the trapped electrons to be released into the sensor material. The release of the electrons will shrink the p-n interface depletion regions and as a result, the resistance will decrease significantly, thus improving the sensor response. It is well considered that the p-n interface can increase the potential barrier height and the sensors resistance, which are responsible for the improved sensor response [74]

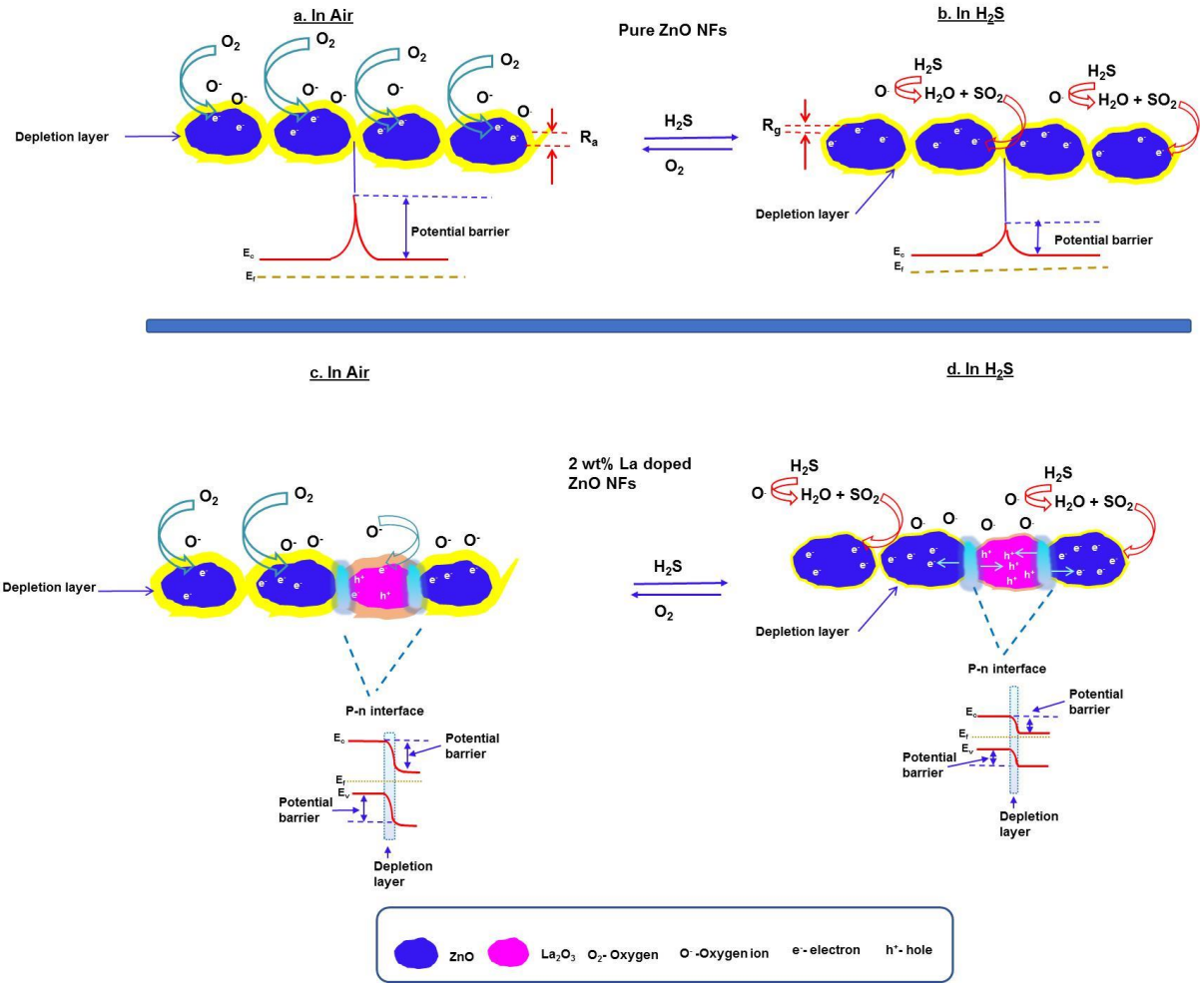

Figure 4.20: Proposed schematic diagram for the H_2S sensing mechanism by the ZnO NFs.

4.8 Conclusion

In summary, we present the sensing performance of the pure and La-doped ZnO NFs based sensors towards H_2S whereby the combined effects of the La-doping and post-annealing were thoroughly investigated. The crystalline nature of the La-doped ZnO based samples through the use of XRD revealed that at the annealing temperature of 500 °C, La is incorporated into the ZnO lattice as La^{3+} while it co-existed with La_2O_3 when the annealing temperature was further increased to 700 and 900 °C. TEM, ToF-SIMS and XPS further confirmed the segregation of the La_2O_3 phase at higher doping levels and annealing temperatures. SEM revealed NFs morphology which evolved

into nanoparticle morphology with the increase in annealing temperature to 900 °C except for the 2 wt% which maintained its fibrous-like structure. The ZnO NFs based sensors revealed high selectivity towards H_2S with the 2 wt% La-doped ZnO and annealed at 900 °C based sensor displaying the highest response at an optimum operating temperature of 175 °C. Additionally, La-doping lowered the response and recovery times which is one of the requirements for a gas sensor. Combined effects of high surface area and increased concentration of oxygen related defects as well as the possible contribution from the p-n interface between the p-La_2O_3 and the n-ZnO have been found to play a significant role in improved H_2S sensing behaviour. Thus from the observed enhanced sensing behaviour towards H_2S by the La-doped ZnO NFs, it suffices to mention that this sensor has great potential for practical application in the detection of H_2S.

4.9 References

[1] E. Ashori, F. Nazari, F. Illas, Int. J. Hydrog. Energy., 39 (2014) 6610-6619.

[2] A. Mirzaei, S.S. Kim, H.W. Kim, J. Hazard. Mater., (2018) 314-331.

[3] Z. Liu, T. Fan, D. Zhang, X. Gong, J. Xu, Sens. Actuators B Chem., 136 (2009) 499-509.

[4] S.S. Badadhe, I. Mulla, Sens. Actuators B Chem., 143 (2009) 164-170.

[5] A. Bodade, A. Bende, G. Chaudhari, Vacuum., 82 (2008) 588-593.

[6] K. Suematsu, N. Ma, K. Watanabe, M. Yuasa, T. Kida, K. Shimanoe, Sensors., 18 (2018) 254.

[7] A. Dey, Mater. Sci. Eng. B., 229 (2018) 206-217.

[8] S.-W. Choi, J.Y. Park, S.S. Kim, Chem. Eng. J., 172 (2011) 550-556.

[9] A. Katoch, S.-W. Choi, J.-H. Kim, J.H. Lee, J.-S. Lee, S.S. Kim, Sens. Actuators B Chem., 214 (2015) 111-116.

[10] J.-M. Choi, J.-H. Byun, S.S. Kim, Sens. Actuators B Chem., 227 (2016) 149-156.

[11] A. Katoch, G.-J. Sun, S.-W. Choi, J.-H. Byun, S.S. Kim, Sens. Actuators B Chem., 185 (2013) 411-416.

[12] B. Lyson-Sypien, M. Radecka, M. Rekas, K. Swierczek, K. Michalow-Mauke, T. Graule, K. Zakrzewska, Sens. Actuators B Chem., 211 (2015) 67-76.

[13] J.Y. Park, K. Asokan, S.-W. Choi, S.S. Kim, Sens. Actuators B Chem., 152 (2011) 254-260.

[14] K.M. Sawicka, P. Gouma, J.Nanopart. Res., 8 (2006) 769-781.

[15] F. Gong, L. Peng, Y. Zhang, Y. Cao, D. Jia, F. Li, Mater. Lett., 218 (2018) 106-109.

[16] J. Kim, K. Yong, J. Phys. Chem. C., 115 (2011) 7218-7224.

[17] G. Korotcenkov, B.K. Cho, Sens. Actuators B Chem., 156 (2011) 527-538.

[18] M.W. Maswanganye, K.E. Rammutla, T.E. Mosuang, B.W. Mwakikunga, Sens. Actuators B Chem., 247 (2017) 228-237.

[19] M.R. Modaberi, R. Rooydell, S. Brahma, A.A. Akande, B.W. Mwakikunga, C.-P. Liu, Sens. Actuators B Chem., 73 (2018) 1278-1290.

[20] K. Shingange, Z.P. Tshabalala, O.M. Ntwaeaborwa, D.E. Motaung, G.H. Mhlongo, J. Colloid Interface Sci., 479 (2016) 127-138.

[21] X. Chen, Y. Shen, P. Zhou, S. Zhao, X. Zhong, T. Li, C. Han, D. Wei, D. Meng, Sens. Actuators B Chem., 280 (2019) 151-161.

[22] K. Diao, J. Xiao, Z. Zheng, X. Cui, Appl.Surf. Sci., 459 (2018) 630-638.

[23] T. Wang, B. Liu, Q. Li, S. Wang, Mater. Lett., 221 (2018) 260-263.

[24] S. Öztürk, N. Kılınç, İ. Torun, A. Kösemen, Y. Şahin, Z.Z. Öztürk, Int. J. Hydrog. Energy., 39 (2014) 5194-5201.

[25] J.-j. Zhang, E.-j. Guo, L.-p. Wang, H.-y. Yue, G.-j. Cao, S. Liang, T Nonferr. Metal. Soc., 24 (2014) 736-742.

[26] F. Gu, D. You, Z. Wang, D. Han, G. Guo, Sens. Actuators B Chem., 204 (2014) 342-350.

[27] L. Yu, F. Guo, S. Liu, B. Yang, Y. Jiang, L. Qi, X. Fan, J. Alloy. Compnd., 682 (2016) 352-356.

[28] Z. El khalidi, E. Comini, B. Hartiti, A. Moumen, H.M.M. Munasinghe Arachchige, S. Fadili, P. Thevenin, A. Kamal, Mater. Des., 139 (2018) 56-64.

[29] X. Liu, Y. Sun, M. Yu, Y. Yin, B. Du, W. Tang, T. Jiang, B. Yang, W. Cao, M.N.R. Ashfold, Sens. Actuators B Chem., 255 (2018) 3384-3390.

[30] A. Hastir, N. Kohli, R.C. Singh, Sens. Actuators B Chem., 231 (2016) 110-119.

[31] A. Hastir, N. Kohli, R.C. Singh, J. Phys. Chem. Solids., 105 (2017) 23-34.

[32] X.L. Xu, Y. Chen, S.Y. Ma, W.Q. Li, Y.Z. Mao, Sens. Actuators B Chem., 213 (2015) 222-233.

[33] Y.J. Jeong, C. Balamurugan, D.W. Lee, Sens. Actuators B Chem., 229 (2016) 288-296.

[34] K. Shingange, Z. Tshabalala, B. Dhonge, O. Ntwaeaborwa, D. Motaung, G. Mhlongo, Mater. Res. Bull., 85 (2017) 52-63.

[35] S.S. Mali, H. Kim, W.Y. Jang, H.S. Park, P.S. Patil, C.K. Hong, ACS Sus. Chem. Eng., 1 (2013) 1207-1213.

[36] J. Li, Z. Cheng, M. Liu, M. Zhang, M. Hu, L. Zhang, H. Jiang, J. Li, J. Appl. Polym. Sci. 132 (2015).

[37] N. Pushpa, M.K. Kokila, J. Lumin., 190 (2017) 100-107.

[38] S.K. Mishra, S. Bayan, R. Shankar, P. Chakraborty, R.K. Srivastava, Sens. Actuators A Phys., 211 (2014) 8-14.

[39] C. Mrabet, O. Kamoun, A. Boukhachem, M. Amlouk, J. Alloy. Compnd., 648 (2015) 826-837.

[40] L.V. Devi, T. Selvalakshmi, S. Sellaiyan, A. Uedono, K. Sivaji, S. Sankar., J. Alloy. Compnd., 709 (2017) 496-504.

[41] J. Lang, X. Li, J. Yang, L. Yang, Y. Zhang, Y. Yan, Q. Han, M. Wei, M. Gao, X. Liu, Appl. Surf. Sci., 257 (2011) 9574-9577.

[42] M. Ashokkumar, S. Muthukumaran, Superlattices Microstruct., 69 (2014) 53-64.

[43] R. Sangeetha, S. Muthukumaran, M. Ashokkumar, Spectrochim Acta A., 144 (2015) 1-7.

[44] S. Kumar, P. Sahare, J. Rare Earth., 30 (2012) 761-768.

[45] G.-H. Lee, Ceram. Int.,42 (2016) 14452-14455.

[46] I. Kim, S. Doh, C. Kim, J.H. Je, J. Tashiro, M. Yoshimoto, Appl. Surf. Sci., 241 (2005) 179-182.

[47] V. Kumar, H.C. Swart, O.M. Ntwaeaborwa, R.E. Kroon, J.J. Terblans, S.K.K. Shaat, A. Yousif, M.M. Duvenhage, Mater. Lett., 101 (2013) 57-60.

[48] J. Xu, Y. Chang, Y. Zhang, S. Ma, Y. Qu, C. Xu, Appl. Surf. Sci., 255 (2008) 1996-1999.

[49] C. Wu, T.W. Kim, T. Guo, F. Li, Sci. Rep., 6 (2016) 38613.

[50] H. Yang, S. Ma, G. Yang, Q. Chen, Q. Zeng, Q. Ge, L. Ma, Y. Tie, Appl. Surf. Sci., 425 (2017) 585-593.

[51] J. Chen, J. Wang, F. Zhang, G. Zhang, Z. Wu, P. Yan,, J. Cryst. Growth., 310 (2008) 2627-2632.

[52] G.H. Mhlongo, D.E. Motaung, S.S. Nkosi, H. Swart, G.F. Malgas, K.T. Hillie, B.W. Mwakikunga, Appl. Surf. Sci., 293 (2014) 62-70.

[53] O.K. Tan, W. Zhu, Q. Yan, L.B. Kong, Sens. Actuators B Chem., 65 (2000) 361-365.

[54] P.-Y. Qiao, L.-X. Zhang, M.-Y. Zhu, Y.-Y. Yin, Z.-W. Zhao, H.-N. Sun, J.-Y. Dong, L.-J. Bie, Sens. Actuators B Chem., 250 (2017) 189-197.

[55] O. Bechambi, A. Touati, S. Sayadi, W. Najjar, Mater. Sci. Semicond. Process., 39 (2015) 807-816.

[56] T.L. Tan, C.W. Lai, S.B. Abd Hamid, Nanomaterials., 2014 (2014) 1.

[57] A. Boontum, D. Phokharatkul, J.H. Hodak, A. Wisitsoraat, S.K. Hodak, Sens. Actuators B Chem., 260 (2018) 877-887.

[58] X. Chu, X. Zhu, Y. Dong, X. Ge, S. Zhang, W. Sun, J. Mater. Process. Technol., 28 (2012) 200-204.

[59] X. Niu, H. Zhong, X. Wang, K. Jiang, Sens. Actuators B Chem., 115 (2006) 434-438.

[60] V. Kapse, S. Ghosh, G. Chaudhari, F. Raghuwanshi, D. Gulwade, Vacuum., 83 (2008) 346-352.

[61] Y. Lü, W. Zhan, Y. He, Y. Wang, X. Kong, Q. Kuang, Z. Xie, L. Zheng, ACS Appl. Mater. Inter., 6 (2014) 4186-4195.

[62] G.H. Mhlongo, K. Shingange, Z.P. Tshabalala, B.P. Dhonge, F.A. Mahmoud, B.W. Mwakikunga, D.E. Motaung, Appl. Surf. Sci., 390 (2016) 804-815.

[63] Y. Wang, B. Liu, S. Xiao, X. Wang, L. Sun, H. Li, W. Xie, Q. Li, Q. Zhang, T. Wang, ACS Appl. Mater. Inter., 8 (2016) 9674-9683.

[64] P.S. Kolhe, A.B. Shinde, S. Kulkarni, N. Maiti, P.M. Koinkar, K.M. Sonawane, J. Alloys. Compnd., 748 (2018) 6-11.

[65] A.R. Nimbalkar, M.G. Patil, Physica B., 527 (2017) 7-15.

[66] H. Liu, S. Gong, Y. Hu, J. Liu, D. Zhou, Sens. Actuators B Chem., 140 (2009) 190-195.

[67] G. Qi, L. Zhang, Z. Yuan, Phys. Chem. Chem. Phys., 16 (2014) 13434-13439.

[68] H.-S. Woo, C.-H. Kwak, I.-D. Kim, J.-H. Lee, J. Mater. Chem., 2 (2014) 6412-6418.

[69] D.E. Motaung, G.H. Mhlongo, A.S. Bolokang, B.P. Dhonge, H.C. Swart, S.S. Ray, Appl. Surf. Sci., 386 (2016) 210-223.

[70] M. Kaur, S. Kailasaganapathi, N. Ramgir, N. Datta, S. Kumar, A. Debnath, D. Aswal, S. Gupta, Appl. Surf. Sci., 394 (2017) 258-266.

[71] Z. Hosseini, A. Mortezaali, Sens. Actuators B Chem., 207 (2015) 865-871.

[72] D. Wang, X. Chu, M. Gong, Nanotechnology., 18 (2007) 185601.

[73] F. Zhang, A. Zhu, Y. Luo, Y. Tian, J. Yang, Y. Qin, J. Phys. Chem C., 114 (2010) 19214-19219.

[74] J. Shu, Z. Qiu, S. Lv, K. Zhang, D. Tang, Anal. Chem., 89 (2017) 11135-11142.

Chapter 5

$LaBO_3$ (B= Fe, Co) nanofibers and their structural, luminescence and gas sensing characteristics

5.1 Introduction

Due to the importance of monitoring and control of hazardous gases in our living spaces, gas sensors have become vital in our life. Acetone for instance, is a very important compound used in many essential applications such as paraffin purification, tissue dehydration and in pharmaceutics [1]. However, inhalation of acetone causes health effects such as headache, nerve system damage and fatigue [2]. Therefore, it is necessary to develop affordable and high performance acetone sensors to monitor acetone molecules at very low concentration levels in the environment for health and safety purposes. Due to this need, a lot of research has been focused into enhancing the performance of the already available acetone sensors mostly with regard to sensitivity and selectivity. One common approach is morphology engineering where different morphologies have been reported for enhancing sensor performance [3, 4]. Of particular interest is one-dimensional (1D) nanofibers (NFs) as they possess high surface area for adsorption-desorption reactions and the presence of nanograins provide large grain boundary areas, ensuring high sensitivity in the sensors [5]. Moreover, the interparticle connectivity have greater contribution to the sensing performance of NFs based sensors as it provides ease of gas diffusion thus allowing more active sites accessibility [6].

Amongst many of the sensing materials used for gas sensing, perovskite oxides (ABO_3) have emerged as excellent candidates due to their catalytic activity, chemical and thermal stability [7]. The gas sensing properties of these perovskite materials strongly depend on the choice of the B-site cation, which can significantly influence the structure, morphology, chemistry as well as the electronic conductivity of the final oxide [8, 9]. Usually the B-site cation for the La-based perovskites is picked from transition metals such as Co, Cr, Fe, etc. due to their excellent catalytic properties and usually the final oxides are of p-type conductivity [8, 10]. Thus, 1D NFs of these La-based perovskites offer promising benefits for gas sensing performance as during the sensing reactions, an overlap of the hole accumulation layers forms along the fiber direction therefore resulting in a continuous hole transfer channels which greatly influence the changes in the sensor's electrical resistance [11].

In this context, this work focuses on the fabrication of La-based perovskites ($LaBO_3$) NFs produced via electrospinning method whereby B= Fe/Co. The B-site cation of the $LaBO_3$ perovskite structure was interchanged to understand the connection between the microstructural and morphological properties of the $LaBO_3$ perovskites and their acetone sensing behaviour at a low acetone concentration range at an operating temperature of 120 °C.

5.2 Experimental procedure

For For the $LaFeO_3$ NFs; equal molar concentrations of $La(NO_3)_3.6H_2O$ and $Fe(NO_3)_3.9H_2O$) salts and 1g of PVP were added to a mixture of 6 ml Dimethylformamide (DMF) and 4 ml ethanol followed by stirring for 2 h to form a homogeneous solution. The precursor solution was then loaded into a 10 ml

syringe for electrospinning whereby a pumping rate of 0.5 μlh^{-1} and voltage of 20 kV was applied. The nanofibers were collected on a drum collector that was placed 15 cm away from the spinneret. After spinning, the obtained composite NFs were annealed at 600 °C for 2 h in air to obtain the $LaFeO_3$ NFs. For $LaCoO_3$ NFs, the same procedure was followed but the starting salt was changed from $Fe(NO_3)_3.9H_2O$) to $Co(NO_3)_3.6H_2O$), respectively.

5.3 Characterization

The phase of the LaBO3 NFs was determined by using an X-ray diffraction (XRD) Panalytical X'pert PRO PW3040/60 X-ray diffractometer with Cu/Kα a Cu-Kα (λ=1.5405 Å) radiation. The surface morphology was observed using a ZEIS-AURIGA field emission-scanning electron microscopy (FESEM) at an acceleration voltage of 3 kV. X-ray photoelectron spectra (XPS) were recorded with a PHI 5000 Versaprobe X-ray photoelectron with monochromatic Al-Kα radiation (hν = 1486.6 eV). Nitrogen (N2) adsorption-desorption isotherms were measured at 77 K using a Micrometirics TRISTAR 300 surface area analyser. Their optical properties were studied using a PL system with a 325 nm He–Cd laser as an excitation source.

5.4 Gas sensors fabrication and measurements

40 mg of each sample was mixed with a solution of ethyl cellulose in turpineol and ground for a few minutes to make thixotropic pastes, which were then coated onto an alumina substrate interdigitated with Pt electrodes. The sensors were then heated at 300 °C for 2 h at a heating rate of 3 °C/min to achieve good adhesion. The sensing performance was assessed using a KSGAS6S gas sensing station (KENOSISTEC, Italy). MKS Instruments Deutschland GmbH mass flow controllers were used to control the atmospheric conditions by supplying

required concentrations levels of acetone (C_3H_6O), ammonia (NH_3), nitrogen dioxide (NO_2), methane (CH_4) and carbon monoxide (CO) into the sensing chamber through diluting the concentrated test gas in synthetic air at a constant flux rate of 500 ml/min. The heating voltage was adjusted to different values while using a thermocouple to measure the output temperature to correspond to temperatures of room temperature (RT) to 180 °C. The fluctuations in electrical resistance in the course of the interaction of the test gas and the surface of the $LaBO_3$ NFs based sensors was measured in air *(Ra)* and in the occurrence of the test gas *(Rg)* by the use of a Keithley 6487 Picoammeter/voltage source meter. Since the $LaBO_3$ based sensors in this work are both p-type, their resistance increase in the presence of a reducing gas and the sensor response can therefore be determined as (Rg/Ra) [12]. The highest response was obtained at 120 °C in the presence of acetone; hence all the sensing measurements will be based on acetone at operation temperature of 120 °C. The time taken by the sensor to obtain 90% of the change in resistance after exposure to the test gas was measured as a response time and the time taken by the sensor to reach 90% of its baseline resistance after removal of the test gas was measured as the recovery time [13, 14]. Figure 5.1 shows the schematic set up for the sensing measurements.

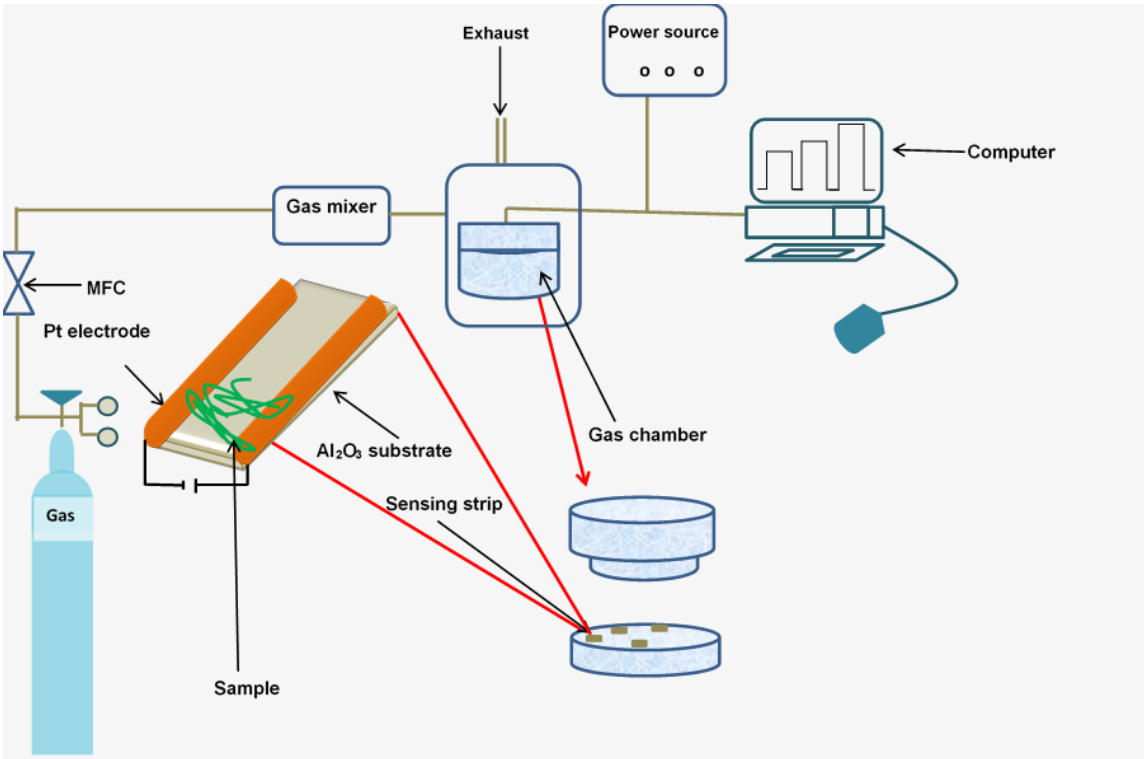

Figure 5.1: Schematic of the set up for the sensing measurements.

5.5 Results

5.5.1 Structural and morphological characteristics

Figure 5.2 displays the diffraction patterns and the SEM images of the $LaFeO_3$ and $LaCoO_3$ NFs. The diffraction patterns of the $LaFeO_3$ and $LaCoO_3$ NFs can be best indexed to a cubic symmetry of $LaFeO_3$ (JCPDS Card no. 75-054) and rhombohedral symmetry of $LaCoO_3$ (JCPDS Card no. 01-075-0279). Moreover, these diffraction patterns didn't contain any unintended diffraction reflections from impurities or other phases, suggesting the successful fabrication of a single phase of $LaFeO_3$ and $LaCoO_3$. The average crystallite sizes of $LaFeO_3$ and $LaCoO_3$ were estimated through Scherrer equation [8] and were found to be 48 nm and 49.5 nm, respectively. Further, surface morphologies of $LaFeO_3$ and $LaCoO_3$ determined through SEM are presented in Figure 5.2 (b and c). Both fabricated

products revealed a NF morphology with each fibre consisting of interconnected particles of an average particle diameter of 20 and 60 nm, respectively.

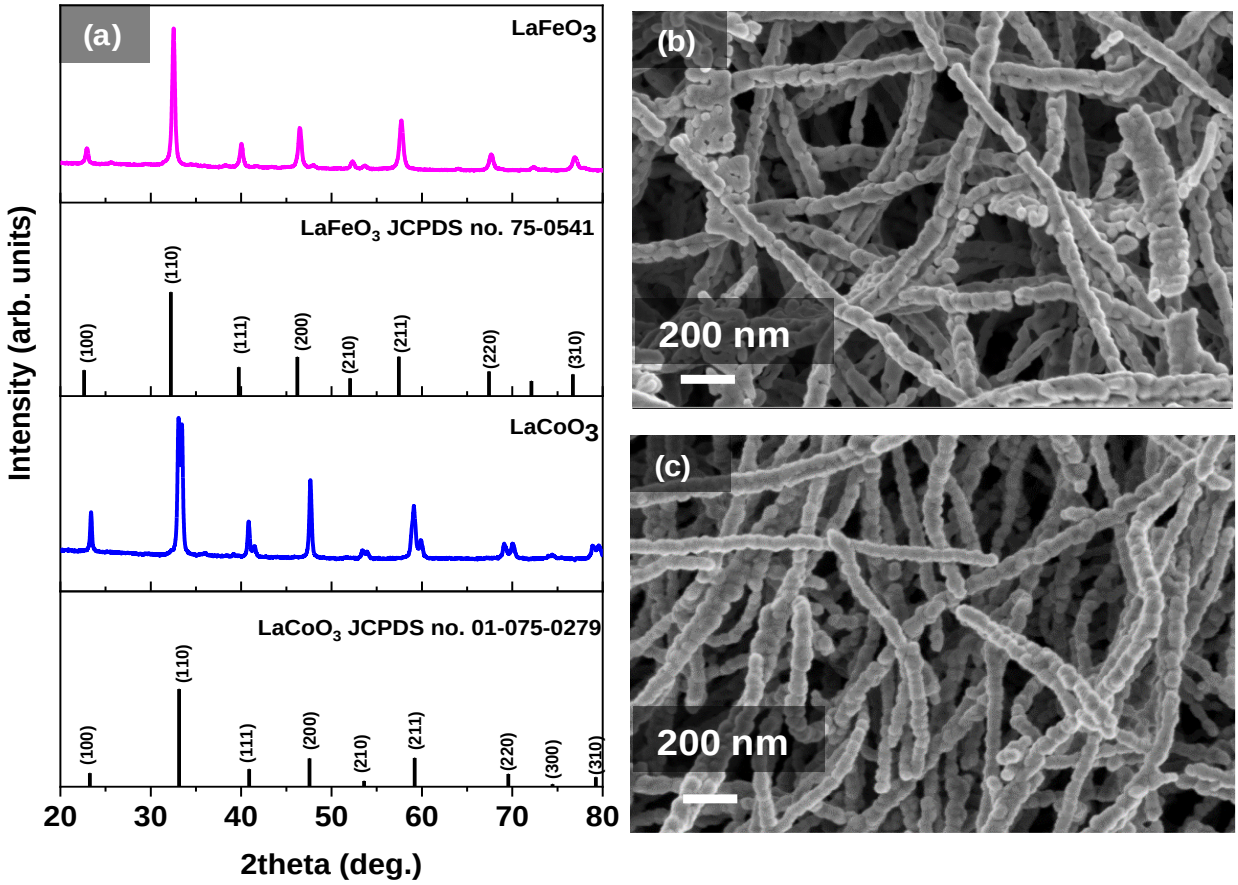

Figure 5.2: Diffraction patterns and SEM micrographs of the (a) $LaFeO_3$ and (b) $LaCoO_3$ NFs.

5.5.2 Chemical composition analyses

XPS measurements were performed to establish the chemical state of the $LaCoO_3$ and $LaFeO_3$ NFs and the results for the high resolution XPS spectra of La 3d, Co 2p, Fe 2p and O 1s core levels are displayed in Figure 3. Figure 5.3 (a-b), demonstrates the XPS spectrum of the La 3d core level consisting of a double peak for each spin-orbit component namely La $3d_{5/2}$ and La $3d_{3/2}$. The spin-orbit

splitting distance of ~16.7 eV between $3d_{5/2}$ and $3d_{3/2}$ is indicative of the La^{3+} state [15]. From the high resolution spectrum of the Co 2p core level presented in Figure 5.3(c), there are two peaks situated at 795.0 eV and 779.7 eV which belongs to Co $2p_{1/2}$ and Co $2p_{3/2}$ separated by 15.3 eV; confirming the Co^{3+} state [12]. Similarly, from the high resolution spectrum of Fe 2p in Figure 5.3(d); two peaks situated at binding energies of 709.9 eV and 723.5 eV corresponding to Fe $2p_{3/2}$ and Fe $2p_{1/2}$ and separated by 13.6 eV were identified, confirming Fe^{3+} ions in an oxide form [16]. The XPS spectrum of the O 1s core level shown in Figure 5.3(e-f) revealed three oxygen components herein labelled as O_L at 528.8 and 528.9 eV. O_V at 530.9 and 531.2 eV and O_C at 532.1 and 532.4 eV for $LaCoO_3$ and $LaFeO_3$, respectively. The O_L corresponds to the lattice oxygen, O_V is assigned to the surface adsorbed oxygen and is related to oxygen vacancies, while the O_C results from chemisorbed oxygen [17-19]. $LaFeO_3$ has more oxygen vacancies as compared to $LaCoO_3$, suggesting that $LaFeO_3$ has more adsorption sites for gas adsorption and desorption reactions.

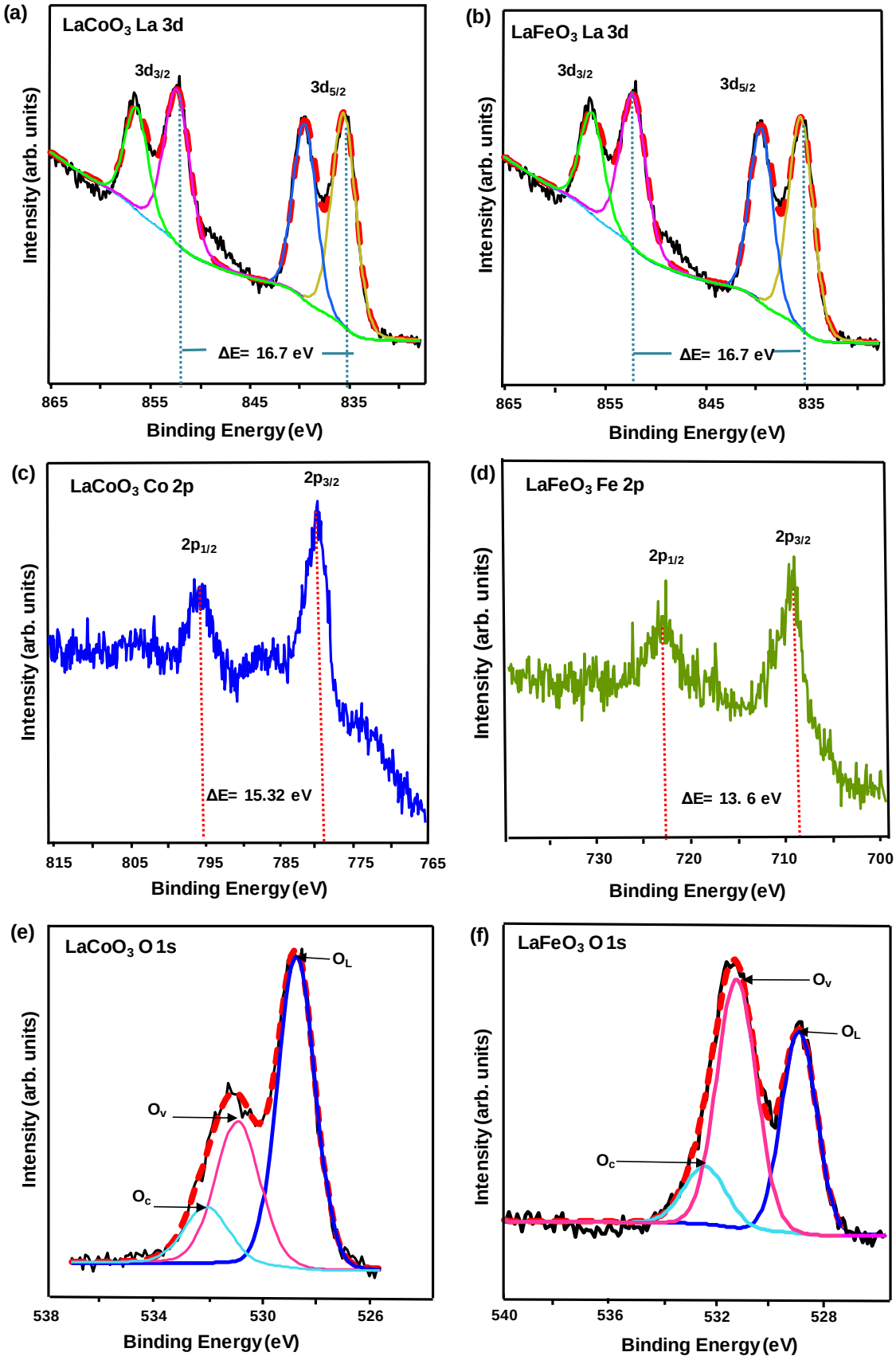

Figure 5.3: XPS spectra of the (a-b) La 3d, (c) CO 2p, (d) Fe 2p, and (e-f) O 1s for the $LaCoO_3$ and $LaFeO_3$ NFs.

5.5.3 Surface area analysis

Since gas sensing processes are surface related, the surface area and porosity are important characteristics to consider. The surface area analysis of the $LaCoO_3$ and $LaFeO_3$ NFs were inspected through the nitrogen adsorption-desorption isotherms via the BET method and the results are presented in Figure 5.4. The obtained N_2 isotherms revealed a type IV isotherm with a H3 hysteresis loop in the high pressure which is an indicative of mesopores [20, 21]. $LaCoO_3$ isotherm showed a negative adsorption-desorption behaviour, which is indication of low surface area of the sample or desorption takes place quicker than adsorption. The surface area values of the $LaCoO_3$ and $LaFeO_3$ NFs were found to be 5.8 and 16.1 m^2/g. The large surface area of $LaFeO_3$ suggests that it consists of more active sites for gas reactions purposes as compared to $LaCoO_3$ NFs.

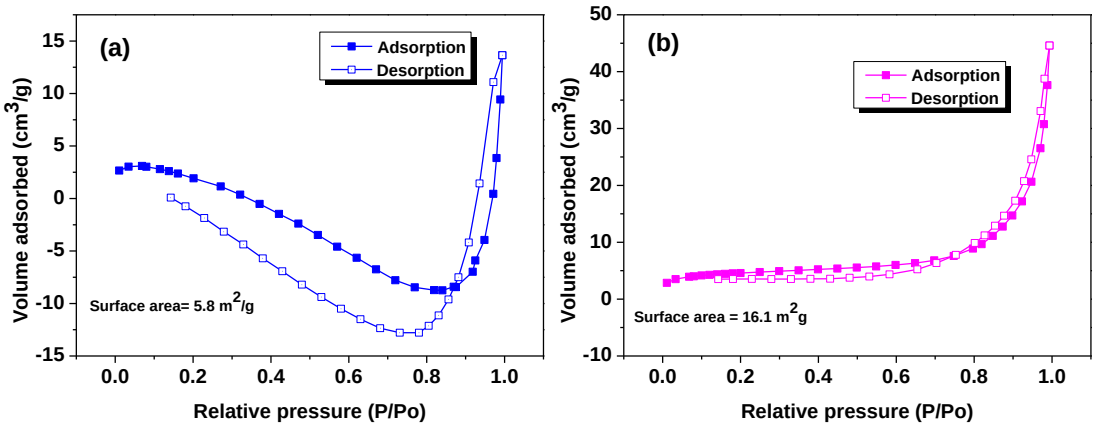

Figure 5.4: Nitrogen adsorption-desorption isotherms of the (a) $LaCoO_3$ and (b) $LaFeO_3$ NFs.

5.5.4 Luminescence characteristics

To further confirm the presence of defects in both $LaFeO_3$ and $LaCoO_3$ NFs, the photoluminescence (PL) emission spectra were measured at an excitation

wavelength of 325 nm at room temperature. Both $LaFeO_3$ and $LaCoO_3$ NFs revealed emission bands in the range between 370 - 700 nm. As presented in Figure 5.5, evidently $LaFeO_3$ displayed the highest PL intensity centred at 425 nm whereas $LaCoO_3$ displayed the lowest intensity centred at 453 nm. Both emission peaks are an indicative of oxygen vacancies with defect centers for maintaining the stoichiometry of the crystal [22, 23]. Thus, the emission intensity is proportional to the amount of these oxygen defects.

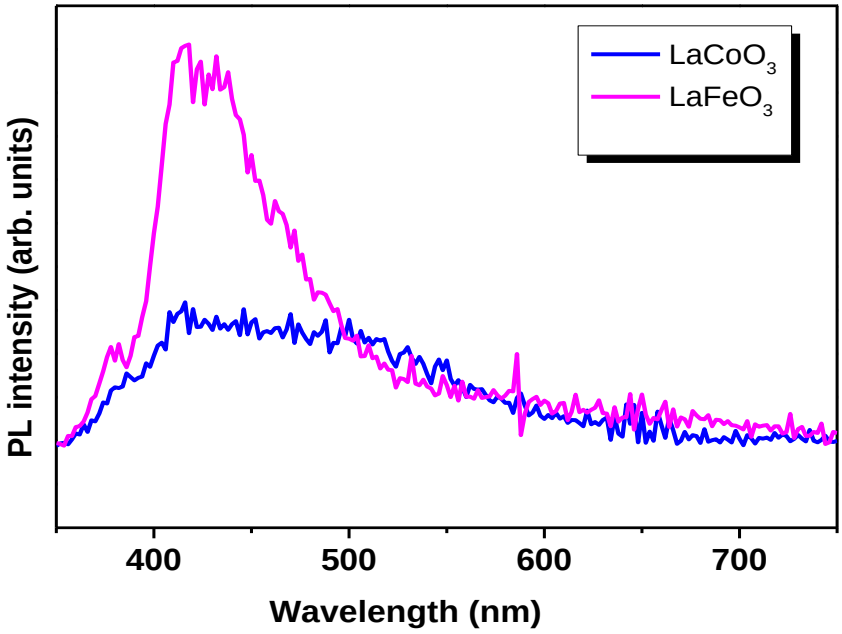

Figure 5.5: PL spectra of the $LaCoO_3$ and $LaFeO_3$ NFs after excitation at 325 nm using He-Cd laser as an excitation source.

5.6 Gas sensing performance

One issue in gas sensor devices derived from nanostructured SMO is how to control their morphology (i.e. size and shape), surface defects, as well as their microstructure. The present work clearly indicates that the size of the particles, specific surface area and surface defects in NF products varied with the

interchanged B-site cation of the $LaBO_3$ perovskite structure. For the aim of evaluating the effects of the aforementioned factors brought by interchanging the B-site cation of the $LaBO_3$ perovskite structure on the sensing behaviour/capabilities of gaseous species herein, some basic gas sensing characteristics were investigated comparatively. Figure 5.6(a) presents the change in current of the $LaFeO_3$ and $LaCoO_3$ based sensors upon contact with acetone at concentrations from 2.5 to 40 ppm at an operating temperature of 120 °C. The $LaFeO_3$ and $LaCoO_3$ based sensors showed a decrease in current and an increase in the resistance upon contact to acetone and recovered back to the baseline; demonstrating reversibility characteristics of the sensors. Further; the responses of the $LaFeO_3$ and $LaCoO_3$ based sensors were calculated to conduct a quantitative study as the ratio of the resistance in gas (*Rg*) to that in air (*Ra*) and the results are demonstrated as the inset of Figure 5.6(a). The response of the $LaFeO_3$ and $LaCoO_3$ based sensors towards acetone showed a linear increase with an increase in acetone concentration; revealing the gas concentration dependence of the sensor response. Although the lowest concentration level experimentally measured was 2.5 ppm in this case, the theoretical limit of detection (signal-to-noise ratio>3) was estimated from the inset of Figure 5.6(a) as 0.186 and 0.135 ppm for $LaCoO_3$ and $LaFeO_3$ NFs, respectively. Both limits of detections are less than 1 ppm indicating that both sensors can detect even low traces of acetone.

Further, the response and recovery kinetic of the sensor is very important for practical applications, thus the response-recovery speeds of the two sensors were determined at 40 ppm of acetone. $LaFeO_3$ NFs based sensor took 14 s to respond and 49 s to recover back to the baseline, while $LaCoO_3$ NFs based sensor

took 446 s to respond and 270 s to recover. From this result, it is obvious that the $LaFeO_3$ NFs based sensor possessed faster response/recovery kinetics than the $LaCoO_3$ NFs based sensor. On top of the response/ recovery kinetics, it is important for a gas sensor to be able to selectively single out a specific gas amongst other gases for real life applications. Therefore, the $LaFeO_3$ and $LaCoO_3$ NFs based sensors were also exposed to 40 ppm of carbon dioxide (CO_2), carbon monoxide (CO), nitrogen dioxide (NO_2), ammonia (NH_3) and methane (CH_4) so as to establish the selectivity property of the two sensors. Figure 5.6 (b) presents the responses of the $LaFeO_3$ and $LaCoO_3$ NFs based sensors to 40 ppm of each of the above mentioned gases at operating temperature of 120 °C. Remarkably, the $LaFeO_3$ and $LaCoO_3$ NFs based sensors demonstrated larger response towards acetone than any other gases, with non-significant responses to the other interfering gases. The common acetone selectivity of the $LaBO_3$ NFs suggests the crucial role that the A-site cation (La) plays in the selection of the specific target gas interaction [8]. Between the two $LaBO_3$ based sensors, the $LaFeO_3$ NFs based sensor revealed the highest response to acetone. This indicates that the $LaFeO_3$ NFs based sensor not only have high response and fast response and recovery kinetics towards acetone, but excellent acetone selectivity as well, making it a good candidate for practical application.

Since it has been established that the $LaFeO_3$ NFs based sensor has interesting gas sensing performance, it remains a crucial task to determine its reproducibility capabilities. For this reason, three consecutive response-recovery cycles to 40 ppm of acetone were measured and the results are demonstrated in Figure 5.6(c). For every cycle, it can be observed that the response and recovery

characteristics of the sensor were similar, indicating that the $LaFeO_3$ NFs based sensor possessed good reproducibility.

5.7 Gas sensing mechanism

The target gas adsorption-reaction-desorption ability on the surface of the semiconductor metal oxide sensing material to adsorb relies on the type of semiconductor(p or n), structure, morphology and surface state of the material [24]. $LaFeO_3$ is a p-type metal oxide, therefore the density of hole charge carriers is more than electrons. So when $LaFeO_3$ is in an ambient atmosphere; oxygen will adsorb on its surface and produce chemisorbed oxygen ions (O^-) at 120 °C [25] by capturing electrons from the valence band. A hole accumulation layer will then form near the surface, which then results in the decrease of sensor resistance. Upon contact with acetone, the acetone molecules adsorb and react with the oxygen ions on the NFs surface based on the equation [26];

$$CH_3COCH_3 + 8O^{2-}_{(ads)} \rightarrow 3CO_2 + 3H_2O + 8e^- \quad (5.1)$$

Acetone decomposes into CO_2 and H_2O, while electrons get released into the valence band resulting in the recombination of electrons and holes [26]. The number of holes will then be decreased, therefore increasing the sensor resistance.

Therefore, the observed remarkable gas sensing performance displayed by the $LaFeO_3$ based sensor can be explained in terms of a number of contributing factors including surface defects, morphology as well as the surface area. The gas sensing properties are known to be significantly influenced by the morphology of the sensing material. While on the other hand, the particle morphology affects the specific surface area of the sensing materials. Higher specific surface area

means large active sites for adsorption and desorption of gas molecules. As a result, this may attract the large number of electrons from the bulk of the sensing material making the sensor having higher surface area more sensitive to the tested gases. In this case, BET specific surface area analyses showed larger surface area for $LaFeO_3$ NFs as compared to $LaCoO_3$ NFs and this explains the observed better sensing performance exhibited by this sensor upon exposure to acetone. As another significant factor that may promote sensor responses of the sensing material, surface defects, including oxygen related ones, act as electron donors to supply more electrons to the conduction band of the sensing material. For this reason, the presence of these oxygen related defects in a sensing material in larger quantities will promote greater adsorptions of oxygen species leading to further increase of response. In the current study, both the XPS and PL analyses exhibited high concentration of oxygen related defects for the $LaFeO_3$ NFs in comparison to the $LaCoO_3$. Existence of such defects in large amounts offer more channels for transportation of target gas molecules and formation of oxygen species thus contributing to the observed enhanced sensing performance obtained for the sensor based on $LaFeO_3$ NFs. Moreover, the interparticle connectivity NF morphology observed from SEM cannot be excluded as one of the contributing factors towards sensor response enhancement as it offers ease of contact to active sites as well as efficient and fast gas diffusion. Moreover, the overlapping of the hole accumulation layers along the NF direction produced a continuous hole transfer channels leading to high acetone response with fast response and recovery times and excellent selectivity towards acetone.

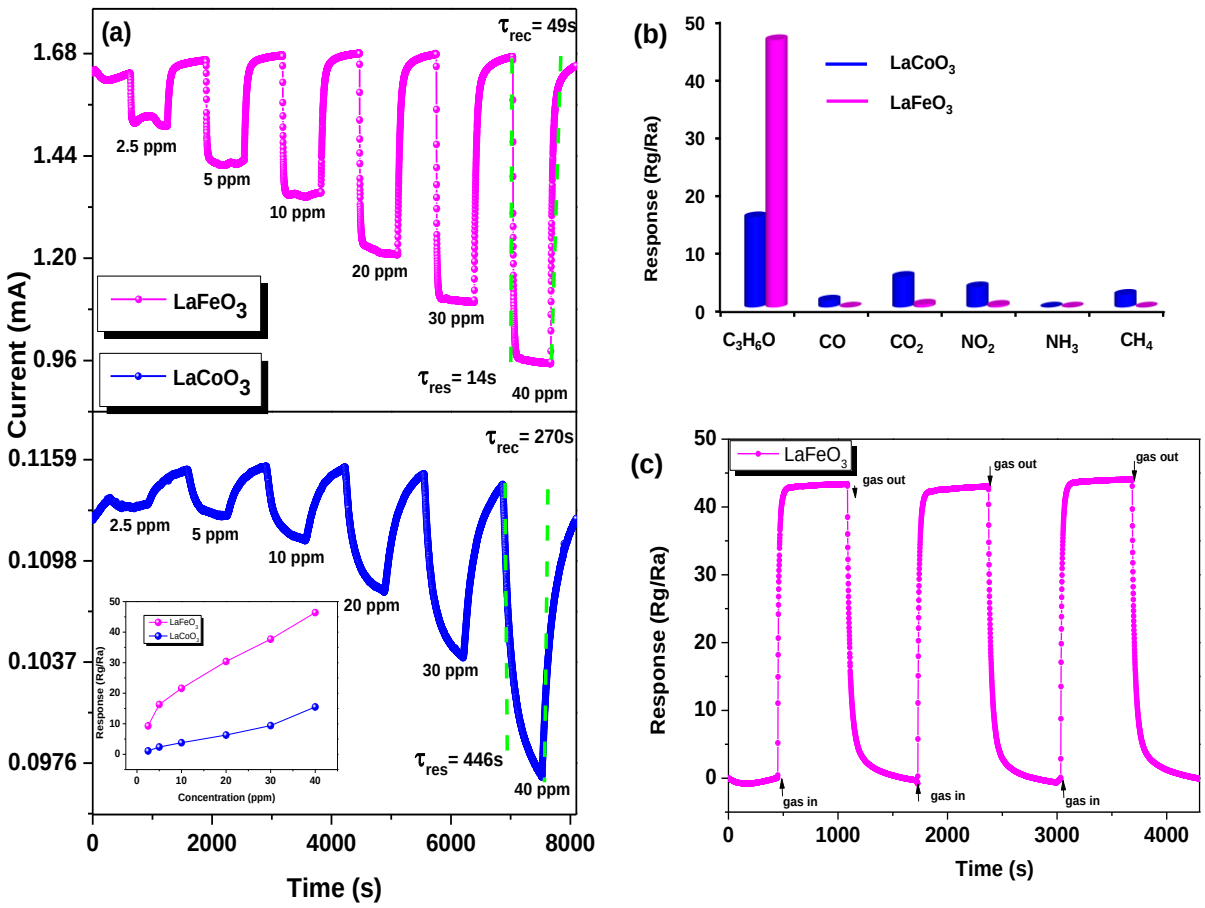

Figure 5.6: (a) Current transients with the response versus gas concentration as inset, (b) responses to 40 ppm of different target gases and (c) repeatability measurements of $LaCoO_3$ and $LaFeO_3$ NFs based sensors.

Several reports on the acetone sensing capability of different metal oxides are reported in literature and are listed in Table 5.1 for comparison to this work. It can be realised that most of the listed acetone sensors are operated at high temperatures to high concentration levels of acetone. Whereas the $LaFeO_3$ NFs based sensor displays high response to low concentration levels of acetone at comparatively low temperature with fast response and recovery times and very low theoretical limit of detection (LoD) values. Based on this, it suffices to say

that $LaFeO_3$ NFs is a promising material for low power consuming acetone detection operation with fast response and recovery times.

Table 5.1: Comparison of gas sensing properties based on nanostructured semiconductor metal oxides reported in literature and this work.

Material	Temp (°C)	Conc.(ppm)/Response	T_{res}/T_{rec} (s)	LoD (ppm)	Ref.
Porous $NiFe_2O_4$ microspheres	250	100/27.4	2/406	0.2	[27]
Porous $ZnFe_2O_4$ nanorods	260	100/52.8	1/11	1	[28]
$CoFe_2O_4$ nanoparticles	220	100/17.3	-	-	[29]
$La_{0.68}Pb_{0.32}FeO_3$	200	50/7	60/20	-	[30]
$LaFeO_3$	400	80/204	15/-	-	[31]
$NiFe_2O_4$ core-in-hollow-shell nanospheres	280	100/10.6	1/7	10	[32]
$LaFeO_3$ NFs	120	40/46.4	14/49	0.135	This work

5.8 Conclusion

In summary; Lanthanum based perovskites namely $LaCoO_3$ and $LaFeO_3$ NFs were synthesized using the electrospinning method. XRD and SEM confirmed the formation of rhombohedral $LaCoO_3$ and cubic $LaFeO_3$ NF's. The gas sensing performance of $LaCoO_3$ and $LaFeO_3$ NFs at an operating temperature of 120 °C revealed selectivity to acetone with the $LaFeO_3$ NFs based sensor showing the highest response with fast response and recovery kinetics. The sensing performance of the $LaFeO_3$ NFs based sensor was attributed to the synergistic effects of the high surface area as well as high oxygen vacancies and chemisorbed oxygen in comparison to the $LaCoO_3$, which provided more active sites for efficient gas adsorption/desorption reactions. Based on the findings, $LaFeO_3$ is a

promising sensing material for consideration in low concentration of acetone detection practical applications.

5.9 References

[1] A. Mirzaei, S. Leonardi, G. Neri, Ceram. Int., 42 (2016) 15119-15141.

[2] Q. Jia, H. Ji, Y. Zhang, Y. Chen, X. Sun, Z. Jin, J. Hazard. Mater., 276 (2014) 262-270.

[3] K. Shingange, Z. Tshabalala, B. Dhonge, O. Ntwaeaborwa, D. Motaung, G. Mhlongo, Mater. Res. Bull., 85 (2017) 52-63.

[4] B. Shouli, C. Liangyuan, L. Dianqing, Y. Wensheng, Y. Pengcheng, L. Zhiyong, C. Aifan, C.C. Liu, Sens Actuators B Chem., 146 (2010) 129-137.

[5] K. Hayat, S.S. Shah, M. Yousaf, M.J. Iqbal, M. Ali, S. Ali, M. Ajmal, Y. Iqbal, Mat Sci. Semicon. Proc., 41 (2016) 364-369.

[6] K. Shingange, H. Swart, G. Mhlongo, J. Alloys. Compd., 797 (2019) 284-301.

[7] H. Zhang, P. Song, D. Han, Q. Wang, Physica E., 63 (2014) 21-26.

[8] W. Haron, A. Wisitsoraat, S. Wongnawa, Ceram. Int., 43 (2017) 5032-5040.

[9] P. Shikha, T.S. Kang, B. Randhawa, J. Alloys. Compd., 625 (2015) 336-345.

[10] J. Yang, R. Li, J. Zhou, X. Li, Y. Zhang, Y. Long, Y. Li, J. Alloys. Compd., 508 (2010) 301-308.

[11] A. Khalil, J.J. Kim, H.L. Tuller, G.C. Rutledge, R. Hashaikeh, Sens. Actuators B Chem., 227 (2016) 54-64.

[12] H. Liu, H. Sun, R. Xie, X. Zhang, K. Zheng, T. Peng, X. Wu, Y. Zhang, Appl. Surf. Sci., 442 (2018) 742-749.

[13] J. Lu, C. Xu, L. Cheng, N. Jia, J. Huang, C. Li, Mater. Sci. Semicond., 101 (2019) 214-222.

[14] K. Shingange, H. Swart, G.H. Mhlongo, Physica B., 535 (2018) 216-220.

[15] L. Predoana, B. Malic, D. Crisan, N. Dragan, M. Anastasescu, J. Calderon-Moreno, R. Scurtu, M. Zaharescu, Ceram. Int., 38 (2012) 5433-5443.

[16] S. Thirumalairajan, K. Girija, V.R. Mastelaro, N. Ponpandian, ACS Appl. Mater. Interfaces., 6 (2014) 13917-13927.

[17] K. Zhao, L. Li, A. Zheng, Z. Huang, F. He, Y. Shen, G. Wei, H. Li, Z. Zhao, Appl. Energy., 197 (2017) 393-404.

[18] G.H. Mhlongo, D.E. Motaung, F.R. Cummings, H.C. Swart, S.S. Ray, Sci. Rep., 9 (2019) 9881.

[19] G.H. Mhlongo, D.E. Motaung, I. Kortidis, N.R. Mathe, O.M. Ntwaeaborwa, H.C. Swart, B.W. Mwakikunga, S.S. Ray, G. Kiriakidis, Mater. Chem. Phys., 162 (2015) 628-639.

[20] Q. Rong, Y. Zhang, J. Hu, K. Li, H. Wang, M. Chen, T. Lv, Z. Zhu, J. Zhang, Q. Liu, Sci. Rep., 8 (2018) 14220.

[21] O. Bechambi, A. Touati, S. Sayadi, W. Najjar, Mat. Sci. Semicon. Proc., 39 (2015) 807-816.

[22] N. Vidyarajan, L. Alexander, Mater. Res. Express, 6 (2018) 015610.

[23] M. Wu, M. Luo, M. Guo, L. Jia, ACS Sustain. Chem. Eng., 5 (2017) 11558-11565.

[24] R. Zhang, T. Zhou, L. Wang, T. Zhang, ACS Appl. Mater. Interfaces., 10 (2018) 9765-9773.

[25] T. Samerjai, N. Tamaekong, K. Wetchakun, V. Kruefu, C. Liewhiran, C. Siriwong, A. Wisitsoraat, S. Phanichphat, Sens. Actuators B Chem., 171 (2012) 43-61.

[26] C. Wang, Q. Rong, Y. Zhang, J. Hu, B. Zi, Z. Zhu, J. Zhang, Q. Liu, Mater. Res. Bull., 109 (2019) 265-272.

[27] S. Zhang, W. Jiang, Y. Li, X. Yang, P. Sun, F. Liu, X. Yan, Y. Gao, X. Liang, J. Ma, G. Lu, Sens. Actuators B Chem., 291 (2019) 266-274.

[28] L. Li, J. Tan, M. Dun, X. Huang, Sens. Actuators B Chem., 248 (2017) 85-91.

[29] H.-J. Zhang, L.-Z. Liu, X.-R. Zhang, S. Zhang, F.-N. Meng, J. Alloys. Compd., 788 (2019) 1103-1112.

[30] L. Zhang, H. Qin, P. Song, J. Hu, M. Jiang, Mater. Chem. Phys., 98 (2006) 358-362.

[31] X. Liu, H. Ji, Y. Gu, M. Xu, Mater. Sci. Eng. B 133 (2006) 98-101.

[32] T. Zhou, T. Zhang, Y. Zeng, R. Zhang, Z. Lou, J. Deng, L. Wang, Sens. Actuators B Chem., 255 (2018) 1436-1444.

Chapter 6

Design of porous p-type $LaCoO_3$ nanofibers with remarkable response and selectivity to ethanol at low operating temperature

6.1 Introduction

Due to the increase in the number of ethanol production plants and consumption of it as a beverage; a safety system to monitor its concentration level for social security and environmental monitoring is required. Airborne ethanol can result in health problems such as headache, drowsiness, irritation of eyes and difficulty in breathing [1]. On the other hand, ethanol serves as a biomarker for obesity-related liver disease caused by pathogens [2]. Also; various concentrations of ethanol are produced on the surface of food such as fruits, vegetables and milk due to microbial activities [3, 4]. Thus, its concentration level are used to monitor the freshness level of food.

Nanostructured semiconducting metal oxides (SMOs) have been the answer to many commercial application challenges including the gas sensing technology. This is driven by the improvement of properties of nano-sized materials brought upon by the high surface area and quantum confinement effects thus enabling development of cost effective and portable sensing devices for different target gases for different applications [5-14]. There are many parameters that influence the gas sensing performance/response of SMOs to different gases such as surface-to-volume-ratios of the surface morphology, surface active sites, lowest unoccupied molecule orbit (LUMO) energy of target gases and target gas concentration [14-16]. So it is of paramount importance to tailor SMOs

nanostructures that can give the utmost gas performance. Amongst several nanostructured forms of SMOs; one dimensional (1D) nanofibers (NFs) have been of great interest in gas sensing technology owing to their small diameter and long length, which provide high specific surface area and a connection across the electrodes for resistance measurements [17-22]. In order to commercialize the use of SMOs NFs as reliable materials for gas sensing, optimizing their morphology and microstructure is of great importance [23, 24]. Several studies have been undertaken to thoroughly analyse the morphology-sensing relationship for different SMOs. For instance, Choi *et al.* [25] observed enhanced response to ethanol (C_2H_5OH) by Zn_2SnO_4 NFs with decreasing grain size and high porosity. Katoch *et al.* [26] realised that crystallinity and grain size in ZnO NFs influences the carbon monoxide (CO) sensing performance. Khalil *et al.* [27] observed resistance variance towards hydrogen (H_2) and ammonia (NH_3) to which they attributed the differences in fiber diameter, surface area, crystallinity and crystallite size.

Both n and p-type SMO based NFs shows remarkable gas sensing performance for different reducing and oxidizing gases. However, n-type SMOs are mostly favoured, given that the response in p-type SMOs is nearly the square root of the response in n-type sensors SMOs [28]. N-type binary SMOs normally display excellent sensing properties, yet their poor long term reliability is a snag to their application. Some of the ternary metal oxides with the perovskite ABO_3 structure have been reported to be more reliable and stable during gas sensing as compared to the binary oxides which could be due to the fact that ternary oxides comprise of two differently sized cations thus enabling tailoring of desired properties and performances [29]. Further, their sensitivity and selectivity

towards target gas can be tuned by alternating the A and B atoms [29, 30]. Among various perovskite oxides, the lanthanum cobaltite ($LaCoO_3$) perovskite reveals high p-type electronic conductivity, significant oxygen ion mobility, and excellent electrochemical and catalytic activity in reactions involving oxygen which makes it a good candidate for gas sensing application [31-35]. A thorough literature study indicates that up to date, so many functional $LaCoO_3$ nanostructures with different architectures have been prepared and their sensing performance towards different gases has been investigated [36-39]. In contrast, literature on a direct analysis of the ethanol gas sensing performance based on electro-spun $LaCoO_3$ NFs is very limited. Moreover, most reported $LaCoO_3$ sensing materials are operated at high temperatures (200-600 °C) to enhance their chemical reactivity, but it ends up consuming a lot of energy and poor sensor stability and this is a drawback for practical applications [40].

In this work, the manipulation of the morphology and microstructure of 1D electro-spun $LaCoO_3$ NFs produced after post-annealing is presented. A full detailed understanding on the link between the morphological and microstructural evolution of $LaCoO_3$ NFs induced by annealing temperature variation and their gas sensing performance, so as to gain more insight on the sensing behaviour of the $LaCoO_3$ NFs based sensors has been investigated.

6.2 Experimental section

6.2.1 Materials

Lanthanum nitrate hexahydrate ($La(NO_3)_3.6H_2O$), cobalt nitrate hexahydrate ($Co(NO_3)_3.6H_2O$) and polyvinylpyrrolidone (PVP) were used as the starting materials without further purification. While N-N Dimethyleformamide (DMF) and Ethanol were used as solvents.

6.2.2 Synthesis of $LaCoO_3$ NFs

Equal molar concentrations of $La(NO_3)_3.6H_2O$ and ($Co(NO_3)_3.6H_2O$) salts were added to a mixture of 6 ml DMF and 4 ml ethanol followed by stirring at 40 °C until completely dissolved. 1g of PVP was then added to the above solution, and the mixture was continuously stirred for 2 h to obtain a homogeneous gel precursor solution. The precursor solution was then loaded into a 10 ml syringe for electrospinning at room temperature. The pumping rate applied was 0.5 μlh^{-1} at an applied voltage of 20 kV. The drum collector was placed 15 cm away from the spinneret. The obtained composite NFs were annealed at 550, 650 and 700 °C at a heating rate of 2 $°Cmin^{-1}$ for 2 h in air to obtain the $LaCoO_3$ NFs.

6.3 Characterization

The composition and crystallinity of the $LaCoO_3$ nanoparticles was determined by using an X-ray diffraction (XRD) Panalytical X'pert PRO PW3040/60 X-ray diffractometer with a Cu-Kα (λ=1.5405 Å) radiation. The surface morphology and microstructure of the $LaCoO_3$ NFs were observed using a ZEIS-AURIGA field emission-scanning electron microscopy (FESEM) at an acceleration voltage of 3 kV, and JEOL TEM-2100 high resolution transmission electron microscopy (HR-TEM) with an accelerating voltage of 200 kV. Nitrogen (N_2) adsorption-

desorption isotherms were measured at 77 K using a Micrometirics TRISTAR 300 surface area analyser. The surface area was evaluated using the Brunauer-Emmett-Telle (BET) method, while the pore diameter distribution was obtained from the desorption branch of the isotherm using the Barrett-Joyner-Halenda (BJH) method. X-ray photoelectron spectra (XPS) were recorded with a PHI 5000 Versaprobe XPS with monochromatic Al-Kα radiation ($h\nu$ = 1486.6 eV).

6.4 Fabrication of gas sensors

40 mg of each sample was mixed with a solution of ethyl cellulose (a temporary binder) in turpineol and ground for 30 minutes to make thixotropic pastes. The pastes were then coated onto an alumina substrate equipped with a pair of platinum (Pt) electrodes on the top surface and a heater on the bottom surface to control the working temperature. All the sensors were then heated at 300 °C for 2 h at a heating rate of 3 °C/min to achieve good adhesion. The gas sensing performance was evaluated using a commercial KSGAS6S gas sensing station (KENOSISTEC, Italy) in different target gas conditions namely, NH_3, C_3H_6O, C_2H_5OH NO_2, CO, CO_2 and CH_4 from room temperature (RT) to 180 °C. The operation temperature was controlled by varying the applied voltage while using a thermocouple to measure the corresponding temperature at different voltages. The required target gas concentration was delivered into the sensing using MKS Instruments Deutschland GmbH mass flow controllers by diluting the concentrated target gas in synthetic air at a constant flux rate of 500 ml/min. The electrical resistance changes during the adsorption and desorption of the target gas molecules on the surface of the $LaCoO_3$ NFs based sensing device was measured in air *(Ra)* and in the presence of the target gas *(Rg)* through the use of a Keithley 6487 Picoammeter/voltage source meter. The sensor response was

then determined as the ratio of the electrical resistance in the gas to that in air (*Rg/Ra)* [41, 42]. Figure 6.1 demonstrates the synthesis and preparation of the sensors based on $LaCoO_3$ NFs.

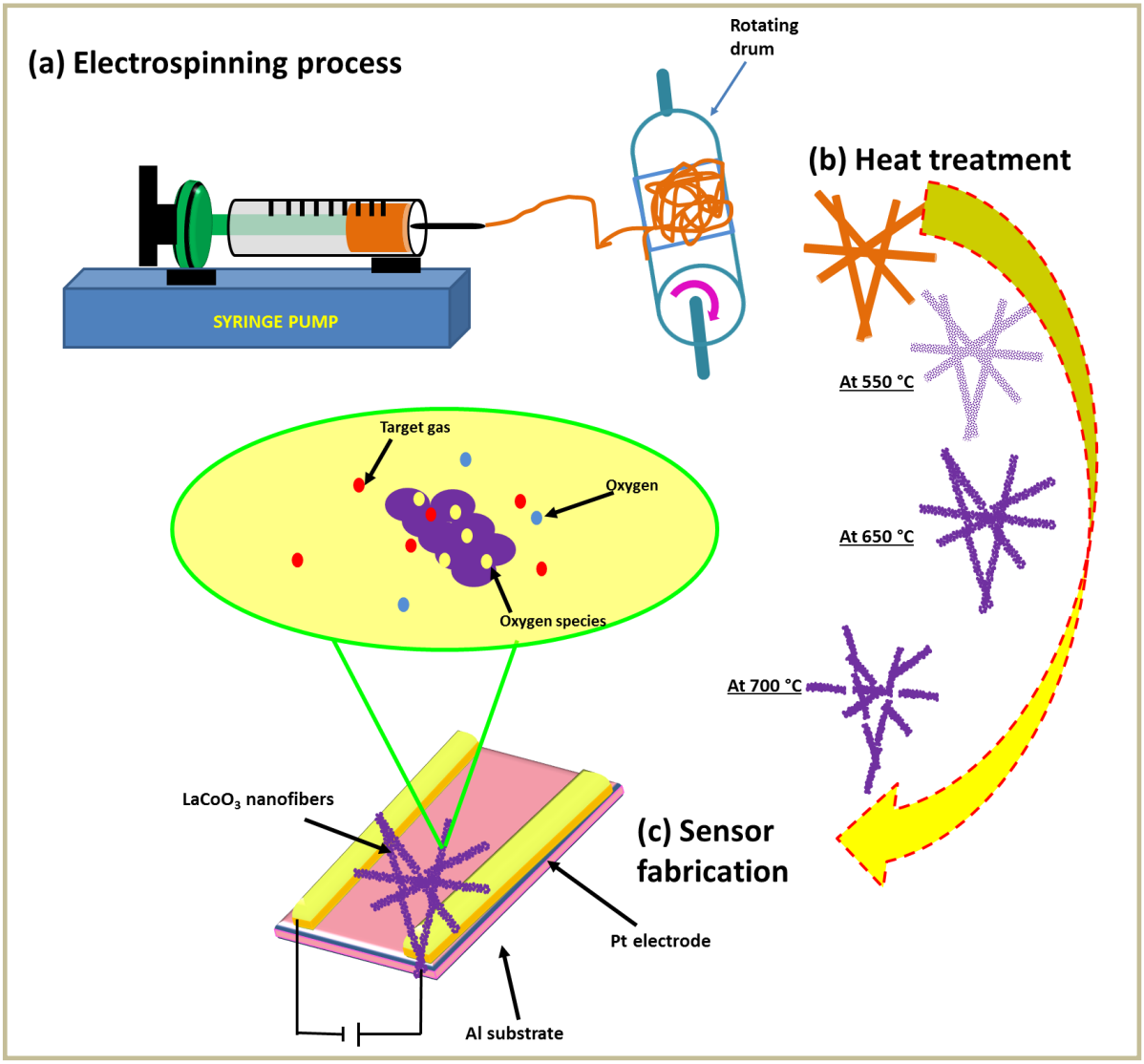

Figure 6.1: Schematic diagram of the $LaCoO_3$ NFs synthesis and the fabrication of the sensors.

6.5 Results and discussions

6.5.1 Structural characteristics

To evaluate the effect of annealing on the structural and phase information of the $LaCoO_3$ NFs, the XRD patterns were recorded (see Figure 6.2). At an annealing

temperature of 550 °C, the NFs crystallized into the cubic phase of $LaCoO_3$ which was demonstrated by the presence of the reflection at 2θ = 33.1°. With increase of annealing temperature to 650 °C, the reflection at 2θ = 33.1° split into a doublet (see Figure 6.2(b)) indicating the rhombohedral symmetry of $LaCoO_3$ [43] (JCPDS card no. 01-075-0279). The rhombohedral structure remained stable even at annealing temperature of 700 °C. Moreover, the sample at 650 °C showed intensified diffraction peaks suggesting a high crystallinity. The average crystallite sizes were estimated using Scherrer's equation [44] based on a full width at half maxima (FWHM) of the (012) peak and the crystallite size values are listed in Table 6.1. The crystallite sizes increased with an increase in annealing temperature demonstrating that annealing of the $LaCoO_3$ promoted crystal size growth. The XRD findings clearly show that the annealing affected the structural properties of the $LaCoO_3$.

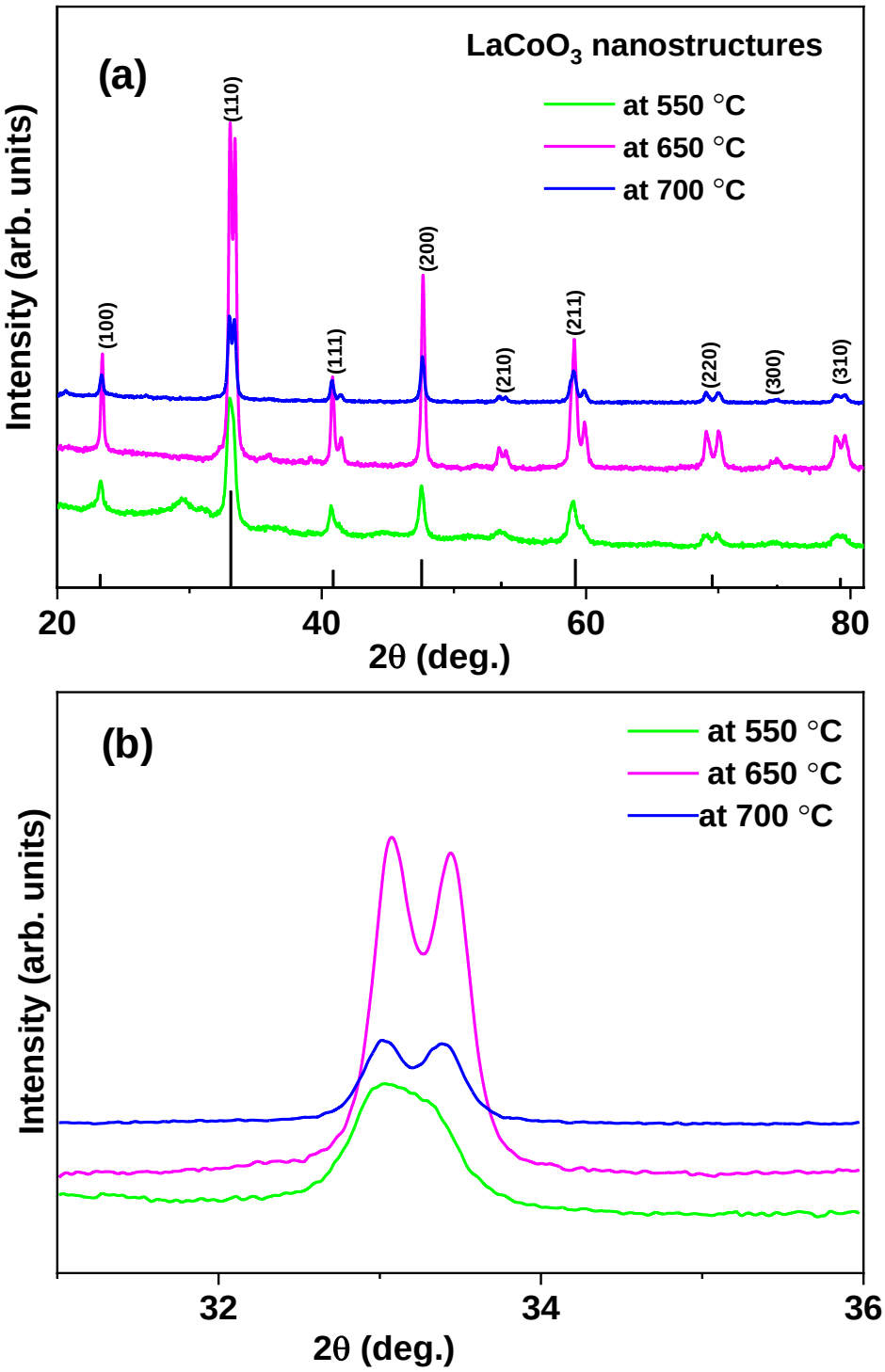

Figure 6.2: (a) XRD patterns and (b) enlarged perovskite peak range of the $LaCoO_3$ NFs annealed at different temperatures of 550, 650 and 700 °C.

Table 6.1: Crystallite size, BET surface area, BET pore size diameter, particle size of the $LaCoO_3$ NFs annealed at 550, 650 and 700 °C, respectively.

Sample annealing temperature (°C)	Crystallite size from XRD (nm)	Particle size from SEM (nm)	BET specific surface area (m^2/g)	BET pore diameter (nm)
550	15	47	5.8	117.2
650	32	58	10.7	63.9
700	25	77	3.4	2.4

6.5.2 Morphological characteristics

To further verify the effect of annealing temperature on the morphological and microstructural properties, SEM and TEM micrographs were captured. Figure 6.3 shows the $LaCoO_3$ NFs at different annealing temperatures of 550, 650, and 700 °C. As depicted in Figure 6.3(a-c), all the samples possessed randomly orientated nanostructures with fiber-like morphology constructed by interconnected particles. The sizes and structures of the randomly orientated $LaCoO_3$ NFs transformed with annealing temperature variation and this can clearly be seen on the TEM images presented in Figure 6.3(d-f). At 550 °C, the NFs consisted of tiny particles with average size of ~47 nm across the diameter of a single NF (see Figure 6.3(d)). When the annealing temperature was increased, the size of the nanoparticles forming each fiber grew bigger (i.e. average particle size of ~58 and ~77 nm for annealing temperatures of 650 and 700 °C, respectively). This growth in particle size with an increase in annealing temperature can be attributed to the reduction in the free energy of the system caused by a reduction in the total grain boundary area [26]. Moreover; further increase in annealing temperature to 700 °C led to disintegration and NFs became short instead. For

quantitative analysis, the particle sizes forming the fibers were measured and their distribution per annealing temperature are shown in Figure 6.3 (j-l) for $LaCoO_3$ NFs at 550, 650 and 700 °C, respectively. These results clearly demonstrate that the NF morphology evolved with the increase in annealing temperature. Further, Figure 6.3(g-i) shows the high resolution TEM images of the NFs, which revealed exposed lines of atoms over the $LaCoO_3$ nanoparticles across a single NF that displayed interplanar spacing of 0.26 and 0.28 nm corresponding to the (110) planes diffracting to a maximum 2θ angle of 23.2° and 0.37 and 0.39 nm corresponding to the (100) plane diffracting to a maximum 2θ angle of 33.1° in the XRD. These results confirm high crystallinity of the $LaCoO_3$ NFs as previously observed from XRD.

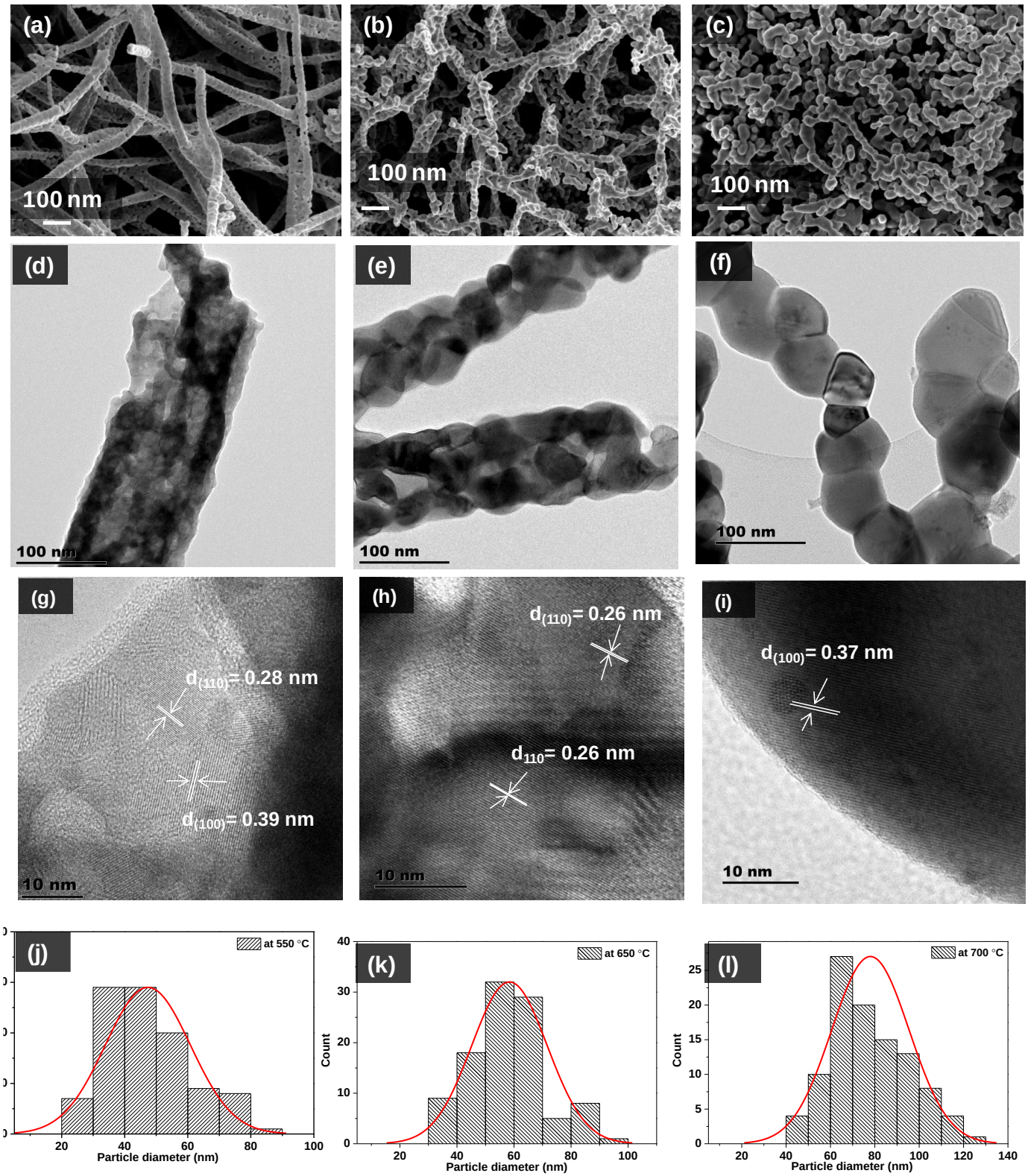

Figure 6.3: SEM, TEM and HR-TEM images of the $LaCoO_3$ NFs obtained at (a, d and g) 550, (b, e and h) 650, (c, f and i) 700 °C, and the corresponding particle size distribution at (j) 550, (k) 650, (l) 700 °C.

6.5.3 Surface chemical composition analyses

The chemical composition of the $LaCoO_3$ was performed to establish the chemical state of the $LaCoO_3$ NFs using the $LaCoO_3$ sample annealed at 550, 650 and 700 °C. Figure 6.4 shows the XPS spectra of La 3d, O 1s and Co 2p for the $LaCoO_3$, respectively. Figure 6.4 (a), demonstrates the XPS spectrum of the La 3d core level consisting of a double peak for each spin-orbit component namely La $3d_{5/2}$ and La $3d_{3/2}$. This La 3d structure resulted from an intense O 2p →La 4f charge transfer events or strong final state mixing of electronic configurations, which is typical of La^{3+} compounds [45-47]. For the spectrum of the Co 2p core level depicted in Figure 6.4(b), two peaks located at 795.0 eV and 779.7 eV belonging to Co $2p_{1/2}$ and Co $2p_{3/2}$ separated by 15.3 eV can be identified confirming the Co^{3+} state [38, 48]. The XPS spectrum of the O 1s core level of the $LaCoO_3$ at 550, 650 and 700 °C shown in Figure 6.4(c-e) revealed three oxygen components herein labelled as O_L, O_V and O_C. The O_L at 528.8 eV corresponds to the lattice oxygen (O^{2-}), O_V located at 530.9 eV assigned to the surface adsorbed oxygen (O_2^{2-}) and is related to oxygen vacancies while the O_C situated at 532.1 eV results from hydroxyls species (OH^-) or carbonate species (CO_3^{2-}) [49]. As much as the surface adsorbed oxygen is reliant on the presence of oxygen vacancies in the crystal lattice, they are not the same oxygen species. Also, the variations in the intensity of the O_V component is in relation to the variations of oxygen vacancies which are very important in gas sensing performance as they are known to act as active sites for the oxygen chemisorption and ionization on the sensor material surface, consequently contributing to the improvement of the sensor performance [50].

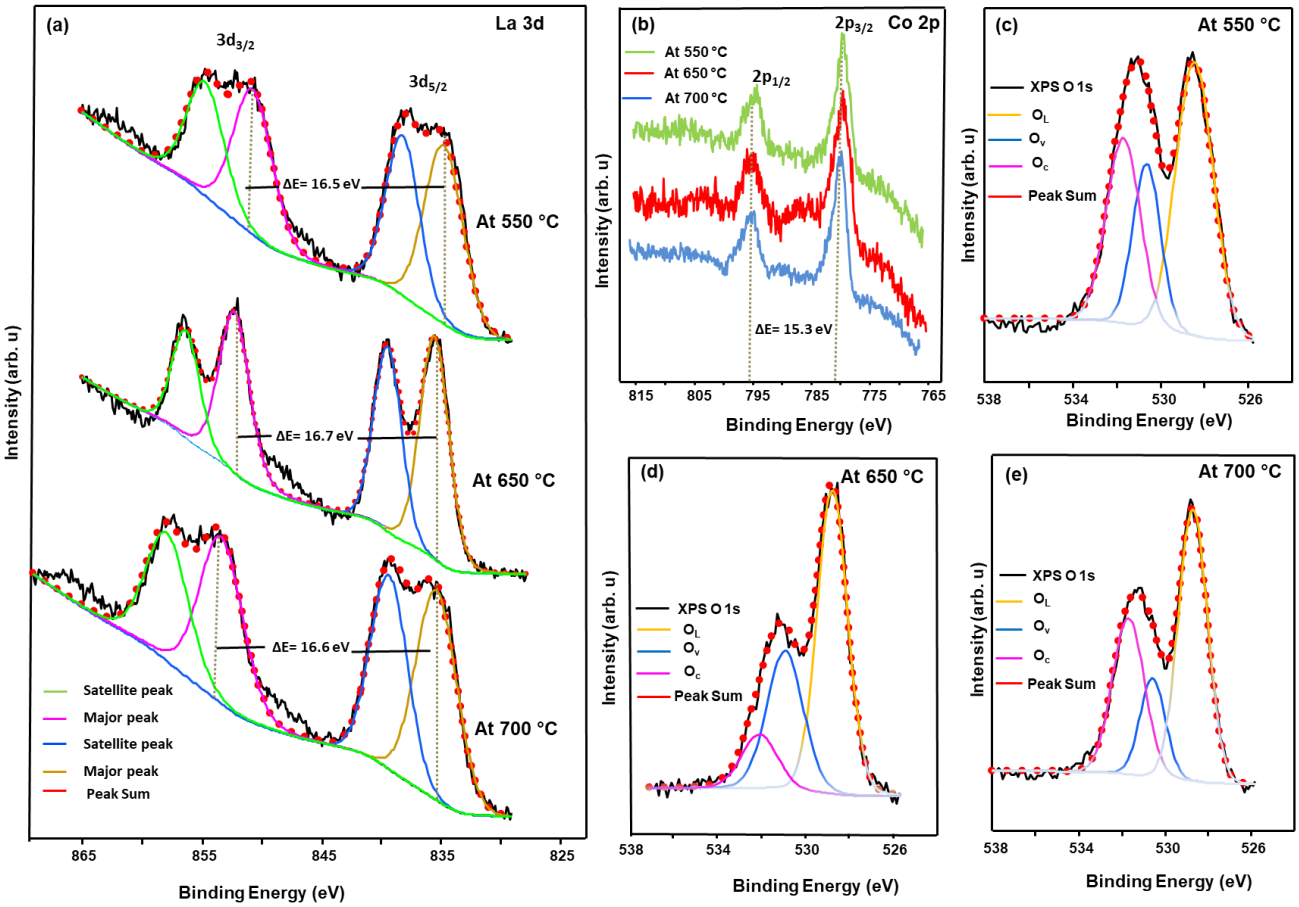

Figure 6.4: XPS spectra of (a) La 3d, (b) Co 2p and (c-e) O 1s for the $LaCoO_3$ NFs annealed at 550, 650 and 700 °C.

Table 2: XPS O 1s spectra relative peak areas

Sample	O_L	O_V	O_C	
	Area (%)	Area (%)	Area (%)	O_V/O_L
At 550 °C	48.6	21.5	29.9	0.44
At 650 °C	56.7	31.1	12.2	0.54
At 700 °C	51.5	16.0	32.5	0.31

6.5.4 Porous characteristics

Since the surface characteristics of materials has an important effect on gas sensing performance; the surface area analysis of the $LaCoO_3$ NFs were investigated based on the nitrogen adsorption-desorption isotherms using the BET method. Figure 6.5 presents the N_2 isotherms, which are type IV with a H3 hysteresis loop in the high pressure range (0.8< P/Po >1), which can be associated with the existence of a mesoporous structure [51-53]. The isotherms of the NFs annealed at 550 and 700 °C displayed negative adsorption-desorption, which is an indication of low surface area. The surface area values of the $LaCoO_3$ NFs were found to be 5.8, 10.7 and 3.4 m^2/g for $LaCoO_3$ NFs obtained after annealing at 550, 650 and 700 °C. $LaCoO_3$ NFs after annealed at 650 °C displayed a high surface area value while those annealed at the highest annealing temperature of 700 °C had a lowest surface area value. From SEM results, NFs annealed at 700 °C revealed the largest particle size as compared to the rest of the NFs and this could be the reason for the very low specific area.

The average pore size diameters were found to be 117.2, 63.9 and 2.4 nm for the $LaCoO_3$ NFs annealed at 550, 650 and 700 °C, respectively. The high specific surface area and big pores offers high availability of active sites, which play an important role for the improvement of gas sensing performance. Based on these results it can be anticipated that the $LaCoO_3$ NFs annealed at 550 and 650 °C may have better sensing performance as compared to those NFs annealed at 700 °C.

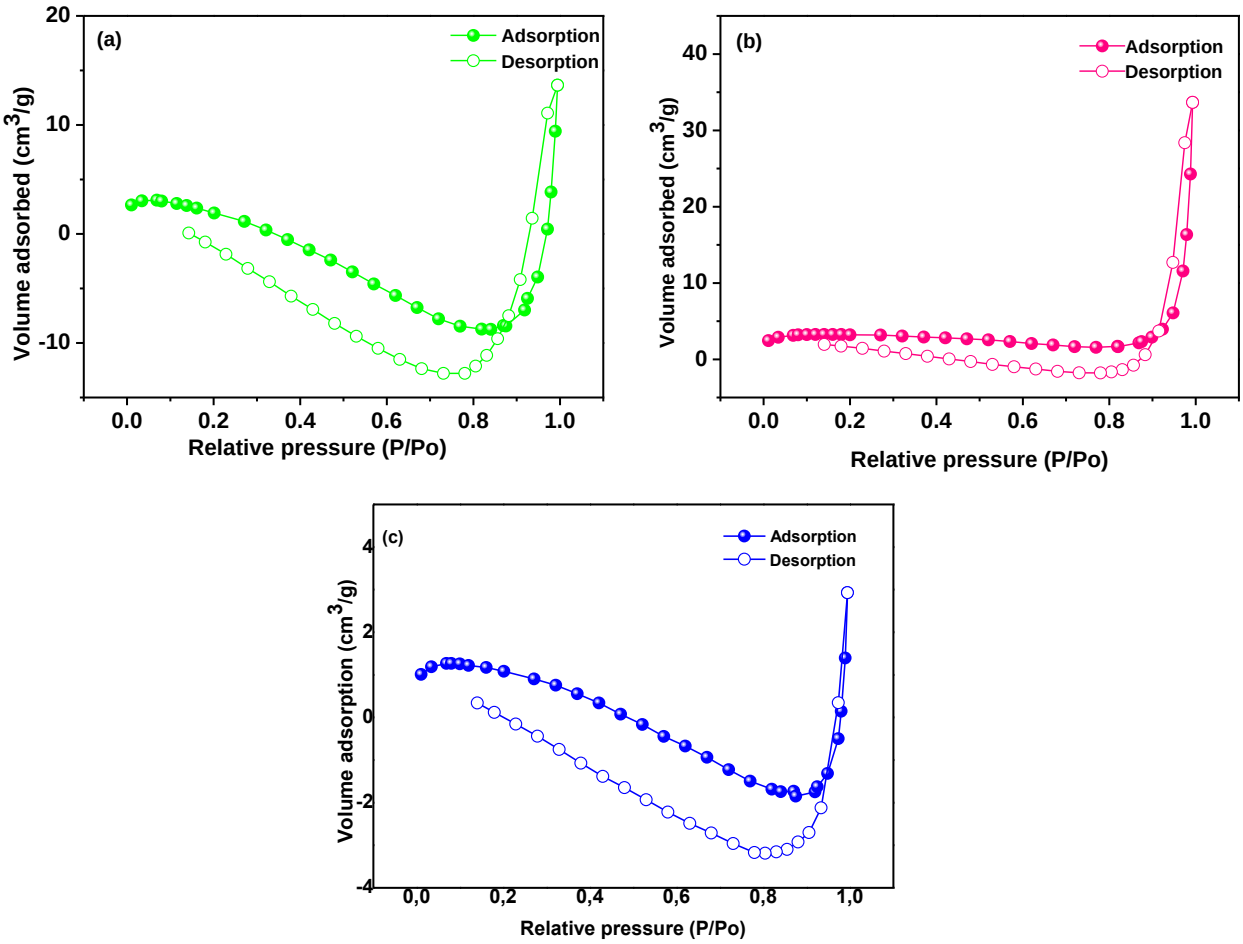

Figure 6.5: Nitrogen adsorption-desorption isotherms for the $LaCoO_3$ NFs annealed at (a) 550, (b) 650 and (c) 700 °C.

6.6 Gas sensing characteristics

An operating temperature is one of the most crucial parameter to consider for the potential practicality application of gas sensors since sensing processes such as gas adsorption and desorption on material's surface are subject to the sensors operating temperature. Thus, it is important to start by analysing the temperature reliance behaviour of the sensors. The sensors were exposed to 40 ppm of ethanol at various temperatures (26-180 °C) and their responses as a function of temperature are presented in Figure 6.6. As observed from the results; the response of all the sensors increased and reached a maximum value

with increasing operating temperature, then decreased with a further increase of operating temperature. Normally, at low working temperatures the reaction between target gas molecules and surface adsorbed oxygen species becomes too passive to give a high response as the target gas molecules do not have enough thermal energy to react with the surface oxygen species. Further increase of the operating temperature activates the target gas molecules to rapidly react with the oxygen species thus leading to a significant increase of sensor response. However, higher working temperatures limit gas adsorption capacity and the usage of the sensing layer, therefore resulting in the decrease of response [53, 56].

For the sensor based on the NFs annealed at 550 °C, the maximum sensor response of 15.1 (15.1%) was reached at an optimum operating temperature of 140 °C. For the sensor based on $LaCoO_3$ NFs annealed at 650 °C, the maximum sensor response was 32.4 (32.4%), which was attained at 120 °C. The NFs obtained after annealing at 700 °C reached a maximum sensor response of 1.6 at the working temperature of 140 °C. It is obvious that the sensor based on $LaCoO_3$ NFs obtained at 650 °C displayed the lowest optimum temperature and a much higher sensor response as compared to the rest of the sensors. Additionally, operating temperature influences the power consumption of the sensor device in real applications. Low power consumption reaching tens of milliwats are preferable, however there are still applications that require sensor devices having relatively high power consumption in order to meet safety requirements [55]. The power consumption of the $LaCoO_3$ NFs obtained at 650 °C was found to be 320 mW at an applied voltage of 4 V. This power consumption is slightly

higher than the reported power consumption for ethanol sensor (210 mW) [56], however it is lower to some SMO based sensors [55].

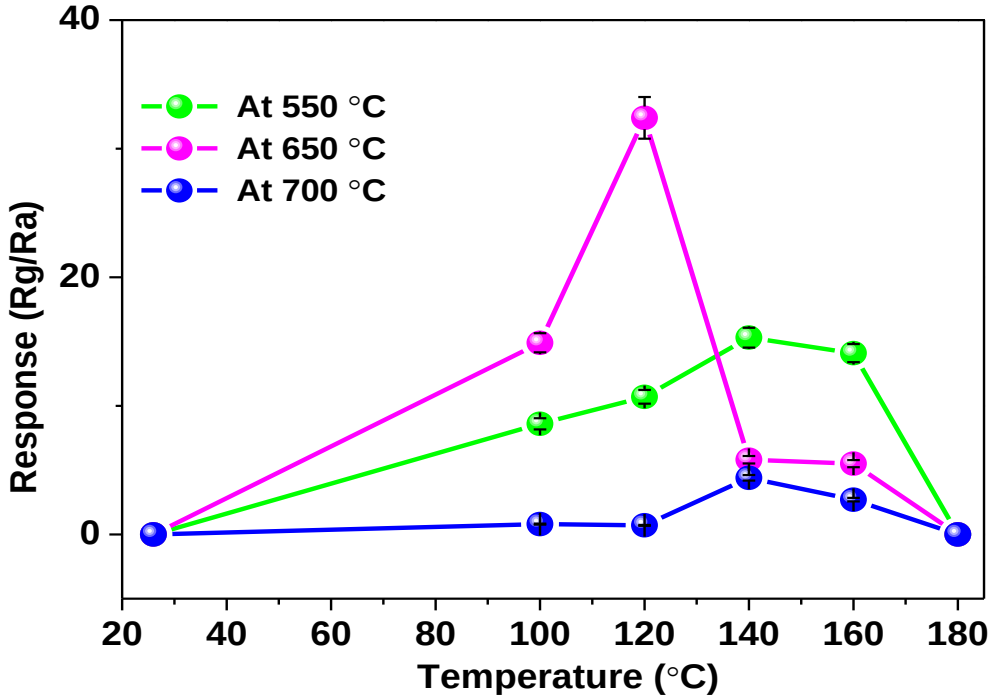

Figure 6.6: Response curves of the $LaCoO_3$ NFs sensors at 550, 650 and 700 °C to ethanol gas at different operating temperatures of the $LaCoO_3$ NFs.

Further, analysis on the $LaCoO_3$ NFs based sensors with regard to different concentrations of ethanol from 2.5-40 ppm as a function of time at the optimal operating temperature of 120 °C was performed and the results are displayed in Figure 6.7. The dynamic resistance curves of all the sensors displayed an increase in electrical resistance upon contact with ethanol gas molecules and recovered back to the baseline upon removal of the ethanol. This behaviour indicated a reversible interaction between the target gas and the sensing

materials. Figure 6.7(b) exhibits the relationship between the sensor response and the ethanol concentration which indicates the dependence of sensor response on target gas concentration. Moreover, the slope of the curves in Figure 6.7(b) gives the sensitivity of the curves which is defined as the ability of the sensor to differentiate small concentration variances of the target gas [57]. The sensitivity is found to be 0.331, 1.751 and 0.051 ppm^{-1} for the $LaCoO_3$ NFs annealed at 550, 650 and 700 °C, respectively. The high sensitivity value for the $LaCoO_3$ NFs obtained at 650 °C suggests its high response capability which favours effective ethanol detection at low concentrations.

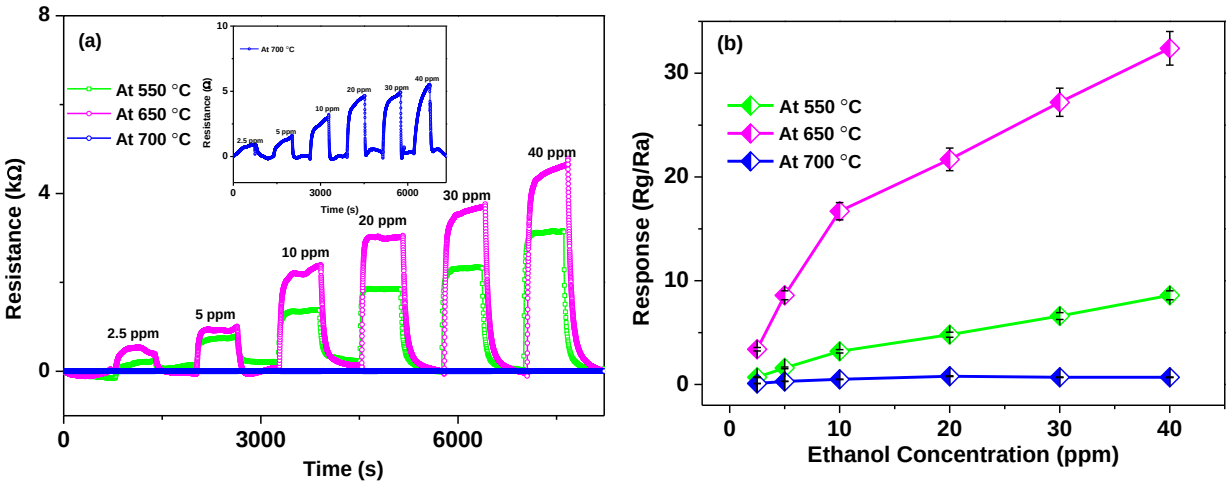

Figure 6.7: (a) Dynamic sensing transients to 2.5-40 ppm ethanol and (b) response of the sensors as a function of ethanol concentration.

In addition, the limit of detection (LoD) of each sensor has been calculated from the experimental data. LoD is defined as the lowest amount of target gas that can be detected with reasonable certainty and is calculated using equation (6.1)[58]:

$$LoD = 3\left(\frac{noise_{rms}}{slope}\right) \tag{6.1}$$

Where *slope* is found by taking a linear fit of the plots in Figure 6.7(b) at their beginning and $noise_{rms}$ is the sensor noise calculated using the variation in the sensor response above the baseline using the root-mean-square deviation (rms). The rms deviation was determined on more than 50 points at the baseline of Figure 6.7(a) as [58]:

$$noise_{rms} = \sqrt{\sum i(S_i - S)^2 / N} \qquad (6.2)$$

Where S_i are the experimental data points and S is the average value of the S_i. The LoDs of the $LaCoO_3$ NFs were found to be 0.658, 0.199 and 30.875 ppm for the NFs annealed at 550, 650 and 700 °C, respectively. This indicates that the sensor based on the $LaCoO_3$ NFs annealed at 650 °C has the lowest detection limit which is beneficial for detecting even small traces of ethanol.

For practical application, gas sensors require not only high response and high sensitivity, but also fast response and recovery times. Herein, the response time is defined as the time taken to reach 90% of its response steady state and recovery time is defined as the time taken by the sensor to reach 10% of its baseline value [59,60]. The response time of the sensors to 40 ppm of ethanol was measured and found to be 30, 26 and 294 s and the recovery time was found to be 47, 66 and 33 s for the sensors annealed at 550, 650 and 700 °C, respectively. The gas response speed of the sensor annealed at 700 °C was so long as compared to the other two samples due to the detained gas diffusion. Additionally, the baseline recovery speed was a bit longer as compared to the response speed for the NFs obtained at 550 and 650 °C. This could be due to the fact that during the target gas detection process; the target gas diffused throughout the sensing material and occupied its active surface. So; the recovery

performance relies on the sensing material's pore structure [40]. In this case the recovery time is a bit longer for the $LaCoO_3$ NFs annealed at 550 and 650 °C having big pores as compared to that of the $LaCoO_3$ sensor annealed at 700 °C, which displayed smaller pores as confirmed by BET results.

In practical application; the occurrence of the target gas is always accompanied with other gases. Thus it is important to analyse the selectivity ability of the gas sensor for identifying a certain gas in the presence of other gases. In order to determine the sensor selectivity, the responses of the sensors based on $LaCoO_3$ NFs to various interfering gases at a fixed gas concentration of 40 ppm and operating temperature of 120 °C were tested and the corresponding results are shown in Figure 6.8. The interfering gases included carbon monoxide (CO), carbon dioxide (CO_2), methane (CH_4), acetone (CH_3COCH_3), methanol (C_3OH), isopropyl alcohol (C_3H_8O), ammonia (NH_3) and Nitrogen dioxide (NO_2). As demonstrated in the figure, the responses to all the interfering gases are less than 13 which are lower than 32.4 obtained towards ethanol by the sensor based on $LaCoO_3$ annealed at 650 °C. This illustrate that the $LaCoO_3$ at 650 °C has an excellent selectivity to discriminate the ethanol gas amongst the interfering gases, which is desirable for practical use. Due to this observation, the selectivity coefficient (K) was introduced to determine the selectivity of the sensor quantitatively, and it was calculated as:

$$K = R_{C_2H_5OH}/R_X \tag{6.3}$$

where $R_{C_2H_5OH}$ is the sensor response in the presence of ethanol and R_X is the sensor response in the presence of the other target gases. The obtained K value for CO, CO_2, CH_4, CH_3COCH_3, C_3OH, C_3H_8O, NH_3, and NO_2 are 21.6, 3.7, 17.0, 2.5,

9.8, 12.4, 108 and 3.2, respectively. The *K* values obtained are much greater than one, indicating that the sensor has greater ability to separate ethanol gas in the company of other gases. The great ethanol selectivity of the sensor may be due to the following; (i) different energies are required for different gases to react with the adsorbed oxygen species [61,62]. At the operating temperature of 120 °C; some interfering gases may not fully react with adsorbed species due to deficient energies. (ii) The second reason may be that some interfering gases may not be strongly adsorbed on the surfaces of the $LaCoO_3$ NFs at the operating temperature of 120 °C.

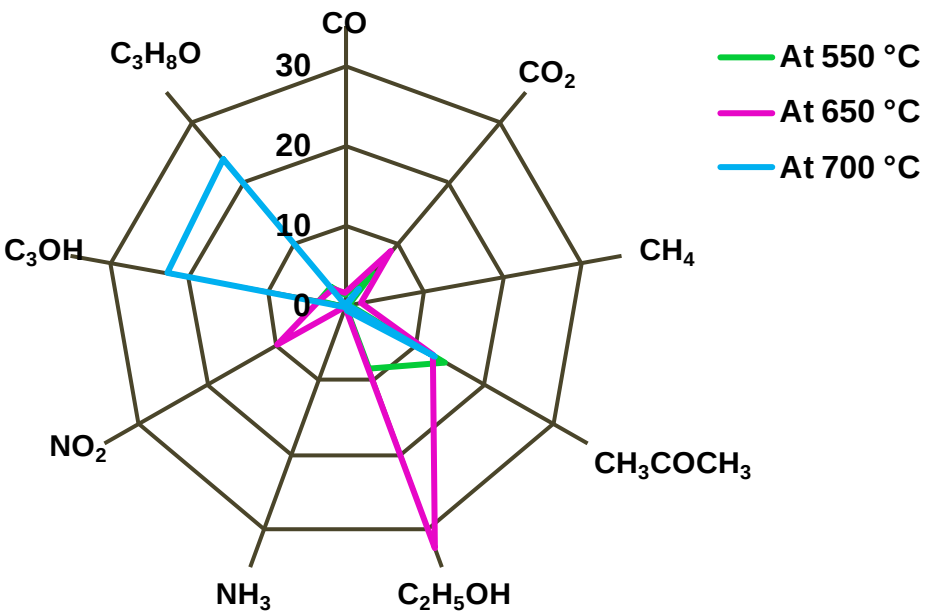

Figure 6.8: The responses of the sensors based on the $LaCoO_3$ NFs to nine kinds of target gases at 40 ppm.

Further, the influence of moisture on the ethanol sensing capabilities of the $LaCoO_3$ NFs based sensors was investigated by subjecting the sensors to relative humid (RH) air of different levels (30, 50, 70 and 90%) and the resulting responses are depicted in Figure 6.9(a). The responses to ethanol for the sensors based on $LaCoO_3$ NFs annealed at 550 and 650 °C were noticeably reduced in RH

atmosphere compared to dry atmosphere. However, for the NFs annealed at 700 °C, the response to ethanol in RH atmosphere was shown to be rather higher than in dry atmosphere (response 1.6 in dry air) with a maximum response of 16.5 at 30% RH, suggesting that this sensor is effective to operate in RH conditions, however, its response is still lower than the $LaCoO_3$ NFs annealed at 650 °C based sensor up to 50% RH. Usually, the presence of humidity disturbs the quality of the response due to water vapour poisoning effect [63]. This is when the water molecules preoccupy the $LaCoO_3$ surface, resulting in less chemisorption of oxygen and ethanol molecules on the NFs surface. Furthermore, the water molecules will react and use-up the adsorbed surface oxygen depriving of the ethanol molecules of adequate electrons from the $LaCoO_3$ surface thus reducing the sensor response [50]. Figure 6.9 (b) shows the response-recovery curves of the $LaCoO_3$ NFs based sensor to 40 ppm ethanol under different RH levels. It can be seen that the response decrease with the increase in RH in the range of 30- 90%. Nonetheless, the $LaCoO_3$ NFs at 650 °C based sensor still maintained higher response until 50% RH in comparison to the other two sensors (see Figure 6.9(a)) suggesting that this sensor is effective until 50% RH. In addition, the humidity sensing capabilities of the $LaCoO_3$ NFs based sensors were investigated in the absence of ethanol gas. Figure 6.9(c) shows the response-recovery curves of the sensors in different humid conditions. The response was defined as the ratio of resistance in humid air (RH 30, 50, 70 and 90%) to that in dry air (Ra). The sensor response increased upon introduction of humid air and decreased by the introduction of dry air. The sensor based on $LaCoO_3$ NFs annealed at 700 °C revealed better sensing performance to humidity rather than ethanol suggesting its effectiveness as a humidity sensor.

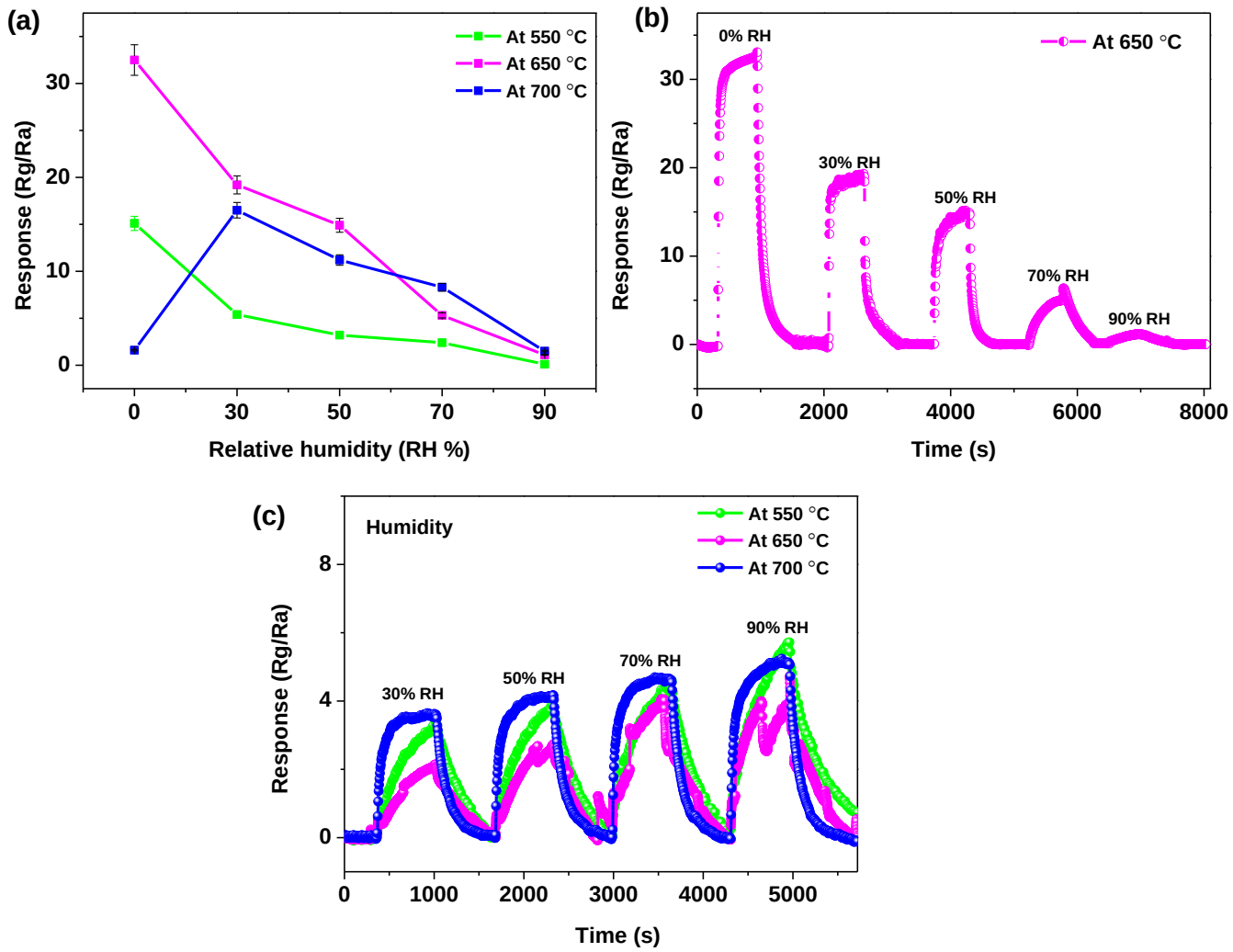

Figure 6.9: (a) The responses of all the $LaCoO_3$ NFs based sensors to 40 ppm ethanol under various RH, (b) the response-recovery curves of the NFs annealed at 650 °C to 40 ppm of ethanol under various RH and (c) responses of all the $LaCoO_3$ NFs based sensors to different humidity conditions without the ethanol.

Further, three different sensors based on the $LaCoO_3$ NFs annealed at 650 °C herein labelled as at 650 °C_ A, at 650 °C_ B and at 650 °C_ C, were prepared 6 months later after the initial recipe of the $LaCoO_3$ NFs annealed at 650 °C based sensor to determine the response reproducibility and the results are displayed in Figure 6.10(a). It was obvious that all three sensors displayed similar response behaviour to the initial $LaCoO_3$ NFs at 650 °C based sensor with minor response

differences. Moreover, the sensors still maintained the response-recovery reversibility characteristic as shown in the inset of Figure 6.10(a) which proves good performance of reproducibility for the $LaCoO_3$ NFs at 650 °C based sensors. Another important sensor characteristic is the long term stability which for the $LaCoO_3$ NFs at 650 °C based sensor was recorded for over 150 days and the results are shown in Figure 6.10(b). Although the resistance and response values were changing every 30 days, it was realised that the sensor maintained 67 and 64 % of its response and resistance towards ethanol on the 150th day (5th month), revealing good long-term stability of the $LaCoO_3$ NFs based sensor.

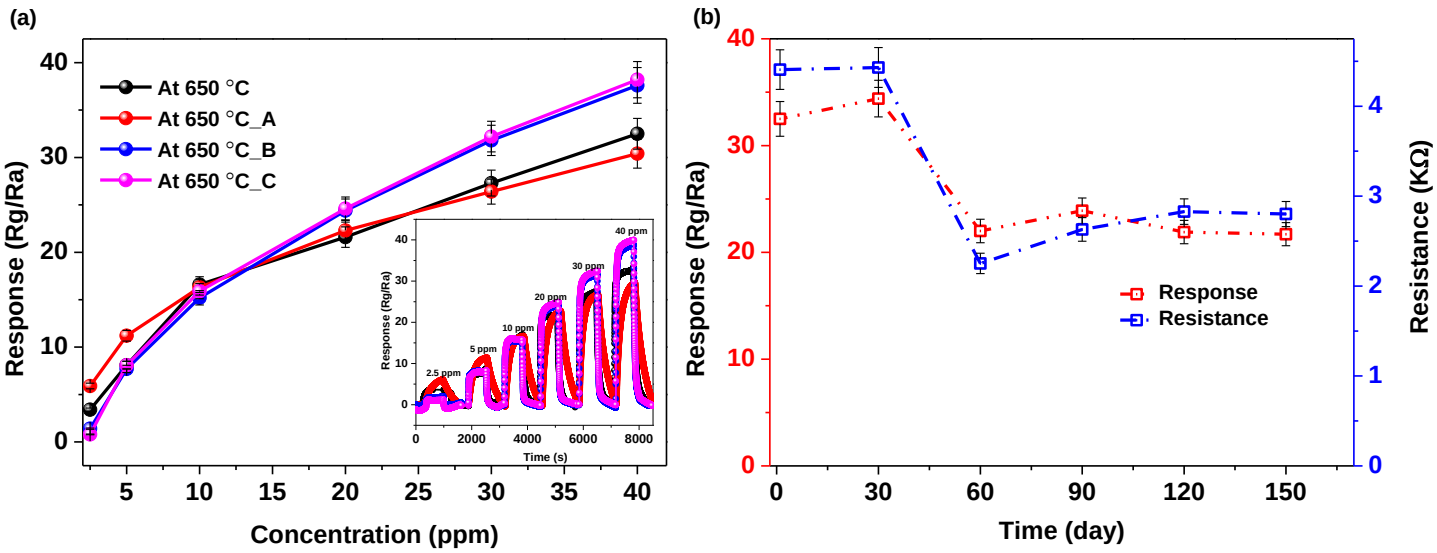

Figure 6.10: Responses to ethanol by three different $LaCoO_3$ NFs at 650 °C based sensors prepared 6 months later from the first recipe of preparation of the $LaCoO_3$ NFs at 650 °C based sensor and (b) response and resistance stability measurements of the $LaCoO_3$ at 650 °C based sensor for over 150 days.

It is of interest to scrutinize the potential contributors to the sensing behaviours of the $LaCoO_3$ NFs in terms of their morphology and phase crystallinity. In actual facts, the gas sensing properties are known to be significantly influenced by the morphology of the sensing material. While on the other hand, the particle morphology affects the specific surface area of the sensing materials. Higher specific surface area provides large active sites for adsorption and desorption of gas molecules. As a result, this may attract the large number of electrons from the bulk of the sensing material making the sensor having higher surface area more sensitive to the tested gases. In this case, BET specific surface area analyses displayed larger surface area for $LaCoO_3$ NFs annealed at 650 °C based sensor as compared to the rest of sensors and this explains the observed better sensing performance exhibited by this sensor upon exposure to ethanol. Further, larger surface area has been demonstrated to result in a larger density of oxygen vacancies which plays a major role in the gas sensing performance of metal oxides [64]. Gas sensing in metal oxide based sensors involves electronic or chemical interactions of the sensor surface with the target gas molecules. Also, oxygen vacancies are known to be crucial in regulating the electronic and chemical properties of metal oxides, therefore the concentration of the oxygen vacancies can be regarded as a contributing factor to the gas sensing performance as they offer more channels for target gas transportation resulting in sensor response increment [50]. Not only can oxygen vacancies regulate the electronic properties of metal oxide based sensors, but they also provide active sites for gas molecules adsorption [65].

In this study, analysis from XPS revealed a high content of oxygen vacancies for the better performing $LaCoO_3$ based sensor which is the one annealed at 650 °C. To verify this observation, a connection of the sensor responses on the oxygen

vacancies with annealing temperature of the $LaCoO_3$ NFs with the relative concentration of O_V/O_L from XPS was done and is shown in Figure 6.11. As observed from the figure, the response towards ethanol is the highest for the $LaCoO_3$ annealed at 650 °C with the high content of the oxygen vacancies, thus demonstrating the dependence of sensor response on the oxygen vacancies. Interestingly, not only does the sensor based on $LaCoO_3$ at 650 °C demonstrates the highest response to ethanol, but the operating temperature (120 °C) is also lower to that of the sensors based on the $LaCoO_3$ NFs at 550 and 700 °C which is at 140 °C, suggesting a strong chemical interaction between the ethanol and the adsorbed oxygen species on the sensor surface at 120 °C [66], which can also be attributed to the concentration of the oxygen vacancies which in this case.

Further, the interparticle connectivity NF morphology observed from SEM cannot be excluded as one of the contributing factors towards sensor response enhancement as it offers ease of contact to active sites as well as efficient and fast gas diffusion. Moreover, the overlapping of the hole accumulation layers along the NF direction produced a continuous hole transfer channels leading to high ethanol response.

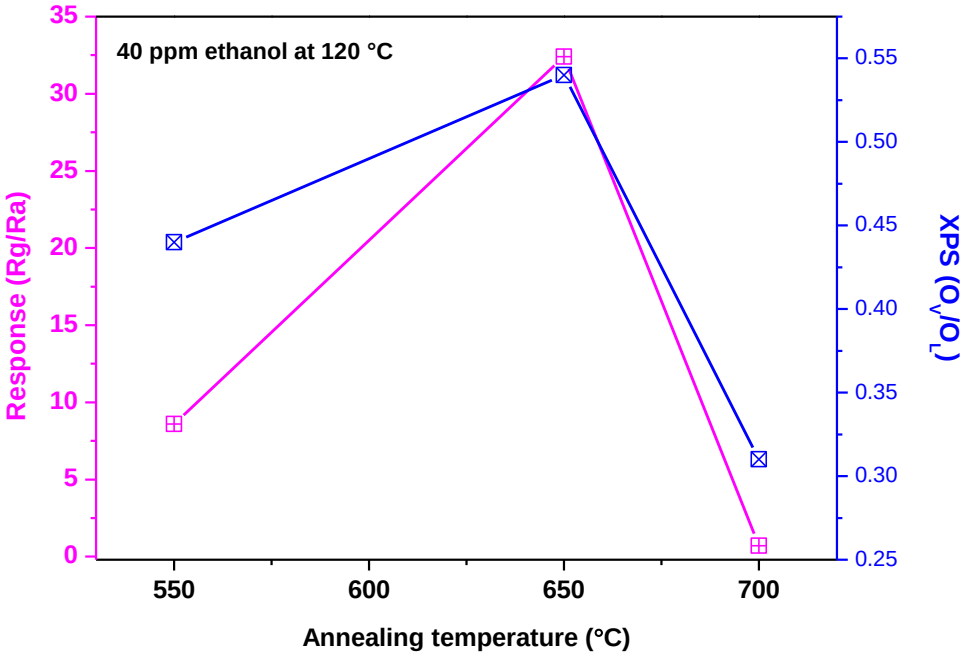

Figure 6.11: Responses of the $LaCoO_3$ NFs annealed at 550, 650 and 700 °C versus XPS (O_V/O_L).

On the other hand, for NFs, long lengths with good interparticle connectivity are proven to give improved sensing performance. For example, from the work Yoon *et al.* [67] did, they showed that sensor response to a given analyte gas decreases by an order of magnitude with decreasing interparticle connectivity. This result suggests that poor interparticle connectivity ascribed to shorter fiber length has an adverse effect on gas sensing performance of metal oxide sensors. Further, subjecting the NFs to higher annealing temperatures grows the nanograins despite growing of the nanograins, higher temperatures also improves the crystallinity as well as phase stability of the grains which can result in improvement of sensor response by altering the gas adsorption kinetics and the quantity of the adsorption sites [68, 69]. The observed enhanced response for NFs sensors annealed at 650 °C herein can therefore be associated with synergetic effects of the improved structure crystallinity, interparticle connected

porous NFs morphology, high surface area and large number of intrinsic defects which ensured phase stability, access to more active sites and ease of gas molecules diffusion.

6.7 Sensing mechanism of $LaCoO_3$ NFs to ethanol gas

The ability of the oxide surface to adsorb and react with a target gas depends mainly on the type of semiconductor, structure, morphology and surface state of the material [70]. $LaCoO_3$ is a p-type metal oxide which means that the density of hole charge carries is more than electrons. Based on the most accepted sensing mechanism for semiconductor metal oxide based sensors, while the sensor is in air, oxygen is adsorbed on the sensor material surface in a temperature range around 100 to 500 °C. The chemisorption of the oxygen thus results in the formation of molecular and atomic oxygen species by trapping electrons from the sensor material's surface. The type of the ionized oxygen species depends on the temperature. At temperature less than 150 °C the dominant species is the molecular O_2^-, while at higher temperatures the most dominant and reactive are the atomic O^- and O^{2-} [71, 72]. The $LaCoO_3$ NFs annealed at 650 °C based sensor revealed high response at operating temperature of 120 °C, O^- is the stable and abundant oxygen species [73-75]. Subsequently, the holes accumulate near the surface of $LaCoO_3$ NFs to form a hole accumulation layer (HAL) as shown on left part of Figure 6.12. The formed hole accumulation layer may overlap with each other along the NFs direction thus producing a continuous hole transfer channels. In the meantime, the resistance *(Ra)* of the sensor is getting reduced. When $LaCoO_3$ NFs are exposed to ethanol as shown from the right part of Figure 6.12, ethanol gas molecules gets oxidized by the oxygen species into CO_2 and H_2O

and at the same time electrons are released back into the $LaCoO_3$ as per reactions (6.4 and 6.5) and decrease the concentration of holes therefore increasing the sensor resistance as per reaction 6 [15, 76]

$$C_2H_5OH + O^- \rightarrow CH_3CHO + H_2O + e^- \quad (6.4)$$

$$CH_3CHO + 5O^- \rightarrow 2CO_2 + 2H_2O + 5e^- \quad (6.5)$$

$$h^+ + e^- = null \quad (6.6)$$

The interactions between ethanol molecules and metal oxide surfaces are rather complicated and the sensor response relies on the nature and density of the surface active sites. Previous studies have demonstrated that the ethanol molecules can decompose to CO_2 and H_2O by following pathways namely dehydration and oxidative dehydrogenation [15, 77, 78]. During dehydration process, ethanol dehydrates into C_2H_4 in the presence of acid surface groups as demonstrated in reaction 6.7; and the second reaction involves ethanol dehydrogenation into CH_3CHO through the help of basic surface groups as shown in reaction 6.8. Then C_2H_4, CH_3CHO, and H_2 will react with chemisorbed oxygen ion species and convert into CO_2 and H_2O.

$$C_2H_5OH \rightarrow C_2H_4 + H_2O \quad (6.7)$$

$$C_2H_5OH \rightarrow CH_3CO + H_2 \quad (6.8)$$

Based on the reactions 6.7 and 6.8, SMOs with acidic, amphoteric and basic surfaces have different interactions with ethanol thus will exhibit different sensing behaviours [79]. The surface of $LaCoO_3$ is basic due to the presence of the basic La, therefore reaction 8 is more favourable than reaction 6.7 under the same conditions [15, 78]. All the $LaCoO_3$ NFs based sensors presented in this study show high response to ethanol in comparison to other gases under the same conditions. This observed characteristic can be explained based on the

values of the LUMO energy of gases which can be used as an indication on the easiness of breaking down the specific gas and for the gas to participate in a sensing reaction with the sensor material [80]. The very low LUMO energy value of ethanol may account for the selective detection of ethanol in this current study.

Owing to the increased surface area, high concentration of oxygen vacancies and better particle interconnectivity, the $LaCoO_3$ NFs annealed at 650 °C based sensor showed an improved ethanol sensing response than the $LaCoO_3$ NFs annealed at 550 and 700 °C based sensors.

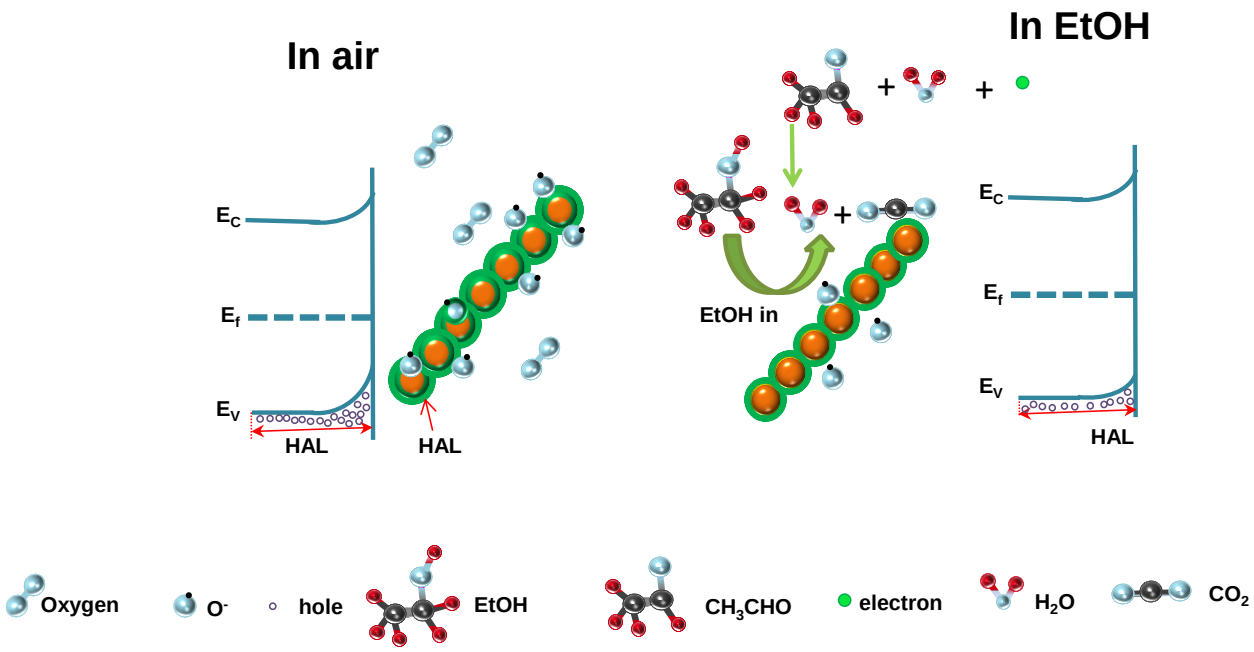

Figure 6.12: Proposed ethanol sensing mechanism of the $LaCoO_3$ NFs.

The obtained results were compared with previous similar studies which demonstrated that several metal oxides with different structures are able to detect ethanol at concentrations of a few parts per million with different sensing performances [60, 81-86]. Table 6.3 lists the ethanol sensing properties of some

1D metal oxide NFs reported previously in the literature in comparison to the results reported in this work. The $LaCoO_3$ NFs obtained at 650 °C exhibit much lower operating temperature; high response, good selectivity and low detection limit towards ethanol as compared with the previously reported ethanol sensors. Moreover, the high response obtained for $LaCoO_3$ NFs based sensors in this work is at very low concentrations (40 ppm) as compared to other ethanol sensors revealing high responses at high ethanol concentrations. Therefore, the sensor based on the porous $LaCoO_3$ NFs in this work is a promising candidate for selective monitoring of ethanol leakages in many fields including industrial and food production

Table 6.3: Comparison of the ethanol sensing performance between the current work and previously reported results from literature.

Material	Conc.(ppm)	Response	T (°C)	$\tau_{res}/\tau_{rec.}$ (s)	Refs.
$ZnSnO_4$	200	32.5	130	115/1597	[52]
SnO_2-ZnO	100	78	300	25/9	[70]
MoO_3	200	53	275	45/138	[71]
Nb_2O_5-TiO_2	500	21.64	250	-	[53]
α-Fe_2O_3/SnO_2	100	22.46	300	-/20	[34]
$LaFeO_3$	200	28.4	200	11/19	[72]
$La_{0.75}Ba_{0.25}FeO_3$	500	136.1	210	42/40	[73]
$LaCoO_3$	40	32.4	120	26/66	this work

6.8 Conclusion

In summary; 1D $LaCoO_3$ NFs have been produced by a simple and cost effective electrospinning method. Their morphology and microstructure were controlled through variation of annealing temperature. In this process; crystallinity and morphology of the NFs significantly evolved upon post annealing. SEM and TEM

observations revealed long continuous NFs made up of tiny interconnected particles at an annealing temperature of 550 °C. However, with the increase in annealing temperature the NFs showed growth and decoupling of the interconnected particles. The XRD pattern revealed transformation from cubic to a more stable rhombohedral phase of the $LaCoO_3$ NFs which was maintained until the highest temperature with the $LaCoO_3$ annealed at 650 °C displaying high crystallinity. Compared to the other $LaCoO_3$ NFs; gas sensing properties of the $LaCoO_3$ NFs annealed at 650 °C revealed best response and good selectivity to ethanol at a low operating temperature of 120 °C. This property demonstrates that the $LaCoO_3$ annealed at 650 °C based sensor is very promising for fabricating sensors with low power consumption. The good ethanol sensing performance could be due to synergetic effects of enhanced surface area and good interconnected porous NF morphology, providing access to active sites for gas interactions. Due to the strong sensor response, fast response and recovery speed and good selectivity to ethanol, the $LaCoO_3$ annealed at 650 °C sensor is a promising candidate for practical application at industry level.

6.9 References

[1] A. Mirzaei, S. Leonardi, G. Neri, Ceram. Int., 42(2016) 15119-41.

[2] S. Nair, K. Cope, R.H. Terence, A.M. Diehl, Am. J. Gastroenterol., 96(2001) 1200-4.

[3] M. Zachut, F. Shapiro, N. Silanikove, Food Chem., 201(2016) 270-4.

[4] G. Wen, Z. Li, M.M. Choi, J. Food Eng., 118(2013) 56-61.

[5] X.-J. Huang, Y.-K. Choi, Sens. Actuators B Chem., 122(2007) 659-71.

[6] L. Zhu, W. Zeng, Sens. Actuators A Phys., 267(2017) 242-61.

[7] G.H. Mhlongo, D.E. Motaung, I. Kortidis, N.R. Mathe, O.M. Ntwaeaborwa, H.C. Swart, B.W. Mwakikunga, S.S. Ray, G. Kiriakidis, Mater. Chem. Phys., 162(2015) 628-39.

[8] K. Shingange, H.C. Swart, G.H. Mhlongo, Physica B., 535(2018) 216-20.

[9] K. Shingange, Z.P. Tshabalala, B.P. Dhonge, O.M. Ntwaeaborwa, D.E. Motaung, G.H. Mhlongo, Mater. Res. Bull., 85(2017) 52-63.

[10] K. Shingange, Z.P. Tshabalala, O.M. Ntwaeaborwa, D.E. Motaung, G.H. Mhlongo, J. Colloid Interface Sci., 479(2016) 127-38.

[11] Q. Abdullah, F. Yam, J. Hassan, C. Chin, Z. Hassan, M. Bououdina, Int. J. Hydrog. Energy, 38(2013) 14085-101.

[12] Q. Abdullah, F. Yam, Z. Hassan, M. Bououdina, Sens. Actuators B Chem., 204(2014) 497-506.

[13] Q. Abdullah, F. Yam, Z. Hassan, M. Bououdina, J. Colloid Interface Sci., 460(2015) 135-45.

[14] Q. Abdullah, A. Ahmed, A. Ali, F. Yam, Z. Hassan, M. Bououdina, M.A Almessiere, Superlatice Microst., 117(2018) 92-104.

[15] Z. Dai, C.-S. Lee, B.-Y. Kim, C.-H. Kwak, J.-W. Yoon, H.-M. Jeong, J.-H Lee., ACS Appl. Mater. Interfaces, 6(2014) 16217-16226.

[16] M.C. McAlpine, H. Ahmad, D. Wang, J.R. Heath, Nat. Mater, 6(2007) 379.

[17] B. Ding, M. Wang, J. Yu, G. Sun, Sensors, 9(2009) 1609-24.

[18] J.Y. Park, S.W. Choi, J.W. Lee, C. Lee, S.S. Kim, Am Ceram Soc., 92(2009) 2551-4.

[19] J. Moon, J.-A. Park, S.-J. Lee, T. Zyung, I.-D. Kim, Sens. Actuators B Chem., 149(2010) 301-5.

[20] Y. Zhang, X. He, J. Li, Z. Miao, F. Huang, Sens. Actuators B Chem., 132(2008) 67-73.

[21] S. Piperno, M. Passacantando, S. Santucci, L. Lozzi, S. La Rosa, J. Appl. Phys., 101(2007) 124504.

[22] Y. Zou, S. Chen, J. Sun, J. Liu, Y. Che, X. Liu, J. Zhang, D. Yang., ACS Sens., 2(2017) 897-902.

[23] K. Shingange, H.C. Swart, G.H. Mhlongo, J. Alloys. Compd., 797(2019) 284-301.

[24] C. Aydin, J. Alloys. Compd., 777(2019) 145-51.

[25] S.-H. Choi, I.-S. Hwang, J.-H. Lee, S.-G. Oh, I.-D. Kim, Chem. Commun., 47(2011) 9315-7.

[26] A. Katoch, G.-J. Sun, S.-W. Choi, J.-H. Byun, S.S. Kim, Sens. Actuators B Chem., 185(2013) 411-6.

[27] A. Khalil, J.J. Kim, H.L. Tuller, G.C. Rutledge, R. Hashaikeh, Sens. Actuators B Chem., 227(2016) 54-64.

[28] M. Hübner, C. Simion, A. Tomescu-Stănoiu, S. Pokhrel, N. Bârsan, U. Weimar, Sens. Actuators B Chem., 153(2011) 347-53.

[29] W. Haron, A. Wisitsoraat, S. Wongnawa, Ceram. Int., 43(2017) 5032-40.

[30] M. Siemons, A. Leifert, U. Simon, Adv Funct Mater., 17(2007) 2189-97.

[31] H. Zhu, P. Zhang, S. Dai, ACS Catal., 5(2015) 6370-85.

[32] E.L. Brosha, R. Mukundan, D.R. Brown, F.H. Garzon, J. Visser, M. Zanini, Z. Zhou, E.M. Logothetis., Sens. Actuators B Chem., 69(2000) 171-82.

[33] J.-C. Ding, H.-Y. Li, Z.-X. Cai, X.-D. Zhang, X. Guo, RSC Adv., 5(2015) 65668-73.

[34] M. Ghasdi, H. Alamdari, Sens. Actuators B Chem., 148(2010) 478-85.

[35] J.-C. Ding, H.-Y. Li, X. Guo, Solid State Ion., 272(2015) 155-9.

[36] L. Gildo-Ortiz, H. Guillén-Bonilla, V.M. Rodríguez-Betancourtt, O. Blanco-Alonso, A. Guillén-Bonilla, J. Santoyo-Salazar, I.C. Romero-Ibarra, J. Reyes-Gómez., Ceram. Int., 44(2018) 15402-10.

[37] H. Liu, Y. Guo, R. Xie, T. Peng, G. Ma, Y. Tang, Sens. Actuators B Chem., 246(2017) 164-8.

[38] H. Liu, H. Sun, R. Xie, X. Zhang, K. Zheng, T. Peng, X. Wu, Y. Zhang., Appl. Surf. Sci., 442(2018) 742-749.

[39] J. Shi, R. Yan, Y. Zhu, X. Zhang, Talanta, 61(2003) 157-64.

[40] S. Yan, J. Xue, Q. Wu, Sens. Actuators B Chem., 275(2018) 322-31.

[41] T. Samerjai, N. Tamaekong, K. Wetchakun, V. Kruefu, C. Liewhiran, C. Siriwong, A. Wisitsoraat, S. Phanichphat., Sens. Actuators B Chem., 171-172(2012) 43-61.

[42] C. Wang, X. Cui, J. Liu, X. Zhou, X. Cheng, P. Sun, X. Hu, X. Li, J. Zheng, G. Lu., ACS Sens., 1(2016) 131-6.

[43] S. Farhadi, S. Sepahvand, J. Alloys. Compd., 489(2010) 586-91.

[44] M. Yazdanbakhsh, H. Tavakkoli, S.M. Hosseini, S. Afr. J. Chem., 64(2011) 71-8.

[45] G. Liu, X. Li, Y. Wang, W. Liang, B. Liu, H. Feng, H. Yang, J. Zhang, J. Sun., Appl. Surf. Sci., 425(2017) 121-9.

[46] A. Machocki, T. Ioannides, B. Stasinska, W. Gac, G. Avgouropoulos, D. Delimaris, W. Grzegorczyk. S. Pasieczna., J. Catal., 227(2004) 282-96.

[47] L. Predoana, B. Malic, D. Crisan, N. Dragan, M. Anastasescu, J. Calderon-Moreno, R. Scurtu, M. Zaharescu, Ceram. Int., 38(2012) 5433-43.

[48] J.-C. Ding, H.-Y. Li, Z.-X. Cai, X.-X. Wang, X. Guo, Sens. Actuators B Chem., 222(2016) 517-24.

[49] K. Zhao, L. Li, A. Zheng, Z. Huang, F. He, Y. Shen, G. Wei, H. Li, Z. Zhao, Appl Energy., 197(2017) 393-404.

[50] G. Mhlongo, D. Motaung, F. Cummings, H. Swart, S. Ray, Sci. Rep., 9(2019) 9881.

[51] S. Oh, K. Kim, Chem. Commun., (1999) 2177-8.

[52] S. Thirumalairajan, K. Girija, N.Y. Hebalkar, D. Mangalaraj, C. Viswanathan, N. Ponpandian, RSC Adv., 3(2013) 7549-61.

[53] N. Zhang, S. Ruan, Y. Yin, F. Li, S. Wen, Y. Chen, ACS Appl. Nano Mater., 1(2018) 4671-81.

[54] X. Li, X. Zhou, H. Guo, C. Wang, J. Liu, P. Sun, F. Liu, G. Lu, ACS Appl. Mater. Interfaces, 6(2014) 18661-7.

[55] C.J. García-Orellana, M. Macías-Macías, H.M. González-Velasco, A. García-Manso, R. Gallardo-Caballero, Sensors., 19(2019) 3183.

[56] F.E.I.F.C.G.S.A.o.h.w.f.s. com/feature/combustible-gas-sensors.html.

[57] V. Schroeder, S. Savagatrup, M. He, S. Lin, T.M. Swager, Chem. Rev., 119(2018) 599-663.

[58] M. Tonezzer, T.T.L. Dang, N. Bazzanella, V.H. Nguyen, S. Iannotta, Sens. Actuators B Chem., 220(2015) 1152-60.

[59] S. Zhao, Y. Shen, P. Zhou, J. Zhang, W. Zhang, X. Chen, D. Wei, P. Fang.Y. Shen, Ceram. Int., 44(2018) 753-9.

[60] C. Balamurugan, A. Maheswari, D.-W. Lee, Sens. Actuators B Chem., 205(2014) 289-97.

[61] X. Xin, J. Zhang, C. Chen, G. Li, J. Qin, Z. Yang, H. Lu, J. Gao.C. Wang. Z. He, J. Alloys. Compd., 780(2019) 228-36.

[62] G. Li, X. Zhang, H. Lu, C. Yan, K. Chen, H. Lu, J. Gao,Z. Yang, G. Zhu, C. Wang, Z. He, Sens. Actuators B Chem., 283(2019) 602-12.

[63] N.-H. Kim, S.-J. Choi, S.-J. Kim, H.-J. Cho, J.-S. Jang, W.-T. Koo, M. Kim, I.-D. Kim, Sens. Actuators B Chem., 224(2016) 185-92.

[64] M. Epifani, J.D. Prades, E. Comini, E. Pellicer, M. Avella, P. Siciliano, G. Faglia, A. Cirera, R. Scotti, F. Morazzoni, J. R. Morante, J. Phys. Chem. C, 112(2008) 19540-6.

[65] K. Shingange, H.C. Swart, G.H. Mhlongo, Physica B., 578 (2019) 411883.

[66] K. Shingange, H.C Swart, G.H. Mhlongo, ACS Omega, 4(2019). 19018-19029

[67] J.-W. Yoon, H.-J. Kim, H.-M. Jeong, J.-H. Lee, Sens. Actuators B Chem., 202(2014) 263-71.

[68] S.-W. Choi, J.Y. Park, S.S. Kim, Chem. Eng., 172(2011) 550-6.

[69] Z.M. Seeley, A. Bandyopadhyay, S. Bose, Mater. Sci. Eng., B, 164(2009) 38-43.

[70] R. Zhang, T. Zhou, L. Wang, T. Zhang, ACS Appl. Mater. Interfaces, 10(2018) 9765-73.

[71] L. Gildo-Ortiz, H. Guillén-Bonilla, V. Rodríguez-Betancourtt, O. Blanco-Alonso, A. Guillén-Bonilla, J. Santoyo-Salazar, I.C. Romero-Ibarraf, J. Reyes-Gómezg, Ceram. Int., 44(2018) 15402-10.

[72] S.C. Chang, J. Vac. Sci. Technol, 17(1980) 366-9.

[73] K. Wetchakun, T. Samerjai, N. Tamaekong, C. Liewhiran, C. Siriwong, V. Kruefu, A. Wisitsoraatb, A. Tuantranontb, S. Phanichphantac, Sens. Actuators B Chem., 160(2011) 580-91.

[74] A.T. Mane, S.B. Kulkarni, S.T. Navale, A.A. Ghanwat, N.M. Shinde, J. Kim, V.B. Patil, Ceram. Int., 40(2014) 16495-502.

[75] K. Zheng, L. Gu, D. Sun, X. Mo, G. Chen, Mater. Sci. Eng., B, 166(2010) 104-7.

[76] A. Ghosh, A. Maity, R. Banerjee, S.B. Majumder, J. Alloys. Compd., 692(2017) 108-18.

[77] V.V. Kovalenko, A.A. Zhukova, M.N. Rumyantseva, A.M. Gaskov, V.V Yushchenko, I.I Ivanova, T. Pagnierb, Sens. Actuators B Chem., 126(2007) 52-5.

[78] T. Jinkawa, G. Sakai, J. Tamaki, N. Miura, N. Yamazoe, J. Mol. Catal. Chem, 155(2000) 193-200.

[79] N. Hosseinpour, A.A. Khodadadi, A. Bahramian, Y. Mortazavi, Langmuir, 29(2013) 14135-46.

[80] Z. Wen, L. Tian-Mo, Physica B., 405(2010) 1345-8.

[81] A. Mirzaei, K. Janghorban, B. Hashemi, A. Bonavita, M. Bonyani, S.G. Leonardi, G. Neri**,** Nanomaterials, 5(2015) 737-49.

[82] L. Mei, J. Deng, X. Yin, M. Zhang, Q. Li, E. Zhang, Z. Xu, L. Chen, T. Wang, Sens. Actuators B Chem., 166(2012) 7-11.

[83] Z. Li, X. Liu, W. Zhao, S. Wang, W. Zhou, L. Wei, M. Yu, Anal. Chem., 86(2014) 2521-5.

[84] M. Suman, M. Freddi, C. Massera, F. Ugozzoli, E. Dalcanale, J. Am. Chem. Soc., 125(2003) 12068-9.

[85] M. Melegari, M. Suman, L. Pirondini, D. Moiani, C. Massera, F. Ugozzoli, E. Kalenius, P. Vainiotalo, J.-C. Mulatier, J.-P. Dutasta, E. Dalcanale, Chem. Eur. J., 14(2008) 5772-9.

[86] R. Pinalli, E. Dalcanale, Acc. Chem. Res., 46(2012) 399-411.

[87] S. Yan, S. Ma, W. Li, X. Xu, L. Cheng, H. Song, X.Y. Liang, Sens. Actuators B Chem., 221(2015) 88-95.

[88] B. Mandal, M. Das, M.T. Htay, S. Mukherjee, Mater. Res. Bull., 109(2019) 281-90.

[89] H.-T. Fan, X.-J. Xu, X.-K. Ma, T. Zhang, PNanotechnology., 22(2011) 115502.

[90] J. Xiang, X. Chen, X. Zhang, L. Gong, Y. Zhang, K. Zhang, Mater. Chem. Phys., 213(2018) 122-9.

Chapter 7

Ultrafast detection of low acetone concentration displayed by Au loaded $LaFeO_3$ nanobelts owing to synergetic effects of porous 1d morphology and catalytic activity of Au nanoparticles

7.1 Introduction

In a quest to better living conditions through industrialization, comes the disadvantage of increase in air pollution by different types of toxic chemical compounds in air which can be harmful to human health. Acetone (C_3H_6O) is one of the potential volatile organic compounds (VOCs) with an aromatic smell used in medicine, coatings and pesticides [1-3]. However; long exposure to certain concentrations of acetone may cause human health impact such as eye, nose, and central nervous system damage [4, 5]. Nonetheless; acetone has been classified as a useful component used as a breath biomarker for non-invasive diagnosis of type-1 diabetes [6]. It is reported that the average acetone concentration level for healthy human breath is 0.9 ppm, whereas for a diabetic patient it's more than 1.8 ppm [7]. Therefore, it is essential to fabricate a sensor exhibiting high sensitivity, quick response/ recovery time and good stability at low concentrations of acetone.

Semiconductor metal oxides (SMO) have been regarded as a promising group of sensing materials because of their ease in fabrication, low cost, and sensitivity to a variety of reducing and oxidizing gases [8-13]. This group of sensing materials can be synthesized in variety of dimensions ranging from 0 to 3 dimensions (0D-3D) with all different dimensions revealing different sensing properties [14-16].

Of all the different dimensions of SMO, 1D nanostructures such as nanorods [17], nanotubes [18], nanofibers [19] and nanobelts [20, 21] have been proven to give better gas sensing performance since they possess large surface area and strong adsorption/desorption ratio of the analyte gas molecules [22-25]. As one of the structures categorized under 1D family; nanobelts (NBs) are of particular interest as they display high surface area with interparticle contact, which are key parameters to facilitate the adsorption/desorption of gas molecules thus contributing towards sensor performance enhancement [26].

SMO with n-type conductivity are mostly utilized as compared to the p-type counterparts since Hubner *et al* [27] validated that the gas response obtained for a p-type material is a square root of the response of a n-type material having the same morphology. Nonetheless, p-type SMO have distinctive catalytic activity with different VOCs [28, 29], thus making them potential candidates for the fabrication of innovative functionality in high performance gas sensor devices. However, to successfully attain such, it is of paramount importance to improve the gas response characteristics of these p-type SMO to satisfy the demand for practical application such as high sensitivity, selectivity, and fast response/recovery speed at low working temperatures to low concentration levels of analyte gas. For this reason, a number of strategies ranging from construction of heterojunction composites [30, 31], control and variation of morphology [32, 33], UV light stimulation [34, 35] and noble metal functionalization [36, 37] have been adopted to overcome these hurdles. The afore mentioned alterations can expose more surface area thus increasing more

active sites and effectively promote electron transfer, therefore resulting in improved gas sensing performance [38].

Incorporation of noble metals such as Ag, Au and Pd has been proven to be more effective since noble metals bring about chemical catalytic effect, whereby the noble metal acts as direct active sites for the adsorption of analyte gas and assisting in the chemical reactions between the analyte gas and the sensing material [1, 18, 39-43]. Additionally, the noble metals can also fast track the transfer of electrons to the surfaces of the sensing material [38, 44]. These effects in gas sensing has been proven in many research works; for instance, Jin *et al* [45] produced SnO_2 nanobelts functionalized with Au, which revealed decreased response and recovery times with higher response towards ethanol as compared to bare SnO_2. In another work by Majhi *et al* [46] it was found that Au@NiO core-shell nanoparticles revealed higher response than the pristine NiO nanoparticles to 100 ppm of ethanol at 200 °C.

Of all the p-type SMO that can be used in gas sensing applications, $LaFeO_3$ has been identified as a promising gas sensor material due to its interesting properties such high electrical conductivity and catalytic activity for surface-driven redox reactions [47-51]. Moreover, its perovskite multi-metal structure allows manipulation of its properties due to overlap between filled O^{2-} p-orbitals and the unfilled orbitals of the metal cations in relation to their mono-metal counterparts [52]. As much as $LaFeO_3$ is a well-known p-type SMO, only a few studies have been reported on the effects of noble metal catalysts (i.e. Ag) loading on its sensing abilities [53, 54]. Moreover, reports on using Au as a catalyst for $LaFeO_3$ sensing are very scarce, especially for acetone sensing.

Therefore, more investigations are needed to elucidate the Au loading effects since Au is commended as a very good catalyst that can induce chemical sensitization thus resulting in enhanced gas sensing characteristics [37, 44, 55, 56].

In this context, this work focuses on the fabrication of Au loaded $LaFeO_3$ NBs at different Au loading levels to investigate the effects that Au brings about on the gas sensing performance of the $LaFeO_3$ NBs. Coupling the 1D NB morphology of $LaFeO_3$ with the catalytic activity of Au; the structural, morphological and most crucial; the gas sensing performance will be thoroughly studied to establish the influence of Au loading. Possible gas sensing mechanism will also be discussed to demonstrate the interaction taking place between the analyte gas and the sensor material surface.

7.2 Experimental section

7.2.1 Materials used

Lanthanum nitrate hexahydrate ($La(NO_3)_3.6H_2O$), ferric nitrate nonahydrate ($Fe(NO_3)_3.9H_2O$), gold (III) chloride solution ($HAuCl_4$) and polyvinylpyrrolidone (PVP) were used as the starting materials without further purification. The solvents used were N-N Dimethyleformamide (DMF) and Ethanol.

7.2.2 Preparation of the electrospinning precursor solutions

Three solutions with different Au concentrations were prepared and the procedure was as follows: 0.493 g of $Fe(NO_3)_3.9H_2O$) and 0.521 g of $La(NO_3)_3.6H_2O$ were dissolved in a mixed solution consisting of 7 ml of DMF and 3 ml of ethanol followed by stirring until completely dissolved. Appropriate

amounts of HAuCl solution required to prepare 0.1, 0.3 and 0.5 wt% Au loaded $LaFeO_3$ were then added into the mixture. Then 1.5 g of PVP was added into the solution and continuously stirred for homogeneous gel precursor solution ready for electrospinning. For comparison purposes; the pure $LaFeO_3$ solution was prepared following the same procedure without the addition of the HAuCl solution.

7.2.3 Fabrication of the pure and Au loaded $LaFeO_3$ NBs

For the electrospinning process; each of the prepared precursor solutions were transferred into a 10 mL glass syringe, with an inner diameter of 0.6 mm. A voltage of 20 kV was applied between the spinneret and the rotating drum collector with a spacing distance of 10 cm. The solution was continuously pumped by a syringe pump at a rate of 0.8 μlh^{-1}. The obtained NB composites were annealed at 550 °C for 2h in air to obtain the Au loaded $LaFeO_3$ NBs at a heating rate of 2 °C min^{-1}. For convenience; the unloaded sample was named S1 and Au loaded $LaFeO_3$ were named S2, S3 and S4 for Au concentrations of 0.1, 0.3 and 0.5 wt%, respectively.

7.3 Characterization of the pure and Au loaded $LaFeO_3$ NBs

The phase purity and crystallinity characteristics of S1-S4 were measured through X-ray diffraction (XRD) using a computer controlled Panalytical X'pert PRO PW3040/60 X-ray diffractometer with a Cu-Kα (λ=1.5405 Å) radiation. The morphology and elemental distribution analyses were performed using a ZEIS-AURIGA field-emission scanning electron microscopy (SEM) and JEOL TEM-2100 transmission electron microscopy (TEM) equipped with electron dispersive X-ray Spectroscopy (EDS). X-ray photoelectron (XPS) patterns were performed on

PHI 5000 Versaprobe XPS equipped with monochromatic Al-Kα radiation ($h\nu$ = 1486.6 eV). The specific surface areas and pore volumes of the samples were examined using a Micromeritics TRISTAR 3000 surface area analyser.

7.4 Fabrication and measurement of gas sensors based on pure and Au loaded $LaFeO_3$ NBs

The sensors based on S1, S2, S3 and S4 were prepared as follows: 40 mg of each sample was mixed with a solution of ethyl cellulose (a temporary binder) in turpineol and ground for a few minutes to make thixotropic pastes. The pastes were then coated onto an alumina substrate equipped with a pair of platinum (Pt) electrodes on the top surface and a heater at the bottom surface to control the operating temperature. The sensors were then heated at 300 °C for 2 h at a heating rate of 3 °C/min to achieve good adhesion. The gas sensing performance was evaluated using a KSGAS6S gas sensing station (KENOSISTEC, Italy). The atmospheric condition was controlled by means of MKS Instruments Deutschland GmbH mass flow controllers supplying desired concentrations of NH_3, C_3H_6O, NO_2, CO and CH_4 into the sensing chamber by diluting the concentrated analyte gas in synthetic air. The operating temperature of the sensors was controlled by adjusting the heating voltage while using a thermocouple to measure the output temperature to correspond to temperatures of room temperature (RT) to 180 °C. The changes in electrical resistance during the interaction of the analyte gas molecules and the surface of the $LaFeO_3$ NBs based sensors was measured in air *(Ra)* and in the presence of the analyte gas *(Rg)* by means of a Keithley 6487 Picoammeter/voltage source meter. Since the NBs were annealed at 550 °C; the gas sensing measurements were below 200 °C, so no thermally induced changes were expected on the

sensing material. It is also important to mention that S1, S2, S3 and S4 are all p-type material whose resistance increase in a reducing gas containing air and the sensor response can be determined as (Rg/Ra) [50]. The time taken by the sensor to reach 90% of the highest change in resistance after exposure to the analyte gas was measured as a response time while the time taken by the sensor to reach 90% of its original resistance was measured as the recovery time.

7.5 Results and discussion

7.5.1 Phase and Morphology analysis

The phase purity and crystallinity of the obtained samples were determined using XRD and the resulting diffraction patterns are shown in Figure 7.1. The X-ray diffraction patterns for S1 could be indexed to $LaFeO_3$ perovskite phase with orthorhombic structure (JCPDS card no. 75-0541). Upon Au loading onto $LaFeO_3$ surface, a slight shift in diffraction peak positions of S2, S3, and S4 as compared to S1 was observed. Additional diffraction peaks located at 38.1, 44.3, 64.5 and 77.5 ° corresponding to (111), (200), (220) and (311) planes indexed to cubic phase of Au (JCPDS Card no. 04-0748) were also noted. Further, the decline in peak intensity upon Au incorporation, suggests poor crystallinity of $LaFeO_3$ caused by the addition of Au. Moreover, peak broadening was observed with Au incorporation, indicating a decrease in crystallite size due to the addition of the Au. Therefore the mean crystallite sizes of the S1, S2, S3 and S4 estimated from Scherrer equation [55] using the (110) plane were found to be 20.7, 14.2, 15.3 and 25.6 nm, respectively. Based on these findings, it can be realised that the introduction of Au onto $LaFeO_3$ has an influence on the structural properties of $LaFeO_3$.

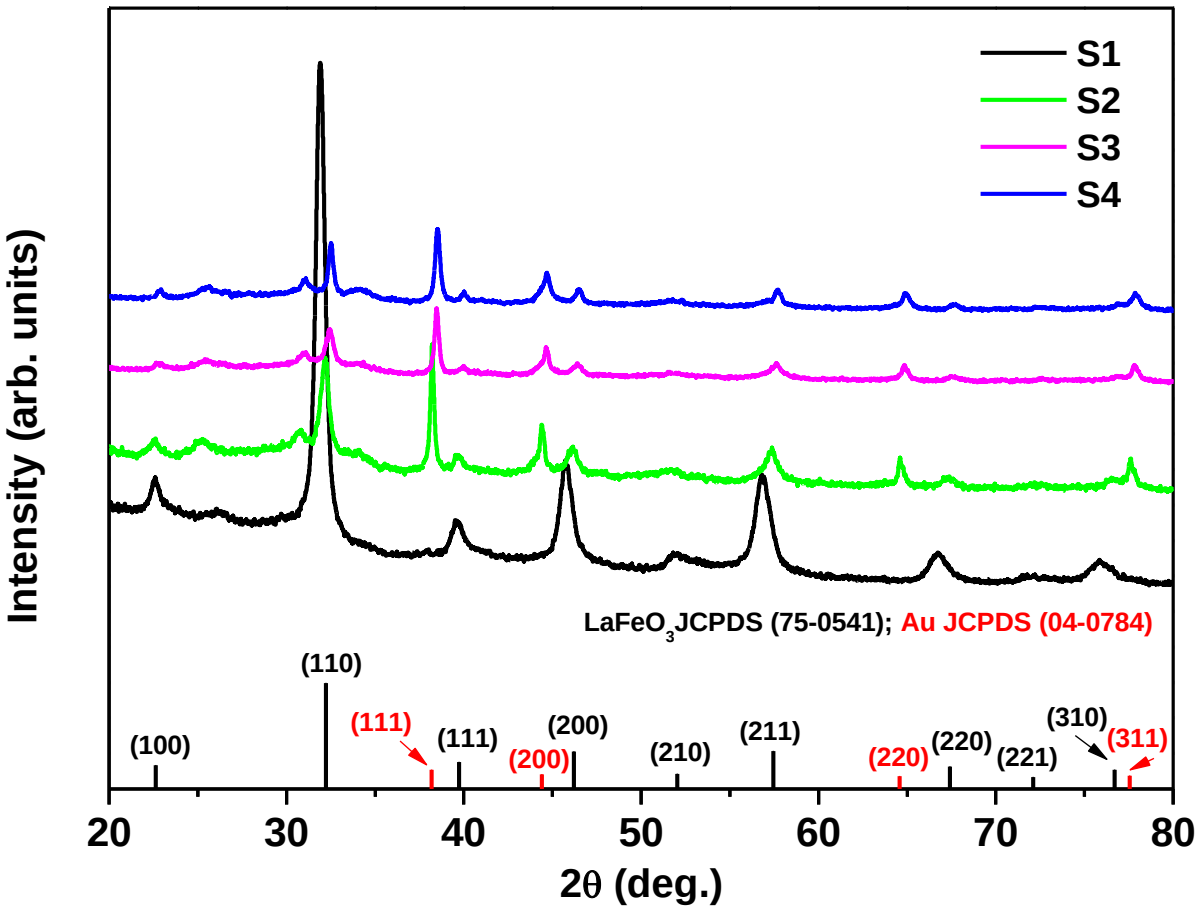

Figure 7.1: Diffraction patterns of S1, S2, S3 and S4 respectively.

Further, the morphological analysis of S1 to S4 was conducted through the use of SEM and the resulting micrographs of S1 to S4 are shown in Figure 7.2. Figure 2(a) presents the NBs before annealing, which revealed long nanobelts to a few microns in length and around 3.2 μm in diameter. It was also noticed that the surface of the NBs was smooth and this is due to the presence of PVP which acts as a template thus assist in maintaining the NB morphology [57]. It is worth mentioning that all as-spun NBs preserved this NB morphology regardless of Au loading level. Thus only one image was used to represent the as-spun products. After annealing; all obtained products (S1-S4) preserved the belt-like

morphology, however their average diameter was reduced to a range of 300 nm due to PVP decomposition during thermal annealing. Moreover, it was realized that the belts became very brittle as some of them were found to break since they contain a thinner section and also due to internal stress caused by the belt-structure shrinkage [58, 59].

Confirmation of the morphology was further done by HRTEM and the obtained images are presented in Figure 7.3. As observed in Figure 7.3(a) the HRTEM micrograph for S1 revealed a belt-like structure composed of several single nanoparticles with an average grain size of ~20 nm which were joined to each other to form a belt structure. As for S2, S3 and S4; a similar morphology to that of S1 was observed, except there were some very small particles belonging to Au distributed on the surface of each belt. The Au particle size distribution was estimated by measuring the diameter of the Au particles and the plots are presented as insets of each TEM image per Au loading concentration. It was realised that the Au particle size grew from 17.5, 19.8 to 30.7 nm with increase in Au loading level. Electron dispersive spectroscopy (EDS) confirmed a uniform distribution of La, Fe, and O in the whole S1 belt and Au was also detected for S2, S3 and S4. Based on these results, it is clear that Au has been successfully loaded onto the surface of the $LaFeO_3$ NBs.

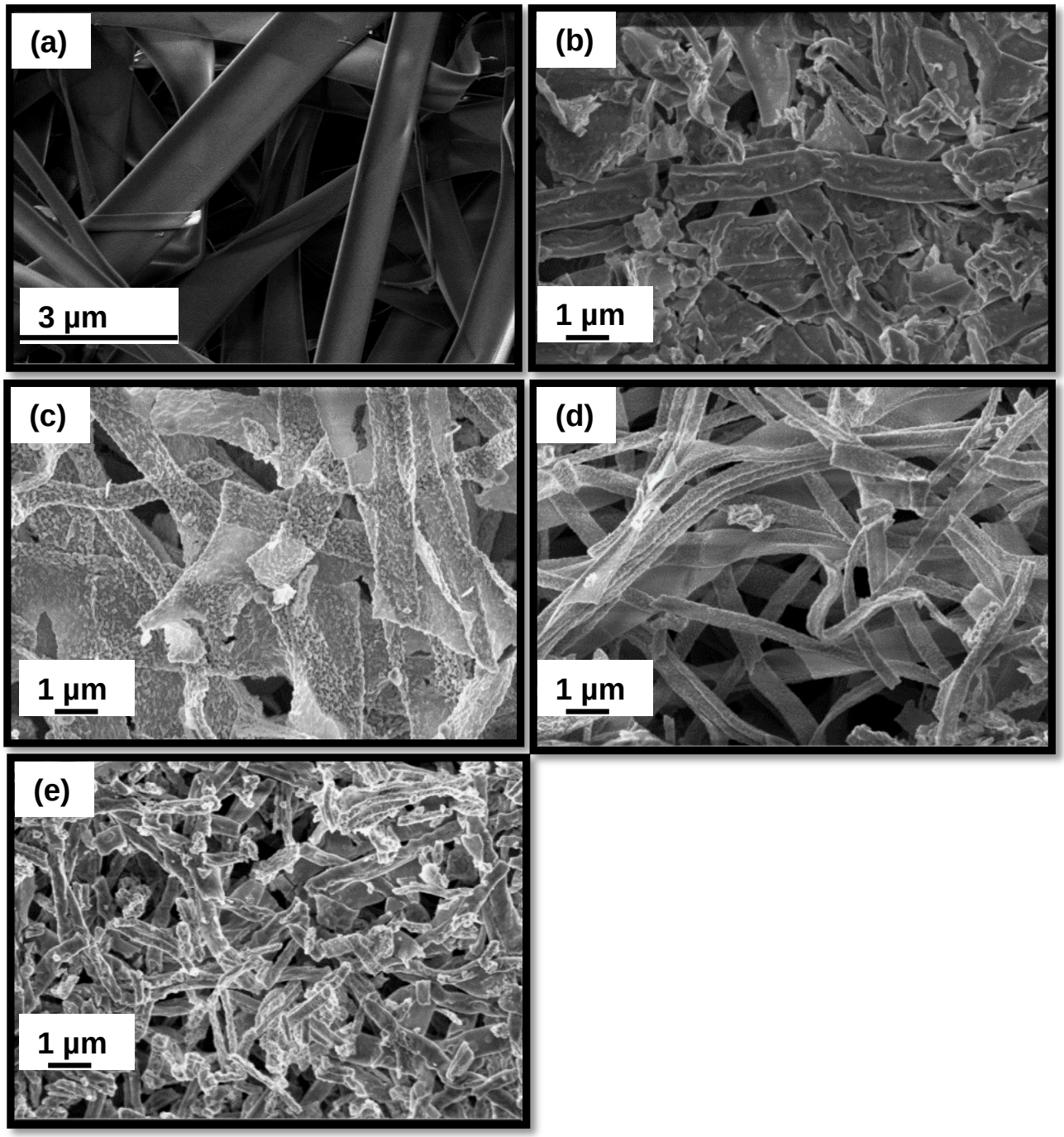

Figure 7.2: SEM images of the (a) as-spun, and (b) S1, (c) S2, (d) S3 and (e) S4 NBs, respectively after annealing at 500 °C.

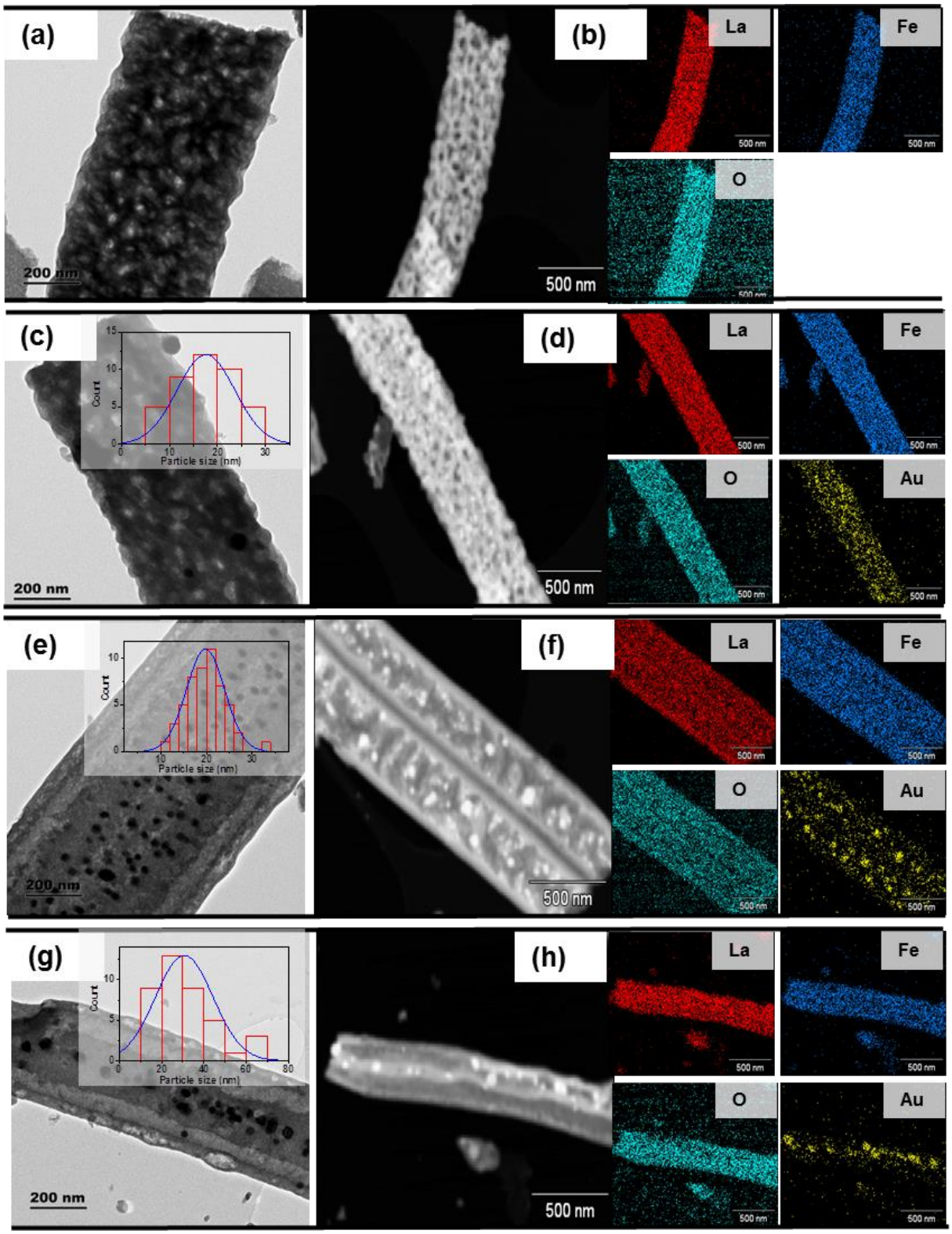

Figure 7.3: TEM images of (a) S1, (c) S2, (e) S3 and (g) S4 with their corresponding EDS maps (b, d, f and h). Particle size distribution of the Au is represented as insets of each figure.

7.5.2 Surface area and porosity analysis

Generally, the sample's relative surface area and porosity are important parameters to determine gas sensing performance as they can be favourable to provide active sites and gas diffusion pathways. Thus, the specific surface areas and the pore size of S1-S4 were determined by the Nitrogen adsorption-desorption measurements. Figure 7.4 displays the nitrogen adsorption-desorption isotherms of S1, S2, S3 and S4. All isotherms exhibit a type IV isotherm, suggesting interconnected mesoporosity and high pore-connectivity of the NBs [39, 60, 61]. According to the adsorption–desorption isotherms, the BET surface area values of S1, S2, S3 and S4 were found to be 5.8, 16.1, 9.1 and 10.9 m^2g^{-1}, respectively. The pore size distribution was determined using the Barrett–Joyner–Halenda (BJH) model analysis (see inserts of Figure 7.4). BJH pore size distribution indicated that S1, S2, S3 and S4 have an average pore diameter of 10.4, 29.4, 38.9 and 46.1 nm, respectively. The enhanced surface area and porosity can be attributed to the absence of clogging of the pores on the surface of $LaFeO_3$ as the Au nanoparticles are homogeneously distributed on the surface of each belt. Moreover, due to their very small size, the Au nanoparticles contribute to the overall surface area and porosity of the nanocomposites. The high surface area and porous structure is deemed beneficial in gas sensing as it can increase the sensing response and recovery speed by aiding the inward diffusion of the analyte gas or oxygen on the sensing material surface and the counter diffusion of reactant gases to the immediate ambient surroundings [62].

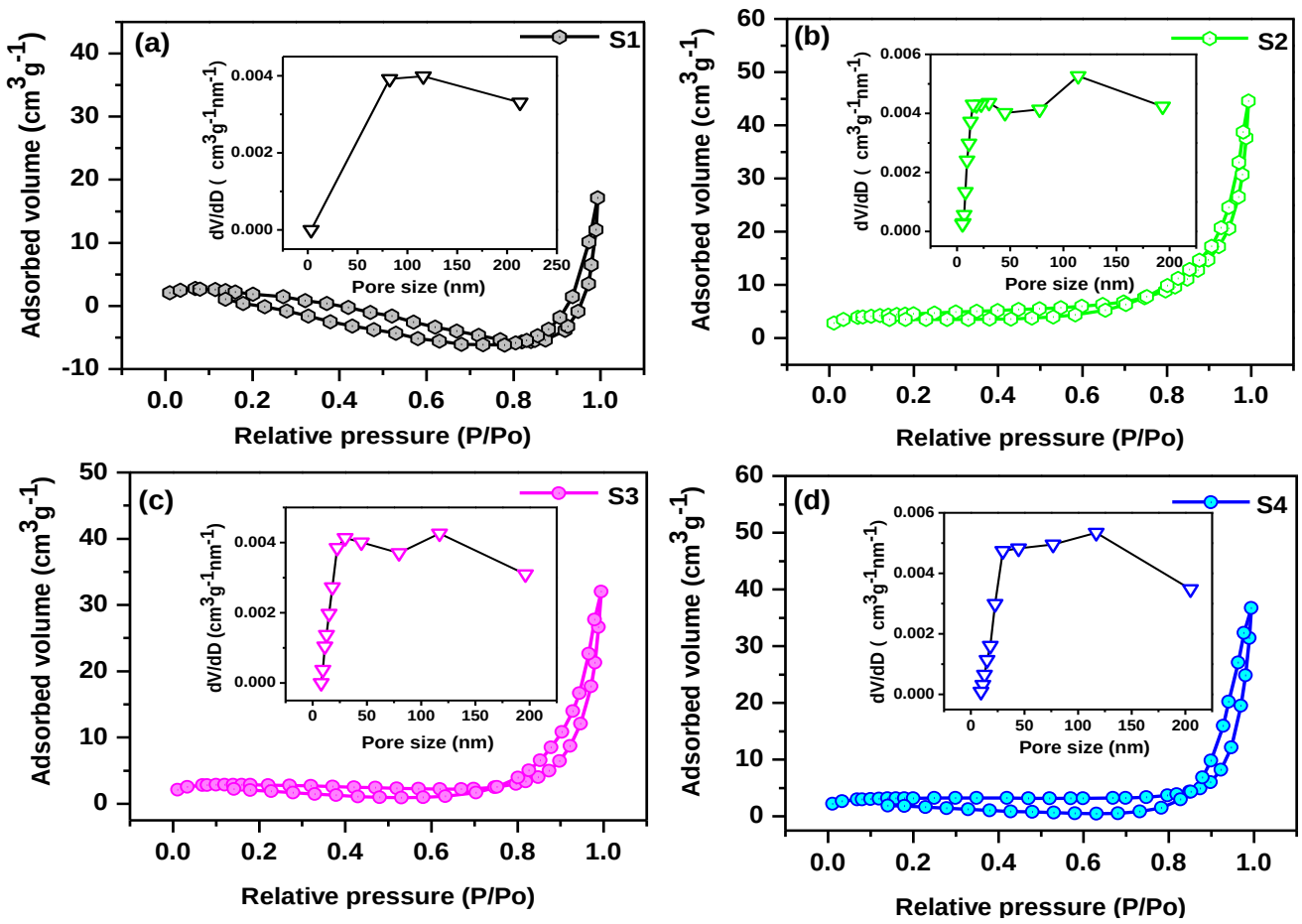

Figure 7.4: Nitrogen adsorption-desorption isotherms and the corresponding pore size distribution curves of S1, S2, S3 and S4.

7.5.3 Chemical composition analysis

The information regarding the electronic states and surface chemical composition of the samples was acquired through XPS measurements. In this case, the pure (i.e. S1) and highly Au loaded (i.e. S4) samples were selected for this analysis. Figure 7.5 presents the recorded high resolution spectra of La 3d, Fe 2p, Au 4f and O 1s core levels of S1 and S4. As displayed in Figure 7.5 (a and b) the La 3d spectra acquired from both the S1 and S4 samples revealed two double peaks representing a spin-orbit splitting components of La $3d_{5/2}$ and La $3d_{3/2}$ located at the 835.6 and 852.3 eV, respectively [63]. The split distance between

the spin-orbit doublet was ~16.7 eV which is indicative of the La^{3+} state [64]. The La 3d spectrum from pure $La(OH)_3$, for example, will have four visible components, as in this case, even though there is only one chemical state [65].

Similarly, the high resolution spectrum of the Fe 2p core level from both the S1 and S4 presented in Figure 7.5(c) exhibited the spin-orbit splitting of the Fe $2p_{3/2}$ and Fe $2p_{1/2}$ core level states located at 709.9 and 723.5 eV with a spin-orbit splitting of 13.6 eV, which corresponds to the Fe^{3+} of $LaFeO_3$, respectively [66,67]. To gain more insight about the chemical state of Au loaded onto NBs surface, the high resolution spectrum of the Au 4f core level was recorded and is shown in Figure 7.5(d). As shown in this figure, the Au 4f spectrum of the Au loaded sample displayed a doublet at 85.1 and 88.6 eV for Au $4f_{7/2}$ and $4f_{5/2}$, respectively, which correspond to A^0 state of metallic Au [68]. An additional peak belonging to Fe 3s was observed at a binding energy of 91.6 eV confirming the interaction between Au with $LaFeO_3$. The high resolution of the O 1s depicted in Figure 7.5(e-f) was Gaussian fitted into three peaks corresponding to three types of oxygen states at the surface herein labelled as O_L at 528.9 and 530.4 eV, O_V at 531.2 and 531.5 eV and O_C at 532.4 and 532.9 eV for S1 and S4, respectively. The O_L can be assigned to O^{2-}, which is related to the bulk lattice oxygen, while O_V can be associated with surface adsorbed oxygen (O^-) and is related to oxygen vacancies, and O_C corresponds to O_2^- which is related to the chemisorbed species such as carbonates and hydroxyls, respectively [69-71].

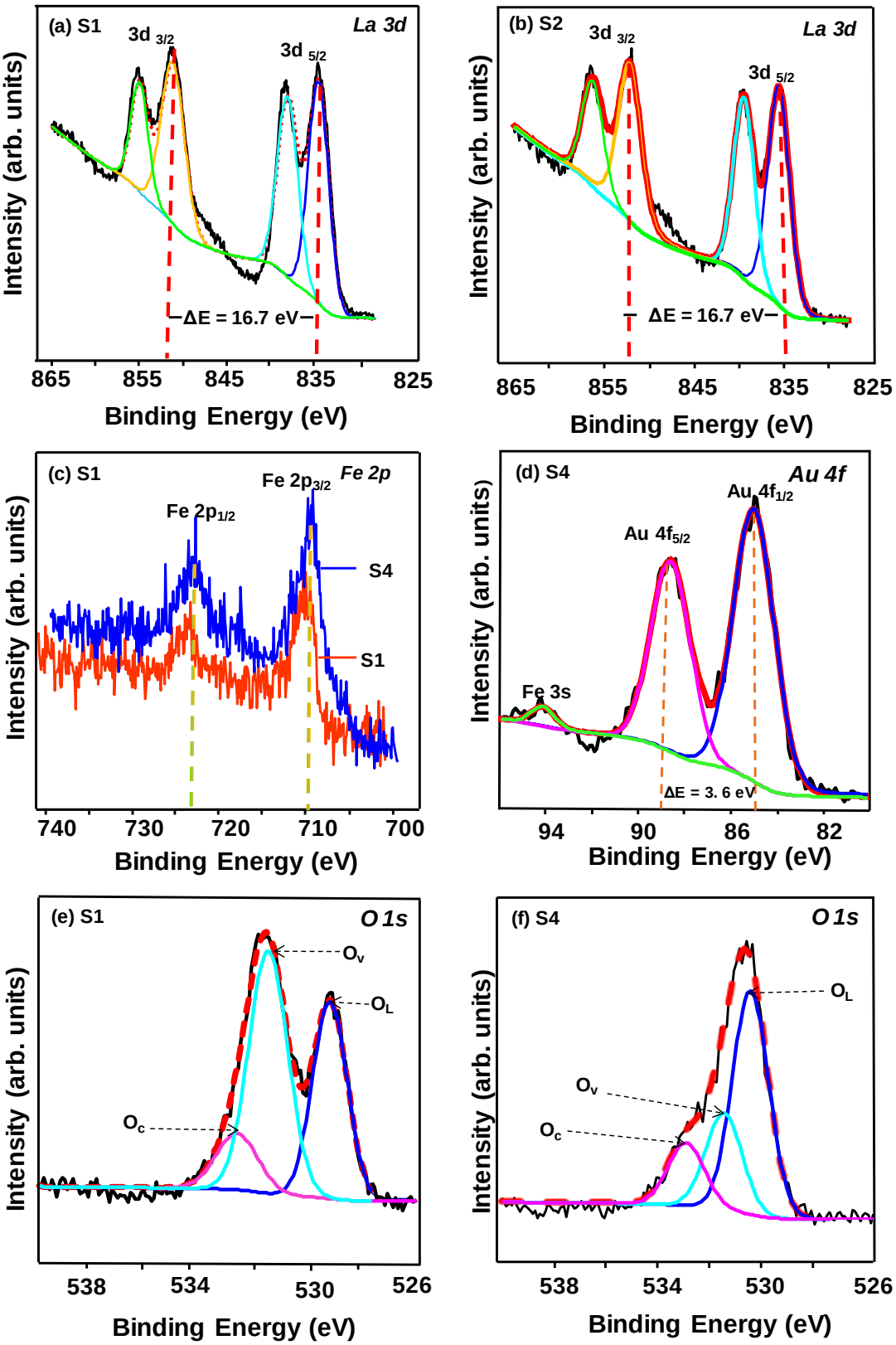

Figure 7.5: (a) High magnification XPS spectra of (a-b) La 3d for S1 and S4, (c) Fe 2p for S1 and S4, (d) Au 4f for S4, (e-f) O 1s core levels of the for S1 and S4.

7.6 Gas sensing performance of the pure and Au loaded $LaFeO_3$ NBs

Normally metal oxide-based gas sensors require heating to appropriate temperatures to achieve maximum response. The sensor response is usually defined as Ra/Rg for reducing gases and as Rg/Ra for oxidizing gases, where Ra is the sensor resistance in air and Rg is the sensor resistance in the presence of the target gas [72]. So, to determine the operating temperature for S1-S4 based sensors; acetone responses at concentration of 40 ppm at RT (23 °C), 100, 120, 140, 160 and 180 °C were measured and the results are illustrated in Figure 7.6. An obvious response dependence on the operating temperature can be observed. With an increase in operating temperature; the responses of all the sensors were shown to increase to a maximum response at 100 °C, then decreased with further increase of temperature towards 140-180 °C. The low responses displayed by all the sensors at low operating temperatures is common behaviour for SMO as the analyte gas molecules does not have enough thermal energy to interact with the adsorbed surface oxygen species thus it gives a low response. But gradual increase of the operating temperature provides the analyte gas molecules with enough thermal energy to get activated and react with the surface adsorbed oxygen species therefore giving a high response. However, with further increase to higher temperatures; the rate of analyte gas adsorption and the usage of the sensing layer become reduced resulting in the weakening of the sensor response [51, 73]. The response values were found to be 112, 102, 125 and 96 for the sensors based on S1, S2, S3 and S4. From the obtained values, it can be clearly seen that the Au loading levels have an impact on the response of the $LaFeO_3$ NBs. The loading concentration determine the distribution and size of Au

nanoparticles on the surface of the $LaFeO_3$ NBs which strongly affect the gas sensing response owing to the electronic and chemical catalytic stimulation of the Au nanoparticles which strongly depend on the Au nanoparticles size and distribution [74]. Thus, it is important to obtain the suitable amount of Au loading for effective improvement of acetone response by $LaFeO_3$ NBs based sensors. Based on the above temperature dependence studies; all acetone measurements on S1, S2, S3 and S4 were operated at 100 °C.

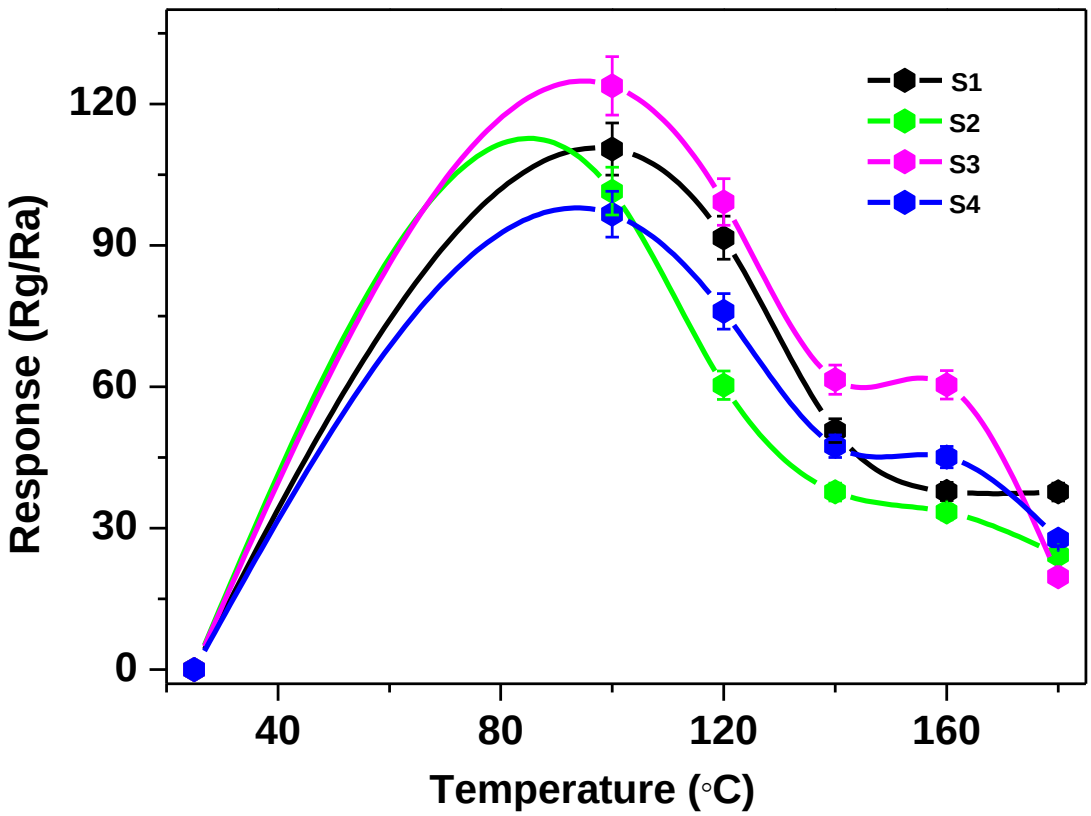

Figure 7.6: Responses of the S1, S2, S3 and S4 based sensors to 40 ppm of acetone at different operating temperatures.

To gain more insight on the effect induced by the Au nanoparticles on the surface of the $LaFeO_3$ NBs; S1-S4 based sensors were subjected to 2.5- 40 ppm of acetone as a function of time at an operating temperature of 100 °C and the resulting curves are shown in Figure 7.7. All the sensors displayed an increase and decrease in sensor resistance upon exposure to acetone and in air which is typical of p-type SMO upon exposure to a reducing gas [75]. Moreover, the increase and decrease in resistance upon contact and removal of the acetone gas demonstrates the reversible interaction between the sensing material and the analyte gas. This reversible interaction takes a specific time i.e. response and recovery time which is very important on the practical application of gas sensors for efficiency and reliability purposes. The response times of the of S1-S4 based sensors to 40 ppm acetone were determined as 100, 70, 26 and 35 s, whereas the recovery times were found to be 17, 22, 20 and 9 s for S1, S2, S3 and S4 respectively. The fast response and recovery times were obtained for S2, S3 and S4, which can be attributed to the better accessibility of active sites and ease in diffusion due to the porous structures, coupled with the Au nanoparticles catalytic effect. Generally, the response of a sensor is dependent on the concentration of the target gas, and this relation is clearly displayed in Figure 7.7(e) for the response to acetone in the range from 2.5 to 40 ppm. Even though the lowest concentration experimentally examined was 2.5 ppm, the theoretical limit of detection (signal-to-noise ratio>3) was estimated from Figure 7.7(e) to be around 0.056, 0.382, 0.267 and 0.733 ppm for S1, S2, S3 and S4, respectively. Limit of detection of less than 1 ppm to acetone with high response validates the promising use of the Au loaded $LaFeO_3$ NBs in high performance sensors for acetone detection.

As much as a sensor can give high response and fast response kinetics; it is also very crucial for the sensor to be able to selectively detect the target gas in the midst of other gases since real application atmospheres consists of a mixture of gases. With that said; the ability to single out acetone in the presence of other gases such as CO, CH_4, NO_2 and NH_3 of S1, S2, S3 and S4 based sensors at 100 °C was measured by exposing the sensors to 40 ppm of each test gas. The obtained results are displayed in Figure 7.8. All sensors demonstrate outstanding selectivity towards acetone molecules with S3 sensor displaying the highest response with minor responses towards interfering gases. The observed high selectivity towards acetone could probably be due to the fact that acetone is more chemical reactive with the adsorbed oxygen species at the optimum temperature (100 °C) [76, 77]. Whereas the response to the other gas species is rather trivial probably due to the relative weak chemical interaction between them and the adsorbed oxygen species on the sensors surface. Further, reproducibility of the sensor response is another important key factor in practical applications. Therefore; the reproducibility test to 5 response/recovery cycles of the sensor based on S3 was conducted and the results are shown in Figure 7.8 (b). The results demonstrated consistent high response with excellent recovery without any obvious degradation on the sensor response indicating good stability and reproducibility.

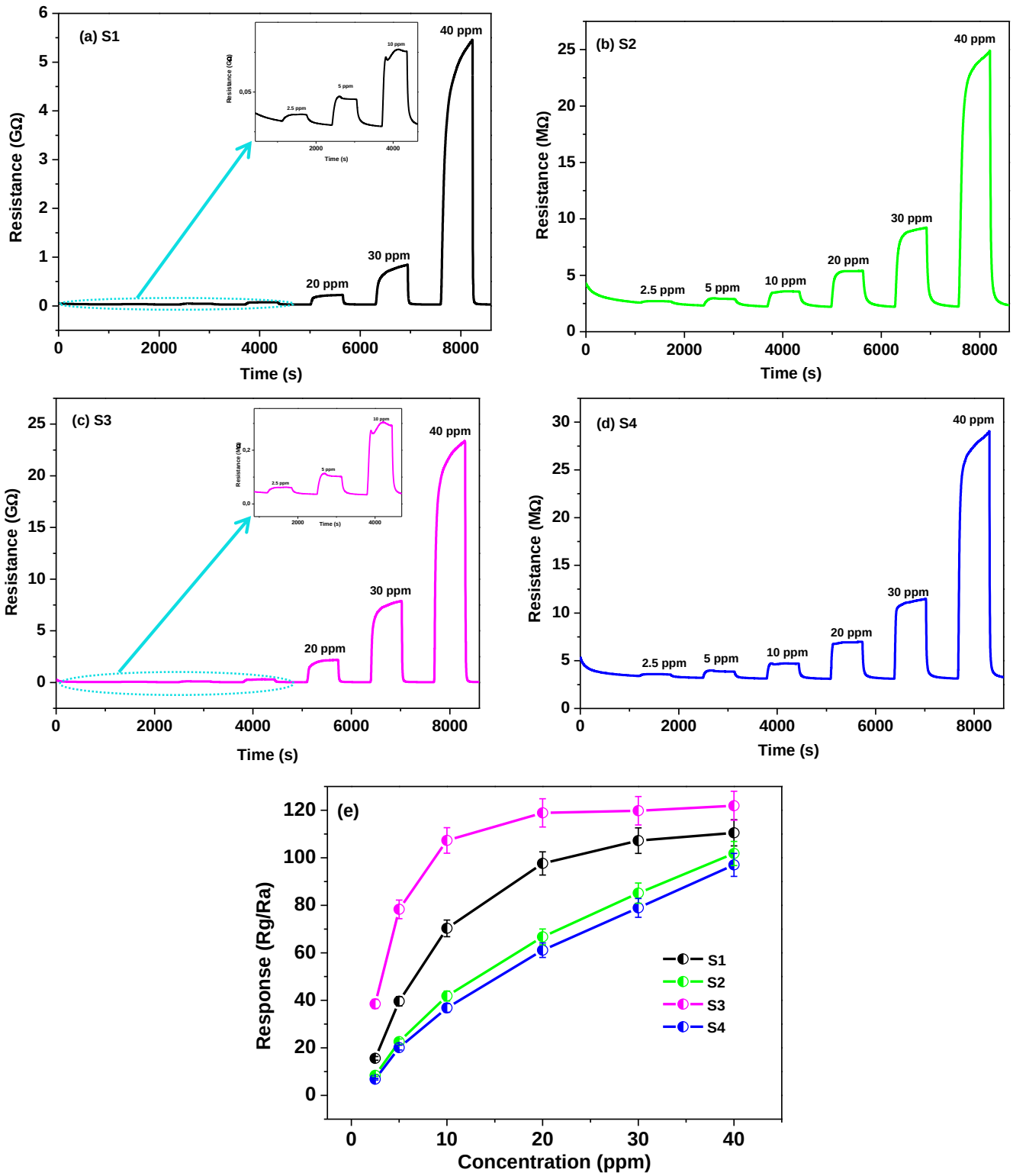

Figure 7.7: Dynamic resistance curves of (a) S1, (b) S2, (c) S3, (d) S4 and (e) corresponding responses of S1-S4 to acetone concentrations ranging from 2.5 to 40 ppm.

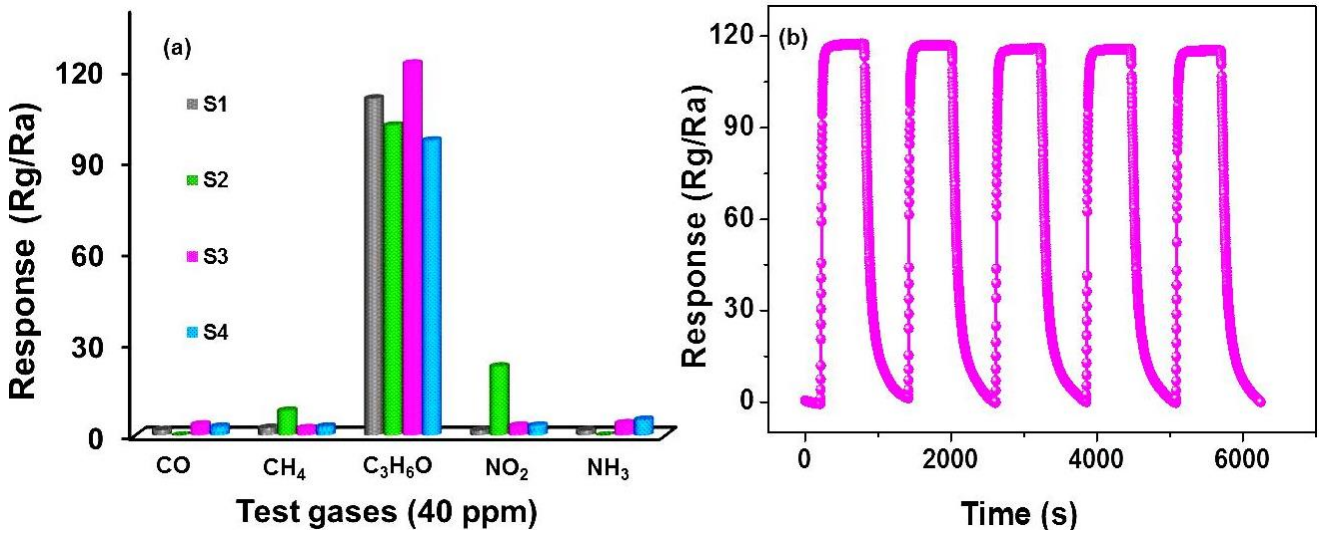

Figure 7.8: (a) Gas responses to 40 ppm of different gases and (b) reproducibility of the S3 to 40 ppm acetone at 100 °C.

Usually, acetone is accompanied by moisture; therefore it is important to take into consideration the effect of moisture on the sensing performance for practical applications. Thus the comparison of the responses of S1-S4 based sensors towards 40 ppm of acetone both in dry and relative humidity (RH) conditions of 30, 70 and 90 % at 100 °C were recorded and are represented by the histogram in Figure 7.9(a). An obvious decline in response to acetone for both the pure and Au loaded $LaFeO_3$ was observed with relative humidity increment from 30 to 90%. The decline of response with increasing relative humidity is a result of the competition between the hydroxyl species and the acetone molecules during the surface reactions, which lowers the oxygen adsorption, therefore reducing the sensor response [78, 79]. Interestingly, S3 based sensor still revealed the highest response in all RH levels whereby it showed a small drop in response at 30 to 70% RH and a significant decrease in its response was observed at a higher

relative humidity of 90%(see Figure 7.9(b)). The good sensing response of S3 even in a wide range of relative humidity conditions validates the practical applicability of the sensor.

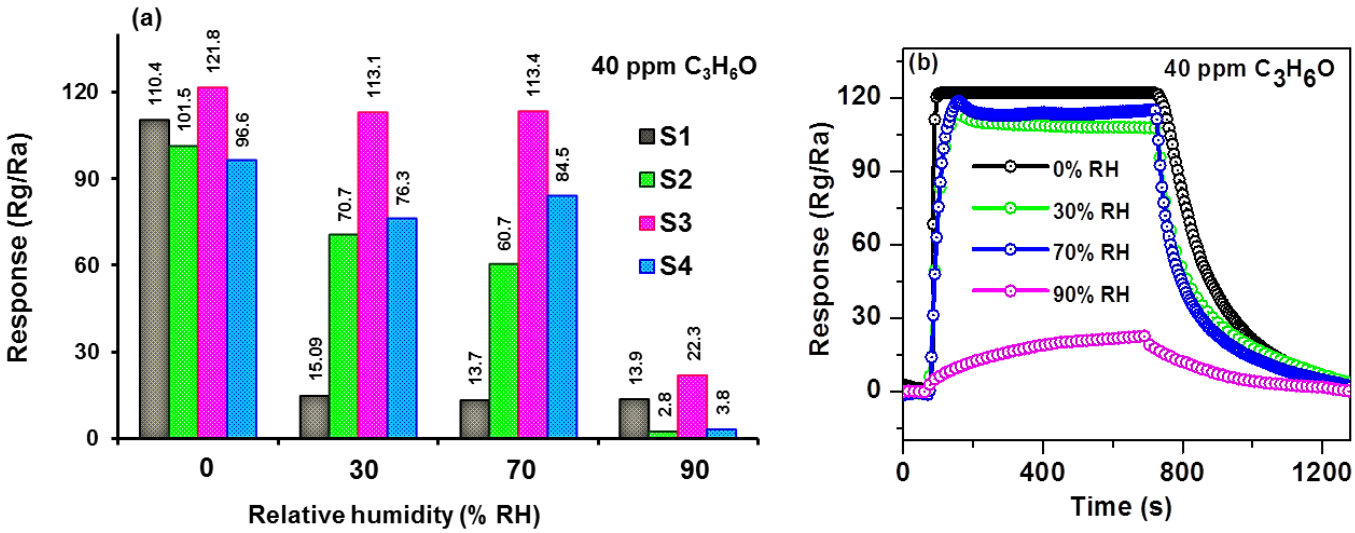

Figure 7.9: (a) Response histogram of S1-S4 based sensors and (b) S3 response and recovery curves to 40 ppm acetone in dry air and under different relative humidity of 30, 70 and 90% at 100 °C.

7.7 Acetone sensing mechanism

In general, for SMO gas sensors; the most widely accepted sensing mechanism relies on the type of material's majority charge carriers (electrons or holes), its surface groups (i.e. O^{2-},O^{-}, O_2^{-}.) and the nature of the surface (acidic or basic surface); which mainly determine the adsorption-desorption interaction between the analyte gas and the sensing material. $LaFeO_3$ is regarded as a p-type SMO with the holes being the majority charge carriers while its gas sensing mechanism is based on the changes of resistance in air and in the presence of the analyte gas.

When considering the pure $LaFeO_3$ NBs in air (Figure 7.10(1a)), neutral oxygen molecules adsorbs on the $LaFeO_3$ surface and get partially ionized into O^{2-}, O^- or O_2^- ions by attracting electrons from the valence band at different temperatures. Since the sensors in this work were operated at 100 °C, so the O^{2-} ions are more dominant than any other oxygen adsorbate [80]. Exposure of the $LaFeO_3$ sensors to the ambient atmosphere then led to the formation of a thick underlying hole accumulation layer, which allowed the sensor to have a relatively low resistance layer covering the whole surface of the sensor. On the other hand, when the $LaFeO_3$ based sensors came into contact with acetone molecules (see Figure 7.10(1b)), a reaction between the acetone molecules and the oxygen adsorbates took place to form CO_2 and H_2O according to the following relation [81]

$$CH_3COCH_3 + 8O^{2-}_{(ads)} \rightarrow 3CO_2 + 3H_2O + 8e^- \qquad (7.1)$$

This reaction then led to the release of electrons to the valence band resulting in the recombination of electrons and holes [81]. As a result, the concentration of the holes was decreased and this led to an increase in the resistance of the $LaFeO_3$ based sensor. In the case of the S3 (0.3 wt% Au loaded $LaFeO_3$) in Figure 7.10 (2(a-b)), the acetone sensing mechanism follows the same process as that on the pure $LaFeO_3$, however the electronic and chemical sensitization of the Au nanoparticles promotes enhancement in the sensing performance of the $LaFeO_3$ NBs based sensor [82]. The significant enhancement in sensing performance of S3 may be explained as follows:

(i) Au is a good catalyst for oxygen dissociation [83] which means that Au nanoparticles aid in ease of oxygen molecules adsorption and the capturing of electrons to produce active oxygen adsorbates (Figure 7.10(2a). Further, acetone

molecules are ionized to active radicals by the Au nanoparticles, and due to the spill-over effect of Au, these active radicals will spill-over the surface of $LaFeO_3$, facilitating the sensing reactions on the surface of $LaFeO_3$ thus enhancing the response and also fast-tracking response and recovery times.

(ii) The surface area and pore diameter increased with Au loading as confirmed from BET analysis and this can provide more surface adsorption sites to adsorb oxygen and acetone molecules and also ease in diffusion, hence the improved gas sensing response.

(iii) The 1D NB morphology of the $LaFeO_3$ also played an important role as it allows overlapping of the hole accumulation layers along the NB direction resulting in a continuous hole transfer channels thus contributing to enhancement of the sensor performance.

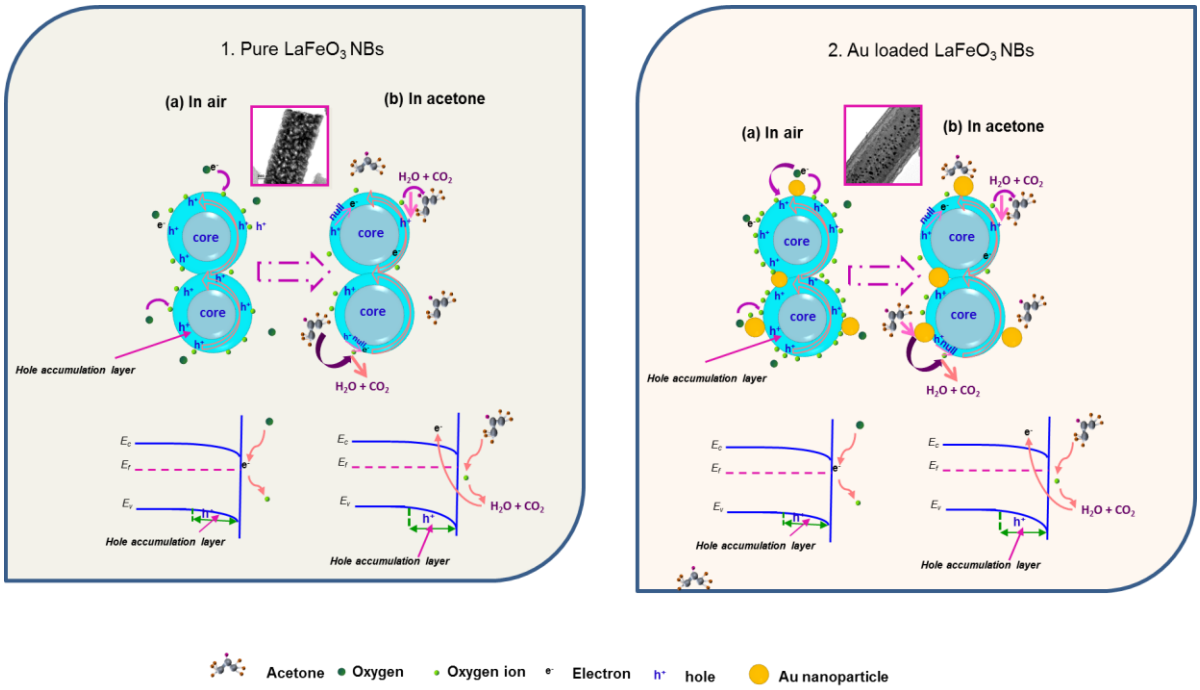

Figure 7.10: Proposed acetone sensing mechanism of the pure and Au loaded $LaFeO_3$ NBs.

Through literature survey it was realised that there are some acetone sensors based on $LaFeO_3$ nanostructures, which display different sensing capabilities. Table 7.1 lists some of the literature sampled through systems which are close to the work reported herein for comparison purposes. In comparison to previous literature; it can be realised that S3 displays high response to low concentration of acetone (40 ppm) at relatively low operating temperature with quick response and recovery speed; thus ensuring low power consuming operation with fast response kinetics. Moreover, S3 revealed good repeatability to a few response-recovery cycles indicating stability and reproducibility which are critical characteristics for practical applications. Thus, the S3 based sensor possesses valuable gas sensing characteristics that deems it fit for practical applications.

Table 7.1: Gas sensing characteristics based on $LaFeO_3$ nanostructures reported in recent literature and this work.

Sensing material	T (°C)	Conc. (ppm)	Rg/Ra	T_{res}/T_{rec} (s)	Ref.
Sr-doped $LaFeO_3$	275	500	0.70	20/270	[84]
2 wt% Pd doped $LaFeO_3$	200	1	1.9	4/2	[85]
MIT Ag-$LaFeO_3$ spheres	155	5	23.3	55/60	[81]
$LaFeO_3$ thick film	260	0.5	2.068	62/107	[86]
$La_{0.68}Pb_{0.32}FeO_3$	200	50	7	60/20	[87]
$LaFeO_3$	400	80	204	15	[88]
Porous $LaFeO_3$	240	200	12.2	9/18	[89]
0.3 wt% Au loaded $LaFeO_3$	100	40	125	26/20	This work

7.8 Conclusion

In summary, a series of 1D Au loaded $LaFeO_3$ NBs have been successfully synthesized via the electrospinning technique. The size and distribution of the Au nanoparticles on the surface of the $LaFeO_3$ NBs was controlled by adjusting the dosage of the HAuCl. When tested for gas sensing performance; all the Au loaded $LaFeO_3$ NBs including the pure $LaFeO_3$ exhibited good selectivity and high response to acetone at an operating temperature of 100 °C with the 0.3 wt% Au loaded $LaFeO_3$ NBs based sensor displaying the highest response in comparison to the other sensors. The gas sensing behaviour displayed by this sensor is closely related to the size and distribution of the Au nanoparticles, which controls the catalytic activity of the Au catalyst. Moreover, the increased surface area and porosity induced by Au addition on the 1D NB structure also played an essential role in the increasing gas sensing performance of the S3 based sensor. The Au doped $LaFeO_3$ sensor with Au content of 0.3 wt% offers a new strategy to prepare noble metal modified $LaFeO_3$ NBs that can be promisingly employed to produce excellent and reliable gas sensor to low target gas concentrations at low operating temperature.

7.9 References

[1] L. Guo, F. Chen, N. Xie, X. Kou, C. Wang, Y. Sun, F. Liu, X. Liang, Y. Gao, X. Yan, Sens. Actuators B Chem., 272 (2018) 185-194.

[2] T. Satoh, K. Omae, H. Nakashima, T. Takebayashi, H. Matsumura, T. Kawai, M. Nakaza, H. Sakurai, Int. Arch. Occup. Environ. Health, 68 (1996) 147-153.

[3] X. Yang, S. Zhang, Q. Yu, P. Sun, F. Liu, H. Lu, X. Yan, X. Zhou, X. Liang, Y. Gao, Sens. Actuators B Chem., 270 (2018) 538-544.

[4] Q. Jia, H. Ji, Y. Zhang, Y. Chen, X. Sun, Z. Jin, J. Hazard. Mater., 276 (2014) 262-270.

[5] L. Wang, A. Teleki, S.E. Pratsinis, P. Gouma, Chem. Mater., 20 (2008) 4794-4796.

[6] X. Sun, H. Ji, X. Li, S. Cai, C. Zheng, Mater. Lett., 120 (2014) 287-291.

[7] A. Rydosz, Sensors, 18 (2018) 2298.

[8] A. Kolmakov, M. Moskovits, Annu. Rev. Mater. Res., 34 (2004) 151-180.

[9] N. Barsan, U. Weimar, J. Electroceram., 7 (2001) 143-167.

[10] M. Arafat, A. Haseeb, S. Akbar, Sensors, 14 (2014) 13613-13627.

[11] F. Fan, Y. Feng, P. Tang, A. Chen, R. Luo, D. Li, Ind. Eng. Chem. Res., 53 (2014) 12737-12743.

[12] G. Mhlongo, D. Motaung, I. Kortidis, N. Mathe, O. Ntwaeaborwa, H. Swart, B. Mwakikunga, S. Ray, G. Kiriakidis, Mater. Chem. Phys., 162 (2015) 628-639.

[13] K. Shingange, H. Swart, G. Mhlongo, J. Alloys. Compd., 797 (2019) 284-301.

[14] K. Shingange, Z. Tshabalala, B. Dhonge, O. Ntwaeaborwa, D. Motaung, G. Mhlongo, Mater. Res. Bull., 85 (2017) 52-63.

[15] H. Ding, J. Ma, F. Yue, P. Gao, X. Jia, J. Solid State Chem., 276 (2019) 30-36.

[16] Y. Mo, F. Shi, S. Qin, P. Tang, Y. Feng, Y. Zhao, D. Li, Ind. Eng. Chem. Res., DOI (2019).

[17] K. Shingange, G.H. Mhlongo, D.E. Motaung, O.M. Ntwaeaborwa, J. Alloys. Compd., 657 (2016) 917-926.

[18] J. Fu, C. Zhao, J. Zhang, Y. Peng, E. Xie, ACS Appl. Mater. Interfaces., 5 (2013) 7410-7416.

[19] S. Zhao, Y. Shen, X. Yan, P. Zhou, Y. Yin, R. Lu, C. Han, B. Cui, D. Wei, Sens. Actuators B Chem., 286 (2019) 501-511.

[20] F. Qu, X. Zhou, B. Zhang, S. Zhang, C. Jiang, S. Ruan, M. Yang, J. Alloys. Compd, 782 (2019) 672-678.

[21] J. Li, H. Liu, H. Fu, L. Xu, H. Jin, X. Zhang, L. Wang, K. Yu, J. Alloys. Compd, 788 (2019) 248-256.

[22] J. Chen, L. Xu, W. Li, X. Gou, Adv. Mater., 17 (2005) 582-586.

[23] Y.-J. Chen, F.-n. Meng, H.-l. Yu, C.-l. Zhu, T.-s. Wang, P. Gao, Q.-y. Ouyang, Sens. Actuators B Chem. , 176 (2013) 15-21.

[24] Y.-J. Choi, I.-S. Hwang, J.-G. Park, K.J. Choi, J.-H. Park, J.-H. Lee, Nanotechnology, 19 (2008) 095508.

[25] V. Kruefu, A. Wisitsoraat, A. Tuantranont, S. Phanichphant, Sens. Actuators B Chem. , 215 (2015) 630-636.

[26] H.-J. Kim, J.-H. Lee, Sens. Actuators B Chem., 192 (2014) 607-627.

[27] M. Hübner, C.E. Simion, A. Tomescu-Stănoiu, S. Pokhrel, N. Bârsan, U. Weimar, Sens. Actuators B Chem., 153 (2011) 347-353.

[28] H. Liu, Y. He, K. Nagashima, G. Meng, T. Dai, B. Tong, Z. Deng, S. Wang, N. Zhu, T. Yanagida, X. Fang, Sens. Actuators B Chem., 293 (2019) 342-349

[29] H.J. Park, S.Y. Hong, D.H. Chun, S.W. Kang, J.C. Park, D.-S. Lee, Sens. Actuators B Chem. , 287 (2019) 437-444.

[30] C.W. Na, H.-S. Woo, I.-D. Kim, J.-H. Lee, Chem. Commun., 47 (2011) 5148-5150.

[31] H.-S. Woo, C.W. Na, I.-D. Kim, J.-H. Lee, Nanotechnology, 23 (2012) 245501.

[32] B. Shouli, C. Liangyuan, L. Dianqing, Y. Wensheng, Y. Pengcheng, L. Zhiyong, C. Aifan, C.C. Liu, Sens. Actuators B Chem., 146 (2010) 129-137.

[33] A. Diéguez, A. Romano-Rodríguez, J.R. Morante, U. Weimar, M. Schweizer-Berberich, W. Göpel, Sens. Actuators B Chem., 31 (1996) 1-8.

[34] S. Park, T. Hong, J. Jung, C. Lee, Curr. Appl. Phys., 14 (2014) 1171-1175.

[35] C.-L. Hsu, B.-Y. Jhang, C. Kao, T.-J. Hsueh, Sens. Actuators B Chem., 274 (2018) 565-574.

[36] L. Wang, Z. Lou, T. Fei, T. Zhang, Sens. Actuators B Chem., 161 (2012) 178-183.

[37] K. Shingange, H. Swart, G.H. Mhlongo, Physica B., 535 (2018) 216-220.

[38] W. Cui, X. Kang, X. Zhang, Z. Zheng, X. Cui, Physica E Low Dimens. Syst. Nanostruct., 113 (2019) 165-171

[39] Q. Rong, Y. Zhang, J. Hu, K. Li, H. Wang, M. Chen, T. Lv, Z. Zhu, J. Zhang, Q. Liu, Sci. Rep., 8 (2018) 14220.

[40] Q. Chen, Y. Wang, M. Wang, S. Ma, P. Wang, G. Zhang, W. Chen, H. Jiao, L. Liu, X. Xu, J. Colloid. Interface. Sci., 543 (2019) 285-299.

[41] L. Wang, H. Fu, Q. Jin, H. Jin, H. Haick, S. Wang, K. Yu, S. Deng, Y. Wang, Sens. Actuators B Chem., 292 (2019) 148-155.

[42] J. Li, L. Wang, Z. Liu, Y. Wang, S. Wang, J. Alloys. Compd., 728 (2017) 944-951.

[43] W.-T. Koo, J.-S. Jang, S.-J. Choi, H.-J. Cho, I.-D. Kim, ACS Appl. Mater. Interfaces., 9 (2017) 18069-18077.

[44] J. Zhang, P. Song, Z. Li, S. Zhang, Z. Yang, Q. Wang, J. Alloys. Compd., 685 (2016) 1024-1033.

[45] C. Jin, H. Kim, S. Park, H.W. Kim, S. Lee, C. Lee, Ceram. Int., 38 (2012) 6585-6590.

[46] S.M. Majhi, G.K. Naik, H.-J. Lee, H.-G. Song, C.-R. Lee, I.-H. Lee, Y.-T. Yu, Sens. Actuators B Chem., 268 (2018) 223-231.

[47] L. Ma, S.Y. Ma, Z. Qiang, X.L. Xu, Q. Chen, H.M. Yang, H. Chen, Q. Ge, Q.Z. Zeng, B.Q. Wang, Mater. Lett., 200 (2017) 47-50.

[48] N.N. Toàn, S. Saukko, V. Lantto, Physica B., 327 (2003) 279-282.

[49] W. Wei, S. Guo, C. Chen, L. Sun, Y. Chen, W. Guo, S. Ruan, J. Alloys. Compd., 695 (2017) 1122-1127.

[50] J. Xiang, X. Chen, X. Zhang, L. Gong, Y. Zhang, K. Zhang, Mater. Chem. Phys., 213 (2018) 122-129.

[51] N. Zhang, S. Ruan, Y. Yin, F. Li, S. Wen, Y. Chen, ACS Appl. Nano. Mater., 1 (2018) 4671-4681.

[52] H. Zhu, P. Zhang, S. Dai, ACS Catal., 5 (2015) 6370-6385.

[53] M. Chen, D. Zhang, J. Hu, H. Wang, Y. Zhang, K. Li, Q. Rong, S. Zhou, J. Zhang, Z. Zhu, Mater. Res. Bull., 111 (2019) 320-328.

[54] Y. Zhang, J. Zhang, J. Chen, Z. Zhu, Q. Liu, Sens. Actuators B Chem., 195 (2014) 509-514.

[55] F. Gu, H. Wang, D. Han, Z. Wang, Sens. Actuators B Chem., 245 (2017) 1023-1031.

[56] G. Korotcenkov, L. Gulina, B. Cho, S. Han, V. Tolstoy, Mater. Chem. Phys., 128 (2011) 433-441.

[57] X. Xia, X. Dong, Q. Wei, Y. Cai, K. Lu, Express. Polym. Lett., 6 (2012).

[58] N. Horzum, D. Taşçıoglu, S. Okur, M.M. Demir, Talanta, 85 (2011) 1105-1111.

[59] N. Horzum, R. Muñoz-Espí, G. Glasser, M.M. Demir, K. Landfester, D. Crespy, ACS Appl. Mater. Interfaces., 4 (2012) 6338-6345.

[60] X. Lin, L. Xiong, G. Qi, S. Shi, C. Huang, X. Chen, X. Chen, ACS Sustain. Chem Eng., 3 (2015) 702-709.

[61] G.M. Clavier, J.L. Pozzo, H. Bouas-Laurent, C. Liere, C. Roux, C. Sanchez, J. Mater. Chem., 10 (2000) 1725-1730.

[62] K.-I. Choi, H.-R. Kim, J.-H. Lee, Sens. Actuators B Chem., 138 (2009) 497-503.

[63] X.-D. Zhang, W.-L. Zhang, Z.-X. Cai, Y.-K. Li, Y. Yamauchi, X. Guo, Ceram. Int., 45 (2019) 5240-5248

[64] Z. Dai, C.-S. Lee, B.-Y. Kim, C.-H. Kwak, J.-W. Yoon, H.-M. Jeong, J.-H. Lee, ACS Appl. Mater. Interfaces., 6 (2014) 16217-16226.

[65] https://xpssimplified.com/elements/lanthanum.php, (Accessed 19 May 2019).

[66] S. Thirumalairajan, K. Girija, V.R. Mastelaro, N. Ponpandian, ACS Appl. Mater. Interfaces., 6 (2014) 13917-13927.

[67] O. Wiranwetchayan, S. Promnopas, S. Phadungdhitidhada, A. Phuruangrat, T. Thongtem, P. Singjai, S. Thongtem, Ceram. Int., 45 (2019) 4802-4809.

[68] M. Casaletto, A. Longo, A. Martorana, A. Prestianni, A. Venezia, Surf. Inter. Anal., 38 (2006) 215-218.

[69] W.-Y. Lee, H.J. Yun, J.-W. Yoon, J. Alloys. Compd., 583 (2014) 320-324.

[70] S. Thirumalairajan, K. Girija, N.Y. Hebalkar, D. Mangalaraj, C. Viswanathan, N. Ponpandian, RSC Advances, 3 (2013) 7549-7561.

[71] K.A. Stoerzinger, R. Comes, S.R. Spurgeon, S. Thevuthasan, K. Ihm, E.J. Crumlin, S.A. Chambers, J. Phys. Chem. Lett., 8 (2017) 1038-1043.

[72] C. Wang, L. Yin, L. Zhang, D. Xiang, R. Gao, Sensors, 10 (2010) 2088-2106.

[73] S. Zhang, P. Song, J. Zhang, H. Yan, J. Li, Z. Yang, Q. Wang, Sens. Actuators B Chem., 242 (2017) 983-993.

[74] K. Shingange, Z. Tshabalala, O. Ntwaeaborwa, D. Motaung, G. Mhlongo, J. Colloid. Interface. Sci., 479 (2016) 127-138.

[75] H.-J. Kim, H.-M. Jeong, T.-H. Kim, J.-H. Chung, Y.C. Kang, J.-H. Lee, ACS Appl. Mater. Interfaces., 6 (2014) 18197-18204.

[76] J. Cao, S. Wang, H. Zhang, T. Zhang, Mater. Sci. Semicond., 101 (2019) 10-15.

[77] F. Qu, T. Thomas, B. Zhang, X. Zhou, S. Zhang, S. Ruan, M. Yang, Sens. Actuators B Chem., 273 (2018) 1202-1210.

[78] G. Mhlongo, D. Motaung, F. Cummings, H. Swart, S. Ray, Sci. Rep., 9 (2019) 9881.

[79] R. Malik, V.K. Tomer, L. Kienle, V. Chaudhary, S. Nehra, S. Duhan, Adv. Mater. Interfaces., 5 (2018) 1701357.

[80] T. Wang, I. Can, S. Zhang, J. He, P. Sun, F. Liu, G. Lu, ACS Appl Mater Interfaces., 10 (2018) 5835-5844.

[81] C. Wang, Q. Rong, Y. Zhang, J. Hu, B. Zi, Z. Zhu, J. Zhang, Q. Liu, Mater. Res. Bull., 109 (2019) 265-272.

[82] P. Rai, R. Khan, S. Raj, S.M. Majhi, K.-K. Park, Y.-T. Yu, I.-H. Lee, P.K. Sekhar, Nanoscale, 6 (2014) 581-588.

[83] Q. Ma, Y. Fang, Y. Liu, J. Song, X. Fu, H. Li, S. Chu, Y. Chen, Physica E., 106 (2019) 180-186.

[84] P. Murade, V. Sangawar, G. Chaudhari, V. Kapse, A. Bajpeyee, Curr. Appl. Phys., 11 (2011) 451-456.

[85] X. Wang, H. Qin, J. Pei, Y. Chen, L. Li, J. Xie, J. Hu, J. Rare Earth., 34 (2016) 704-710.

[86] Y. Chen, H. Qin, X. Wang, L. Li, J. Hu, Sens. Actuators B Chem., 235 (2016) 56-66.

[87] L. Zhang, H. Qin, P. Song, J. Hu, M. Jiang, Mater. Chem. Phys., 98 (2006) 358-362.

[88] X. Liu, H. Ji, Y. Gu, M. Xu, Mater. Sci. Eng., B, 133 (2006) 98-101.

[89] P. Song, H. Zhang, D. Han, J. Li, Z. Yang, Q. Wang, Sens. Actuators B Chem., 196 (2014) 140-146.

Chapter 8

Design of $La_{1-x}Ce_xCoO_3$ ($0 \leq x \leq 0.2$) nanofibers and their improved ethanol sensing abilities at low operating temperatures

8.1 Introduction

Reliable and energy saving gas sensors for the recognition of volatile organic compounds (VOCs) have been proven to be of high need for the management of environmental discharges from industries, diagnosis of diseases in healthcare and foodstuff processing [1-4]. Ethanol is one of the important VOCs and is widely used in the chemical industry, quality monitoring of foodstuff and for monitoring of drunken driving [5]. Evaporation of ethanol raises concerns over explosion risks as its flammable range is wider than that of gasoline. So to avoid such risks, low concentrations of ethanol must be detected early. So far, substantial advancement of ethanol sensors has been achieved, yet the sensing material which is mostly semiconductor metal oxides (SMOs) still need to be improved for better selectivity and sensitivity of low concentrations.

Since their discovery as good sensing materials, SMOs have been extensively studied and more research has been dedicated into their growth and improvement for gas sensing applications [6-8]. Of particular interest is the development of them in nanostructured forms such as nano-flowers, nano-particles, nano-fibers and nano-rods as these materials are able to enhance gas performances compared with bulk SMOs [9, 10]. Motivation behind the enhanced sensing performance of nanostructured materials is their properties such as large surface area to volume ratio brought upon by their tiny size as the higher

surface-to-volume ratio can offer more active surface areas for gas molecules interactions therefore resulting in higher sensing performance.

Among the wide variety of SMOs sensing materials, the family of mixed-metal oxides with a perovskite type structure (ABO_3) has proven to be good sensing materials due to their chemical and thermal stability [11-13]. The activity of perovskites is basically determined by their cations which play an important role in adsorption of gas species and their catalytic activities [14-16]. Moreover, due to stability and flexibility of their crystal structures, partial substitution on the A or B site cation becomes accommodated resulting in oxides with tuned structural, electrical and chemical properties [17-19]. Therefore, a strategic substitution of A or B cations creates possibilities of manipulation of properties devoted to enhancing gas sensing performance. For instance, Liu *et al* [20] observed enhanced acetone sensing performance for $La_{1-x}Sr_xCoO_3$ (x=0.1) nanoparticles at room temperature. They attributed the improved performance to the increase in holes brought upon by the Sr^{2+} doping. Ghasdi *et al* [21] obtained much improved response to 100 ppm CO with $La_{1-x}Ce_xCoO_3$ as compared to pure $LaCoO_3$ to which they attributed to the increased surface oxygen brought upon by the Ce doping which facilitated the adsorption and oxidation processes.

Being a member of the perovskites family, $LaCoO_3$ is one of the competitive and promising material for gas sensing due to its interesting physical properties such as catalytic oxidation of compounds and sensitivity to some gases [22, 23]. $LaCoO_3$ is a p-type semiconductor with a rhombohedral perovskite structure with unit cell parameters a= 5.4 and c= 13.1 Å [24, 25]. $LaCoO_3$ based sensors

have been reported before, however they suffer from some draw backs such as high operating temperatures which can consume a lot of energy [26]**.** Given that partial substitution of either the A or B site on the perovskite lattice can improve the sensing performance of the oxide material, this study focuses on investigating the effect of the partial substitution of La by Cerium (Ce). Therefore partial substitution of Ce on the A site in cobalt or manganese-based perovskites often result in an increase in oxidation catalytic activity [27-29]. Gas sensing mechanism is a surface mechanism whereby the target gas reacts with the surface oxygen. The availability of more oxygen on the surface may result in higher catalytic activity which may improve the gas performance. Partial substitution of La^{3+} by Ce^{4+} results in the reduction of a fraction of Co^{3+} to Co^{2+} and/or a change in oxygen stoichiometry to ensure the charge compensation [21, 30]. An increase in the Ce level on the structure is expected to increase the number of surface oxygen, thus increasing gas molecules adsorption sites.

On top of the chemical composition, the morphology characteristics of perovskite materials have a significant influence on their response to gases. One dimensional (1D) nanofibers offer the potential for a substantial increase in the performance of gas sensors due to their high surface area and tiny inter-connected particles and high porosity which actually promote adsorption and diffusion of gas molecules, thus improving sensing performance [31, 32].

In view of this, the work presented here focuses in introducing different levels of Ce in the $LaCoO_3$ lattice to study the influence of the Ce on structure, morphology surface state and gas sensing performance of the $La_{1-x}Ce_xCoO_3$ NFs.

8.2 Experimental details

8.2.1 Synthesis of $La_{1-x}Ce_xCoO_3$ NFs

$La_{1-x}Ce_xCoO_3$ (x= 0, 0.05, 0.1, 0.15, 0.2) nanostructured NFs labelled as Ce_x (x=mol fraction of partially substituting in La-site), were prepared by electrospinning method. Lanthanum nitrate hexahydrate ($La(NO_3)_3.6H_2O$), cobalt nitrate hexahydrate ($Co(NO_3)_3.6H_2O$), cerium nitrate dihydrate($Ce(NO_3)_3.6H_2O$ and polyvinylpyrrolidone (PVP) were used as the starting materials without further purification. N-N dimethyleformamide (DMF) and ethanol were used as solvents. They were subsequently weighed at the required molar ratio for each formulation and mixed in a mixture of 6 ml DMF and 4 ml ethanol followed by stirring at 40 °C until completely dissolved. 1g of PVP was then added to the above solution and the mixture was continuously stirred for 2 h to obtain a homogeneous gel precursor solution. The precursor solution was then loaded into a 10 ml syringe for electrospinning at room temperature. The pumping rate of was 0.5 μlh^{-1} was applied at an applied voltage of 20 kV. The drum collector was placed 15 cm away from the spinneret. The obtained composite NFs were annealed at 650 °C at a heating rate of 2°$Cmin^{-1}$ for 2 hours in air to obtain the $La_{1-x}Ce_xCoO_3$ NFs.

8.3 Characterization of $La_{1-x}Ce_xCoO_3$ NFs

The composition and crystallinity of the $La_{1-x}Ce_xCoO_3$ NFs was determined by using an X-ray diffraction (XRD) Panalytical X'pert PRO PW3040/60 X-ray diffractometer with Cu/Kα a Cu-Kα (λ=1.5405 Å) radiation. The surface morphology of the $La_{1-x}Ce_xCoO_3$ NFs was observed using a ZEIS-AURIGA field emission-scanning electron microscopy (FESEM) at an acceleration voltage of 3

kV. Nitrogen (N_2) adsorption-desorption isotherms were measured at 77 K using a Micrometirics TRISTAR 300 surface area analyser for surface area and porosity measurements. X-ray photoelectron spectra (XPS) were recorded with a PHI 5000 Versaprobe X-ray photoelectron with monochromatic Al-Kα radiation ($h\nu$ = 1486.6 eV).

8.4 Preparation and gas sensing procedure of $La_{1-x}Ce_xCoO_3$ NFs

The $La_{1-x}Ce_xCoO_3$ based sensors were prepared as follows: Equal powder mass of 40 mg of each sample was mixed with a solution of ethyl cellulose in turpineol and ground for a few minutes to make thixotropic pastes. The obtained pastes were coated onto an alumina substrate fitted out with a pair of platinum (Pt) electrodes on the top surface (sensor part) and a heater on the bottom surface to control the operating temperature. The sensors were then subjected to heating at 300 °C for 2 hours to achieve good adhesion of the pastes. The gas sensing measurements were carried out using a KSGAS6S gas sensing station (KENOSISTEC, Italy) in a variety of test gases namely acetone, ethanol, methanol, isopropyl alcohol, ammonia, nitrogen dioxide, carbon dioxide and carbon monoxide from room temperature (RT) to 180 °C. The required target gas concentration was delivered into the sensing chamber using MKS Instruments Deutschland GmbH mass flow controllers by diluting the concentrated target gas with reference synthetic air. The electrical resistance fluctuations during the introduction and withdrawal of the target gas molecules in the sensing chamber containing the $La_{1-x}Ce_xCoO_3$ NFs based sensor devices were measured both in air *(Ra)* and in target gas *(Rg)* using a Keithley 6487 Picoammeter/voltage source meter. Since the sensors are of p-type conductivity, the sensor response was then

determined as the ratio of the electrical resistance in the gas to that in air (*Rg/Ra)* [33].

8.5 Results and discussion

8.5.1 Crystal phase composition, morphology, pore structure and surface chemistry of the $La_{1-x}Ce_xCoO_3$ composites

The crystallinity and phase purity of the $La_{1-x}Ce_xCoO_3$ composites were determined through XRD and are shown in Figure 8.1. The XRD patterns for the pure $LaCoO_3$ (x= 0) revealed that the synthesized products fully crystallized in rhombohedral perovskite phase (JCPDS card no. 01-075-0279). This phase was maintained up to x= 0.05. As from x≥ 0.1, the composites displayed XRD patterns of cubic $LaCoO_3$ and this was indicated by the clearly merging of the two reflections positioned at 33.0 and 33.2 ˚into one diffraction peak [34]. Moreover, with increasing Ce content, a new diffraction peak at 28.1˚ corresponding to CeO_3 appeared. The solubility of cerium in these samples was low and limited to x≤ 0.1. Further, the average crystallite sizes were estimated using Scherrer's equation [31] based on a full width at half maxima (FWHM) of the (012) peak and the resulting values are listed in Table 8.1. The crystallite sizes decreased with increasing Ce values (see Table 8.1), suggesting that the addition of Ce hinders crystal size growth. From these XRD results, it can be said that partial substitution of La with increasing content of Ce resulted in the hindrance of the crystal growth, appearance of additional phase and change of the rhombohedral to cubic perovskite structure.

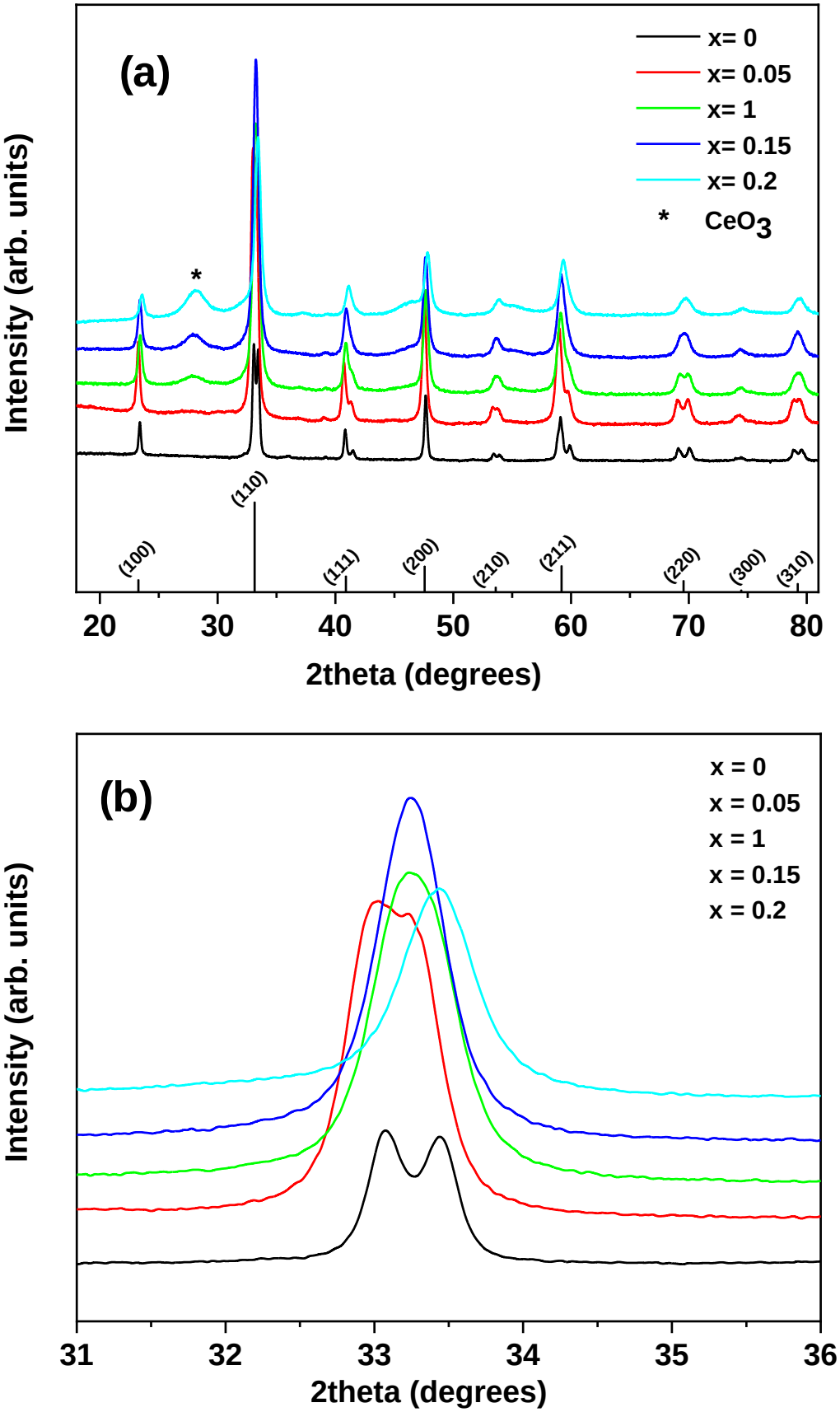

Figure 8.1: XRD patterns of the $La_{1-x}Ce_xCoO_3$ (x = 0, 0.05, 0.1, 0.15 and 0.2) NFs.

Figure 8.2 reveals the morphology of the obtained samples through SEM imaging. As observed, the images revealed inter-joined particles of average particle size of 15-60 nm forming a fiber like morphology for all the samples. The substitution of La with Ce reduced the particle size of the inter-joined particles with increasing Ce content which led to compactness of the fibers. The reduced size of the particles implies improvement of the surface-to-volume ratio of the NFs which may be beneficial during gas sensing by providing abundant active sites for oxide and target gas interactions thus improving the sensing performance of the sensors.

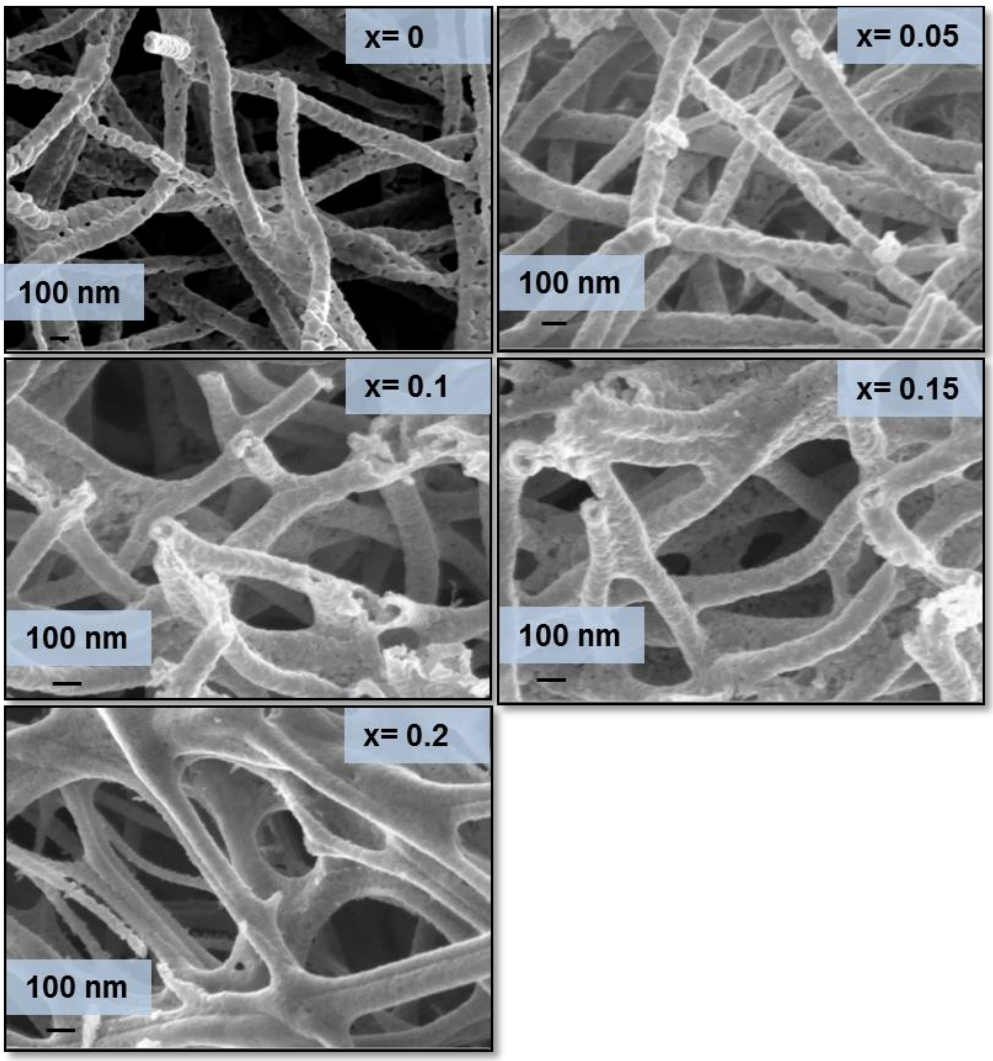

Figure 8.2: SEM images of the $La_{1-x}Ce_xCoO_3$ NFs at different Ce content.

Gas sensing is a surface based mechanism which highly relies on available active sites brought upon by the surface area. So to establish the surface area and porosity characteristics of the $La_{1-x}Ce_xCoO_3$ samples, nitrogen adsorption measurements were carried out. Figure 8.3 depicts the resulting N_2 adsorption/desorption isotherms with their corresponding pore size distribution as insets. The shape of the isotherms was characterized as type IV according to the IUPAC. In addition, a hysteresis loop was observed at high relative pressures for all the composites, indicating the presence of bulk mesopores (2- 50 nm in diameter) formed between the particles [35]. The BET surface area increased linearly with the increase of Ce indicating that the increase of the stoichiometric ratio of Ce improves the surface area of the NFs. In general, the specific surface area is related to the particle size, the smaller the particle size, the greater surface area exposed [31] which is what was observed from the SEM studies. Moreover, when the surface area is large, the catalytic active site also increases and as a result, the gas sensor performance tends to be enhanced. On the other hand, the pore diameter (see Table 8.1) was found to decrease with the Ce content, which could also favour the response kinetics; namely the recovery rate as smaller pore diameter is advantageous for quick gas desorption thus shortening the recovery time [26].

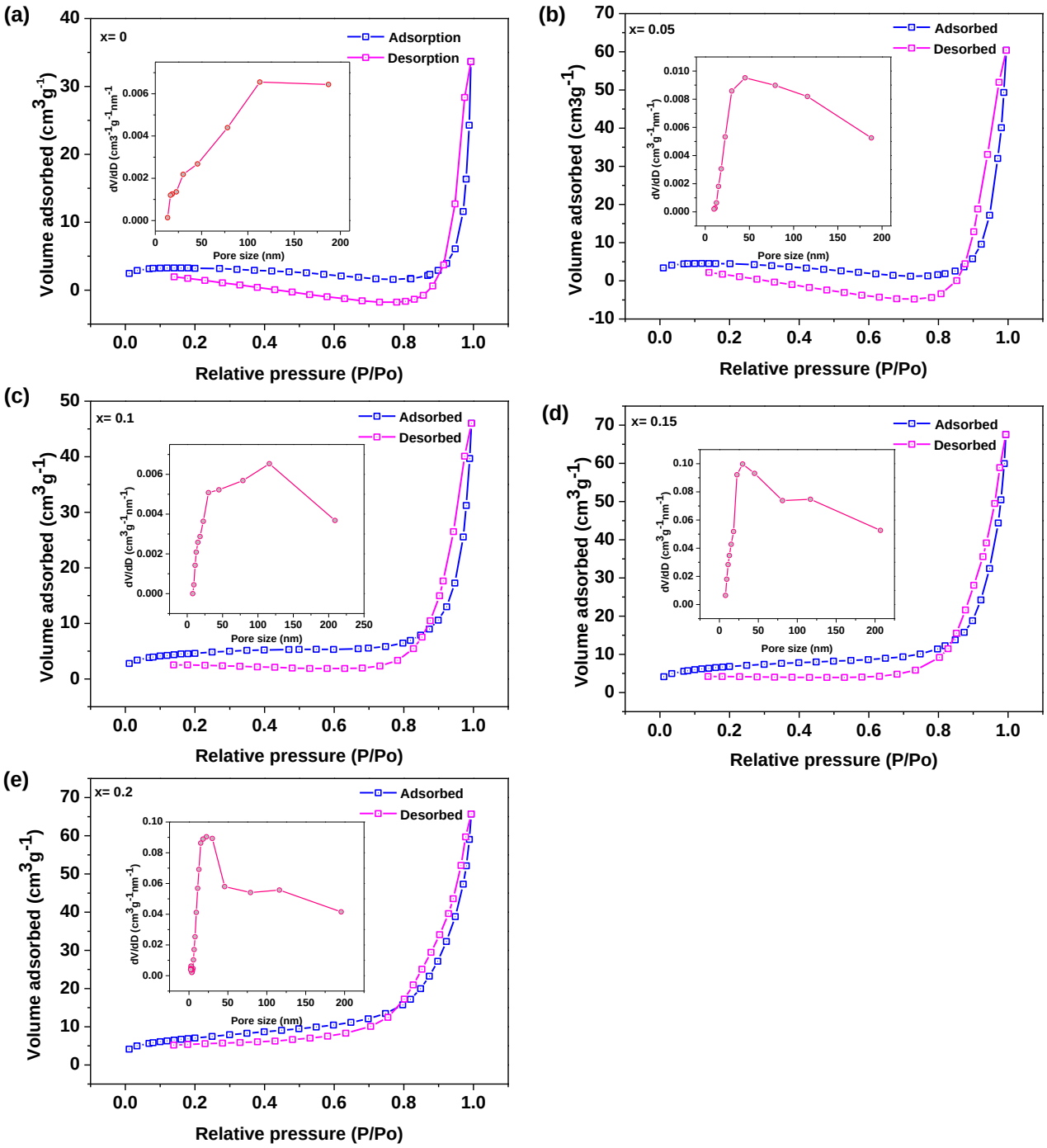

Figure 8.3: Nitrogen adsorption-desorption isotherms for the $La_{1-x}Ce_xCoO_3$ and their corresponding pore distribution as insets.

Table 8.1: Summary of XRD (crystallite size), SEM (particle size) and BET (surface area, pore diameter and volume) characteristics.

Sample	XRD D (nm)	SEM D (nm)	Surface area (m^2g^{-1})	Pore diameter (nm)	Total pore volume (cm^3g^{-1})
x= 0	32.4	58.0	10.79	63.92	0.0537
x= 0.05	23.1	31.4	14.86	45.60	0.0998
x= 0.1	19.0	24.4	16.36	41.19	0.0695
x=0.15	16.6	24.2	24.25	33.83	0.0102
x= 0.2	16.0	15.3	25.37	21.39	0.1017

For gas sensing, the surface chemistry characteristics of the material are always of importance, thus XPS was used to identify the chemical state and the relative abundance of the elements on the surface of the $La_{1-x}Ce_xCoO_3$ samples. Figure 8.4 shows the XPS spectra of La 3d, Co 2p, Ce 3d, and O 1s for the $La_{1-x}Ce_xCoO_3$, respectively. The XPS spectra of the La 3d consisting of a double peak for each spin-orbit component namely La $3d_{5/2}$ and La $3d_{3/2}$ core level located at 833.5-837.7 for La $3d_{5/2}$ and at 850.3-854.5 eV for La $3d_{3/2}$ are shown in Figure 8.4(a). The binding energy of La $3d_{5/2}$ and La $3d_{3/2}$ corresponds to that of pure lanthanum oxide, indicating that the La ions existed as La^{3+} state in all the $La_{1-x}Ce_xCoO_3$ samples [31, 36]. No apparent changes were observed on La 3d core level with the partial substitution of La by Ce.

The XPS spectra of the Co 2p core level in Figure 8.4(b) showed double peaks resulting from Co $2p_{3/2}$ contribution located at 779.1-779.6 eV and its corresponding satellite peak at 783.6-785.8 eV as well as the contribution from Co $2p_{1/2}$ at 794.3-794.8 eV along with its satellite peak at 801.7-803.6 eV. The

spin-orbit splitting of the Co $2p_{3/2}$ and Co $2p_{1/2}$ makes up to 15.2-15.5 eV which lies between 15 eV observed for the pure Co^{3+} state and 16 eV typical for the Co^{2+} state, indicating the coexistence of Co^{2+} and Co^{3+} in the materials [37, 38].

The high resolution spectra belonging to the Ce 3d is shown in Figure 8.4(c). At x= 0.05 and 0.1, the Ce 3d core level spectra could be divided into four peaks. As the Ce concentration was increased to x= 0.15 and 0.2, the Ce 3d spectra broadened and could be divided into six peaks. The peaks of the Ce $3d_{5/2}$ were positioned at 880.9-8821.1, 883.5-884.2, and 886.8-887.3 eV respectively, while the peaks of Ce $3d_{3/2}$ were located at 896.9-897.7, 899.5-900.4 and 903.8-904.7 eV. Out of these peaks, the ones at 883.5-884.2 and 903.8-904.7 eV belong to Ce^{3+} state, whereas the rest of the peaks belong to Ce^{4+} state [37, 39]. It can be noticed that at low Ce amounts of 0.05 and 0.1 only Ce^{4+} state exists over the surface of the samples, whereas higher Ce amounts leads to the coexistence of the Ce^{3+} and Ce^{4+} ions.

The XPS spectrum of the O 1s core level shown in Figure 8.4(d) revealed three oxygen components in $La_{1-x}Ce_xCoO_3$, respectively. The first peak located at lower binding energy of 527.4-528.7 eV can be attributed to the bulk-bound O^{2-}, the second peak positioned at 529.4-530.9 eV could be due to the contribution from surface adsorbed oxygen species O_2^{2-}/O^-. The third peak resulting from hydroxyls and carbonate species (OH^- and CO_3^{2-}) was observed around of 531.2-532.1 eV [40, 41]. From these results, it was realized that the quantity of the surface adsorbed oxygen species increased with the substitution of Ce (see Table 8.2), indicating larger populations of O_2^{2-}/O^-. Normally, partial substitution of Ce on the La site introduces surplus of negative charges in the lattice and has to be

compensated by oxidation of Co^{3+} to Co^{4+}, or by creation of oxygen vacancies to keep the electro-neutrality conditions [21, 37]

Furthermore, for gas sensing, the quantity of oxygen vacancies contributes to the sensor response due to availability of adsorption sites. Therefore, the increase of the oxygen vacancies in this case can possibly be favourable for the gas interactions with the oxide material.

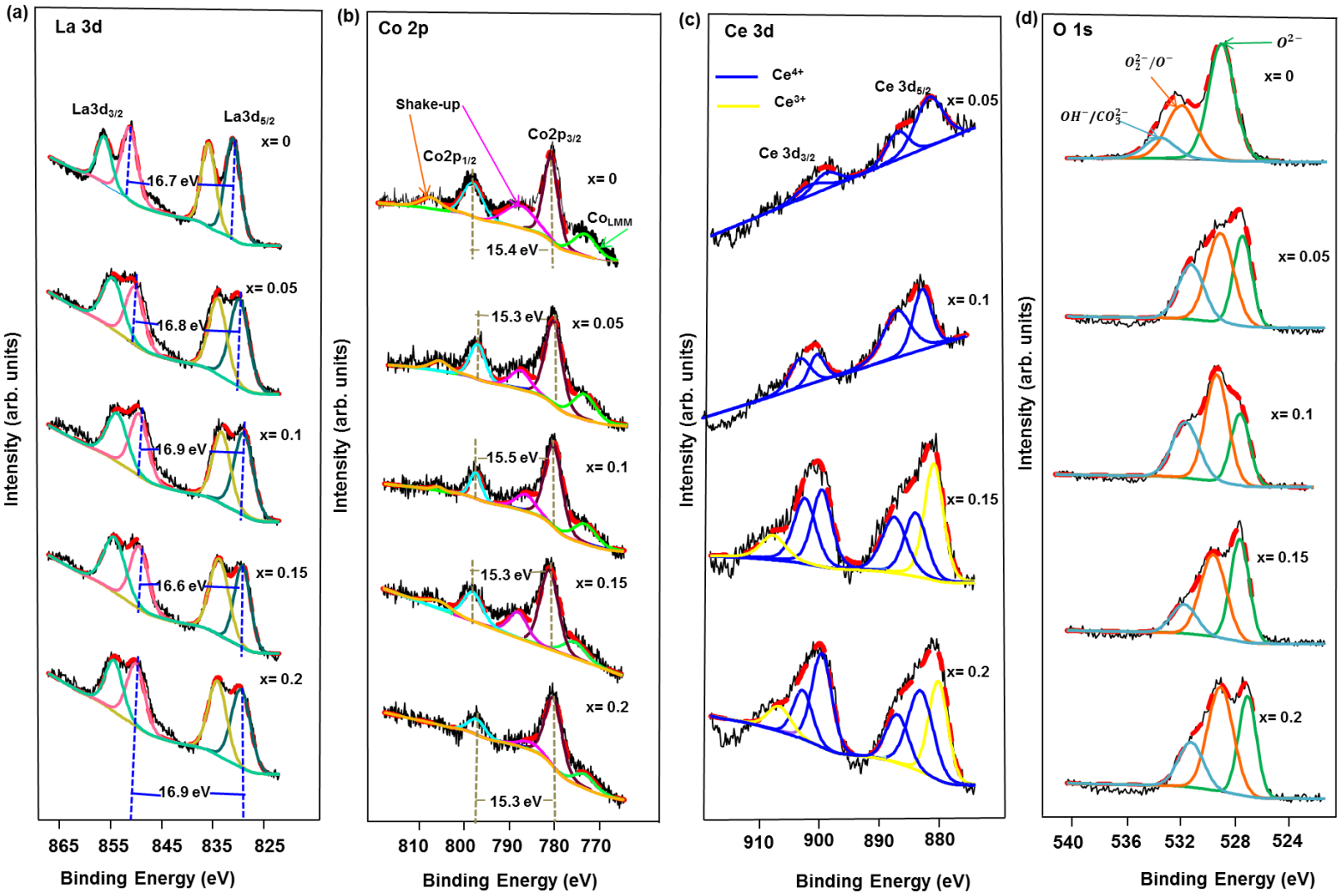

Figure 8.4: XPS spectra for (a) La 3d, (b) Co 2p, (c) Ce 3d and (d) O 1s for different Ce concentration.

Table 8.2: XPS O 1s core level binding energies

Sample	O^{2-}	O_2^{2-}/O^-	OH^-, CO_3^{2-}
x = 0	56.7	31.1	12.3
x = 0.05	30.4	43.6	25.9
x = 0.1	25.7	46.5	27.8
x = 0.15	40.0	44.6	15.4
x = 0.2	32.5	47.5	19.9

8.6 Gas sensing properties

The gas sensing mechanism and kinetics are normally influenced by the operating temperature. Based on this, it was important to evaluate the response of the $La_{1-x}Ce_xCoO_3$ composites based sensors to ethanol at different operating temperatures and to determine the best sensor amongst them and their optimal operating temperature. The response is based on the resistance change of the sensing material influenced by adsorption and desorption of target gas on the sensor material surface and is obtained by taking the ratio of the resistance in gas *(Rg)* to that in air *(Ra)* [11]. Figure 8.5 shows the responses of $La_{1-x}Ce_xCoO_3$ NFs based sensors to 40 ppm of ethanol at working temperature ranging from room temperatures to 180 °C. The responses of the sensors were found to increase with the increase in operating temperature, and then reached a maximum response, followed by a decrease in response with further increase in the temperature.

Normally, the response of SMO based sensors is reported to improve in proportion with the operating temperature. This is due to the fact that at low working temperatures the reaction between target gas molecules and surface adsorbed oxygen species doesn't give high response as the target gas molecules

do not have enough thermal energy to engage in a reaction with the surface oxygen species. Whereas further increase of the operating temperature gives enough thermal energy to activate the target gas molecules resulting in a rapid reaction with the oxygen species therefore leading to an increase in sensor response. However, at higher working temperatures the gas adsorption capacity and the usage of the sensing layer gets limited, thus resulting in the decrease of the sensor response [42]. Sensors based on Ce content levels of x = 0 and x = 0.1 reached their maximum responses of 32.4 and 70.8 at 120 °C, whereas the rest of the sensors (1.e. x = 0.05, 0.15 and 0.2) reached their maximum responses of 35.9, 39.9 and 83.4 at 100 °C, respectively.

The difference in optimum temperatures of the sensors can be due to their differences in the catalytic oxidation of ethanol by the samples at different temperatures [42, 43]. Moreover, the Ce partially substituted sensors revealed improved ethanol response with the x = 0.2 revealing a response more than twice as high as x = 0 which clearly indicate that the ethanol sensing response was improved by the addition of Ce. Further, the optimum operating temperature of x = 0.2 was lower than that of x = 0, which is a good sensor characteristics as sensors operating at low temperatures reduce energy consumption and also ensures measuring safety [44]

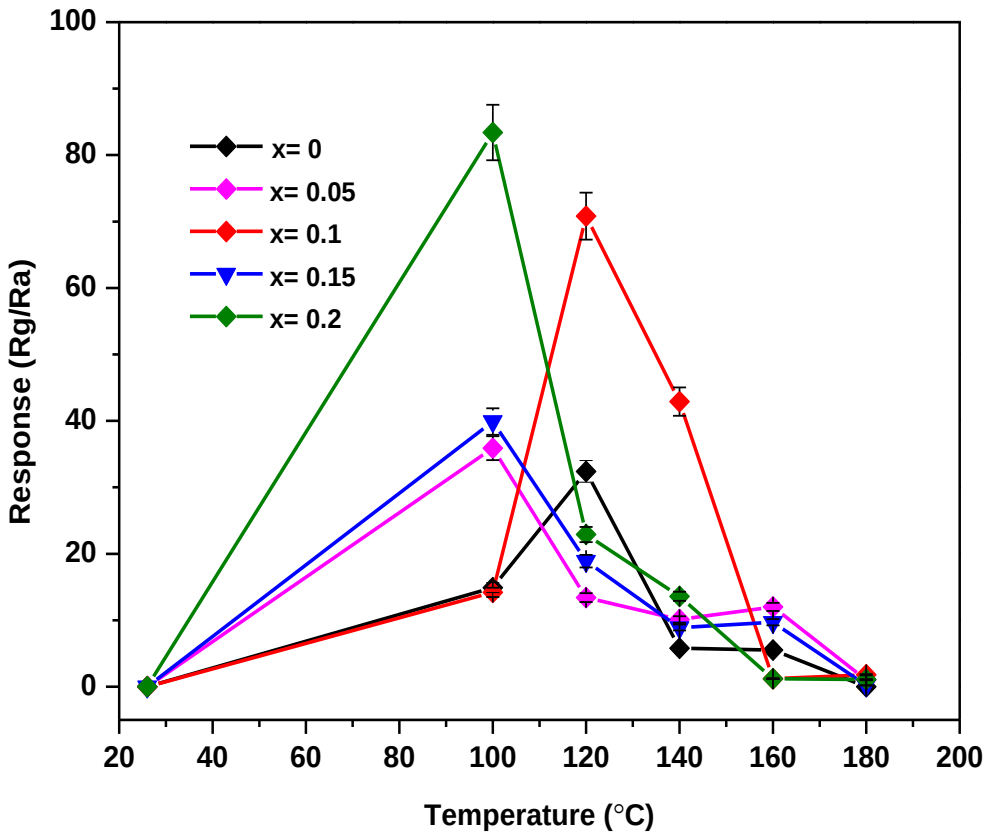

Figure 8.5: Response curves of the $La_{1-x}Ce_xCoO_3$ NFs sensors to 40 ppm ethanol gas at different operating temperatures.

Further investigations regarding the differences in gas sensing properties of the $La_{1-x}Ce_xCoO_3$ were performed at 100 °C. Figure 8.6(a-e) shows the resistance variations of the $La_{1-x}Ce_xCoO_3$ based sensors when exposed to ethanol. The resistance of the sensors increased sharply in the presence of ethanol and dropped rapidly to resistance values close to initial resistance when exposed to air. Further, the resistance of the sensors showed a proportional relation with the increase in ethanol, demonstrating dependence of the resistance on target gas concentration. For a p-type sensor, the resistance is expected to increase in the presence of a reducing gas such as ethanol [44], which is the kind of trend

observed in this case. As mentioned earlier, the response of the sensors in this work was evaluated as the ratio of the sensor resistance in the target gas to the sensor resistance in air and the resulting responses by the sensors as shown in Figure 8.6(f). A linear relation is observed clearly demonstrating the dependence of the response on the ethanol concentration.

Another important characteristic is the amount of time the sensor takes to respond to the target gas and to also recover to its initial state when the target gas has been withdrawn, namely response and recovery times. The response times of the sensors were determined to be 240, 23, 118, 24 and 10 s, whereas the recovery times were determined to be 286, 44, 159, 27 and 19 s, respectively. It's interesting to note the longer recovery time in comparison to the response time for all samples. This could be explained in terms of the material's pore structure as during gas detection process; the target gas diffused all the way through the sensing material and occupied the active sites. If the pore structure is large, desorption will be delayed, therefore leading to longer recovery time [26]. In this case the sensor based on x = 0.2 displayed the shortest recovery time in comparison to the rest of the sensors due to its smaller pores as established from BET studies. Even so, all the Ce partially substituted sensors demonstrated shorter response and recovery times in comparison to the pure $LaCoO_3$ under the same conditions. The quick response and recovery times may be attributed to the enhanced catalytic activity brought upon by Ce for the oxidation of ethanol.

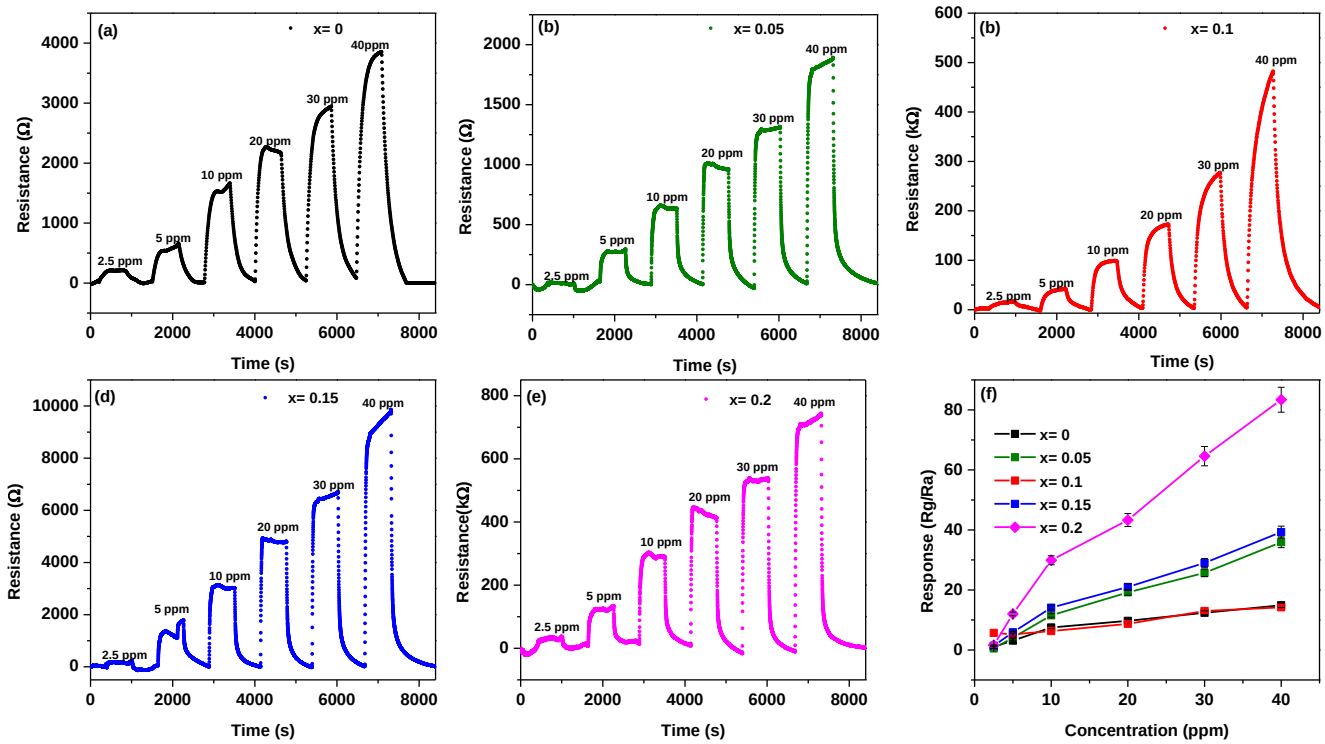

Figure 8.6: (a-e) Dynamic sensing transients to 2.5-40 ppm ethanol and (f) response of the sensors as a function of ethanol concentration.

For a sensor to be deemed as good for practical applications, its ability to give high response and fast response kinetics should be coupled with the ability to selectively distinguish the target gas in the mixture of other gases. Therefore, to demonstrate this characteristic, the sensors were all exposed to 40 ppm of other gases namely carbon monoxide (CO), carbon dioxide (CO_2), acetone (CH_3COCH_3), methanol (C_3OH), isopropyl alcohol (C_3H_8O), ammonia (NH_3) and nitrogen dioxide (NO_2) at 100 °C. The obtained results are displayed in Figure 8.7(a). All sensors demonstrated exceptional selectivity to ethanol with exception for sensor based on x = 0.1 which showed a slightly higher response to acetone than ethanol. The sensor based on x = 0.2 revealed the highest response to ethanol

with minor responses towards other gases. The selectivity towards ethanol might be due to matching of the lowest unoccupied molecular orbital energy level of ethanol with the activation energy of the sensing material's surface, low activation energy and low dipole moment of ethanol [45-47]. The compromised ethanol response in the presence of acetone molecules for the sensor based on x = 0.1 may be that the x = 0.1 surface strongly interacts with acetone molecules than ethanol at this given temperature. Additionally, repeatability of the sensor response is another significant aspect of a good gas sensor in practical applications. So, the sensor response repeatability test to 5 response/recovery cycles of the sensor based on x = 0.2 was carried out and the results are depicted in Figure 8.7 (b). The results established steady high response with excellent recovery without any obvious changes on the sensor response signifying stable response. Further, the stability of the sensor was also studied by measurement of the gas response to 40 ppm of ethanol at 100 °C every 7 days for two months. The sensor can be classified as stable according to the results in Figure 8.7 (c). Even though the gas response has fluctuations, the sensor maintained 74.5 % of its response. Based on these findings, the sensor based on x = 0.2 demonstrated fitness for the application in the detection of ethanol at low concentrations.

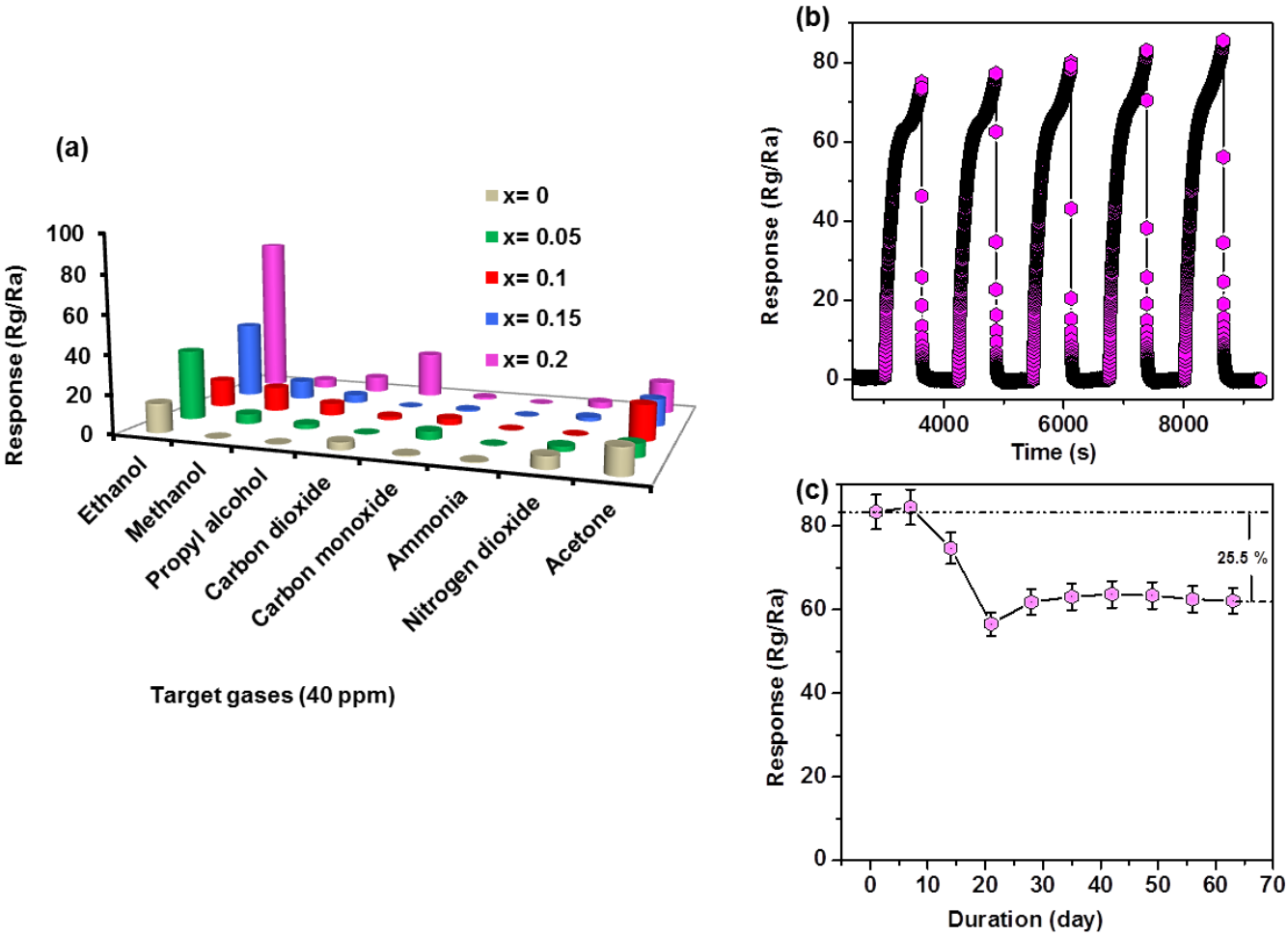

Figure 8.7: (a) The responses of the sensors based on the $La_{1-x}Ce_xCoO_3$ NFs to different kinds of target gases at 40 ppm (b) Repeatable responses to 40 ppm ethanol for x = 0.2 and (c) Response stability of x = 0.2 to 40 ppm ethanol over two months.

Humidity is one of the most influencial parameters in determining the overall sensing performance of sensors. With reference to the sensor technology, humidity has always been considered an obstacle and always results in different sensor response [45]. With that said, the ethanol sensing capabilities of the $La_{1-x}Ce_xCoO_3$ NFs based sensors was investigated by subjecting the sensors to

relative humid (RH) air environment consisting of 30, 50, 70 and 90% levels of RH. Figure 8.8 shows the obtained results which revealed degradation in the sensor response with increaseing RH levels. Normally, humid air interrupts the quality of the response due competition between the water molecules and the target molecules to occupy the active sites on the surface resulting in less chemisorption of oxygen and ethanol molecules on the sensor material's surface. Moreover, the water molecules will react and use most of the adsorbed surface oxygen resulting in less electrons to react with the ethanol gas [48].

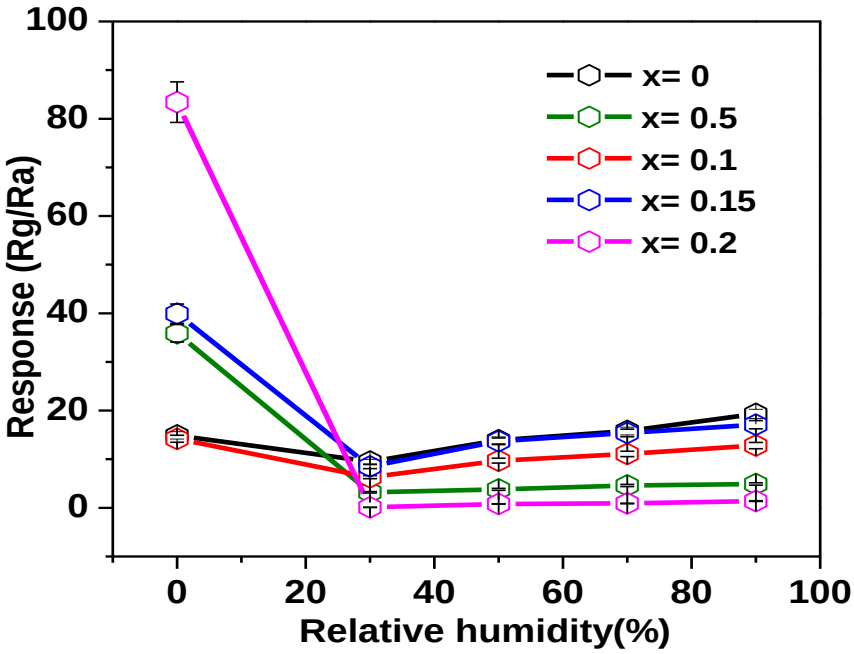

Figure 8.8: Response to 40 ppm ethanol at different RH levels of 30, 50, 70 and 90%.

8.7 Gas sensing mechanism of the $La_{1-x}Ce_xCoO_3$ NFs

$La_{1-x}Ce_xCoO_3$ is of p-type conductivity, therefore the quantity of the hole charge carries is more than electrons. When $LaCoO_3$ NFs are exposed in the ambient air,

the oxygen molecules adsorb on the surface of the $LaCoO_3$ NFs and convert into ionic species of O_2^-, O^- and O^{2-} by extracting electrons from the valence band. The type of the ionic species depends on the operating temperature [31]. In this case the optimal temperature is 100 °C, therefore O^- is the stable and dominating oxygen species [31]. The holes accumulate on the surface of $La_{1-x}Ce_xCoO_3$ NFs to form a hole accumulation layer (HAL) resulting in a resistance (Ra) drop. Morphology also plays a crucial role in the sensing mechanism, for the NFs based sensors, the formed hole accumulation layer may overlap with each other along the NFs direction; thus creating a continuous hole transfer channels. In the case where the $La_{1-x}Ce_xCoO_3$ NFs are exposed to ethanol, the ethanol gas molecules adsorb and react with the chemisorbed oxygen species according to the equation (8.1)

$$C_2H_5OH + O^- \rightarrow CH_3CHO + H_2O + e^- \quad (8.1)$$

$$CH_3CHO + 5O^- \rightarrow 2CO_2 + 2H_2O + 5e^- \quad (8.2)$$

Then CH_3CHO gets oxidized to CO_2 and H_2O through equation (8.2).

Ethanol molecules are then decomposed into CO_2 and H_2O, while electrons are released back into the valence band and recombined with the holes, resulting in a decrease of the hole accumulation layer and increase in resistance *(Rg).* The response of the $La_{1-x}Ce_xCoO_3$ NFs depends on the decomposition rate of the ethanol to CO_2 and H_2O on the surface of the NF. Thus the improved response of the $La_{1-x}Ce_xCoO_3$ NFs should be attributed to the reduced crystallite and particle size which brought upon enhanced surface area to accommodate more active sites for gas/oxide interactions. Further, Ce introduced more surface oxygen as

displayed by XPS findings which is beneficial during gas sensing processes. Additionally, the NF morphology provides porous channels, which are beneficial for the ethanol gas molecules adsorption and diffusion to the active sites.

8.8 Conclusion

In summary, nanostructured $La_{1-x}Ce_xCoO_3$ perovskite oxides ($0 \leq x \leq 0.2$) NFs were synthesized through the electrospinning method. XRD and SEM revealed that the crystallite and particle size decreased with increasing Ce level. From BET it was discovered that the specific surface area increased linearly up to 25 m^2/g with increasing Ce level. Ce segregation as CeO_2 was observed from the XRD patterns when the Ce addition level was x ≥0.1. The NFs displayed high selectivity towards ethanol with the $La_{1-x}Ce_xCoO_3$ (x = 0.2) reaching a response more than twice the one obtained for pure $LaCoO_3$ at operation temperature of 100 °C with quick response and recovery times of 10 and 19 s. The improved sensing performance can be attributed to the increased surface area and increased amount of surface oxygen brought upon by the addition of Ce. Not only did the Ce addition improve response and response kinetics, but it also reduced the operating temperature. Based on this, the $La_{1-x}Ce_xCoO_3$ (x = 0.2) based sensor can be regarded as a potential energy saving material to be used for the application of detecting low levels of ethanol molecules.

8.9 References

[1] M.M. Rahman, A. Jamal, S.B. Khan, M. Faisal, Biosens. Bioelectron, 28 (2011) 127-134.

[2] A. Loutfi, S. Coradeschi, G.K. Mani, P. Shankar, J.B.B. Rayappan, J. Food Eng., 144 (2015) 103-111.

[3] D. Smith, C. Turner, P. Španěl, J. Breath Res., 1 (2007) 014004.

[4] R.A. Kadir, R.A. Rani, A.S. Zoolfakar, J.Z. Ou, M. Shafiei, W. Wlodarski, K. Kalantar-zadeh, Sens. Actuators B Chem., 202 (2014) 74-82.

[5] A. Mirzaei, S. Leonardi, G. Neri, Ceram. Int., 42 (2016) 15119-15141.

[6] V.S. Bhati, M. Hojamberdiev, M. Kumar, Energy. Rep., Sep 20 (2019)

[7] S. Das, V. Jayaraman, Prog. Mater. Sci., 66 (2014) 112-255.

[8] X. Gao, T. Zhang, Sens. Actuators B Chem., 277 (2018) 604-633.

[9] K. Shingange, G. Mhlongo, D. Motaung, O. Ntwaeaborwa, J. Alloys. Compd., 657 (2016) 917-926.

[10] K. Shingange, Z. Tshabalala, B. Dhonge, O. Ntwaeaborwa, D. Motaung, G. Mhlongo, Mater. Res. Bull., 85 (2017) 52-63.

[11] H. Xiao, C. Xue, P. Song, J. Li, Q. Wang, Appl. Surf. Sci., 337 (2015) 65-71.

[12] M. Ghasdi, H. Alamdari, Sens. Actuators B Chem., 148 (2010) 478-485.

[13] H. Liu, H. Sun, R. Xie, X. Zhang, K. Zheng, T. Peng, X. Wu, Y. Zhang, Appl. Surf. Sci., 442 (2018) 742-749.

[14] S. Khan, R.J. Oldman, C.R.A. Catlow, S.A. French, S.A. Axon, J. Phys. Chem C., 112 (2008) 12310-12320.

[15] S. Thirumalairajan, K. Girija, N.Y. Hebalkar, D. Mangalaraj, C. Viswanathan, N. Ponpandian, RSC Adv., 3 (2013) 7549-7561.

[16] E.L. Brosha, R. Mukundan, D.R. Brown, F.H. Garzon, J. Visser, M. Zanini, Z. Zhou, E. Logothetis, Sens. Actuators B Chem., 69 (2000) 171-182.

[17] B. Bashir, M.F. Warsi, M.A. Khan, M.N. Akhtar, Z.A. Gilani, I. Shakir, A. Wadood, Ceram. Int, 41 (2015) 9199-9202.

[18] X. ZHANG, L. Huaju, L. Yong, S. Wenjie, Chinese J. Catal., 33 (2012) 1109-1114.

[19] T. Arakawa, H. Kurachi, J. Shiokawa, J. Mater. Sci, 20 (1985) 1207-1210.

[20] H. Liu, Y. Guo, R. Xie, T. Peng, G. Ma, Y. Tang, Sens. Actuators B Chem., 246 (2017) 164-168.

[21] M. Ghasdi, H. Alamdari, S. Royer, A. Adnot, Sens. Actuators B Chem., 156 (2011) 147-155.

[22] I. Lee, B. Jung, J. Park, C. Lee, J. Hwang, C.-O. Park, Sens. Actuators B Chem., 176 (2013) 966-970.

[23] A. Salker, N.-J. Choi, J.-H. Kwak, B.-S. Joo, D.-D. Lee, Sens. Actuators B Chem., 106 (2005) 461-467.

[24] H.R. Aliabad, V. Hesam, I. Ahmad, I. Khan, Physica B., 410 (2013) 112-119.

[25] A. Chainani, M. Mathew, D. Sarma, Phys. Rev B., 46 (1992) 9976.

[26] S. Yan, J. Xue, Q. Wu, Sens. Actuators B Chem., 275 (2018) 322-331.

[27] C. Gong, G. Fan, Y. Hou, C. Song, Q. Huang, Z. Zhang, Front. Chem. Eng. China., 1 (2007) 6-10.

[28] N. Bion, F. Can, X. Courtois, D. Duprez, In Metal Oxides in Heterogeneous Catalysis, Elsevier (2018), pp. 287-353.

[29] Y. Wen, C. Zhang, H. He, Y. Yu, Y. Teraoka, Catal. Today, 126 (2007) 400-405.

[30] R. Leanza, I. Rossetti, L. Fabbrini, C. Oliva, L. Forni, Appl. Catal B Environ., 28 (2000) 55-64.

[31] K. Shingange, H. Swart, G. Mhlongo, J. Alloys. Compd., 797 (2019) 284-301.

[32] Y. Zou, S. Chen, J. Sun, J. Liu, Y. Che, X. Liu, J. Zhang, D. Yang, ACS Sens., 2 (2017) 897-902.

[33] J.-C. Ding, H.-Y. Li, T.-C. Cao, Z.-X. Cai, X.-X. Wang, X. Guo, Solid State Ion., 303 (2017) 97-102.

[34] S. Farhadi, S. Sepahvand, J. Alloys. Compd., 489 (2010) 586-591.

[35] A.S. Ahammad, N. Odhikari, S.S. Shah, M.M. Hasan, T. Islam, P.R. Pal, M.A.A. Qasem, M.A. Aziz, Nanoscale Adv., 1 (2019) 613-626.

[36] Z. Dai, C.-S. Lee, B.-Y. Kim, C.-H. Kwak, J.-W. Yoon, H.-M. Jeong, J.-H. Lee, ACS Appl. Mater. Interfaces, 6 (2014) 16217-16226.

[37] X. Zhu, S. Zhang, Y. Yang, C. Zheng, J. Zhou, X. Gao, X. Tu, Appl. Catal B Environ., 213 (2017) 97-105.

[38] C. Fettkenhauer, X. Wang, K. Kailasam, M. Antonietti, D. Dontsova, J. Mater Chem A, 3 (2015) 21227-21232.

[39] K. Kuntaiah, P. Sudarsanam, B.M. Reddy, A. Vinu, RSC Adv., 3 (2013) 7953-7962.

[40] H.-J. Kim, H.-M. Jeong, T.-H. Kim, J.-H. Chung, Y.C. Kang, J.-H. Lee, ACS Appl. Mater. Interfaces., 6 (2014) 18197-18204.

[41] Y. Jiang, J. Deng, S. Xie, H. Yang, H. Dai, Ind. Eng. Chem. Res., 54 (2015) 900-910.

[42] X. Li, X. Zhou, H. Guo, C. Wang, J. Liu, P. Sun, F. Liu, G. Lu, ACS Appl. Mater. Interfaces., 6 (2014) 18661-18667.

[43] C. Wang, X. Cheng, X. Zhou, P. Sun, X. Hu, K. Shimanoe, G. Lu, N. Yamazoe, ACS Appl. Mater. Interfaces., 6 (2014) 12031-12037.

[44] S.-H. Hwang, Y.K. Kim, S.H. Hong, S.K. Lim, Sensors., 19 (2019) 3151.

[45] P. Shankar, J.B.B. Rayappan, ACS Appl. Mater. Interfaces., 9 (2017) 38135-38145.

[46] P. Shankar, J.B.B. Rayappan, ACS Appl. Mater. Interfaces., 8 (2016) 24924-24932.

[47] C. Cheng, G. Xu, H. Zhang, Y. Luo, J. Nanosci. Nanotechnol, 7 (2007) 4439-4442.

[48] G. Mhlongo, D. Motaung, F. Cummings, H. Swart, S. Ray, Sci. Rep., 9 (2019) 9881.

Chapter 9

Conclusion and future prospects

9.1 Conclusion

In summary, 1D La based complexes were successfully prepared using an electrospinning method followed by annealing method. It was realised that La doping into ZnO can dramatically enhance H_2S sensing and also improve the response kinetics and this can be attributed to synergetic effects of higher surface area, large number of intrinsic defects and the catalytic activity of La.

Further, on a separate study between $LaCoO_3$ and $LaFeO_3$ NFs, it was found that $LaFeO_3$ revealed a high selective response towards acetone due to improved surface area and high density of oxygen defects. The study on annealing $LaCoO_3$ nanofibers at different temperatures demonstrated the importance of crystallinity and nanofiber particle connectivity which was found to be the main reason behind the observed highly selective and stable ethanol sensing performance of $LaCoO_3$ obtained at 650 °C since the synergetic effects of enhanced surface area and good interconnected porous NF morphology provided access to active sites for gas interactions.

From the study focused on the effect of Au on $LaFeO_3$ NBs sensing performance, it was found that the Au/$LaFeO_3$ NBs based sensor with the optimal Au content of 0.3 wt% revealed better acetone sensing performance and its gas sensing behaviour was related to the size and distribution of the Au nanoparticles, which

controls the catalytic activity of the Au catalyst. Also the increased surface area and porosity induced by Au addition on the 1D NB structure also contributed to the increased gas sensing performance of the Au/$LaFeO_3$ NBs based sensor with the optimal Au content of 0.3 wt%.

Partial substitution of La by Ce was shown to improve the gas sensing performance of $LaCoO_3$ towards ethanol, which is evidenced by the enhanced response and lowering of the operating temperature. Such positive effects were attributed to the increased surface area and increased amount of surface oxygen brought upon by the addition of Ce.

9.2 Future prospects

As much as this work has shown the potential of using 1D La based oxides complexes as sensing materials, a lot still has to be considered to fully exploit these materials for market use. Firstly, the electrospinning method has shown to be a very good technique method for the development of 1D SMOs with different morphologies. However, it would be interesting to explore the combination of various fabrication methods such as Physical vapor deposition (PVD), Chemical vapor deposition (CVD) and Atomic layer deposition (ALD) to obtain nanostructures with different morphologies (bi-layer, core-shells or branched nanostructures) and dimensions. These above mentioned fabrication techniques allows for selective growth of nanostructures on patterned substrates and development of multi-layered nanostructures.

Not only is the exploration of fabrication methods beneficial for tuning the sensing properties, it is also ideal for determining a reproducible method of

fabrication as this has an influence on the sensing performance reproducibility of a material which is very important for devices that are aimed for practical applications, as their mass scale production will require a stable and reproducible fabrication method to be effective.

Another aspect to consider is the method for fabrication of the sensor strip/film. The sensing material (in this case the La based oxides complexes), has to interface with the sensor device surrounding electronics such as the Pt electrodes used in this work. Therefore, the design and reliability of these electrodes need to be taken into consideration as they may have effects on the overall performance of the sensor device especially at high operating temperatures. The method of depositing the sensing material onto the alumina substrate requires optimization to obtain the perfect layer thickness that gives better sensing performance.

One other aspect that this work has shown is that the fabrication of heterostructures i.e. La doped ZnO, Au loaded $LaFeO_3$ and Ce substituted $LaCoO_3$ can modify the sensing performance. These heterostuctures introduces secondary material onto the host material which give rise to effects such as p-n junctions, band bending and spill-over. And as much as there are models proposed at explaining the general sensing mechanism of SMOs, it becomes complicated when now a secondary material is introduced onto the host material. Therefore, it is important to understand singularly each occurrence (p-n junctions, band bending and spill-over) through experiments designed at confirming the presence of physical effects induced and this will require a high degree of control over the fabrication of such materials.

Based on this, the present work can stimulate more investigations towards the La based oxide complexes for the application in gas sensors as their flexibility allows for tuning of properties. Moreover, their sensitivity towards ethanol (especially $LaCoO_3$ NFS based sensors), can pave a way for them to be used for food security assurance to detect ethanol emissions from food stuffs such as milk and fruit. However, their ethanol sensing capabilities still have to be tested at higher concentration levels greater than 500 ppm which is way more than the range this work was focused on and also at humidity range around 60-90%. This work has shown that humidity deteriorates the response signal, therefore it is important to find materials that can be incorporated with the La based oxide complexes to assist in stabilizing the response in the presence of humidity or to find other methods that can produce the La based oxides complexes that can be stable in the presence of humidity.

Therefore, the La based oxide complexes have the potential to be applied for real time monitoring of gases provided more investigation is conducted on them.